Mechanical Characterization, Constitutive Modeling and Applications of Ultra-Soft Magnetorheological Elastomers

by

Miguel Ángel Moreno Mateos

A dissertation submitted by in partial fulfilment of the requirements for the degree of Doctor of Philosophy in

Mechanical Engineering and Industrial Organization

Universidad Carlos III de Madrid

Advisors:

Daniel García González
Ángel Arias Hernández

February 2023

Acknowledgements

Quiero agradecer a mis padres por haberme apoyado siempre, en todas las decisiones que he tomado y en los momentos en los que he necesitado un empujón. Mis padres y mis hermanas María y Lucía saben todo lo que ha supuesto llegar hasta aquí. Agradecer también a todos mis tíos, especialmente a mi tío Luis. Pero, sobre todo, a mi madre, un pilar fundamental.

Agradecer también a mis tutores Daniel García y Ángel Arias por darme la oportunidad de realizar esta tesis. A Daniel por su dedicación en este proyecto y por guiarme a lo largo de él de forma inmejorable. Ha sido y será mi ejemplo a seguir. A Ángel por la confianza que ha depositado en mí desde el primer momento, así como por sus sabios consejos.

A special gratitude goes to Paul Steinmann, professor at the Applied Mechanics Institute of the Friedrich-Alexander-Universität Erlangen-Nürnberg, and my supervisor during my research stay. I would like to thank Mokarram Hossain as well, professor at the University of Swansea, for his support and his belief in me. Likewise, Kostas Danas, professor at the École Polytechnique of Palaiseau, for all the insightful scientific discussion. Finally, my colleges at the LTM in Erlangen, who helped me feel like home during my research stay.

También agradecer al Departamento de Mecánica de Medios Continuos y Teoría de Estructuras y compañeros en el proyecto 4D-BIOMAP por el apoyo para realizar esta tesis doctoral. Gracias a Marisa, Sergio, Jorge, Miguel, Javier, Fran, Carlos, Sara, Clara, Andrés, Arrate y Diego, así como al resto de compañeros.

Finally, I want to acknowledge the support from the Ministerio de Ciencia, Innovacion Universidades, Spain (FPU19/03874), and the European Research Council (ERC) under the European Union's Horizon 2020 research and innovation programme (grant agreement No. 947723, project: 4D-BIOMAP).

Published and submitted content

Articles published in JCR journals:

1. D Garcia-Gonzalez, **MA Moreno**, L Valencia, A Arias, D Velasco. (2021). "Influence of elastomeric matrix and particle volume fraction on the mechanical response of magneto-active polymers," *Composites Part B: Engineering*, vol. 215, p. 108796. DOI: 10.1016/j.compositesb.2021.108796.

   The material contained in this article has been not included.

2. **MA Moreno**, J. Gonzalez-Rico, ML Lopez-Donaire, A Arias, D Garcia-Gonzalez. (2021). "New experimental insights into magneto-mechanical rate dependences of magnetorheological elastomers," *Composites Part B: Engineering*, vol. 224, p. 109148. DOI: 10.1016/j.compositesb.2021.109148.

   The material contained in this article has been wholly included in Chapter 3. The material from this source included in this thesis is not singled out with typographic means and references.

3. **MA Moreno-Mateos**, J Gonzalez-Rico, E Nunez-Sardinha, C Gomez-Cruz, ML Lopez-Donaire, S Lucarini, A Arias, A Muñoz-Barrutia, D Velasco, D Garcia-Gonzalez. (2022). "Magneto-mechanical system to reproduce and quantify complex strain patterns in biological materials," *Applied Materials Today*, vol. 27, p. 101437. DOI: 10.1016/j.apmt.2022.101437.

   The material contained in this article has been partially included in Chapter 3, Chapter 4 and Chapter 5. The material from this source included in this thesis is not singled out with typographic means and references.

4. **MA Moreno-Mateos**, ML Lopez-Donaire, M Hossain, D Garcia-Gonzalez. (2022). "Effects of soft and hard magnetic particles on the mechanical performance of ultra-soft magnetorheological elastomers," *Smart Materials and Structures*, vol. 31, p. 065018. DOI: 10.1088/1361-665X/ac6bd3.

   The material contained in this article has been wholly included in Chapter 3. The material from this source included in this thesis is not singled out with typographic means and references.

5. **MA Moreno-Mateos**, M Hossain, P Steinmann, D Garcia-Gonzalez. (2022). "Hybrid magnetorheological elastomers enable versatile soft actuators," *npj Computational Materials*, vol. 8, p. 162. DOI: 10.1038/s41524-022-00844-1.

   The material contained in this article has been wholly included in Chapter 3, Chapter 4 and Chapter 5. The material from this source included in this thesis is not singled out with typographic means and references.

6. S Lucarini, **MA Moreno-Mateos**, K Danas, D Garcia-Gonzalez. (2022). "Insights into the viscohyperelastic response of soft magnetorheological elastomers: competition of macrostructural versus microstructural players," *International Journal of Solids and Structures*, vol. 256, 111981. DOI: 10.1016/j.ijsolstr.2022.111981.

   The material contained in this article has not been included.

7. D Garcia-Gonzalez, T Ter-Yesayants, **MA Moreno-Mateos**, ML Lopez-Donaire. (2022). "Hard-magnetic phenomena enable autonomous self-healing elastomers," *Composites Part B: Engineering*, vol. 248, 110357. DOI: 10.1016/j.compositesb.2022.110357.

   The material contained in this article has not been included.

Articles submitted to JCR journals:

8. **MA Moreno-Mateos**, M Hossain, P Steinmann, D Garcia-Gonzalez. "Hard magnetics in ultra soft magnetorheological elastomers enhance fracture toughness and delay crack propagation," *Journal of the Mechanics and Physics of Solids*. Under review.

   The material contained in this article has been wholly included in Chapter 4 and Chapter 5. The material from this source included in this thesis is not singled out with typographic means and references.

Other research merits

Patents of invention:

1. Daniel García González, **Miguel Ángel Moreno Mateos**, María Arrate Muñoz Barrutia, Emanuel David Nuñez Sardinha. (2022). "Method For Generating And Controlling Complex Strain Patterns On Biological Materials, Magneto-Mechanical Stimulation System For Generating Complex Strain Patterns In Biological Materials". European Patent EP22382103.4. University Carlos III of Madrid.

Dissemination of works at international conferences:

1. **MA Moreno**, A Arias, D Garcia-Gonzalez. (2021). "Magneto-mechanical characterization and constitutive modelling at finite strains of magneto-active polymers". VI ECCOMAS Young Investigators Conference (YIC 2021). Oral presentation, Valencia, Spain.

2. **MA Moreno**, J Gonzalez-Rico, ML Lopez-Donaire, A Arias, D Garcia-Gonzalez. (2021). "Rate dependences in the magneto-mechanical response of magnetorheological elastomers: an experimental study". 7th International Conference on Mechanics of Composites (MECHCOMP7). Oral presentation - Porto, Portugal.

3. **MA Moreno-Mateos**, J Gonzalez-Rico, E Nunez-Sardinha, ML Lopez-Donaire, S Lucarini, A Arias, A Muñoz-Barrutia, D Velasco, D Garcia-Gonzalez. (2022). "Magnetorheological elastomers as active cellular substrates". 18th European Mechanics of Materials Conference (EMMC18). Oral presentation - Oxford, United Kingdom.

4. S Lucarini, **MA Moreno-Mateos**, K Danas, D Garcia-Gonzalez. (2022). "Homogenisation modelling of the viscoelastic response of soft magneto-rheological elastomers". 18th European Mechanics of Materials Conference (EMMC18). Oral presentation - Oxford, United Kingdom.

5. **MA Moreno-Mateos**, J Gonzalez-Rico, E Nunez-Sardinha, ML Lopez-Donaire, S Lucarini, A Arias, A Muñoz-Barrutia, D Velasco, D Garcia-Gonzalez. (2022). "Intelligent system based on magnetorheological elastomers to stimulate biological materials". 8th European Congress on Computational Methods in Applied Sciences and Engineering (ECCOMAS). Oral presentation - Oslo, Norway.

6. **MA Moreno-Mateos**, M Hossain, P Steinmann, D Garcia-Gonzalez. (2022). "Magneto-mechanical behaviour of extremely soft MREs: insights into the use of soft and hard magnetic particles". 11th European Solid Mechanics Conference (ESMC11). Oral presentation - Galway, Ireland.

7. **MA Moreno-Mateos**, ML Lopez-Donaire, T Ter-Yesayants, A Arias, M Hossain, P Steinmann, D Garcia-Gonzalez. (2022). "Hard Magnetics in Soft Magnetorheological Elastomers Enhance Fracture Behaviour and Enable for Magnetic Self Healing". 9th GACM Colloquium on Computational Mechanics. Oral presentation - Essen, Germany.

International Ph.D visiting research:

Dates: February, 2022 - May, 2022.
Institution: Friedrich-Alexander-Universität Erlangen-Nürnberg (FAU).
Supervisor: Prof. Paul Steinmann.

Abstract

Smart materials are bringing sweeping changes in the way humans interact with engineering devices. A myriad of state-of-the-art applications are based on novel ways to actuate on structures that respond under different types of stimuli. Among them, materials that respond to magnetic fields allow to remotely modify their mechanical properties and macroscopic shape. Ultra-soft magnetorheological elastomers (MREs) are composed of a highly stretchable soft elastomeric matrix in the order of 1 kPa and magnetic particles embedded in it. This combination allows large deformations with small external actuations.

The type of the magnetic particles plays a crucial role as it defines the reversibility or remanence of the material magnetization. According to the fillers used, MREs are referred to as soft-magnetic magnetorheological elastomers (sMREs) and hard-magnetic magnetorheological elastomers (hMREs). sMREs exhibit strong changes in their mechanical properties when an external magnetic field is applied, whereas hMREs allow sustained magnetic effects along time and complex shape-morphing capabilities. In this regard, end-of-pipe applications of MREs in the literature are based on two major characteristics: the modification of their mechanical properties and macrostructural shape changes. For instance, smart actuators, sensors and soft robots for bioengineering applications are remotely actuated to perform functional deformations and autonomous locomotion. In addition, hMREs have been used for industrial applications, such as damping systems and electrical machines.

From the analysis of the current state of the art, we identified some impediments to advance in certain research fields that may be overcome with new solutions based on ultra-soft MREs. On the mechanobiology area, we found no available experimental methodologies to transmit complex and dynamic heterogeneous strain patterns to biological systems in a reversible manner. To remedy this shortcoming, this doctoral research proposes a new mechanobiology experimental setup based on responsive ultra-soft MRE biological substrates. Such an endeavor requires deeper insights into the magneto-viscoelastic and microstructural mechanisms of ultra-soft MREs. In addition, there is still a lack of guidance for the selection of the magnetic fillers to be used for MREs and the final properties provided to the structure. Eventually, the great advances on both sMREs and hMREs to date pose a timely question on whether the combination of both types of particles in a hybrid MRE may optimize the multifunctional response of these active structures.

To overcome these roadblocks, this thesis provides an extensive and comprehensive experimental characterization of ultra-soft sMREs, hMREs and hybrid MREs. The experimental methodology uncovers magneto-mechanical rate dependences under numerous loading and manufacturing conditions. Then, a set of modeling frameworks allows to delve into such mechanisms and develop three ground-breaking applications. Therefore, the thesis has lead to three main contributions. First and motivated on mechanobiology research, a computational framework guides a sMRE substrate to transmit complex strain patterns *in vitro* to biological systems. Second, we demonstrate the ability of remanent magnetic fields in hMREs to arrest cracks propagations and improve fracture toughness. Finally, the combination of soft- and hard-magnetic particles is proved to enhance the magnetorheological and

magnetostrictive effects, providing promising results for soft robotics.

Resumen

Los materiales inteligentes están generando cambios radicales en la forma que los humanos interactúan con dispositivos ingenieriles. Distintas aplicaciones punteras se basan en formas novedosas de actuar sobre materiales que responden a diferentes estímulos. Entre ellos, las estructuras que responden a campos magnéticos permiten la modificación de manera remota tanto de sus propiedades mecánicas como de su forma. Los elastómeros magnetorreológicos (MREs) ultra blandos están compuestos por una matriz elastomérica con gran ductilidad y una rigidez en torno a 1 kPa, reforzada con partículas magnéticas. Esta combinación permite inducir grandes deformaciones en el material mediante la aplicación de campos magnéticos pequeños.

La naturaleza de las partículas magnéticas define la reversibilidad o remanencia de la magnetización del material compuesto. De esta manera, según el tipo de partículas que contengan, los MREs pueden presentar magnetización débil (sMRE) o magnetización fuerte (hMRE). Los sMREs experimentan grandes cambios en sus propiedades mecánicas al aplicar un campo magnético externo, mientras que los hMREs permiten efectos magneto-mecánicos sostenidos a lo largo del tiempo, así como programar cambios de forma complejos. En este sentido, las aplicaciones de los MREs se basan en dos características principales: la modificación de sus propiedades mecánicas y los cambios de forma macroestructurales. Por ejemplo, los campos magnéticos pueden emplearse para inducir deformaciones funcionales en actuadores y sensores inteligentes, o en robótica blanda para bioingeniería. Los hMREs también se han aplicado en el ámbito industrial en sistemas de amortiguación y máquinas eléctricas.

A partir del análisis del estado del arte, se identifican algunas limitaciones que impiden el avance en ciertos campos de investigación y que podrían resolverse con nuevas soluciones basadas en MREs ultra blandos. En el área de la mecanobiología, no existen metodologías experimentales para transmitir patrones de deformación complejos y dinámicos a sistemas biológicos de manera reversible. En esta investigación doctoral se propone una configuración experimental novedosa basada en sustratos biológicos fabricados con MREs ultra blandos. Dicha solución requiere la identificación de los mecanismos magneto-viscoelásticos y microestructurales de estos materiales, según el tipo de partículas magnéticas, y las consiguientes propiedades macroscópicas del material. Además, investigaciones recientes en sMREs y hMREs plantean la pregunta sobre si la combinación de distintos tipos de partículas magnéticas en un MRE híbrido puede optimizar su respuesta multifuncional.

Para superar estos obstáculos, la presente tesis proporciona una caracterización experimental completa de sMREs, hMREs y MREs híbridos ultra blandos. Estos resultados muestran las dependencias del comportamiento multifuncional del material con la velocidad de aplicación de cargas magneto-mecánicas. El desarrollo de un conjunto de modelos teórico-computacionales permite profundizar en dichos mecanismos y desarrollar aplicaciones innovadoras. De este modo, la tesis doctoral ha dado lugar a tres bloques de aportaciones principales. En primer lugar, este trabajo proporciona un marco computacional para guíar el diseño de sustratos basados en sMREs para transmitir patrones de deformación com-

plejos *in vitro* a sistemas biológicos. En segundo lugar, se demuestra la capacidad de los campos magnéticos remanentes en los hMRE para detener la propagación de grietas y mejorar la tenacidad a la fractura. Finalmente, se establece que la combinación de partículas magnéticas de magnetización débil y fuerte mejora el efecto magnetorreológico y magnetoestrictivo, abriendo nuevas posibilidades para el diseño de robots blandos.

Contents

List of Figures

List of Tables

1 Introduction

This doctoral dissertation provides novel experimental and computational approaches to understand the magneto-mechanical behavior of ultra-soft magnetorheological elastomers (MREs), i.e., brain-like stiffness. Moreover, it provides guidance for the design of applications based on soft-magnetic MREs, hard-magnetic MREs and, eventually, hybrid MREs combining both types of fillers.

1.1 Motivation

The research presented in this PhD thesis is framed within the European Research Council project 4D-BIOMAP. The main objective of the project is to propose new methodologies to enable for remote magneto-mechanical stimulation of biological structures and reversible evolution of their mechanical surrounding simulating relevant physiological and pathological processes. The project bets equally on experimental and computational approaches to develop novel solutions based on soft magneto-responsive structures and controlled by external magnetic fields. Therefore, the project lies in two main blocks: mechanistic-based biological processes and magneto-responsive soft materials. The research conducted herein addresses the main challenges associated to the synthesis, experimental characterization and computational modeling of such soft magneto-responsive materials.

Overall, smart materials are bringing sweeping changes in the way humans interact with engineering devices. A myriad of state-of-the-art applications are based on novel ways to actuate on structures that respond under different types of stimuli such as light [1], temperature [2, 3], electricity [4, 5], changes in the pH [6] and magnetic fields [7, 8]. Among them, materials that respond to magnetic stimuli enable to remotely modify their mechanical properties and macroscopic shape. Soft magnetorheological elastomers (MREs) are composed of a highly stretchable soft elastomeric matrix and magnetic particles embedded on it. Ultra-soft elastomeric matrices, i.e., stiffness in the order of 1 kPa, allow large deformations with small external actuations. Moreover, they are in the range of biological tissues, which is beneficial for mechanobiology applications.

The type of the magnetic particles plays a crucial role as it defines the reversibility or remanence of the material magnetization. In this way, MREs can contain two major sets of fillers, referred to as soft-magnetic magnetorheological elastomers (sMREs) and hard-magnetic magnetorheological elastomers (hMREs). sMREs exhibit strong changes in their mechanical properties when an external magnetic field is applied [9]. However, when the field

stops acting, such a change reverts to the original state, i.e., the magnetization of the sample is lost. The emergence of hMREs changed the paradigm by allowing sustained magnetic effects along time [7, 10]. hMREs, however, stand out not only for their self-sustained magnetorheological stiffening, but also for major shape changes. Unlike soft-magnetic structures, hard-magnetic ones have been proposed as ideal candidates not only when magnetorheological effects are desired, but also for morphological changes [11]. Engineering applications demand accurate control of the material properties to achieve desired material behaviors. In the literature, end-of-pipe applications of MREs are based on two major characteristics: i) the modification of their mechanical properties (i.e., magnetorheological (MR) effect) and ii) macrostructural shape changes. Smart actuators and sensors are based on the deformation that results from magnetic internal torques [12–20]. Soft robotics, namely for bioengineering applications, such as cell manipulation, drug delivery, and non-invasive surgery, are remotely actuated to perform complex and repeatable movements [14, 19, 21–32]. In addition, hMREs have been used as multifunctional shape-changing structures, e.g., metamaterials and self-healing structures [15, 33–40], and for industrial applications such as damping systems and electrical machines [41, 42].

From the analysis of the current state of the art, some impediments that are preventing progress in this field can be identified. Although some relevant works on soft sMREs have been published [43–45], and fewer on hMREs [46, 47], to the best of the authors' knowledge there is still a gap of knowledge on extremely soft MREs. In the mechanobiology field there are not experimental methodologies to remotely control the mechanical environment of biological systems in a reversible manner and controlling complex heterogeneous strain patterns. In order to remedy this shortcoming, we propose a new mechanobiology experimental setup based on responsive MRE biological substrates. Therefore, the need of deeper insights into the magneto-viscoelastic mechanisms of MREs and the identification of the microstructural mechanisms governing the structural behavior is necessary to foster the eventual design of such novel applications. In addition, to the best of our knowledge there is still a lack of guidance for the selection of the magnetic fillers to be used for MREs and the final properties provided to the structure. Moreover, the great advances on both sMREs and hMREs to date pose a timely question on whether the combination of both types of particles in a hybrid MRE may optimize the multifunctional response of these active structures.

To overcome these roadblocks, this doctoral research starts providing an extensive and comprehensive experimental characterization of ultra-soft sMREs, hMREs and hybrid MREs. The experimental methodology uncovers magneto-mechanical rate dependences under numerous loading and manufacturing conditions. Then, a set of modeling frameworks allows to deepen on such mechanisms and develop three ground-breaking applications. Therefore, the thesis has lead to three main contributions. First and motivated on mechanobiology research, a computational framework guides a sMRE substrate to transmit complex strain patterns *in vitro* to biological systems. Second, we demonstrate the ability of remanent magnetic fields in hMREs to arrest cracks propagations and improve fracture toughness. Finally, the combination of soft- and hard-magnetic particles is proved to enhance the magnetorheological and magnetostrictive effects, providing promising results for soft robotics.

1.2 Objectives and methodology

The main objective of this doctoral dissertation is to uncover the magneto-mechanical behavior of ultra-soft MREs and provide guidance to design methodologies in the mechanobiology field, high-performance soft polymers and soft robots based on ultra-soft sMREs, hMREs and hybrid MREs. To this end, novel experimental and computational methods are expounded along the way. The following specific objectives (O) deepen on the aim of the present work:

O.1. Uncover magneto-viscoelastic mechanisms under different magneto-mechanical actuation modes of ultra-soft MREs. Elucidate the nature of such deformation mechanisms attending to the elastomeric matrix used and the type of magnetic fillers, i.e., soft-magnetic, hard-magnetic or a combination of both types of particles.

O.2. Develop constitutive and computational tools to describe and explore the underlying magneto-mechanical mechanisms that govern the material response attending to its microstructural features.

O.3. Conceptualize new ultra-soft MREs that combine superior magnetorheological and magnetostrictive responses.

O.4. Develop a new methodology based on ultra-soft MREs for mechanobiology studies. It must enable the remote stimulation of cell cultures through a remotely actuated sMRE substrate. To this end, it must allow to reproduce complex strain patterns found in biological materials, e.g., strain patterns within the brain under traumatic brain injury scenarios.

O.5. Conceptualize and characterize fracture-resistant ultra-soft MREs with remanent magnetic fields. The magneto-mechanical coupling must arrest cracks propagation and be tolerant of flaws.

O.6. Define soft actuators based on high-performance hybrid MREs. These must be endowed with a magnetorheological stiffening and enhanced shape-morphing capabilities under magnetic actuation.

The previous objectives are specified in the following Tasks (T), which can be further classified as experimental, modeling and applications categories:

Experimental tasks:

T.1. Design an experimental methodology to provide comprehensive characterizations of the macroscopic rheological behavior of ultra-soft MREs, under mechanical and magnetic loading.

T.2. Characterize the magneto-mechanical rate dependencies of MREs, the influence of the particles content, the stiffness of the matrix, and the pre-magnetization state. The methodology is to be extended to all sMREs, hMREs and hybrid MREs.

T.3. Provide a microstructural characterization through nanoindentation techniques.

Modeling tasks:

T.4. Define a macroscopic constitutive framework to provide guidance in the mechanobiological methodology. It must model the sMREs substrates under the actual operating conditions, i.e., reproduce the experimental strain patterns obtained with digital image correlation. Once calibrated, it can help define the mechanobiological experiment with the cell culture.

T.5. Conceptualize a macroscopic phase-field model for fracture of hMREs. The magneto-mechanical coupled problem must consider the influence of the magnetic state on the propagation of cracks.

T.6. Develop a microstructural homogenization framework for ultra-soft hybrid MREs. It must provide insights into the behavior of pre-magnetized MREs for different directions of the magnetic actuating field and multiple mixing ratios of soft- and hard-magnetic particles.

Applications tasks:

T.7. Define and characterize a sMRE substrate for mechanobiology studies. To this end, digital image correlation may provide continuous measures of the deformed surface of the substrate.

T.8. Design highly stretchable MREs with enhanced fracture performance.

T.9. Implement a virtual testbed to design micron-sized soft actuators and apply it on a bimorph hybrid MRE cantilever beam. It must allow to measure the magnetorheological stiffening as well as the shape-morphing capability.

The tasks are related to the main objectives according to Table 1.1.

Table 1.1: Connection between Tasks and Objectives.

Objective	**Related Tasks**
O.1.	T.1., T.2., T.3.
O.2.	T.4., T.5., T.6., T.9.
O.3.	T.2., T.6., T.9.
O.4.	T.2., T.3., T.4., T.7.
O.5.	T.8., T.5.
O.6.	T.2., T.6., T.9.

1.3 Outline

This thesis uncovers the magneto-mechanical behavior of ultra-soft MREs and explores original applications. The thesis is structured in three main chapters that encompasses experimental results, modeling and applications. In addition, two introductory chapters expound the motivation and state of the art of the research. A final chapter highlights the original contributions derived from the objectives presented above.

- **Chapter 1 - Introduction**. An overview of the motivation and objectives of this doctoral dissertation is presented. Specific tasks are linked to specific objectives.
- **Chapter 2 - State of the art**. This chapter presents a review on the experimental manufacturing and characterization methodologies, modeling and applications of MREs. First, a brief description on soft-/ hard-magnetic particles and ultra-soft matrices introduces the main features of the MREs in this work. Some conventional and more recent additive manufacturing methodologies expound some key aspects to fabricate such MREs. Moreover, the fundamentals of magneto-mechanical rheology are introduced, since it is the main experimental technique used in this thesis. Second, the discourse enters the foundations for the constitutive modeling of MREs at finite strains, i.e., kinematics, field equations and microscale-/macroscale-based constitutive approaches. Third, some state-of-the-art applications of soft MREs are reviewed.
- **Chapter 3 - Experimental**. The magnetorheological effect and shape-morphing capabilities are the mean features of ultra-soft MREs. Here, magneto-mechanical rheology encompasses the macroscopic characterization and nanoindentation covers the microscopic study. sMREs, hMREs and hybrid MREs are manufactured and tested for more than a hundred test conditions under mechanical and magnetic loading, e.g., monotonous compression, relaxation tests, DMA, oscillatory frequency sweeps, and a novel test under mechanically confined expansion and magnetic actuation. Besides, free deformation tests are performed to unveil the shape-morphing capability of hMREs. All these experiments allow to deepen into magneto-mechanical rate dependencies of ultra-soft MREs.
- **Chapter 4 - Modeling**. This chapter expands the constitutive framework used in this thesis. It starts with the definition of models for each phase of the MREs, i.e., matrix and magnetic particles. Then, a homogenization framework based on such a microstructural description establishes the scale transition scheme. The framework lies in the definition of periodic boundary conditions and it can prescribe macroscopic boundary conditions on either the primary fields or on the conjugate fields. Finally, two continuum models are introduced. The first reproduces the behavior of a sMRE substrate for mechanobiology studies. The second is a magneto-mechanical framework that includes a damage field to elucidate how remanent magnetic fields in hMREs arrest the propagation of cracks and, overall, enhance the fracture performance.
- **Chapter 5 - Applications**. Once provided the comprehensive characterization in Chapter 3 and the constitutive framework in Chapter 2, we explore three applications of ultra-soft sMREs, hMREs and hybrid MREs. The first application consists in a mechanobiology

methodology to stimulate biological material (i.e., cell cultures) with a sMRE substrate. The substrate is fabricated with different matrix mixing ratios to achieve four stiffness values. Then, digital image correlation is used to measure the strain of the deformed MRE. Four external permanent magnets are thoroughly placed with the aid of a numerical framework to reproduce complex strain patterns representative of physiological and pathological processes. To validate the methodology, the framework mimics the strains on the brain during a traumatic brain injury event. The second application comprises the conceptualization of fracture-resistant hMREs, where remanent magnetic fields arrest cracks propagation and enhance fracture toughness. Experimental and computational methodologies are combined to understand and characterize this effect. The third application lies in hybrid MREs to design soft actuators with enhanced magnetorheological stiffening and shape-morphing capability. The homogenization framework is applied to explore the effects of pre-magnetization and to explain how the combination of soft- and hard-magnetic particles affects the material behavior. Finally, a virtual testbed facilitates the design of a multifunctional bimorph micron-sized cantilever actuator.

- **Chapter 6 - Conclusions and future work**. A final chapter provides an outlook on the contributions of this doctoral dissertation. These relate to the objectives and hypotheses stated at the beginning of the thesis and foster future areas to explore.
- **Appendices A.1, A.2, A.3**. Three supplementary appendices contain additional results for the Experimental, Modeling and Applications chapters.

State of the art 2

This chapter presents an outlook on the experimental manufacturing and characterization methodologies, modeling and applications of MREs. First, a brief description of the types of magnetic fillers and ultra-soft matrices introduces the main features of the MREs in this work. Some conventional and more recent additive manufacturing methodologies expand key aspects to fabricate such MREs. Moreover, the fundamentals of magneto-mechanical rheology and the main rheological parameters are introduced. Second, the chapter addresses the foundations for the constitutive modeling of MREs at finite strains, regarding the main approaches and main ingredients of any magneto-mechanical material model. Finally, some state-of-the-art applications of MREs are reviewed.

2.1 Experimental

The design of novel applications based on MREs requires a thorough knowledge of their mechanical response. Overall, this response is governed by the magneto-mechanical interactions between the particles and between the carrier matrix and the particles. Consequently, the magneto-mechanical coupling in MREs motivates the combination of traditional experimental methods with the application of external magnetic fields [48]. Some works in the literature document experimental characterizations of both sMREs and hMREs. These experimental investigations, on the one hand, are dedicated to elucidate the mechanical properties of both sMREs and hMREs through a wide range of deformation modes (e.g., uniaxial tension/compression, pure/simple shear and equi-biaxial tension) under mechanical and magneto-mechanical loadings [49–55]. On the other hand, pure rheological and magnetorheological tests have been conducted to understand the effects of magnetic actuation on various rheological properties, such as the storage and loss moduli. For sMREs, the works by Stepanov et al. [56], Kallio [51] and Gordaninejad et al. [50] laid the foundations of a few experimental works that were performed under large mechanical stretching and coupled with the application of a magnetic field. In addition to the widely-used uniaxial tensile and compression experiments, Schubert and Harrison [52, 53] performed a series of shear and equi-biaxial tensile tests on isotropic and anisotropic sMREs. For a review on experimental characterizations of sMREs, the paper by Bastola and Hossain [57] could be consulted. Note that, although experimental studies of sMREs are available in the current literature, similar experimental characterizations for their hard-magnetic counterparts are quite limited at this point. Stepanov and co-workers [46, 58, 59] conducted some elementary mechanical and

magneto-mechanical tests on hMREs while other recent works on these promising composites can be found in Antonel et al. [60], Kramarenko et al. [58] and Koo et al. [13].

For a complete understanding of the mechanical behavior of MREs, a material characterization at two different scales is needed, i.e., macroscopic and microscopic scales. The macroscopic response of the MRE is governed by a strong structural component, i.e., local magneto-mechanical responses are governed by the structural/macroscopic coupling in the MRE [61]. In this regard, the magnetorheological mechanism is based on the differences in magnetic permeability between the continuous phase (carrier matrix) and the dispersed phase (magnetic particles). The magnetic particles get magnetized when they are subject to a magnetic field. Consequently, each particle becomes a magnetic dipole leading to interaction forces with the remaining particles and the external magnetic field. Opposed to these forces, the polymeric matrix acts as a deformation barrier transmitting the internal stresses within the composite. The consequence is a macroscopic deformation or, in case of being confined, an increase in material stiffness (the so-called magnetorheological effect) [57]. The magnitude of such a deformation or change in the material properties depends on the particles volume fraction, size, their magnetic properties (i.e., relative permeability, magnetic saturation) and the matrix's stiffness. Figure 2.1 illustrates the main types of magneto-responsive materials attending to the stiffness of the matrix. Note that the soft matrices in ferrofluids, hydrogels and ultra-soft elastomers allow the arrangement of particles. Overall, the spatial arrangement of the fillers determines the intensity and orientation of the interaction forces between them (i.e., isotropic and anisotropic structures).

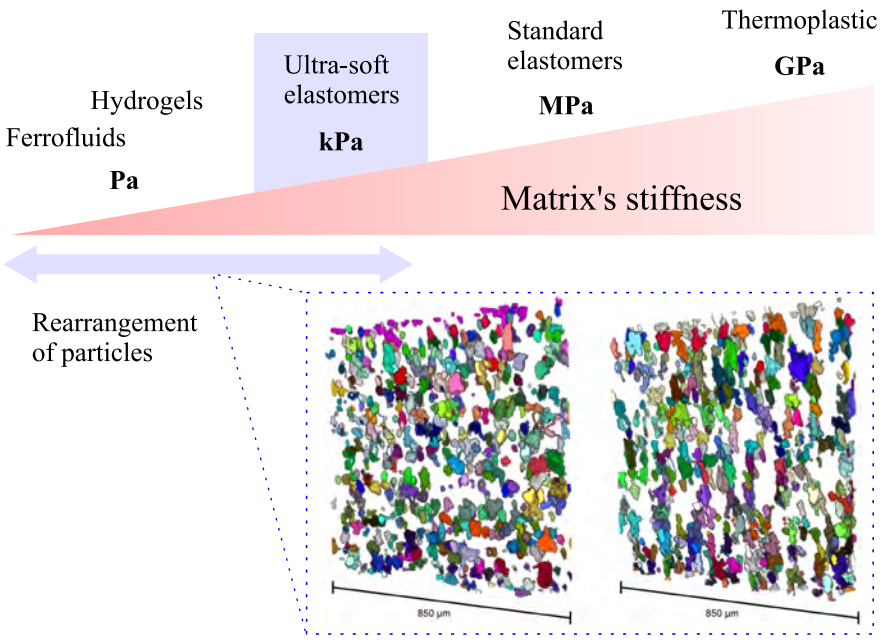

Figure 2.1: (Top) Types of magneto-responsive materials attending to the matrix's stiffness. (Bottom) 3D tomography of the particles within the composite. On the left, isotropic arrangement in the absence of magnetic actuation. On the right, the particles particles rearrange under magnetic actuation [43].

The most common experimental methods to bring information about the macroscopic response are [57]: compression/tensile tests, biaxial counterparts, simple shear test, fatigue test, dynamic mechanical analysis (DMA) and vibration analysis. Uniaxial compression ex-

periments bring relevant information, since the material is deformed in the same direction as the applied magnetic field [62, 63]. Furthermore, the viscous nature of MREs motivates the use of magneto-mechanical rheology to characterize visco-elastic materials in multiple modes, i.e., shear, axial, temperature or magnetic modes [44, 64–68]. In turn, the microscopic characterization provides information about the local stiffness of the material. Customarily, nanoindentation techniques have been used to characterize biological materials [69–71], hydrogels [72], film materials [73, 74], fiber composites [75] and particle-reinforced composites [76]. Nanoindentation bypasses structural effects providing a measure of the stiffness at a certain region within the surface of a sample.

2.1.1 Manufacturing

Soft- and hard-magnetic particles

Nowadays, the most used micron-sized magnetic particles are: mineral-based particles (e.g., magnetite and iron derived minerals), Terfenol-D particles and carbonyl iron powder (CIP) [77]. Among other factors, the chemical composition and the microstructure of the particles determine the magnetization that they experience when they are subjected to a magnetic field. In what concerns the microstructure, it can be either polycrystalline or onion-like [63]. According to their capability to retain the magnetization, the magnetic particles are classified as soft-magnetic particles and hard-magnetic particles. On the one hand, soft-magnetic particles totally demagnetize when the external magnetic field is removed. In this regard, note that particles with polycrystalline microstructure have a larger magnetization than onion-like microstructures. On the other hand, hard-magnetic particles have a larger magnetic coercivity and retain certain magnetization after being immersed in external magnetic fields. This effect owes to permanent microstructural changes and the rearrangement of the magnetic domains. Overall, Figure 2.2 summarizes the main features of sMREs and hMREs, i.e., conservative/dissipative magnetic behavior, volumetric/complex shape changes, and two representative applications for drug-delivery systems and soft actuators, respectively.

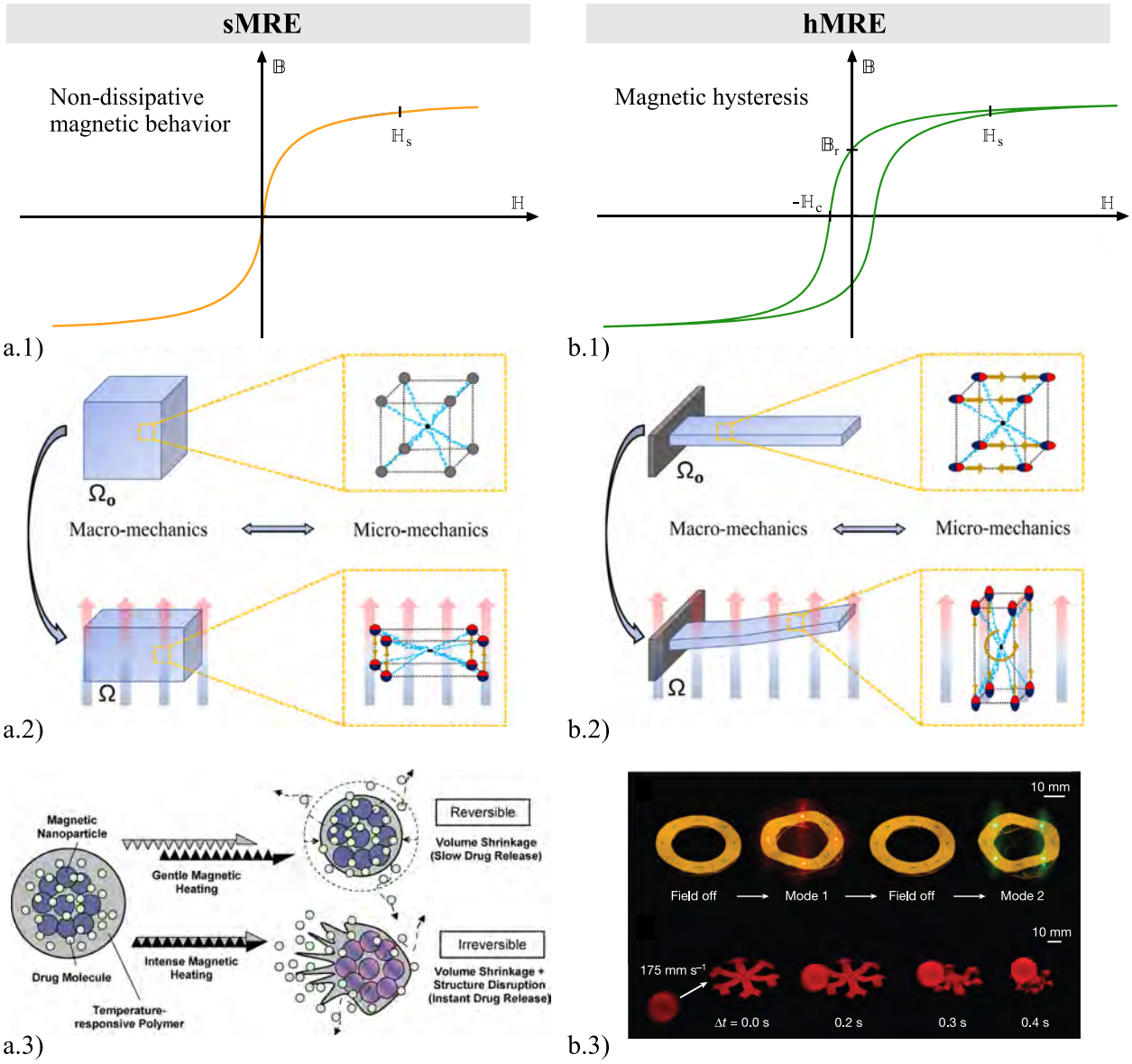

Figure 2.2: Fundamental comparison of sMREs and hMREs. (a.1) Non-dissipative magnetic behavior, (a.2) macro- and micro-mechanical interplays between matrix-particles and particles-particles leading volumetric changes [55], and (a.3) an illustrative application of a drug-delivery system [78]. Likewise, for hMREs, (b.1) dissipative magnetic behavior, (b.2) macro- and micro-mechanical interplays between matrix-particles and particles-particles leading complex shape changes [55], and (b.3) an illustrative application of a soft actuator [78].

Ultra-soft elastomeric matrix

The mechanical features of the carrier matrix strongly determine the overall behavior of the resulting MRE. Some common polymeric matrices are silicone rubbers, vinyl rubbers (VR), polyurethanes (PU), thermosetting and thermoplastic elastomers, and natural rubbers [79–86]. A common matrix used in the literature is Sylgard 184 [87], but this elastomer presents high stiffness limiting the magnetostrictive response of the composite. To overcome such a limitation, other authors have used softer elastomers, i.e., Eco-Flex silicone rubber [44, 45, 88]. In the literature, however, extremely soft PDMS matrices have been

scarcely used [87, 89, 90]. This doctoral thesis envisages such ultra-soft[1] MREs to amplify the magneto-mechanical response, i.e., magnetorheological and magnetostrictive effects. The previous Figure 2.1 depicts the stiffness range of magneto-responsive materials and the particles rearrangement phenomenon that occurs with soft matrices.

Molding and other conventional manufacturing techniques

A traditional method to manufacture MREs consists in mixing the raw materials, degassing the mixture to remove air bubbles, and curing the blend under high temperature to trigger the polymerization of the matrix [57, 63]. Note that a percolation threshold defines the maximum amount of fillers that can be added into the matrix. Beyond this point, the mobility of the particles along the mixture before curing is hindered [63]. Moreover, additives can also be added in the preprocessing to enhance the mechanical attachment between the particles and the matrix [91–93], and to prevent the oxidation of the particles [94]. After the polymerization, the particles lose their mobility and remain in fixed positions in the cross-linked matrix [95]. In this regard, extremely soft matrices may encounter sedimentation issues at the earliest stages of the curing [96]. To accelerate the polymerization and prevent the deposition of the particles, the curing temperature can be increased [97, 98]. Attending to the final arrangement of the magnetic particles, MREs are classified as isotropic and anisotropic [82, 83, 99, 100]. Isotropic MREs result when the blend of the raw materials is homogeneous and the curing is done in the absence of magnetic fields [83, 101–106]. However, a magnetic field can be applied during the curing to form anisotropic structures, e.g., microstructural chain-like formations [82, 83, 99, 101, 102, 104, 106–108]. Note that anisotropic MREs often present a larger magnetorheological stiffening [109–111]. Figure 2.3 illustrates the procedure just described.

[1] In this doctoral thesis, the term "soft MRE" is used to insist on the extremely soft nature of the matrix (∼1 kPa). It should not be confused with the term "soft-magnetic MRE" (sMRE), which describes the magnetic non-dissipative nature of soft-magnetic particles.

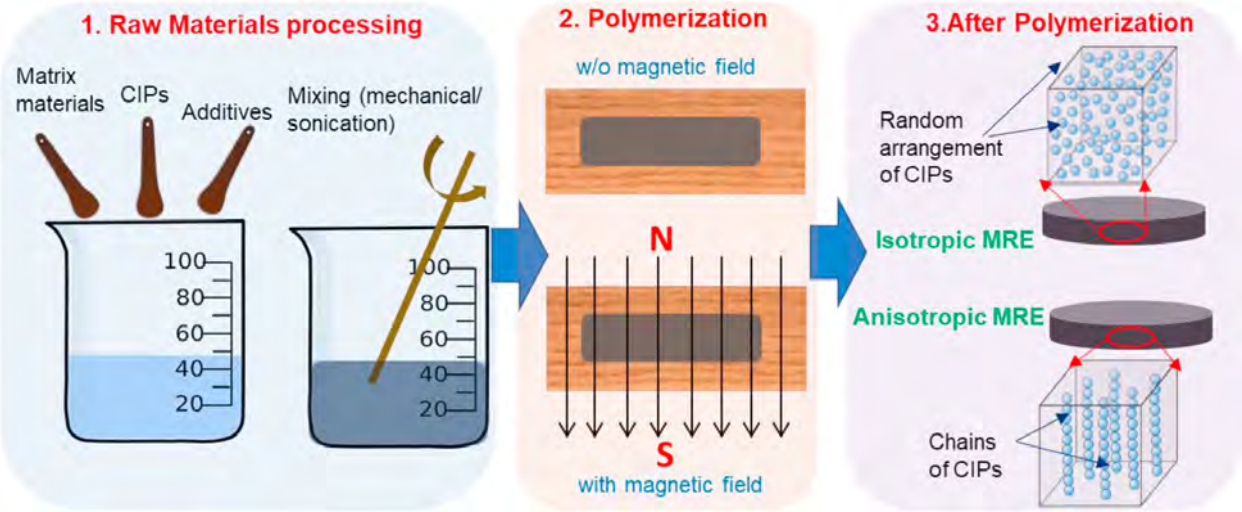

Figure 2.3: Traditional method to fabricate MREs. First, the raw materials for the matrix, the magnetic powder and, optionally additives, are blended according to the manufacturing guidelines. Then, the blend, properly poured in a mold, is cured in an oven. An external magnetic field can be applied during the curing processes to align the magnetic particles and form microscopic anisotropic structures. Finally, the MRE sample is extracted from the mold. It has magneto-mechanical isotropic behavior if the curing has been done in the absence of magnetic actuation, and anisotropic when a magnetic field has been applied. Figure courtesy of [57].

Moreover, works in the literature report some further conventional manufacturing techniques. Solution mixing or casting has been used for magnetorheological polymers with thermoplastic matrix [112]. It requires using a solvent to separate the polymeric chains (i.e., dissolve the polymer), adding the magnetic fillers and, eventually, pouring the solution into a mold and extract the solvent in a vacuum oven. In other words, the polymer is dissolved to be mixed with the magnetic powder. A technique suitable to produce nano-fibers is electro-spinning [113, 114]. In addition, hot-pressing, sandwich layers, UV-polymerization, synthesis, spray deposition and coating [115].

Additive manufacturing

Additive manufacturing (AM) technologies, also known as 3D printing, have caught great attention in the last decade. These techniques allow to create structures with intricate geometries and with a controlled porosity (morphology and distribution of pores) [116]. Moreover, multi-material printing allows to combine more than one component within the same target structure. All these features make AM strategies ideal to fabricate architected structures [117–119]. When 3D printing is applied to manufacture multifunctional materials, a new dimension is added and the technique is called 4D printing [120–122]. Such a new dimension relates to the ability of these materials to modify their properties along time under a certain type of stimulus, e.g., magnetic actuation for MREs.

Nowadays, a wide variety of AM strategies are available in the literature [115]. The main ones are Direct Ink Writing (DIW), Fused Deposition Modeling (FDM), Inkjet, Light-assisted AM, and Selective Laser Sintering (SLS). Figure 2.4 provides an illustration of these methods. DIW is based on pressing of a viscous ink (i.e., raw material before curing) through a nozzle

to print the consecutive layers of the final geometry [7, 123]. Since the rheological properties of the ink vary with numerous factors, e.g., the amount of magnetic particles, temperature, and kinetics of the polymerization reaction, its rheological characterization is crucial to optimize the printing parameters [124]. FDM melts and extrudes filaments of thermoplastic polymers (e.g., PLA, TPU, ABS, PC, polyamides) for the final geometry layer by layer. Note that the filament must be prepared previously to include the magnetic particles, for instance by solution mixing. The Inkjet method consists in the deposition of droplets of ink through many nozzles. Unlike the previous methods, Inkjet is limited to Newtonian fluids. An application with a magneto-active fluid can be found in [125]. Light-assisted AM comprises Stereolitography (SLA), Digital Light Processing (DLP) and Two-photon Polymerization (2PP). The foundations of these techniques lie in the photo-curable nature of a raw resin [126]. Some works concerning MREs can be found in [127, 128]. Finally, SLS is a recent technology that uses a laser to melt polymeric powder and build up the desired geometry [129, 130]. Overall, AM strategies provide flexibility, are ideal to manufacture complex geometries and to tune the mechanical properties of the printed material [131].

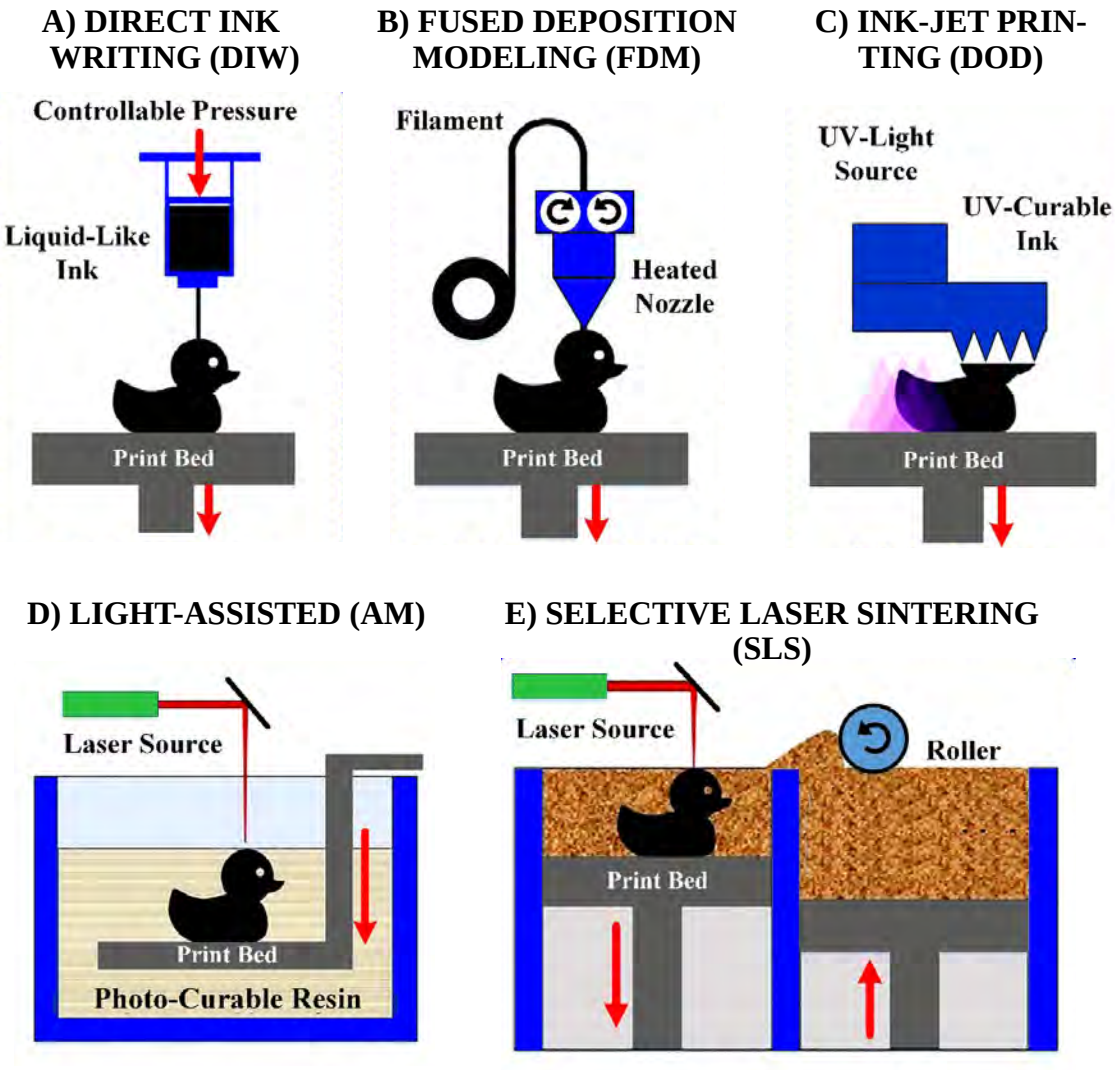

Figure 2.4: 4D printing strategies for MREs, adapted from [115]. A) Direct Ink Writing (DIW), B) Fused Deposition Modeling (FDM), C) Inkjet, D) Light-assisted Additive Manufacturing, and E) Selective Laser Sintering (SLS).

2.1.2 Experimental characterization

The multifunctional nature of MREs is due to the magneto-mechanical coupling between matrix and magnetic particles. To characterize the magneto-mechanical behavior of MREs, traditional techniques need to be re-adapted to impose magnetic fields at the same time that the material is mechanically deformed. Some of these experiments are uniaxial compression tests [50, 51, 132], uniaxial tensile test [56], simple shear test [7, 24, 28, 52, 107, 109, 133–135], biaxial tension test [53], fatigue test [136–138]. Additionally, dynamic tests are meant to explore the viscoelastic behavior of soft polymers, which depends, among other parameters, on the excitation frequency, amplitude of the deformation and intensity of the magnetic field. Here, rheology is a paramount technique to characterize soft viscoelastic solids. To provide a cleared vision of the characterization strategies, Figure 2.5 summarizes six examples extracted from the literature. Overall for all tests, the magnetorheological (MR) effect quantifies the modification of the mechanical properties, namely mechanical stiffness, under magnetic actuation [99, 139–142].

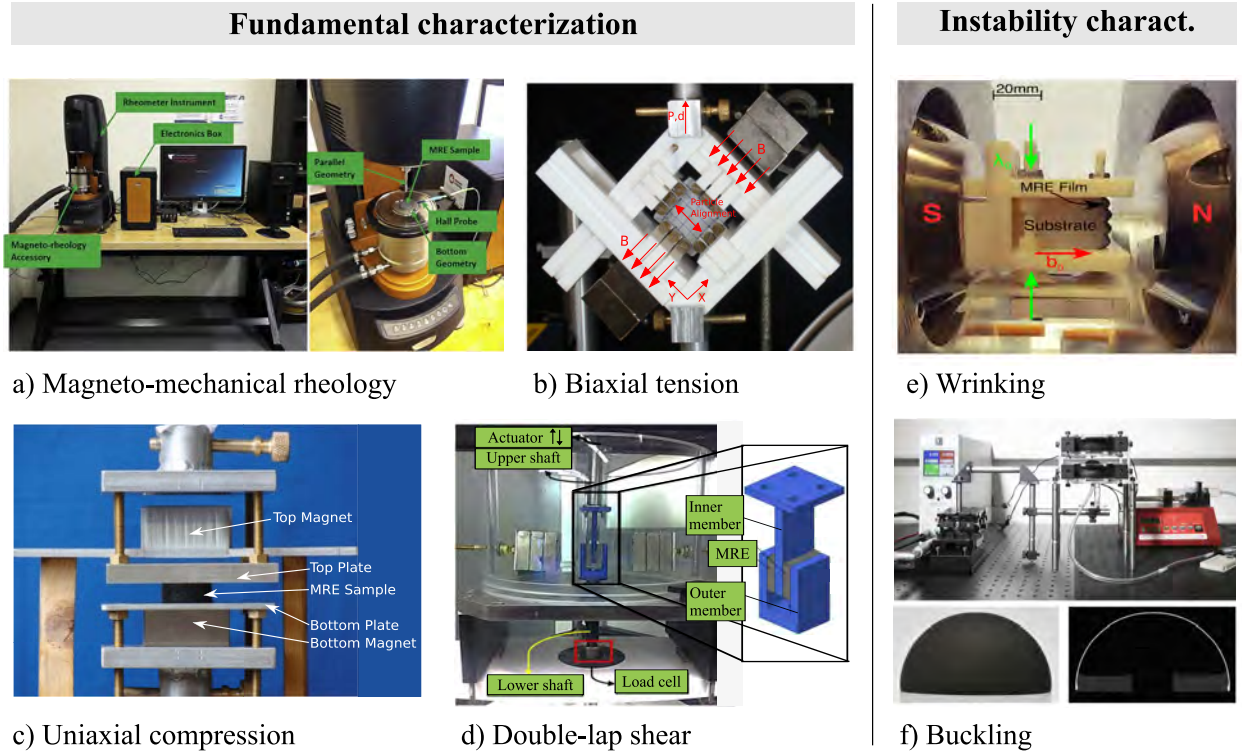

Figure 2.5: Characterization strategies of MREs. (a) Magneto-mechanical rheology to characterize MREs under oscillatory shear and magnetic actuation in the perpendicular direction [88]. (b) Equi-biaxial tension tests on a anisotropic MRE and under magnetic actuation [53]. (c) Uniaxial compression test and magnetic actuation with permanent magnets [52]. (d) Double-lap shear test with two MRE test samples [44]. The inner member moves in the vertical direction. (e) Setup with a pre-compressed MRE layer to characterize the wrinkling patterns that develop under magnetic actuation with a far magnetic field [143]. (f) Characterization of the buckling threshold of magneto-responsive shells [144].

Due to the significance of rheology to characterize soft polymers, the following subsections provide more detail on this technique for mechanical rheology and for magneto-mechanical rheology.

Mechanical rheology

Rheology is the science that studies the deformation and flow processes of materials. Otherwise, it is the science that sets the methods to determine the rheological properties of materials based on the relation between stress and strain. To this end, traditional rheology concerns energy arguments to characterize the viscous constitutive response of materials. In this doctoral thesis, the focus is on viscoelastic solids. Table 2.1 summarizes the basic parameters used in rheology.

Table 2.1: Basic rheological parameters.

Parameter	**Definition**	**Description**
Shear stress	$\tau = F/A$	F: shear force applied on a surface A
Shear strain	$\gamma = \mathrm{d}x/\mathrm{d}h$	Relative shear displacement $\mathrm{d}x$ of two parallel surfaces at a distance $\mathrm{d}h$
Shear strain rate	$\dot{\gamma} = \mathrm{d}\dot{x}/\mathrm{d}h$	$\dot{x}$: velocity of the displacement of the plane
Viscosity	$\eta = \tau/\dot{\gamma}$	Flow resistance
Complex shear modulus	$G^* = \vec{\tau}/\vec{\gamma}$	Shear strain stiffness accounting for viscous dissipation
Storage modulus	$G' = \mathrm{Re}\{G^*\}$	Related to the elastic energy storage
Loss modulus	$G'' = \mathrm{Im}\{G^*\}$	Related to the energy dissipated
Loss factor	$\tan\delta = G''/G'$	Phase-shift between shear stress and shear strain

The viscosity of fluids may depend on the shear strain rate. Hence, strain rate sweeps or, equivalently, frequency sweeps for soft viscoelastic solids, help characterize such a dependency. The fluid can be classified according to its behavior as illustrated in Figure 2.6. First, Newtonian fluids have a viscous response that does not depend on the strain rate. Second, shear thinning describes a behavior where the viscosity decreases at increasing strain rates. Viscoelastic fluids and gels show this response. Finally, shear thickening relates to increases of viscosity at increasing strain rates. This is typical for colloidal dispersions. For the case of viscoelastic solids, the decomposition of the complex shear modulus into the storage and loss components characterizes the viscoelastic performance. Here, the loss modulus sets the ratio between them.

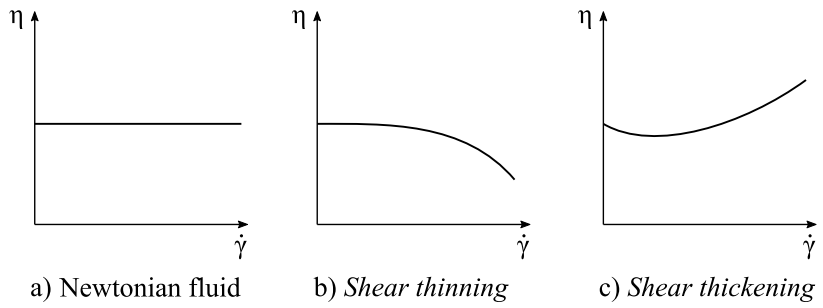

Figure 2.6: Types of material behavior according to the dependence of the viscosity with the strain rate.

Nevertheless, traditional mechanical rheology is not enough to characterize MREs. To

properly examine the magneto-mechanical functional behavior of soft MREs, rheology has to be able to apply magnetic fields while mechanically deformation.

Magneto-mechanical rheology

The magnetorheological mechanism is based on the differences in the magnetic permeabilities of the magnetic particles and the matrix. When the particles are magnetized under magnetic actuation, they exert a force on the matrix, which balances the particles interactions. The macroscopic effect relates to the increase of the material stiffness and/or the shape of the morphology. To apply a magnetic field, the rheometer is equipped with a device (i.e., magnetorheological device [68, 145]) that sets magnetic fields in the perpendicular direction with respect to the deformation axis. Figure 2.7 illustrates the functioning of the device. Overall, the magnetic field is established by means of a set of electric coils. Moreover, a cooling system extracts the heat generated by the coils.

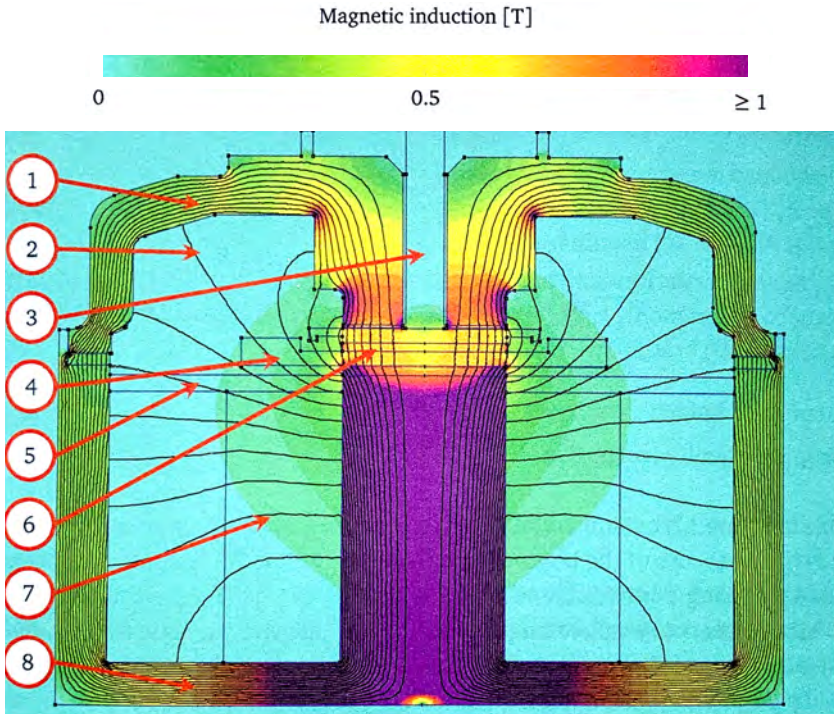

Figure 2.7: Scheme of the axil-symmetric cross-section of the Magnetorheological Device used in magneto-mechanical rheology (Figure courtesy of Pelteret *et al.* [63]). 1) Upper magnetic yoke, 2) Free space, 3) Plate of the rheometer to mechanically deform the sample, 4) Peltier plate, 5) Plate for structural support, 6) Cylindrical MRE sample placed between the upper place and the Peltier plate, 7) Electric coil to generate the magnetic field, 8) Lower magnetic yoke.

2.2 Modeling

Mathematical modeling and numerical simulation of coupled problems has been an active field of research in the last years. It helps understand the underlying non-linear magneto-mechanical coupled behavior of MREs. In this regard, numerical frameworks are a tool to further explore the full potential of MREs by facilitating the design and optimization of multi-functional soft and flexible smart devices. MREs exhibit nonlinear and time-dependent behavior, with a nearly incompressible bulk elastomeric matrix [146–148], resulting in further complexities of their numerical simulations. The mathematical foundations of the coupling of electromagnetic fields at finite strains are well documented in some early publications, see for example the works by Pao [149], Eringen and Maugin [150], Maugin [151] and the references cited therein. More recent works related to the constitutive modeling for MREs are due to Ogden, Dorfmann, Bustamante, Shariff and co-workers [147, 152–156]. While the aforementioned works discarded time-dependent phenomena of MREs, some other works considered time-dependent phenomena in the polymeric matrix [157–166].

2.2.1 Magneto-mechanical modeling approaches

To date multiple approaches to model the response of MREs have been proposed (see Figure 2.8). To start with, microstructural-based models are based on the description of the microstructure and the interplays that occur between particles and between particles and matrix. In turn, microstructural-based strategies are classified as lattice-based models and full-field models. Lattice-based approaches do not model the microstructure but describe the macroscopic behavior of MREs incorporating some microstructural information (e.g., particles distribution) [167–170]. They are efficient and make computationally possible to model complex geometries and structures. Despite their high efficiency, lattice-based models may disregard some underlying mechanisms that can only be accounted for by modeling the microscopic domain.

To overcome this issue, full-field, bottom-up or multi-scale homogenization methods directly transfer microscopic details of the MRE composition to the macroscopic scale. They involve solving the magneto-mechanical equilibrium in a microscopic domain, applying some macroscopic loads, and homogenizing the results to macroscopic scale properties. To this end, the domain is limited to a representative portion of the mesostructural composition of the MRE, i.e., a Representative Volume Element (RVE). Within the RVE, a variational homogenization of local potentials of each phase defines the problem [171–177]. The outcome of this approach is the response of the composite directly from the consideration of the microstructural interactions between the phases. Some further outstanding works are reported in [164–166, 178–185, 185–187]. As a drawback, homogenization approaches may lead to massive computational expensive models when considering large domains. Hence, this strategy is limited to local representative domains of a homogeneous domain of a structure.

Phenomenological or top-down models provide a more efficient approach by modeling MREs from a macroscopic and continuum point of view [158, 184, 188, 189]. They predict well the overall response of the material and, when implemented in FEM environments,

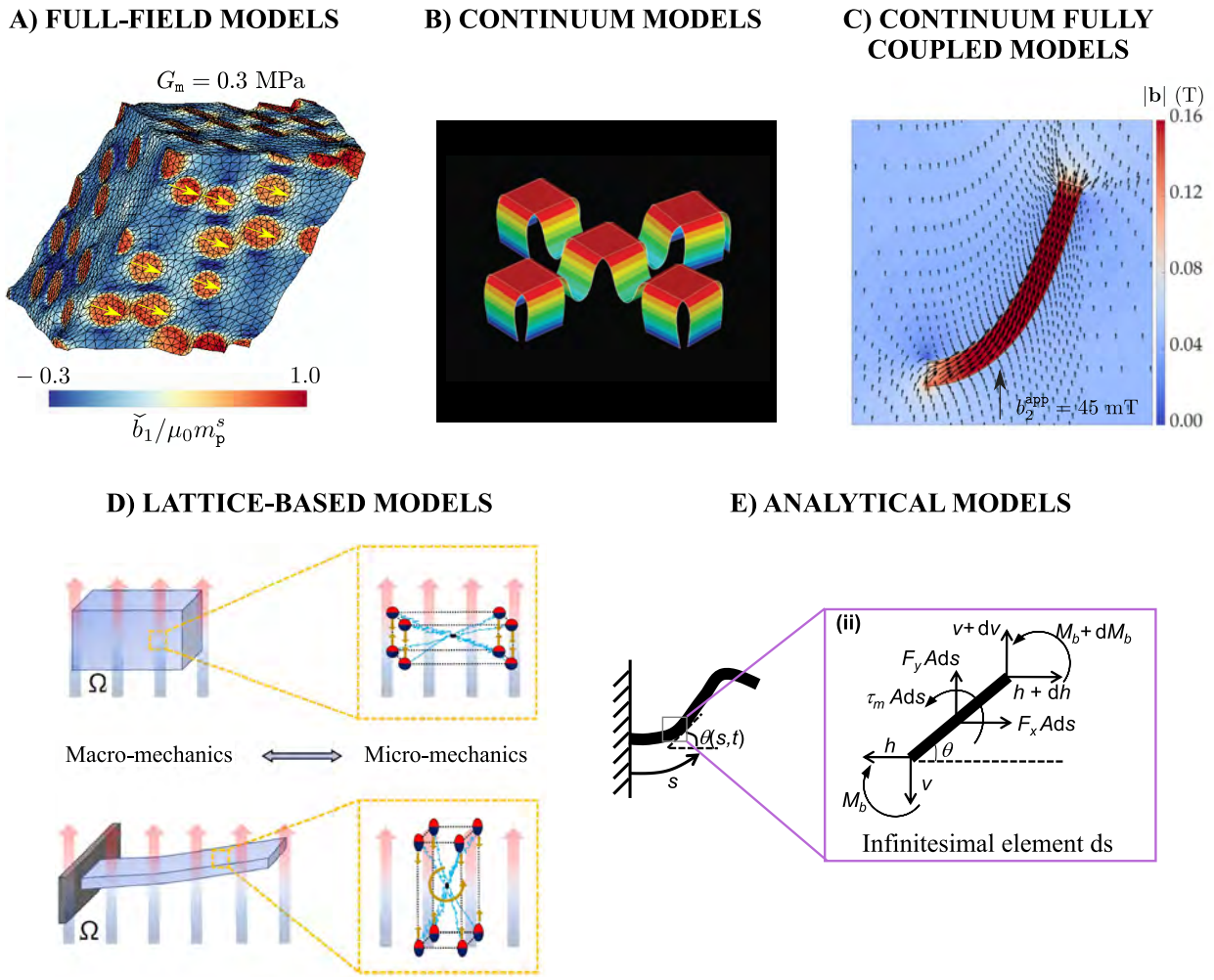

Figure 2.8: Illustration of the existing approaches to model MREs. (a) Full-field approaches model the behavior of MREs through the reproduction of the magnetic particles and the matrix at the microscale [164]. (b) Continuum model of a quadrupedal structure consisting in the combination of magnetically active and passive segments that fold with respect to each other [7]. (c) FE model that solves the coupled magneto-mechanical problem to characterize the deflection of a cantilever actuator under external magnetic actuation [164]. (d) Two lattice-based illustrations for the mechanisms governing the functional response of sMREs (dipole-dipole interactions) and hMREs (transmission of torques from the particles to the matrix) [55]. (e) Analytical model of a cantilever beam based on theoretical and kinematics formulations [27].

they allow to reduce the computational cost. Phenomenological models are not based on microstructural parameters, but they are calibrated directly from experimental and/or computational data.[2] A drawback, however, is that they miss information of their underlying micro-structural composition and microstructural mechanisms. To overcome this limitation,

[2]Some approaches in the literature place phenomenological models at the end of the pipeline as a guidance for the design of functional structures. The reason is that they are efficient to deal with complex magneto-active structures (i.e., macrostructural domain considering shape effects). Traditionally, these models have been calibrated from experimental data. However, a drawback is that these data are usually bounded to specific geometrical effects. As an alternative, the multifunctional mechanisms can be previously understood by means of full-field models. For this reason, some recent approaches in the literature suggest fitting phenomenological models from meaningful data generated with homogenization frameworks [183, 184, 190].

the relation with the microstructure has been implicitly incorporated by the addition of coupling terms [184, 187]. Customarily, these terms are calibrated by fitting either with experimental or numerical data obtained from microstructural simulations.

Finally, analytical models are posed for the description of simple structural elements, such as rods and slender beams [27, 30, 191–193]. They have a closed form solution and can be easily used to gain knowledge about the physics of MREs. Furthermore, approaches to explore instability-induced patterns in soft composites [194–196].

2.2.2 Magneto-mechanical modeling fundamentals

Kinematics

The deformation of ultra-soft MREs is formulated in a finite strain framework. A function $\mathbf{x} = \boldsymbol{\varphi}(\mathbf{X})$ maps the coordinates in the undeformed or material configuration $\mathbf{X} \in \Omega_0$ to the coordinates in the deformed or spatial configuration $\mathbf{x} \in \Omega$. The displacement field, i.e., the first unknown field of the coupled problem, is $\mathbf{u} = \boldsymbol{\varphi}(\mathbf{X}) - \mathbf{X}$, and the deformation gradient,

$$\mathbf{F} = \boldsymbol{\nabla}_0 \mathbf{u} + \mathbf{I}, \qquad J := \det \mathbf{F}, \tag{2.1}$$

where $\boldsymbol{\nabla}_0$ denotes the gradient operator with respect to $\mathbf{X}$ and J the Jacobian of $\mathbf{F}$.

Alternative strain measures are defined to fulfill objectivity, i.e., independence of rotations. The right and left Cauchy-Green tensors read, respectively, as

$$\mathbf{C} := \mathbf{F}^{\mathrm{T}} \cdot \mathbf{F}, \quad \mathbf{b} := \mathbf{F} \cdot \mathbf{F}^{\mathrm{T}}. \tag{2.2}$$

The magnetic problem incorporates three additional vector variables. These are the magnetic intensity $\mathbb{H}$, the magnetization $\mathbb{M}$ and the magnetic induction $\mathbb{B}$ in the reference configuration, and their counterparts $\mathbb{h}$, $\mathbb{m}$ and $\mathbb{b}$ in the current configuration. Both configurations are related by

$$\mathbb{b} = J^{-1}\mathbf{F} \cdot \mathbb{B}, \quad \mathbb{h} = \mathbf{F}^{-\mathrm{T}} \cdot \mathbb{H}, \quad \mathbb{m} = \mathbf{F}^{-\mathrm{T}} \cdot \mathbb{M}. \tag{2.3}$$

Related to the previous transformation, Mukherjee and co-authors have demonstrated that stretches of the medium ($\mathbf{U}$) do not affect the spatial magnetization [184]. Therefore, Equation 2.3_3 is rewritten as

$$\mathbb{m} = \mathbf{R}\mathbb{M}. \tag{2.4}$$

One of these three magnetic variables is to be chosen as the second unknown field of the problem. Frequently, either the reference magnetic intensity ($\mathbb{H}$) or the magnetic induction ($\mathbb{B}$) is selected [184, 190, 197].[3] Moreover, the magnetic variables are linked by the standard constitutive relation

$$\mathbb{b} = \mu_0 \left[\mathbb{h} + \mathbb{m}\right]. \tag{2.5}$$

Alternatively, in the reference configuration

$$\mathbb{B} = J\mu_0 \mathbf{C}^{-1} \left[\mathbb{H} + \mathbb{M}\right]. \tag{2.6}$$

[3] Note that the unknown fields in an alternative spatial framework could be the Eulerian counterparts, i.e., $\mathbb{h}$ and $\mathbb{b}$.

Field equations in the reference configuration

For the mechanical problem, the conservation of linear momentum is imposed by

$$\boldsymbol{\nabla}_0 \cdot \mathbf{P} + \mathbf{f}_0 = \rho_0 \ddot{\mathbf{u}}, \quad \text{in } \Omega_0, \tag{2.7}$$

with $\boldsymbol{\nabla}_0 \cdot$ the divergence operator, $\mathbf{f}_0$ the body force vector, and $\ddot{\mathbf{u}}$ the acceleration, all in the reference configuration.

In addition, the conservation of angular momentum is often prescribed directly through the constitutive law and does not require to be reinforced by a field equation. In the absence of internal torques, it guarantees the symmetry of the Cauchy stress tensor, i.e.,

$$\boldsymbol{\sigma} = \boldsymbol{\sigma}^{\mathrm{T}}. \tag{2.8}$$

However, when internal torques appear in the material, as it may occur with hMREs under magnetic actuation, the Cauchy stress tensor may be asymmetric. Consequently [198, 199],

$$\boldsymbol{\epsilon} : \frac{\boldsymbol{\sigma} - \boldsymbol{\sigma}^{\mathrm{T}}}{2} + \boldsymbol{\tau} = \mathbf{0}, \quad \text{in } \Omega_0, \tag{2.9}$$

with $\boldsymbol{\epsilon}$ the third order permutation tensor and $\boldsymbol{\tau}$ the body torque.

For the magnetic problem, the Maxwell equations in the absence of free currents state

$$\boldsymbol{\nabla}_0 \times \mathbb{H} = \mathbf{0}, \qquad \boldsymbol{\nabla}_0 \cdot \mathbb{B} = 0, \quad \text{in } \Omega_0, \tag{2.10}$$

with $\boldsymbol{\nabla}_0 \times$ the curl operator in the reference configuration. Note that Equation 2.10_1 is automatically satisfied when $\mathbb{H}$ is derived from a magnetic scalar potential field ϕ as

$$\mathbb{H} = -\boldsymbol{\nabla}_0 \, \phi, \quad \text{in } \Omega_0. \tag{2.11}$$

Alternatively, Equation 2.10_2 is automatically satisfied when $\mathbb{B}$ is derived from a magnetic vector potential field $\mathbb{A}$ [49], i.e.,

$$\mathbb{B} = \boldsymbol{\nabla}_0 \times \mathbb{A}, \quad \text{in } \Omega_0. \tag{2.12}$$

Thermodynamics and constitutive equations

An energy density (Ψ) for the magneto-mechanical problem can be established as a function of $\mathbf{F}$, $\mathbb{H}$ or $\mathbb{B}$, and scalar and tensor internal variables δ and $\boldsymbol{\delta}$, respectively.

$$\Psi^{\mathrm{H}}\left(\mathbf{F}, \mathbb{H}, \delta, \boldsymbol{\delta}\right), \quad \text{or} \quad \Psi^{\mathrm{B}}\left(\mathbf{F}, \mathbb{B}, \delta, \boldsymbol{\delta}\right). \tag{2.13}$$

The total energy Ω of the coupled problem is obtained when the Maxwell contribution (i.e., magnetic free space) is added to the previous energies. Depending on the choice for the magnetic independent variable,

$$\begin{aligned} \Omega^{\mathrm{H}}\left(\mathbf{F}, \mathbb{H}, \delta, \boldsymbol{\delta}\right) &= \Psi^{\mathrm{H}}\left(\mathbf{F}, \mathbb{H}, \delta, \boldsymbol{\delta}\right) + \Psi^{\mathrm{H}}_{\mathrm{vac}}\left(\mathbf{F}, \mathbb{H}\right), \\ \Omega^{\mathrm{B}}\left(\mathbf{F}, \mathbb{B}, \delta, \boldsymbol{\delta}\right) &= \Psi^{\mathrm{B}}\left(\mathbf{F}, \mathbb{B}, \delta, \boldsymbol{\delta}\right) + \Psi^{\mathrm{B}}_{\mathrm{vac}}\left(\mathbf{F}, \mathbb{B}\right). \end{aligned} \tag{2.14}$$

The contribution due to the free space reads as

$$\Psi_{\text{vac}}^{\text{H}}(\mathbf{F},\mathbb{H}) = \frac{1}{2J\mu_0}\mathbb{B}\cdot[\mathbf{C}\cdot\mathbb{B}] = \frac{1}{2J\mu_0}[\mathbb{b}\cdot\mathbb{b}] = \Psi_{\text{vac}}^{\text{h}}(\mathbb{b}),$$
$$\Psi_{\text{vac}}^{\text{B}}(\mathbf{F},\mathbb{B}) = -\frac{J\mu_0}{2}\mathbb{H}\cdot[\mathbf{C}^{-1}\cdot\mathbb{H}] = -\frac{J\mu_0}{2}[\mathbb{h}\cdot\mathbb{h}] = \Psi_{\text{vac}}^{\text{b}}(\mathbb{b}), \tag{2.15}$$

with μ_0 the magnetic permeability of the vacuum.

Moreover, the Clausius-Duhem inequality states the second principle of thermodynamics and the admissible evolution of the mechanical and magnetic variables. For both H-/B-based formulations, it reads as

$$\mathbf{P}:\dot{\mathbf{F}} + \mathbb{H}:\dot{\mathbf{B}} - \dot{\Psi}^{\text{H}} + \eta\dot{\theta} \geq 0,$$
$$\mathbf{P}:\dot{\mathbf{F}} + \mathbb{B}:\dot{\mathbf{H}} - \dot{\Psi}^{\text{B}} + \eta\dot{\theta} \geq 0, \tag{2.16}$$

with η_0 the entropy and θ the absolute temperature. Note that the last term in Equation 2.16 vanishes for isothermal processes. The evolution of the internal variables must fulfill $-\frac{\partial\Psi}{\partial\delta}:\dot{\delta}\geq 0$ and $-\frac{\partial\Psi}{\partial\boldsymbol{\delta}}:\dot{\boldsymbol{\delta}}\geq 0$.

Finally, the constitutive equations are derived according to the Coleman-Noll argumentation [200]

$$\mathbf{P} = \frac{\partial\Psi^{\text{H/B}}}{\mathbf{F}}; \qquad \mathbb{B} = -\frac{\partial\Psi^{\text{H}}}{\partial\mathbb{H}} \quad \text{or} \quad \mathbb{H} = \frac{\partial\Psi^{\text{B}}}{\partial\mathbb{B}}. \tag{2.17}$$

Microstructurally-informed constitutive models

Microstructural-based models are defined by parameters with a strong microstructural meaning. Usually, they are lattice models that assume specific spatial arrangements of the particles. The constitutive behavior results from several contributions, i.e., polymeric matrix and magnetic particles. Moreover, the energy potential consists of a mechanical and a magnetic contribution. In this regard, the polymeric matrix contribution is linked to the mechanical contribution, whereas the magnetic particles contribute to both the mechanical and the magnetic terms,

$$\Psi(\mathbf{F},\mathbb{H}) = \Psi_{\text{mech}}(\mathbf{F}) + \Psi_{\text{mag}}(\mathbf{F},\mathbb{H}). \tag{2.18}$$

The mechanical contribution may be defined by a microstructural-based hyperelastic model. For instance, the Arruda-Boyce or eight-chain model [201], i.e.,

$$\Psi_{mech}(\mathbf{F}) = n_e k_B\theta\sum_{k=1}^{K}\frac{C_k}{N_e^{k-1}}\left[I_{1,\text{h}}^k - 3^k\right], \tag{2.19}$$

with n_e the number of chains per reference volume[4], k_B the Boltzmann constant, θ the temperature, and N_e is the number of Kuhn segments per polymer chain.[5] $I_{1,h} = X[\text{tr}(\mathbf{C}) - 3] + 3$ is the modified first invariant of the right Cauchy-Green deformation tensor to account for

[4]The number of chains n_e is directly associated with shear modulus as $G = [n_e k_B\theta]$.

[5]The number of Kuhn segments per polymeric chain determines the extensibility and blockage of the polymeric chains [202–206].

the particles acting as a mechanical reinforcement of the polymeric matrix [207]. To this end, the amplification factor $X = 1 + 0.67g\phi + 1.62\left[g\phi\right]^2$ is defined as a function of the particles volume fraction (ϕ) and a factor (g) describing the asymmetric nature of the aggregated clusters. Moreover, the inverse of the Langevin function can be approached taking five terms in the Padé approximation ($K = 5$), i.e., $[C_1, C_2, C_3, C_4, C_5] = \left[\frac{1}{2}, \frac{1}{20}, \frac{11}{1050}, \frac{19}{7000}, \frac{519}{673750}\right]$ [208].

Remark. Note that the energy function in Equation 2.19 must be constrained with a Lagrange multiplier (p) and the term $-p\left(J-1\right)$ in case of incompressibility assumption [87, 162]. Consequently, the term $-p\mathbf{F}^{-\mathrm{T}}$ has to be included in Equation 2.17_1. In case of compressibility assumption, however, a volumetric contribution must be added,

$$\Psi_{\mathrm{vol}} = \frac{\kappa}{2}\left[J-1\right]^2, \tag{2.20}$$

with κ the bulk modulus. Moreover, in Equation 2.19 the isotropic deformation gradient ($\mathbf{F}_{\mathrm{iso}}$) instead of $\mathbf{F}$ must be used, i.e.,

$$\mathbf{F}_{\mathrm{iso}} = J^{-1/3}\mathbf{F}. \tag{2.21}$$

For sMREs the magnetic contribution is defined as [87, 167–169, 209],

$$\Psi_{\mathrm{mag}}\left(\mathbf{F}, \mathbb{M}\right) = -\frac{\mu_o}{4\pi}\frac{\phi^2}{\gamma}\sum_{i=1}^{N_n}\left[\frac{3\left[\left[\mathbf{F}^{-\mathrm{T}}\mathbb{M}\right]\cdot\left[\mathbf{F}\vec{R}_i^0\right]\right]\left[\left[\mathbf{F}^{-\mathrm{T}}\mathbb{M}\right]\cdot\left[\mathbf{F}\vec{R}_i^0\right]\right]}{\left\|\mathbf{F}\vec{R}_i^0\right\|^5} - \frac{\left[\boldsymbol{F}^{-\mathrm{T}}\mathbb{M}\right]\cdot\left[\boldsymbol{F}^{-\mathrm{T}}\mathbb{M}\right]}{\left\|\mathbf{F}\vec{R}_i^0\right\|^3}\right], \tag{2.22}$$

with $\vec{R}_i^0$ the dimensionless vectorial distance between particles in the material configuration and γ a dimensionless parameter to consider the number of particles in the representative lattice (see [168]). Moreover, N_n is the number of adjacent particles in the reference volume.

The dependence of the magnetization field ($\mathbb{M}$) on the magnetic intensity ($\mathbb{H}$) can be defined with the Frohlich-Kenelly equation

$$\mathbb{M} = \frac{M_s\left[\mu_r - 1\right]\mathbb{H}}{M_s + \left[\mu_r - 1\right]\left\|\mathbb{H}\right\|}, \tag{2.23}$$

with M_s the saturation magnetization of the magnetic particles and μ_r the relative magnetic permeability of the particles [167, 168, 210, 211].

For hMREs, the magnetic contribution depends on the remanent magnetization of the hard-magnetic particles, the external magnetic field, and their relative positions [162]. In turn, it is split into dipole-dipole and Zeeman contributions,

$$\Psi_{\mathrm{mag}}\left(\mathbf{F}, \mathbb{H}\right) = \Psi_{\mathrm{mag}}^{\text{d-d}}\left(\mathbf{F}, \mathbb{H}\right) + \Psi_{\mathrm{mag}}^{\mathrm{z}}\left(\mathbf{F}, \mathbb{H}\right). \tag{2.24}$$

The former is defined according to the the independence of the magnetization with the stretch, i.e., $\mathbb{m} = \mathbf{R}\mathbb{M}$. The latter models the interactions of the remanent magnetic field with the externally applied magnetic field. They read, respectively, as

$$\Psi_{\mathrm{mag}}^{\text{d-d}}\left(\mathbf{F}\right) = -\frac{\mu_o}{4\pi}\frac{\phi^2}{\gamma}\sum_{i=1}^{N_n}\left[\frac{3\left[\left[\boldsymbol{R}\mathbb{M}\right]\cdot\left[\mathbf{F}\vec{R}_i^0\right]\right]\left[\left[\boldsymbol{R}\mathbb{M}\right]\cdot\left[\mathbf{F}\vec{R}_i^0\right]\right]}{\left\|\mathbf{F}\vec{R}_i^0\right\|^5} - \frac{\left[\boldsymbol{R}\mathbb{M}\right]\cdot\left[\boldsymbol{R}\mathbb{M}\right]}{\left\|\mathbf{F}\vec{R}_i^0\right\|^3}\right], \tag{2.25}$$

and,

$$\Psi_{\mathrm{mag}}^{\mathrm{z}}\left(\mathbf{F}, \mathbb{B}\right) = -\left[\mathbf{R}\mathbb{M}\right]\cdot\left[\mathbf{F}\mathbb{B}\right]. \tag{2.26}$$

Macrostructural constitutive models

Likewise microstructurally-informed models, macrostructural or phenomenological models treat the MRE as a continuum. However, these use parameters that are fitted with experimental or computational data. Therefore, they are quite efficient to accurately reproduce the constitutive behavior of MREs but lack of microstructural physical information. Usually, they are built as the sum of a mechanical hyperelastic contribution $\Psi_{\text{mech}}(\mathbf{F})$ and a magnetic contribution $\Psi_{\text{mag}}(\mathbf{F}, \mathbb{H})$,

$$\Psi(\mathbf{F}, \mathbf{H}) = \Psi_{\text{mech}}(\mathbf{F}) + \Psi_{\text{mag}}(\mathbf{F}, \mathbb{H}). \tag{2.27}$$

The neo-Hookean model can be used to define the hyperelastic contribution,

$$\Psi_{\text{mech}}(\mathbf{F}) = \frac{G}{2}\left[\text{tr}\left(\mathbf{F}^{\text{T}} \cdot \mathbf{F}\right) - 3\right], \tag{2.28}$$

where G is the shear modulus.

Here again, one must constrain the energy in the case of incompressibility assumption. Alternatively, for compressibility assumption, the volumetric contribution and the isochoric split of the deformation gradient in Equations 2.20 and 2.21 should be considered.

With respect to the magnetic contribution in sMREs, it can be defined by means of a linear law with the magnetic intensity field, i.e.,

$$\begin{aligned}\Psi_{\text{mag}}(\mathbf{F}, \mathbb{H}) = -\frac{\mu_0}{2} J \chi_{\text{e}} \left[\mathbf{F}^{-\text{T}} \cdot \mathbb{H}\right] \cdot \left[\mathbf{F}^{-\text{T}} \cdot \mathbb{H}\right] = \\ = -\frac{\mu_0}{2} J \chi_{\text{e}} \left[\mathbb{h} \cdot \mathbb{h}\right] = \Psi_{\text{mag}}(\mathbb{h}),\end{aligned} \tag{2.29}$$

with χ_{e} the magnetic susceptibility of the medium.[6]

For hMREs with constant remanent magnetization, the energy is split into energetic and remanent contributions

$$\Psi_{\text{mag}}(\mathbf{F}, \mathbb{H}) = \Psi_{\text{mag,e}}(\mathbf{F}, \mathbb{H}) + \Psi_{\text{mag,r}}(\mathbf{F}, \mathbb{H}). \tag{2.30}$$

In the previous equation, the remanent magnetic contribution can be written as

$$\begin{aligned}\Psi_{\text{mag,r}}(\mathbf{F}, \mathbb{H}) = \mu_0 J \left[1 + \chi_{\text{e}}\right] \mathbb{H} \cdot \mathbf{C}^{-1/2} \cdot \mathbb{H}_{\text{r}} = \\ = \mu_0 J \left[1 + \chi_{\text{e}}\right] \mathbb{h} \cdot \mathbb{h}_{\text{r}} = \Psi_{\text{mag,r}}(\mathbb{h}),\end{aligned} \tag{2.31}$$

with $\mathbb{H}_{\text{r}}$ the constant remanent magnetic intensity field. Note that a definition of an internal variable to regard time-varying remanent magnetization can be consulted in [164].

[6] The superscript "e" relates to the energetic magnetic field $\mathbb{h}$, and not to the remanent contribution $\mathbb{h}_{\text{r}}$.

2.3 Applications

End-of-pipe applications of MREs lie in two major features: i) the modification of their mechanical properties (i.e., magnetorheological effect) and ii) the modification of their morphology (i.e., magnetostrictive effect). Some exploitable areas of MREs are engineering, materials and biomedical sciences [212]. Common applications comprise soft robotics for untethered navigation within biological matter [22, 25, 28, 213, 213, 214], mechanical isolating and damping systems [82, 107, 215–222], sandwich structures [223, 224], energy harvesters [225–227], tactile displays and sensors [134, 144, 228–230], microfluid transportation systems [231, 232], and peristaltic pumps [233]. As industrial applications, these materials can be used as damping systems and electrical machines [41, 42]. Note that, contrary to sMREs that only express complex shape changes when there are gradients in the magnetic fields, hMREs can also express such complex changes in shape under uniform fields [234]. In this regard, smart actuators and sensors are based on the deformation that results from the internal torques [12–20, 235, 236]. Soft robots are mainly meant for bioengineering applications, such as cell manipulation, drug delivery, and non-invasive surgery. These are remotely actuated to perform complex and repeatable movements that enable them to negotiate obstacles [14, 18, 19, 21–28, 30–32, 237–239]. In this regard, sMRE-based drug delivery systems promise to locally treat pathologies with higher effectiveness and fewer side effects [28, 240]. Moreover, hMREs have been used as multifunctional shape-changing structures, e.g., metamaterials and self-healing structures [15, 33, 35, 37–39, 241, 242]. A good amount of these applications demonstrate the benefits of using soft matrices to increase the range of deformations and enhance the functional response of the structure.

Hereafter, some applications are further explored and illustrated with examples from the literature, i.e., smart actuators and sensors, soft robots, metamaterials, biomedical applications (i.e., drug delivery, tissue engineering, diagnosis and imaging), and dynamic systems. Note that some of them lie in the magnetorheological effect whereas some others do on the shape-morphing capability. The former typically relates to soft-magnetic particles,[7] and the latter, to hard-magnetic particles.

2.3.1 Smart actuators and sensors

hMRE-based actuators receive the external magnetic stimulus as input and perform a functional morphological change. On the contrary, sensors undergo mechanical deformations and translate them into electromagnetic signals. These devices are advantageous since magnetic fields can penetrate a wide variety of materials. The shape-morphing capability owes to the transmission of torques from the pre-magnetized particles to the soft matrix. Depending on the deformation, MRE sensors are classified as bending actuators, gripper actuators, pumping actuators and remote sensors [55]. Figure 2.9 illustrates a few smart actuators and

[7] Note that soft-magnetic particles can also drive morphological changes. However, these are limited to volumetric and other simple responses.

sensors reported in the literature.

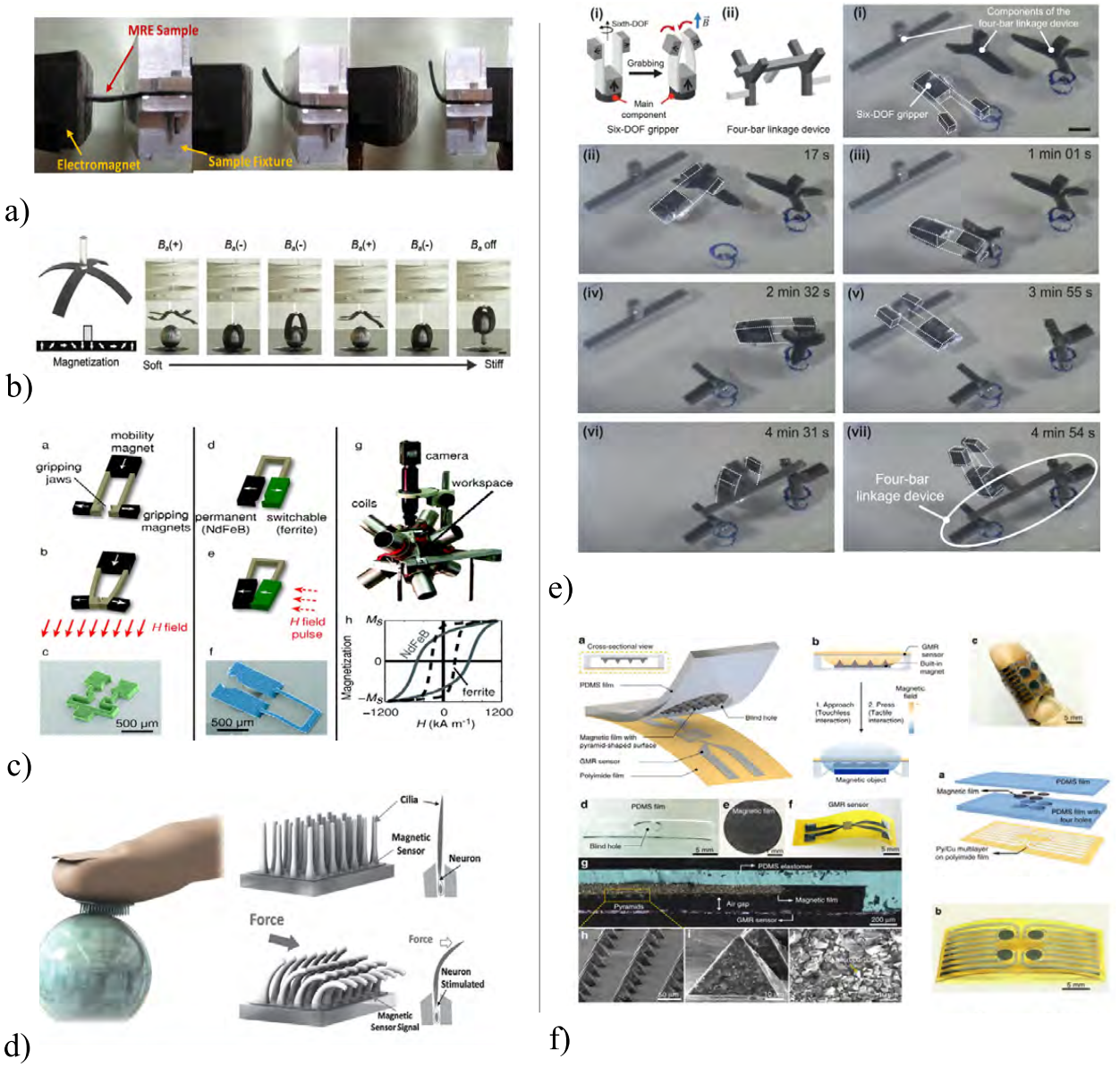

Figure 2.9: Applications of hMREs on smart actuators and sensors. (a) hMRE cantilever beam under perpendicular magnetic actuation [13]. (b) Performance of a four-arm gripper [19]. (c) Design of grippers to be remotely actuated [243]. (d) A cilia tactile sensor based on the measurement of the contact force [244]. (e) A gripper able to grab, transport and release objects [17]. (f) Soft magneto-electro-mechanical sensors [245].

2.3.2 Soft robots

Soft robots also take advantage of the shape-morphing capability of hMREs to perform a functional locomotion, navigate through soft mater and manipulate their surrounding. Their deformation mechanisms include deflexion (bending), elongation, contraction, coiling, crawling and jumping [234]. Moreover, magnetic soft robots benefit from a remote and fast magnetic actuation. Some swimming robots mimic artificial cilia locomotion or any other fish-like propelling system [28, 246, 247]. Figure 2.10 shows some representative examples.

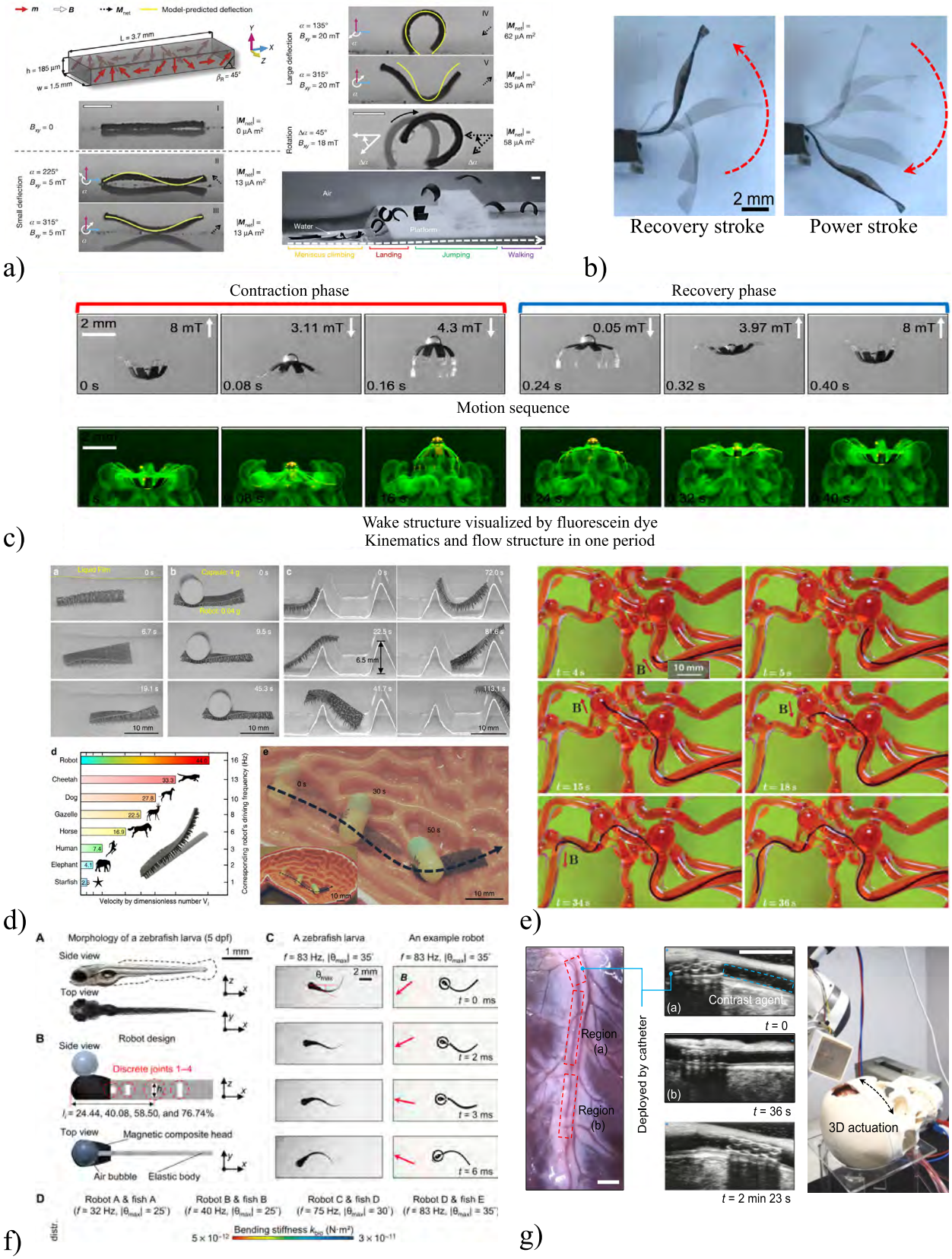

Figure 2.10: hMRE soft robots. (a) Shape-morphing mechanisms and multimodal locomotion of soft robots under magnetic actuation [24]. (b) Pre-magnetized propelling system activated under external magnetic actuation [27]. (c) A jellyfish-like swimming soft robot. The motion sequence and wake morphology characterizes the untethered robot [28]. (d) Illustration of the navigation of a soft robot along tortuous biological tissue [26]. (e) Navigation of a soft robot through a model of the cerebrovascular network [25]. (f) Larval zebra-fish inspired undulatory swimming soft robot [246]. (g) Demonstration of the capability of soft robots to navigate through porcine arteries under external magnetic actuation [8].

2.3.3 Metamaterials and auxetic structures

Shape morphing structures can perform intricate shape changes at small scales [7]. They are usually based on soft hMREs to create several pre-magnetized domains that tend to align with the applied magnetic field. Some approaches to manufacture the magnetic domains comprise the creation of multi-layer structures [248] and the design of local magnetization patterns [27, 249]. Moreover, the generation of torques that drives the shape-morphing ability depends on the external magnetic field and vanishes when the magnetic actuation is removed. Nevertheless, recent sequential actuation strategies have made possible to achieve shape-locking even after turning off the external magnetic field [19, 250]. Figure 2.11 shows some examples of architected structures and metastructures.

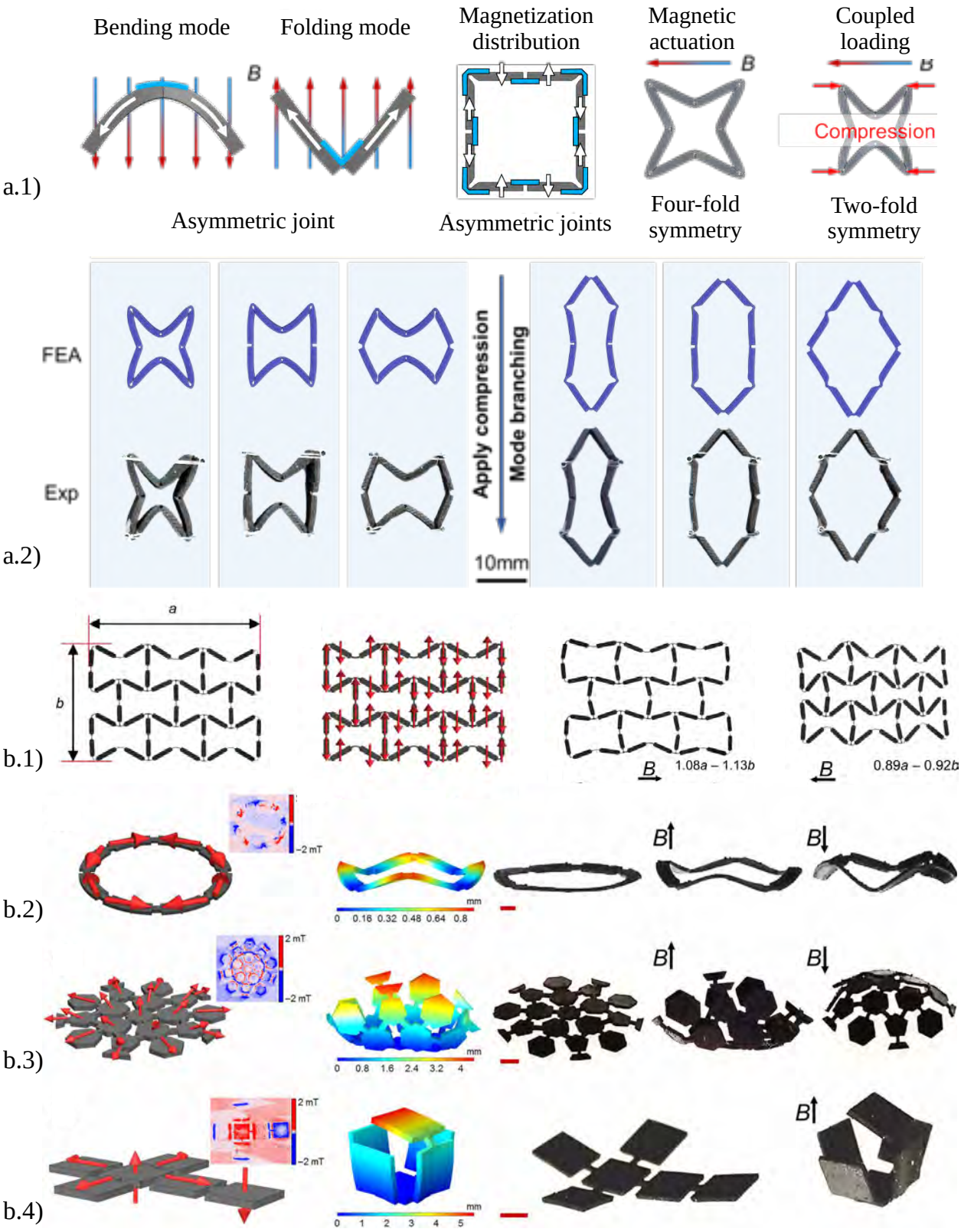

Figure 2.11: Magneto-mechanical metastructures based on hMREs. (a) Metamaterial unit cells [37]: (a.1) deformation modes and (a.2) comparison of the experimental and *in silico* deformation. (b) Soft meta-structures with 3D magnetization [251]: (b.1) auxetic meta-structure with a discrete magnetization pattern and (b.1-3) FE modeling and experimentation to approach the deformation problem of three 3D magnetizated meta-structures with different geometries.

2.3.4 Drug delivery

Drug delivery systems based on sMREs and hydrogels foretell great advances in medical treatment with the reduction of side-effects [252–257]. In regards to cancer, localized drug delivery would prevent the interaction of the medicine with non-target tissues [258–260]. External magnetic fields would set magnetic gradients to guide the MR structure through the organism. Then, it would be squeezed via magnetic actuation, enzymatic action, pH variation, temperature or osmosis to deliver the drug (i.e., diffusion of the drug as the solvent within the MR material) [257, 261, 262]. Moreover, alternating magnetic fields can produce heat dissipation in the MRE beneficial to kill cancer cells [263]. Figure 2.12 illustrates the mechanism by which the drug is solved in the MR structure and then delivered at the target area.

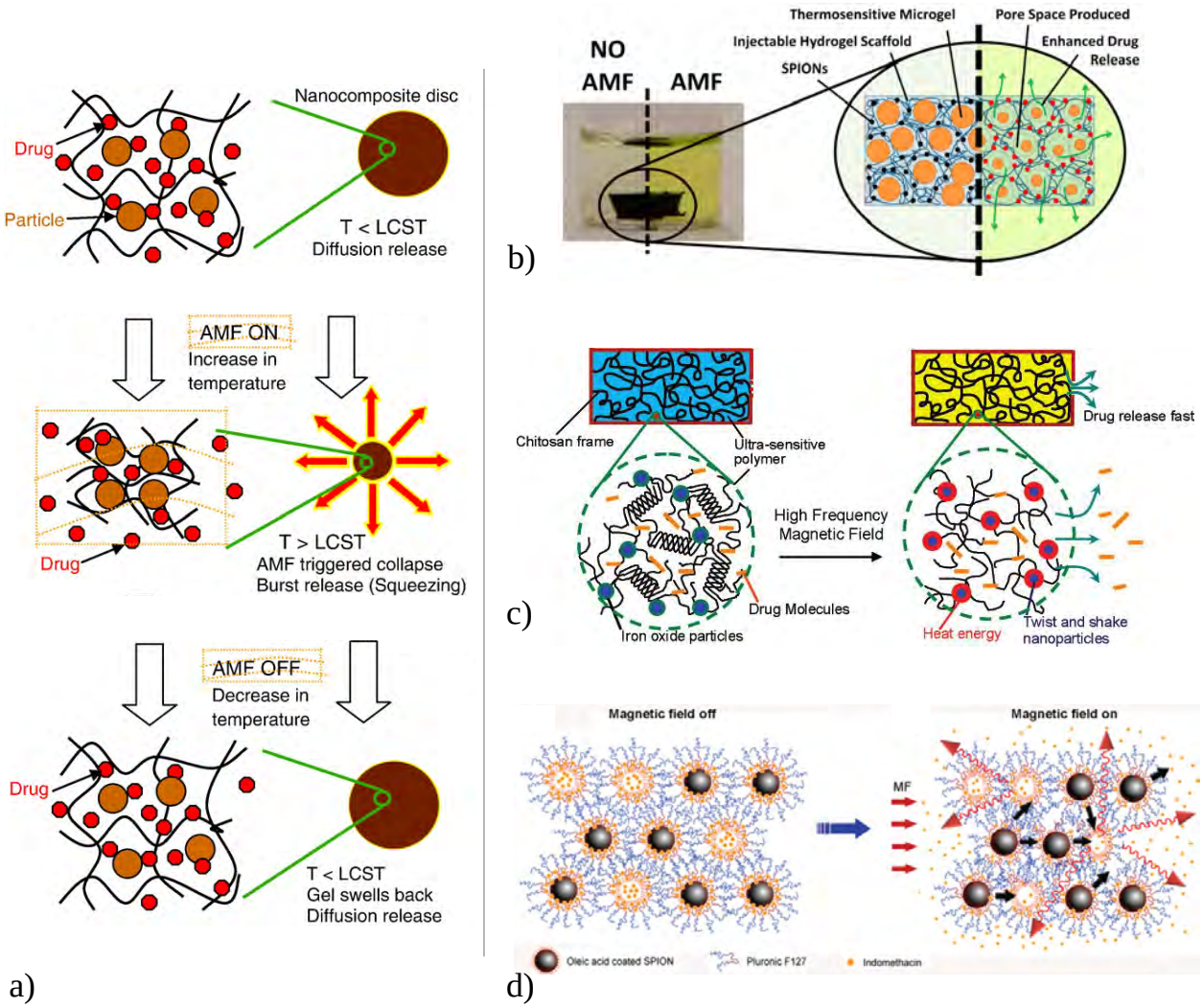

Figure 2.12: Illustration of the drug-delivery mechanisms on soft MR polymers and hydrogels. (a) Heat generation to drive drug-delivery by shrinking of the elastomeric network [252]. (b) Pores in a hydrogel to accommodate the drug [253]. (c) The frequency of the oscillatory magnetic field is tuned to adjust the generation of heat that drives the shrinking to expel the drug [254]. (d) Turning on and off the external magnetic field to drive the release of the drug [255].

2.3.5 Diagnosis and imaging

Medical diagnosis techniques benefit from the magnetic characteristic of sMREs as they could be easily detected. Therefore, drug release could be precisely executed at the exact target zone. In addition, magnetic nanoparticles have demonstrated to be useful contrast agents to measure the relative blood volume in specific regions of the body [264, 265]. Figure 2.13 contains two examples of magnetic imaging with magnetic elements used as contrast materials.

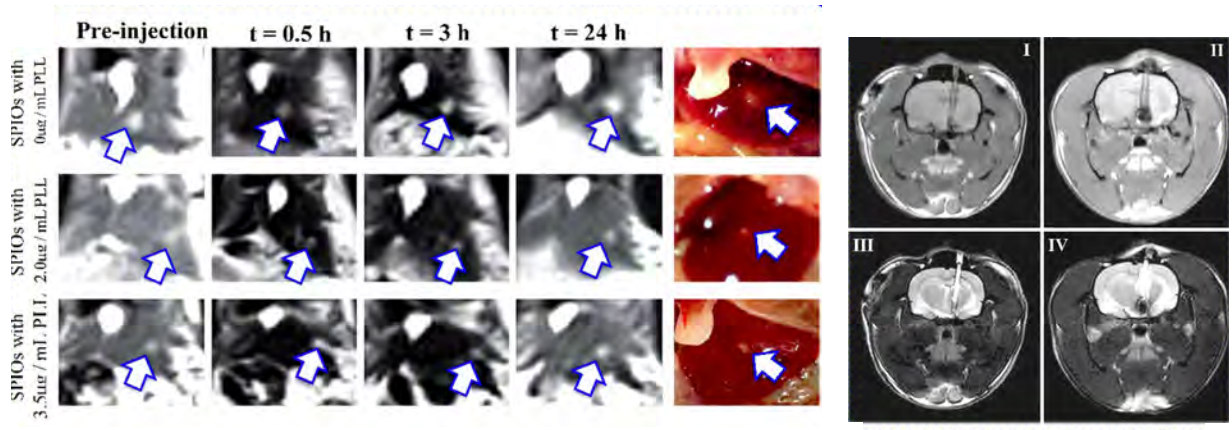

a) b)

Figure 2.13: Use of sMREs with magnetic resonance imaging for medical diagnosis purposes (figure courtesy of [115]). (a) Liver imaging using superparamagnetic iron oxide nanoclusters as MRI contrast substance [266]. (b) Imaging with magnetic Pt-Ir electrodes implanted in the brain [267].

2.3.6 Tissue Engineering

Soft polymers have been proposed to create artificial tissues and organs. Their soft nature is ideal to mimic the stiffness of the skin[8] and other organs [269]. Bioengineering scaffolds for bone tissue bioengineering must consider mineralization and vascularization of the surrounding tissue to facilitate bone growth [270, 271]. In this regard, the application of MR polymers has been reported to improve mineralization and osteogenesis [272]. In addition, they have been applied for nerve [273], cardiac [274], and cartilage tissue engineering [275, 276]. Recent approaches suggest using polydimethylsiloxane (PDMS) [277–280], and some of them even ultra-soft MREs [240, 281–283], as artificial substrates to conduct biological studies, such as collective cell migration during healing processes [284]. Figure 2.14 synthesizes the applicability of MR polymers in tissue engineering.

[8]The stiffness of the skin ranges from 30 kPa to 140 MPa [268].

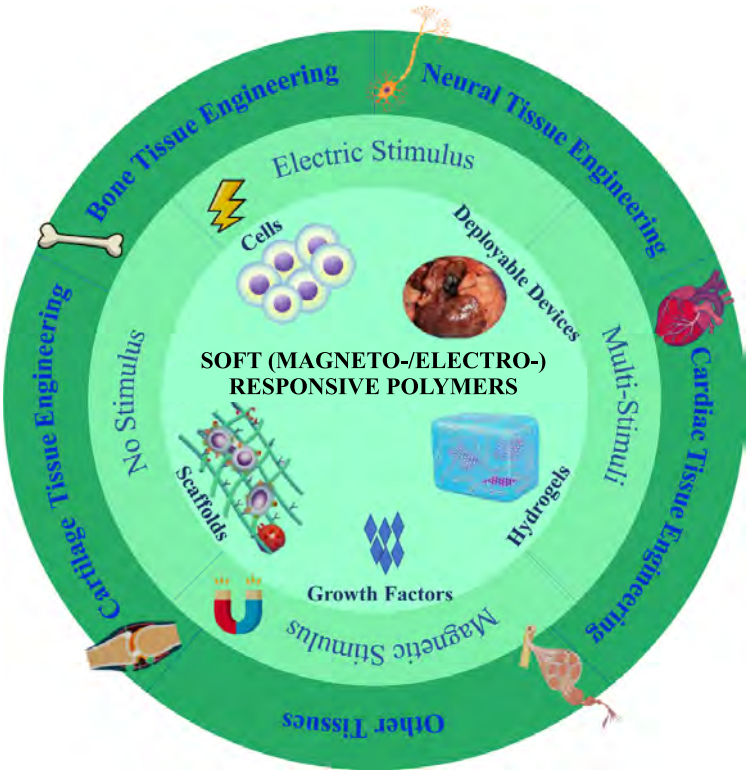

Figure 2.14: Scheme of the application of soft polymers and MR materials for tissue engineering. Illustration adapted from [115].

3 Experimental

This chapter first introduces the experimental methods, i.e., rheology and nanoindentation tests. Then, the experimental results are grouped according to the type of MRE (sMREs, hMREs and hybrid MREs). Each subsection encompasses the following macrostructural experiments: uniaxial loading (compression), shear loading (torsion) and mechanically confined tests under magnetic loading. The first type of tests comprises the results for mechanical uniaxial loading (compression), with monotonous compression tests, relaxation test and DMA tests. Then, the methodology is expanded to shear deformation mode (constant oscillatory tests and frequency sweeps). Finally, mechanically confined experiments under magnetic actuation are presented as a method to macroscopically measure the magneto-mechanical interplays that develop at the microscale. Note that additional free deformation experiments allow to explore the shape-morphing capabilities of permanently magnetized hMREs. Moreover, and given the importance of the matrix phase, an in-detail study of the influence of its stiffness is provided for sMREs. To this end, the mixing ratio of the elastomeric matrix is modified to achieve different stiffnesses and, consequently, tune the material response. In what concerns the microscopic characterization, nanoindentation tests are reported only for sMREs since the results do not depend on the applied magnetic field (note that the nanoindentations are locally done on the matrix, which presents negligible strain hardening, see also Figure A.1.a). Overall, the chapter presents an integral comprehensive characterization to explore the multifunctional performance of ultra-soft MREs. The characterization also motivates further theoretical and computational studies.

3.1 Experimental methods

A magneto-mechanical rheometer was used to evaluate the macrostructural response. The experiments allow to test the MREs under uniaxial compression and shear deformation modes in a wide range of magnetic field conditions. A TA HR-20 rheometer with Magneto-Rheology Accessory from Waters TA Q600 (TA instrument, New Castle, DE, USA) is used (see Figure 3.1). The magnetic field is applied by a magnetorheological accessory that sets a magnetic field in the axial direction to the sample. Note that the device is equipped with a close loop system to control the applied magnetic field measuring it in the vicinity of the sample. To prevent temperature variations due to Joule effect from the coils and keep a constant temperature, a cooling system is integrated with the device to set a constant temperature within the sample of 25 °C. An important remark is that, to ensure homogeneous

fields, an upper yoke is added. This limits the sample size to 1 mm height and 20 mm diameter. Note that the parallel plates are made of low magnetic permeability stainless steel. In addition, the device has a magnetic axial bearing that allows to carry out oscillatory tests under both shear and axial loading conditions.

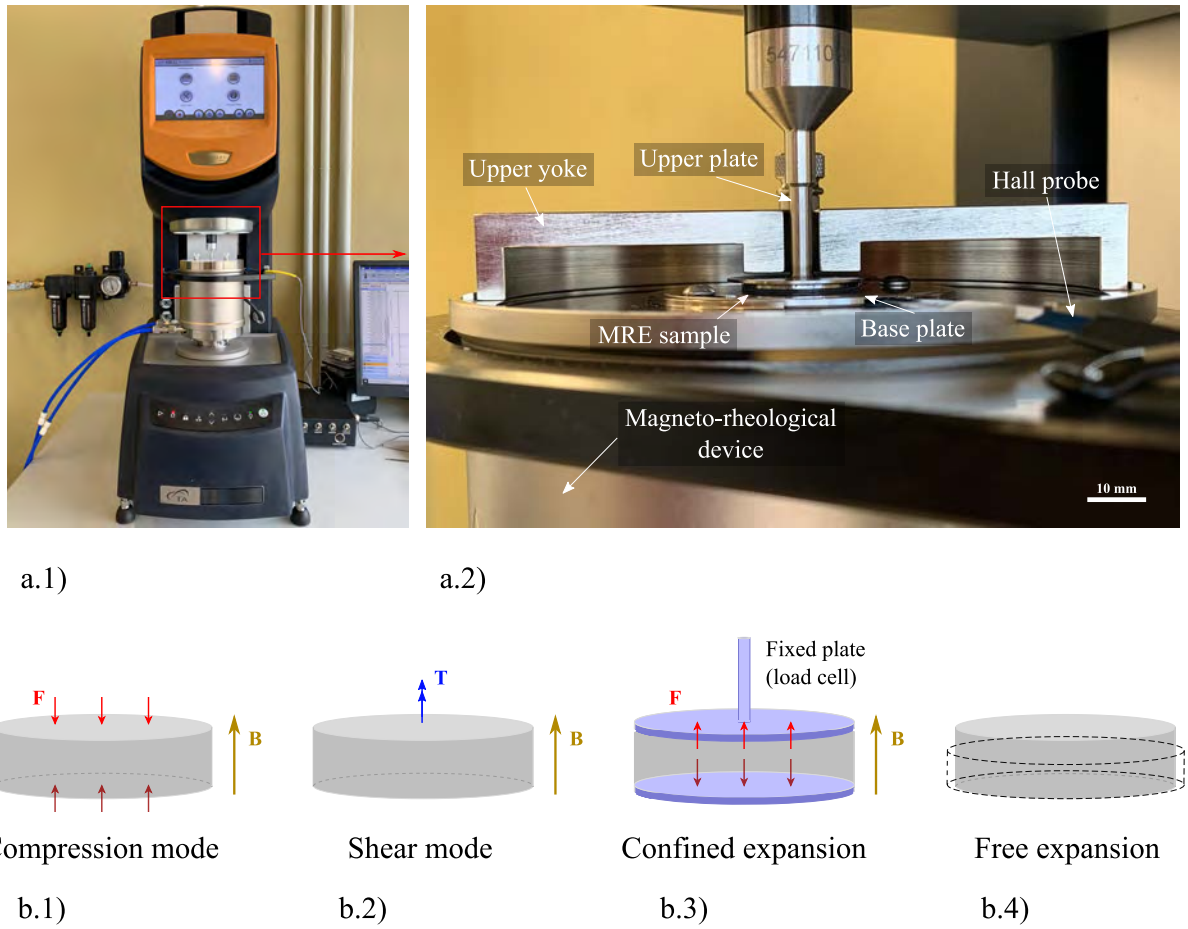

Figure 3.1: Experimental setup for rheology experiments and deformation modes. (a) Experimental setup: (a.1) HR-20 rheometre equipped with the magnetorheological device; (a.2) a detail of the sample placed between the upper plate (geometry) and the lower plate of the magnetorheological Peltier. One half of the upper yoke is removed for better visualization of the sample region. (b) Scheme of the magneto-mechanical tests performed in this work.

The microstructural response was evaluated with a nanoindenter. Micron-sized indentations were conducted with a Chiaro nanoindentation system (Optics11 Life, Netherlands) equipped with a 50 µm radius and 0.25 N m^{-1} spherical tip (see Figure 3.2). The optical calibration of the cantilever was performed in the liquid medium used with the samples, i.e., phosphate-buffered saline (PBS). This medium helps avoid the adhesion of the tip to the sticky sample. To eliminate air bubbles on the probe, it was pre-wetted with the same solution. In addition, isopropanol, milli-Q water and fiberless tissue was used to clean the probe between samples. The nanoindenter was mounted on a microscope, and the setup, on a Nexus optical table (Thorlabs, United Kingdom). To manipulate the nanoindenter, the Dataviewer software was used.

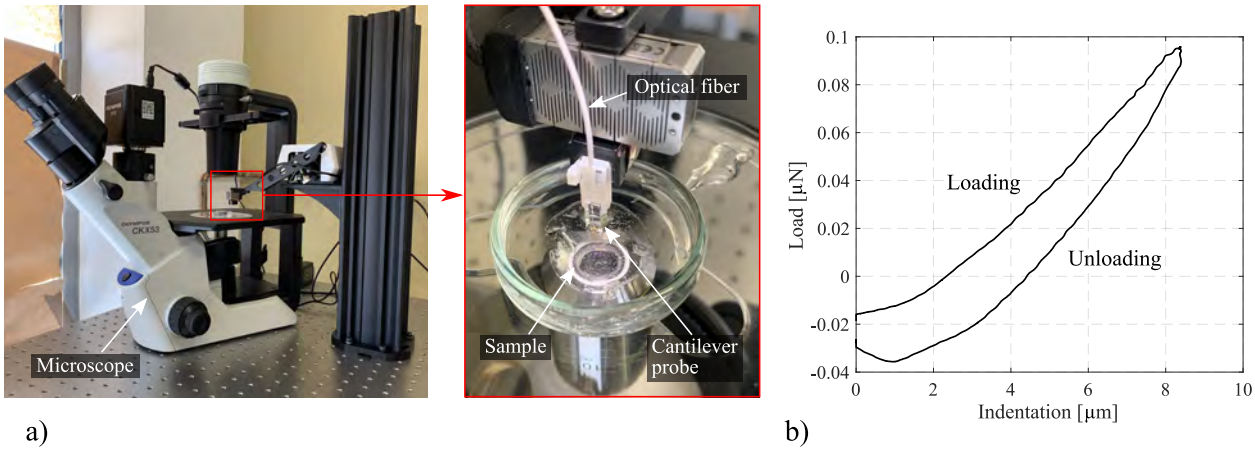

a) b)

Figure 3.2: Nanoindentation framework. (a) Experimental setup for nanoindentation experiments with a detail of the nanoindenter showing the probe and a illustrative sample. (b) Representative curve of a monotonous loading-unloading indentation.

Monotonous indentation measurements were performed with a final indentation depth of 10 µm and a rate of 1 µm s^{-1}. A surface-finding stage with force threshold of 2.5 nN and approaching speed of 20 µm s^{-1} preceded every indentation. After making contact, the probe was raised 10 µm above the surface to start the measurement indentation. Indentations were displacement-controlled to minimize the noise in the signal. The Hertz contact model allowed to obtain the Young's modulus (E) from the loading branch of the load-indentation curves. These were fitted up to 25 % of the maximum load, being the contact point determined for the 5 % of this maximum, according to the following equation

$$E = \frac{3}{4} f\, r^{-1/2} h^{-3/2} \left[1 - \nu^2\right], \tag{3.1}$$

where f is the indentation force, r is the tip radius, h is the indentation and ν is the Poisson's ratio, which was defined as 0.5 following incompressibility assumption.

The relaxation tests started with an indentation at 20 µm s^{-1} and continued for 60 s with a constant-indentation step. From these, characteristic relaxation times were computed for an exponential decay of 63.21 %. To ensure repeatability, at least ten repetitions, each on a different location, were done.

3.2 Soft-magnetic MREs

3.2.1 Materials and synthesis

For the present study, MREs composed of a soft elastomeric matrix and soft magnetic particles were considered. With the aim of developing optimal extremely soft MREs for bioengineering applications [285, 286], the chosen elastomeric phase is Dowsil CY52-276 (DowSil, Midland, MI, USA) (PDMS), provided in two phases. Both phases get cross-linked by the so-called curing process as they are combined in a ratio of 1:1, according to the manufacturer indications. To avoid discrepancies in the raw material, the same batch is used to manufacture all the samples. Regarding the magnetic particles, these are soft SQ carbonyl iron powder (CIP) (BASF, Germany), obtained from thermal decomposition of iron pentacarbonyl and with a mean diameter of $3.9 - 5$ µm. These particles present soft-magnetization characteristics that make them highly suitable for applications that require tuning the mechanical properties of the structure. The size of the particles, contrary to smaller nanometric magnetic fillers, enables for sufficient magnetization and enhances the magnetorheological response of the MRE.

For the selection of PDMS-magnetic particles' ratios used in this work, the following two limitations were considered: i) the mixture can become too viscous to be processed above 40 vol.% according to Lokander [287], and ii) the existence of a percolation threshold, which is related to the capacity of the particles to move along the carrier matrix and occurs above 20 vol.% [63]. Therefore, four different samples have been considered consisting of PDMS with phases volume ratio 1:1 and particles' volume fraction (ϕ) of 0, 0.1, 0.2 and 0.3. Moreover, additional samples were prepared with alternative mixing ratios to elucidate the effect of the stiffness of the matrix, i.e., 6:5, 9:10, and 5:6. Figure 3.3 depicts the manufacturing process.

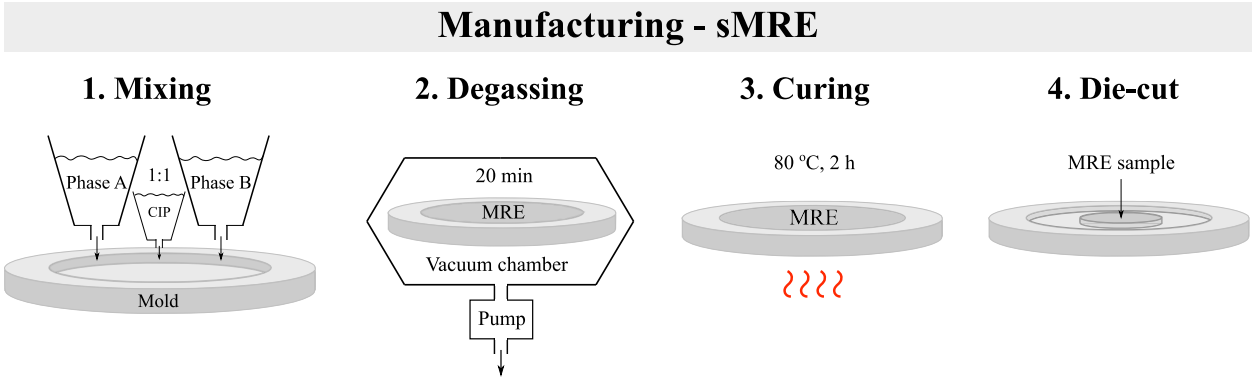

Figure 3.3: Scheme of the experimental manufacturing methodology using a mold made of polytetrafluoroethylene (PTFE). The manufacturing methodology is composed of four steps: (1) blending of the components, i.e., the two phases of the elastomeric matrix (phases A and B) and the soft-magnetic powder; (2) degassing in a vacuum chamber; (3) curing in an oven, and (4) die-cutting 1 mm height and 20 mm diameter samples. Note that ice is used to prevent the chemical reaction during the first synthesis stages.

The morphology of the matrix and distribution of the magnetic particles was assessed using field emission scanning electron microscopy (FESEM). To obtain cross-section micro-

graphs, virgin samples were frozen into liquid nitrogen prior to physical fracturing. The samples were coated with gold by using the Leica EM ACE600 (Leica, Wetzlar, Germany). Transversal micrographs were taken using a TENEO-LoVac (FEI, Hillsboro, Oregon) working at 5-10 kV. The results are presented in Figure 3.4, where a homogeneous random distribution of the particles can be observed.

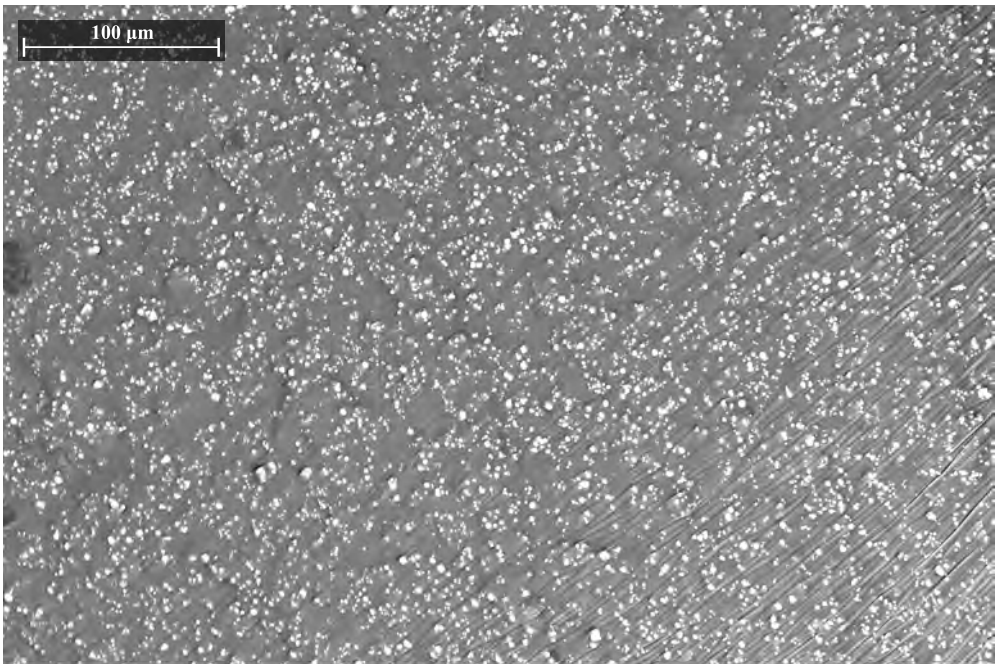

Figure 3.4: Field emission scanning electron microscopy (FESEM) images of the microstructural arrangement before magnetic actuation of soft-magnetic MREs for a particles content of 30 vol.%.

3.2.2 Magneto-mechanical characterization under uniaxial loading

An important consideration about uniaxial compression loading relates to barreling effect, widely reported when deforming cylindrical samples [288–290]. In this regard, the adhesion along the sample-machine interface gives rise to frictional contact that may not correspond to free-slip boundary conditions. Therefore, radial shear stress components should be considered on the sample-plate interfaces, leading to higher macroscopic stiffness of the structure. For this reason, and to ensure free displacement of both upper and lower surfaces, a lubricant coating on the sample was applied (on both upper and lower surfaces) before performing every test. In this way, it is guaranteed that the lubrication conditions are repetitive for all tests and radial shear stresses on the interfaces can be neglected.

The following subsections report the results for monotonous compression, relaxation and frequency sweeps (i.e., dynamic mechanical analysis, DMA) tests. Note that all the tests were performed under compression loading.

Monotonous uniaxial compression tests

Mechanical monotonous compression tests were performed to a final strain of 45 % and with three strain rates $\dot{\epsilon} = \{0.03, 0.3, 0.7\}$ s^{-1}, for each particles' volume fraction $\phi = \{0, 0.1, 0.2, 0.3\}$. Six repetitions for each experimental condition ensure repeatability. The results are collected in Figure 3.5 by means of engineering stress versus engineering strain showing average curves and experimental dispersion. Moreover, Table 3.1 provides a quantitative summary of the tangent modulus at the strains of 10 % and 30 %, as well as the relative stiffening due to the fillers embedded in the matrix (i.e., mechanical stiffening).

The average curves in each sub-figure correspond to different magnetic particle's volume fractions for a same strain rate. In addition, scatter areas are drawn as an intuitive way to define the space that comprises the raw experimental data, for the same test conditions. These results show clear trends in the mechanical response of the MREs. For every condition, the stress-strain curve presents a quasi-linear region at small displacements that becomes non-linear for larger strains. In addition, the stiffness of the samples always increases with the amount of magnetic particles, regardless which deformation rate is considered. Such an increase is explained by the much higher stiffness of the particles and their contribution hindering the polymer chains movement within the carrier matrix. Special attention is given to the stiffening from $\phi = 0.2$ to $\phi = 0.3$, for which the difference is notably smaller than the one that occurs as the magnetic particle's volume fraction increases from 0 to 0.2. This observation is explained by the percolation threshold that, from $\phi = 0.2$ on, promotes the formation of clusters and other sorts of aggregates. This feature would justify the decrease in the stiffening effect of the magnetic particles at high volume fractions [63]. Furthermore, the study of the strain rate dependency uncovers valuable information about the viscoelastic effects. In this regard, higher compression rates result in higher MRE stiffness. This rate dependency is directly related to stress states owing to viscous dissipation phenomena, which is deeper investigated in the following sections.

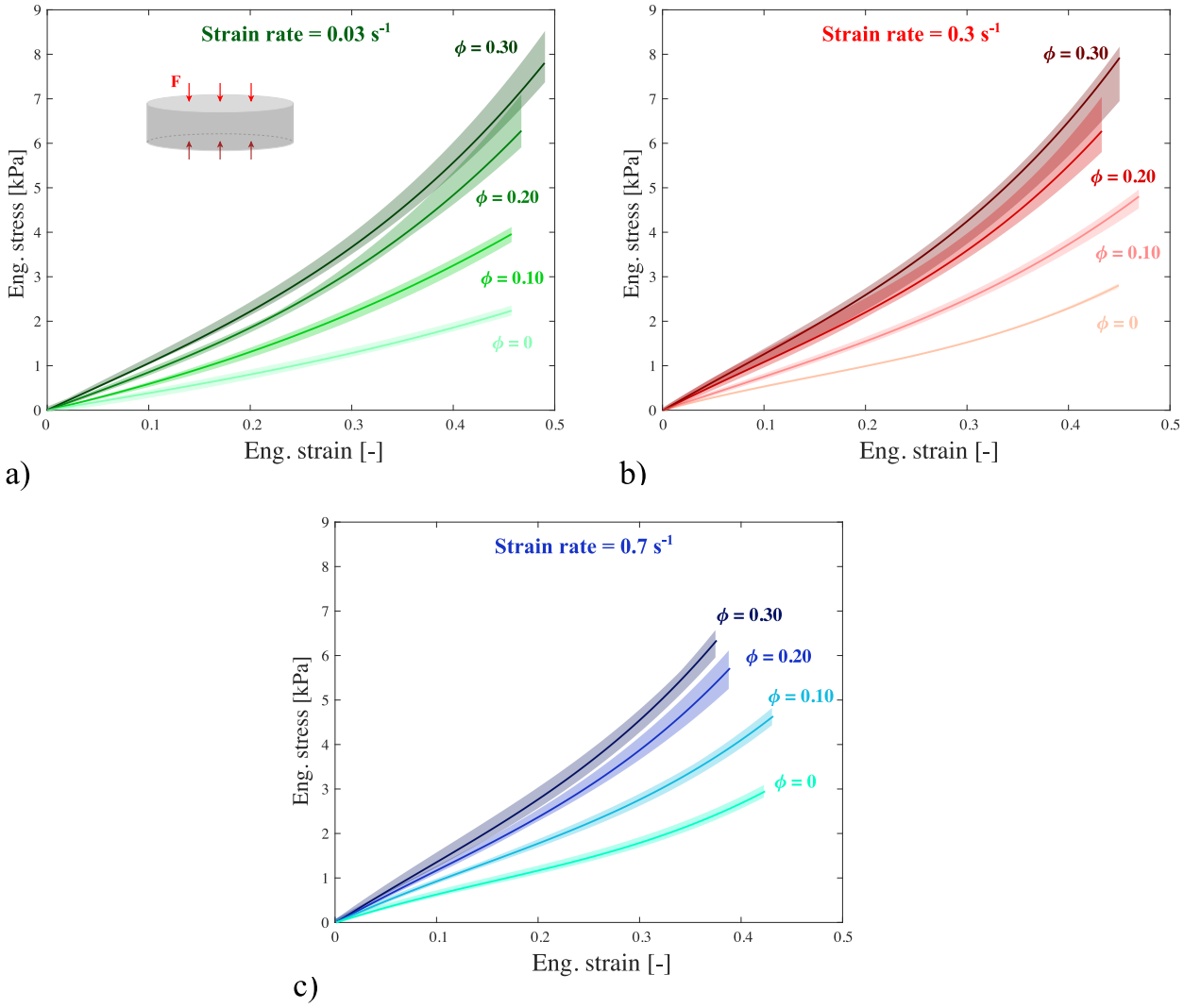

Figure 3.5: Experimental results for the monotonous uniaxial compression tests upon 1 mm height and 20 mm diameter cylindrical sMRE samples. Engineering stress is plotted against engineering strain for three different strain rates: (a) 0.03 s^{-1}, (b) 0.3 s^{-1}, and (c) 0.7 s^{-1}, and for magnetic particles' volume fractions of $\phi = \{0, 0.1, 0.2, 0.3\}$. A scatter area around each mean curve is depicted to quantify the variability of experimental data sets.

Table 3.1: Quantitative summary of the trends revealed by mechanical uniaxial monotonous compression tests on sMRE samples with magnetic particles' volume fractions of $\phi = \{0, 0.1, 0.2, 0.3\}$ and magnetic fields of $B = \{0, 200, 500, 1000\}$ mT. The results are given for three strain rates $\dot{\epsilon} = \{0.03, 0.3, 0.7\}$ s^{-1}. All the results provided correspond to the mean values over the six experimental repetitions.

Case study: Mechanical tests - Compression		**CIPs amount (ϕ)**			
Parameter	**Test conditions**	**0**	**0.1**	**0.2**	**0.3**
Tangent modulus at 10 % strain, E [kPa]	0.03 s^{-1}	4.0	6.5	9.0	10.8
	0.3 s^{-1}	4.7	7.6	10.6	12.6
	0.7 s^{-1}	5.6	8.5	11.4	13.4
Tangent modulus at 30 % strain, E [kPa]	0.03 s^{-1}	5.2	9.6	14.7	16.4
	0.3 s^{-1}	6.3	10.7	16.0	19.2
	0.7 s^{-1}	7.3	11.4	17.7	20.8
CIPs stiffening ratio at 10 % strain, $E_{\phi=i}/E_{\phi=0}$ [-]	0.03 s^{-1}	-	1.6	2.3	2.7
	0.3 s^{-1}	-	1.6	2.3	2.7
	0.7 s^{-1}	-	1.5	2.0	2.4
CIPs stiffening ratio at 30 % strain, $E_{\phi=i}/E_{\phi=0}$ [-]	0.03 s^{-1}	-	1.8	2.8	3.1
	0.3 s^{-1}	-	1.7	2.6	3.1
	0.7 s^{-1}	-	1.6	2.4	2.8

Relaxation tests

Relaxation tests allow to examine viscous mechanisms by applying a fixed strain and monitoring the evolution of the stress state along time. The initial deformation step is prescribed by setting a fast strain rate of 0.7 s^{-1} (maximum value allowed by the experimental system), which is followed by a relaxation time at constant strain of 90 s. These results, for the different MREs tested, are depicted in terms of engineering stress versus engineering strain curves for strains of 40 % and 25 %, see Figure 3.6.

The calculation of the characteristic relaxation time[9] helps analyze the results. Overall, these results show different tendencies. A clear increase in the characteristic relaxation time is observed when increasing the particles content. Thus, relaxation times range from around 1 s, for the case of PDMS without magnetic particles, to 6.5 s, for the case of $\phi = 0.3$ (see further details in Table 3.2). In this regard, the inclusions in the carrier matrix hinder the mobility of the polymeric chains resulting in slower viscous relaxation processes. Another finding from these tests is that the relaxation times barely depend on the applied strains.

[9]Here, the characteristic relaxation time is defined as the time that an exponentially decreasing variable takes to accomplish a 63.21 % of the stress relaxation for infinite time (i.e., exponential decay).

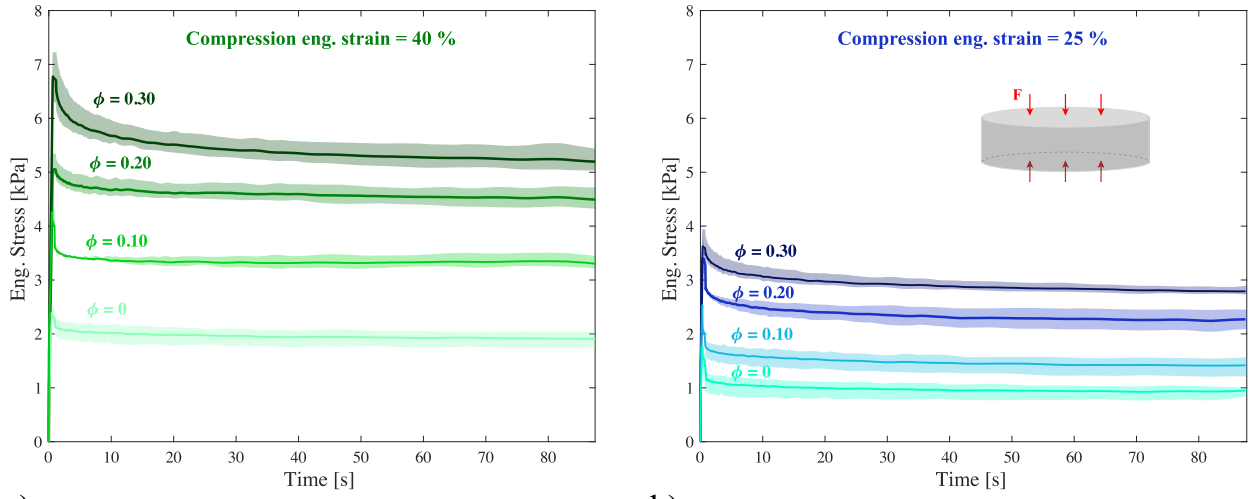

Figure 3.6: Experimental results for the relaxation tests upon 1 mm height and 20 mm diameter cylindrical sMRE samples. Engineering stress is plotted against time for (a) 40 % and (b) 25 % applied strains and magnetic particles' volume fractions of $\phi = \{0, 0.1, 0.2, 0.3\}$. A scatter area around each mean curve is depicted to illustrate the limits of experimental data sets.

Table 3.2: Quantitative summary of the characteristic relaxation time, defined as the time that it takes to accomplish a 63.21 % of the total stress relaxation, obtained from the uniaxial compression rheology tests. The values correspond to the mean values over the six experimental repetitions.

Case study: Mechanical tests - Compression		**CIPs amount (ϕ)**			
Parameter	**Test conditions**	**0**	**0.1**	**0.2**	**0.3**
Characteristic relaxation time [s]	Mean value	1.0	1.1	4.7	6.5

Dynamic mechanical analysis (DMA) under magneto-mechanical loading

Dynamic mechanical analysis is performed to investigate the viscoelastic behavior of the MREs under uniaxial compression loading and different external magnetic fields. This analysis provides, for the different manufacturing and magnetic conditions tested, the evolution of the storage (E'), loss (E'') and complex (E^*) moduli with the excitation frequency. Note that these moduli are determined by the linearization of the material stiffness at small strain and within the linear viscoelastic region, i.e., tangent modulus. Another interesting parameter is $\tan\delta = \frac{E'}{E''}$ (loss factor), which provides a measure of the ratio between the stored and dissipated energies. Frequency sweeps are conducted from 0.01 Hz to 16 Hz for magnetic particles' volume fractions of $\phi = \{0, 0.1, 0.2, 0.3\}$ and for axial magnetic flux densities of $B = \{0, 200, 500, 1000\}$ mT. Moreover, an amplitude of 25 µm (i.e., 2.5 % strain) was used. The results are shown in Figure 3.7 and in Figure 3.8 for external magnetic actuations of 0 mT, 200 mT, 500 mT, and 1000 mT, respectively. In addition, Figure A.2 contains the results for the elastomeric matrix (i.e., with no fillers inside).

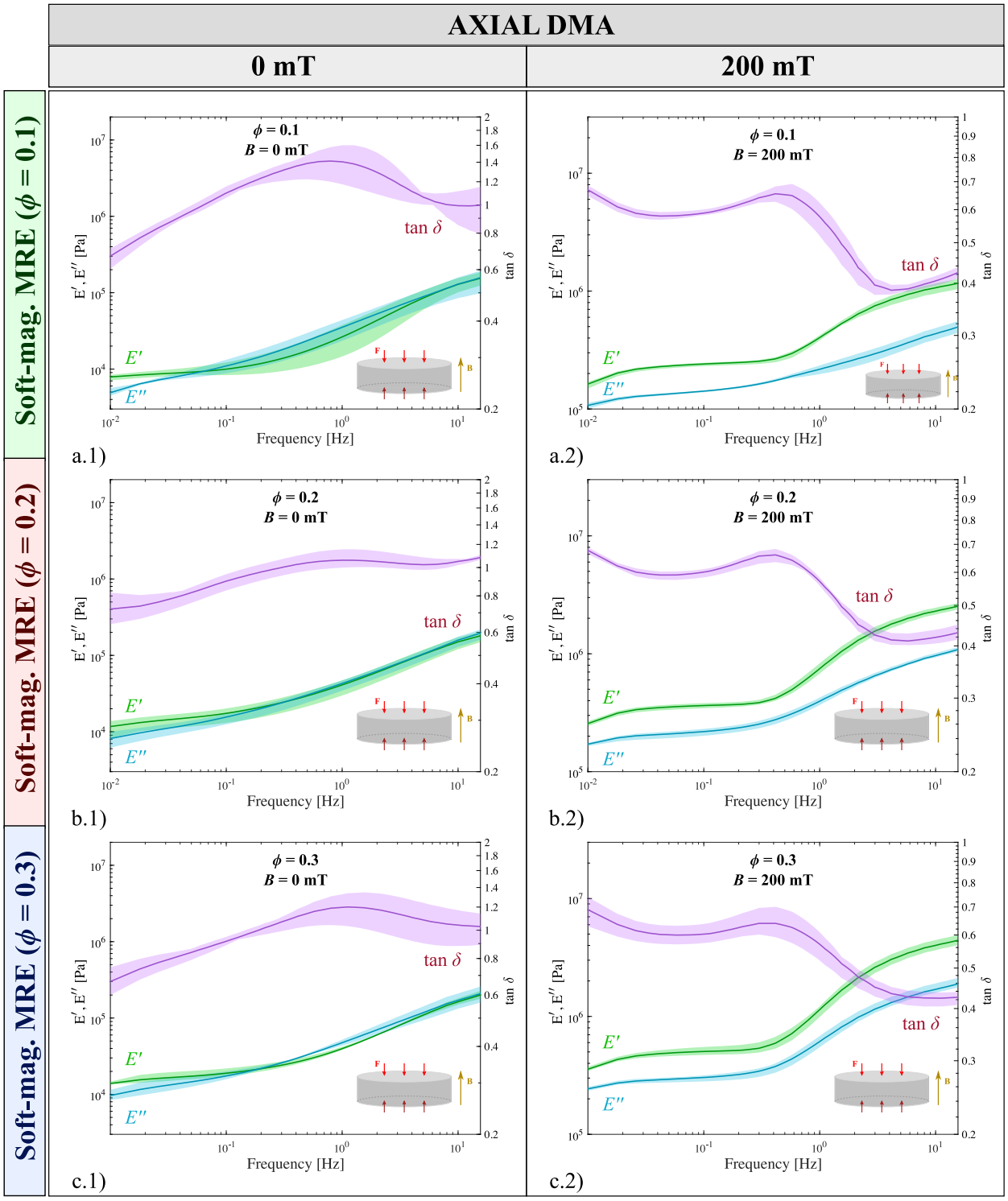

Figure 3.7: Experimental results for frequency sweeps from 0.01 to 16 Hz under uniaxial compressive DMA, 1 mm height and 20 mm diameter cylindrical samples and with magnetic particles volume fractions (ϕ) of 0.1, 0.2 and 0.3. Storage modulus (E'), loss modulus (E'') and loss factor ($\tan\delta$) are plotted against frequency. Magnetic fields of a-b.1) 0 mT and a-c.2) 200 mT are externally applied on the samples. Scatter areas around each mean curve are depicted to quantify the variability of experimental data sets.

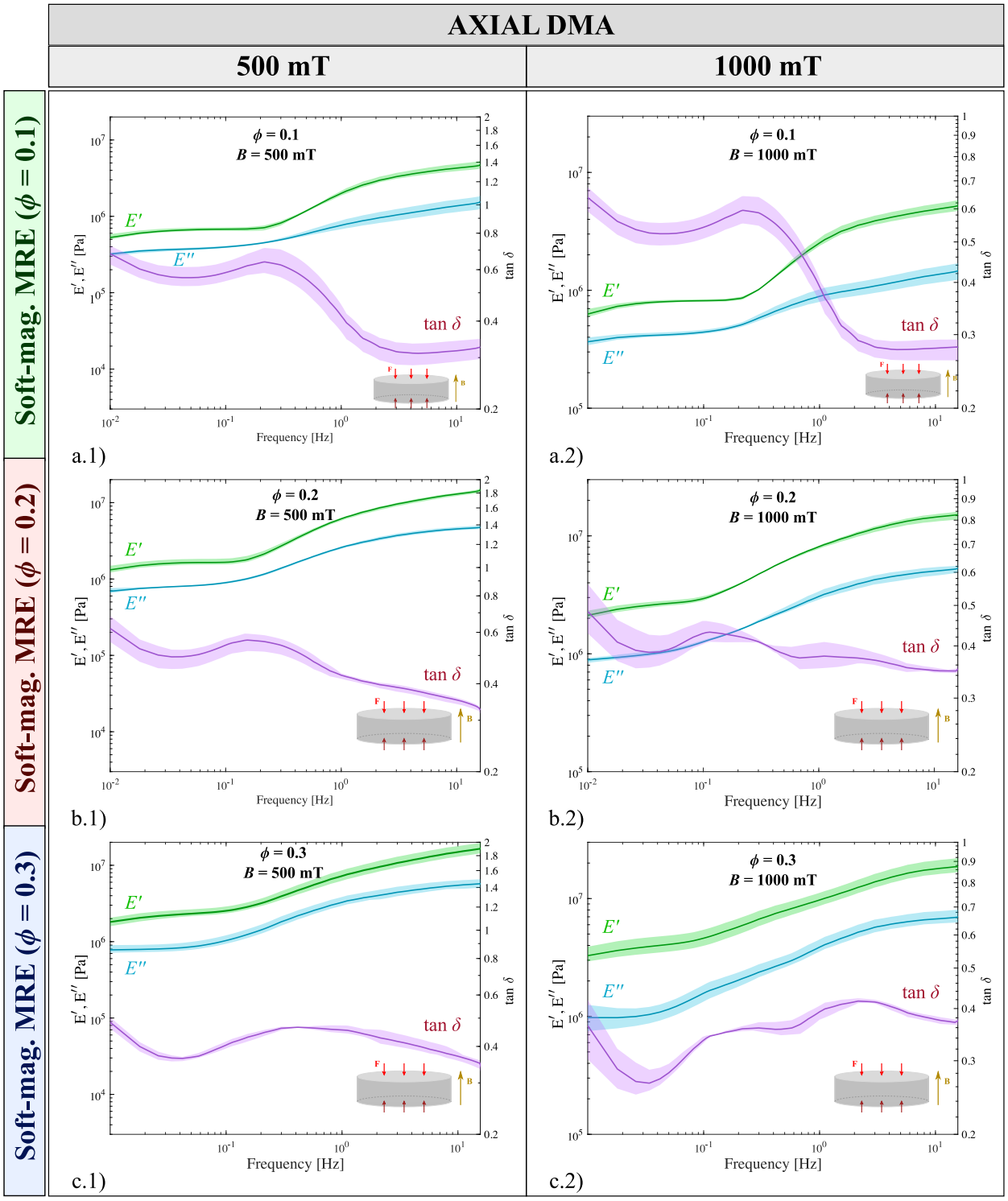

Figure 3.8: Experimental results for frequency sweeps from 0.01 to 16 Hz under uniaxial compressive DMA, 1 mm height and 20 mm diameter cylindrical samples and with magnetic particles volume fractions (ϕ) of 0.1, 0.2 and 0.3. Storage modulus (E'), loss modulus (E'') and loss factor ($\tan\delta$) are plotted against frequency. Magnetic fields of a-b.1) 500 mT and a-c.2) 1000 mT are externally applied on the samples. Scatter areas around each mean curve are depicted to quantify the variability of experimental data sets.

Several findings can be highlighted from these DMA tests. For every B-field (magnetic flux density field) value and for every magnetic particles concentration, both storage and loss moduli monotonously increase with frequency due to the viscous nature of the MRE

samples (i.e., strain rate dependency). The wavy behavior of the factor suggests that different relaxation mechanisms become excited at different frequencies. The presence of the magnetic particles hinders the mobility of polymeric chains, hence the macroscopic stiffness results to be from two to three times larger than its counterpart without magnetic particles. When an external magnetic actuation is applied, a remarkable stiffening of the MRE samples takes place. This stiffening can be quantified by the magnetorheological effect, defined as $MR_{Effect} = \frac{E'_{B=i}}{E'_{B=0}}$. Thus, the MR_{Effect} ranges from 7.4 to 235.9 for 200 mT and 1000 mT, respectively (see further analysis in Table 3.3). In fact, by applying a 1000 mT magnetic field (Figure 3.8), the complex modulus experiences a relevant increase from the order of a few kPa to MPa. Moreover, under magnetic field conditions, tan δ values show an abrupt decrease, indicating that the mechanical behavior approaches to that of an ideal elastic solid.

Table 3.3 synthesizes major tendencies from axial compression tests. First, the characteristic stress relaxation time is found to be significantly influenced by the amount of magnetic particles, with values from around 1 s for smaller amounts up to 6.5 s for the highest concentrations. Such an effect is demonstrated numerically in a work by the authors [291]. In this regard, the polymeric network can be understood as a mix of a cross-linked network and free elastomeric chains. When the MRE is quickly deformed, the cross-linked network pushes the remaining elastomeric chains resulting in a higher instantaneous stiffness. These free chains tend to slip within the polymeric network relaxing the stiffness along time. However, the presence of the stiff magnetic particles hinders such a relaxation leading to higher characteristic times. Although this effect is quite limited at low particles content (i.e., $\phi = 0.1$), it is significant at higher ones. Moreover, relaxation times are found to not significantly change with the imposed strain, i.e., the tendencies found on relaxation tests for 25 % and 40 % strain present no significant changes. This indicates that alternative compression states do not lead to different viscous relaxation mechanisms, thus presenting similar relaxation processes. Still associated with viscous effects, all the MREs tested show a direct relationship between apparent stiffness and strain rate. Furthermore, when externally applying a magnetic field, the magneto-mechanical coupling plays a major role determining the response of the material. To frame this coupling in a quantitative fashion, representative mechanical parameters are shown at low, medium and high excitation frequencies in DMA $f = \{0.01, 8, 16\}$ Hz. Furthermore, the relative influence of the magnetic field on the mechanical properties of the composite is defined by means of the so-called magnetorheological effect ratio (MR_{Effect}). For large amount of magnetic fillers, the MRE becomes up to 235.9 times stiffer. Also, note that the MR effect is around twice larger for smaller excitation frequencies. All in all, such a broad set of quantitative results extracted from the charts from previous sections allows for easy comparison of the behavior of the MRE in compression mode. Note that the amount of magnetic fillers encounters certain limitations when large amounts are added to the composite. For this reason, MRE samples with very high content of particles are mechanically less efficient than their counterparts with fewer fillers. Kallio et al. [51] reported that BASF SQ CIP has a critical particle volume concentration (CPVC) of 29.1 %, defined from the apparent and bulk densities of CIPs for the particles to be in contact. Thus, the MR effect shows a maximum at the CPVC value. The results fulfill this tendency, i.e., the increase in the MR effect from magnetic particle's volume fraction

$\phi = 0.1$ to $\phi = 0.2$ is bigger than that from $\phi = 0.2$ to $\phi = 0.3$. For compression, the averaged MR effect increase (ΔMR_{Effect}), for the three excitation frequencies shown, from $\phi = 0.1$ to $\phi = 0.2$ and for 1000 mT is of $\Delta MR_{Effect} = 70.6$, whereas it is only an increase of $\Delta MR_{Effect} = 25.4$ from $\phi = 0.2$ to $\phi = 0.3$. These analyzed ΔMR_{Effect} suggest that the CPVC is close to $\phi = 0.3$, hence the magnetorheological stiffening is less efficient for larger amounts of magnetic fillers.

Table 3.3: Quantitative summary and comparison of the trends revealed by magneto-mechanical compression DMA tests on MRE samples with magnetic particles' volume fractions of $\phi = \{0, 0.1, 0.2, 0.3\}$ and magnetic fields of $B = \{0, 200, 500, 1000\}$ mT. Values are given for three oscillation frequencies, i.e., 0.01 Hz, 8 Hz and 16 Hz. All the results provided correspond to the mean values over the six experimental repetitions.

Case study: Magneto-mechanical tests - Compression		**CIPs amount (ϕ)**			
Parameter	**Test conditions**	**0**	**0.1**	**0.2**	**0.3**
Complex modulus E^* [kPa] for 0 mT	0.01 Hz	7	9	14	17
	8 Hz	83	162	195	213
	16 Hz	116	221	265	291
Complex modulus E^* [kPa] for 200 mT	0.01 Hz	-	195	308	432
	8 Hz	-	1102	2380	4147
	16 Hz	-	1265	2740	4767
Complex modulus E^* [kPa] for 500 mT	0.01 Hz	-	618	1490	1973
	8 Hz	-	4133	13160	15169
	16 Hz	-	4800	14840	17222
Complex modulus E^* [kPa] for 1000 mT	0.01 Hz	-	697	2188	3421
	8 Hz	-	4873	14862	18613
	16 Hz	-	5369	15963	19890
MR Effect, $\frac{E'_{B=200\text{mT}}}{E'_{B=0\text{mT}}}$ [-]	0.01 Hz	-	20.6	21.9	25.7
	8 Hz	-	9.0	16.4	26.1
	16 Hz	-	7.4	13.7	21.4
MR Effect, $\frac{E'_{B=500\text{mT}}}{E'_{B=0\text{mT}}}$ [-]	0.01 Hz	-	67.0	112.7	130.4
	8 Hz	-	36.3	92.8	97.1
	16 Hz	-	29.0	76.5	79.3
MR Effect, $\frac{E'_{B=1000\text{mT}}}{E'_{B=0\text{mT}}}$ [-]	0.01 Hz	-	79.7	181.1	235.9
	8 Hz	-	41.2	105.0	118.9
	16 Hz	-	32.5	79.1	86.7

3.2.3 Magneto-mechanical characterization under shear loading

This section addresses the experimental results related to the magneto-mechanical behavior of the MREs tested under different torsional shear loading conditions. Contrary to the compression tests, no lubricant is used as no slip between the sample and the upper and bottom plates is desired. In this regard, Walter et al. [292, 293] have thoroughly examined the boundary conditions in experimental magneto-mechanical rheology, highlighting their importance and providing guidance to achieve slip-free interfaces between the plates and the

sample when working in shear mode. The sticky nature of the elastomeric matrix ensures the contact at the interfaces preventing from wall slippage. Such a contact is characterized by the azimuthal shear stress (τ) on the interfaces, which varies with radial coordinate r (i.e., zero at $r = 0$ and maximum at $r_{max} = 10$ mm). Hereafter, the stress and strain values are referred to a radial coordinate of $r = \frac{2}{3}r_{max}$. From the torsion angle (α) and torque (M) on the rheometer axis, and assuming that the torsion angle is linearly distributed along the axial coordinate of the sample, the stress and strain are calculated for the representative points as

$$\tau(M) = \frac{4M}{3\pi r_{max}^3}, \qquad \gamma(\alpha) = \frac{2}{3}\frac{\alpha r_{max}}{H}, \tag{3.2}$$

with H the initial height of the sample.

Constant oscillatory shear

To start with, constant amplitude and frequency oscillatory finite shear tests are conducted on cylindrical MRE samples. In these experiments, the upper plate applies a torque on the cylindrical sample to perform a sine-shaped angular displacement. This deformation profile is defined for a 48 % strain and fixed angular velocities of $\omega = \{0.1, 2\}$ rad s^{-1}. The strain amplitude is such that the sample deforms beyond the infinitesimal strain regime. In this regard, Figure A.1 contains additional results for amplitude sweep experiments. Moreover, the axial position of the upper plate ensures initial sample-plate contact with negligible compressive axial stress. Note that all these tests are carried out under different magnetic flux densities of $B = \{0, 200, 500, 1000\}$ mT. As for the compression tests, six repetitions for each test condition guarantee repeatability.

Figure 3.9 shows, for the different magnetic field conditions, the results in the form of shear stress versus shear strain for the chosen angular velocities (each sub-figure) and for magnetic particle's volume fractions of $\phi = \{0, 0.1, 0.2, 0.3\}$. Such a representation is often known as the Lissajous figure, which conveys interesting information, e.g., about the energy lost by viscous dissipation mechanisms, in a visual way.

Clear trends can be found from these constant oscillatory shear tests. For all the experimental conditions, larger maximum stresses are reached for higher amounts of magnetic particles. This is due to the same stiffening effect of magnetic particles formerly described in compression tests, where the magnetic fillers hinder the displacement of the polymeric chains leading to increased macroscopic stiffness. Moreover, when external magnetic field is applied, the MRE sample undergoes additional stiffness as a result of internal magnetic interaction forces, with values of the MR effect (defined as $G'_{B=i}/G'_{B=0}$, with G' the shear storage modulus for a magnetic induction B) up to 12.3. As the magnetic field increases, it is also concluded that the Lissajous loops progressively lose their quasi-ellipsoidal shape, in agreement with a previous work by Dargahi et al. [44]. This latter point relates to a pronounced nonlinear response of the composite when increasing the presence of stiffer particles, as observed in compression (Figure 3.5) and tensile tests [87]. Other major factors influencing the mechanical response of the sample are viscous mechanisms. In this regard, maximum stresses appear with the highest deformation rate showing a clear strain rate dependency,

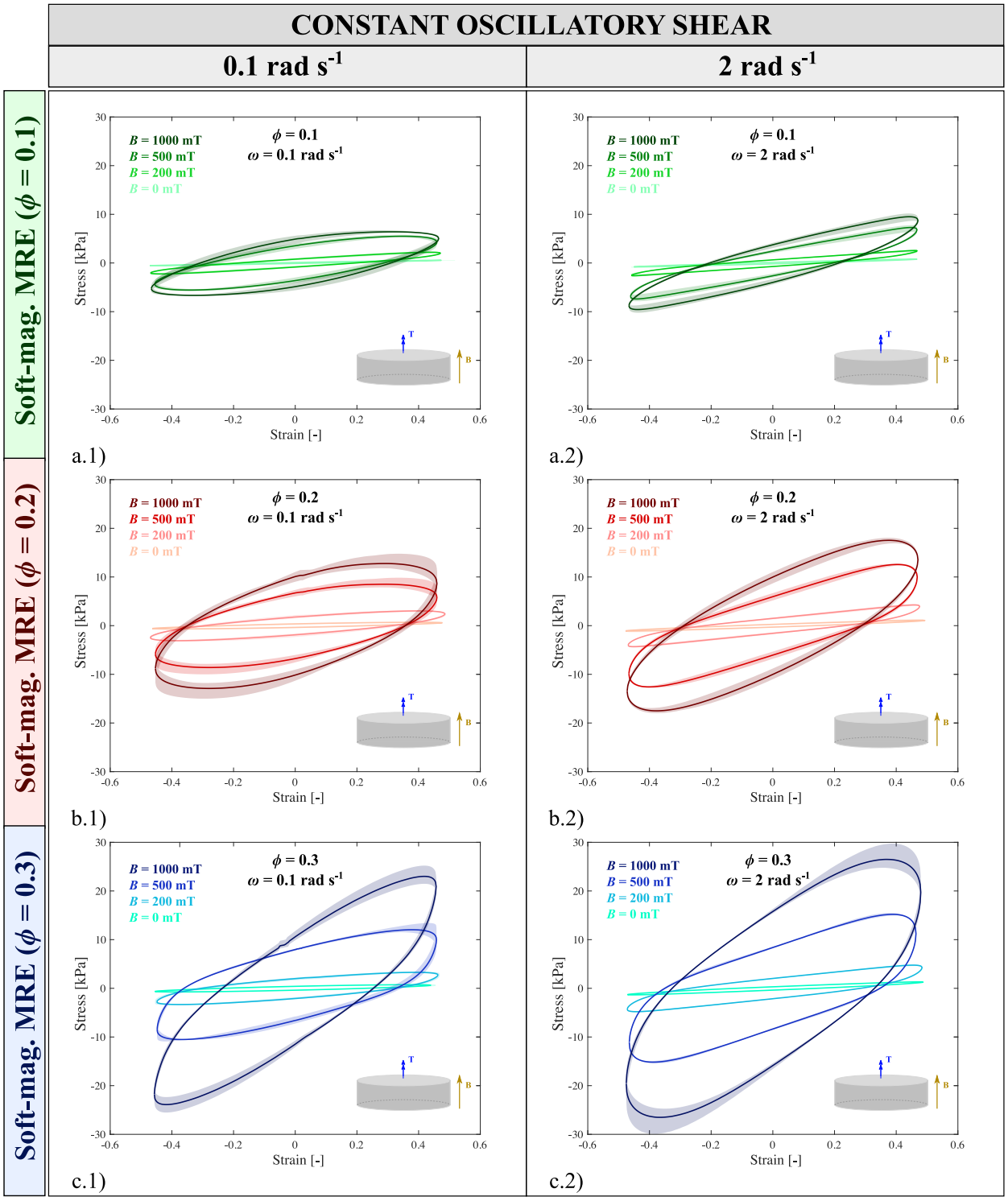

Figure 3.9: Experimental results for oscillatory shear rheology on 1 mm height and 20 mm diameter cylindrical sMRE samples with magnetic particles' volume fractions of $\phi = \{0.1, 0.2, 0.3\}$ and angular velocities of a-c.1) 0.1 rad s^{-1} and a-c.2) 2 rad s^{-1}. The azimuthal shear stress (τ) is plotted against the shear strain (γ). Magnetic fields of $B = \{0, 200, 500, 1000\}$ mT are externally applied on the samples. Scatter areas around each mean curve are depicted to quantify the variability of the experimental data sets.

similarly as observed in compression tests.

Dynamic mechanical analysis (DMA) under shear loading

These experiments can be understood as an extension of constant oscillatory shear ones, where different angular velocities are consecutively applied. For this analysis, as similarly done for compression, the evolution of the storage (G'), loss (G'') and complex (G^*) shear moduli with the excitation frequency is analyzed. The loss factor in shear mode reads as $\tan\delta = \frac{G''}{G'}$.

Frequency sweeps have been conducted from 0.01 Hz to 16 Hz for magnetic particles' volume fractions of $\phi = \{0, 0.1, 0.2, 0.3\}$ and for axial magnetic inductions of $B = \{0, 200, 500, 1000\}$ mT. Note that the results for the matrix (i.e., with no fillers inside) are provided in Figure A.2 in Appendix. Furthermore, note that the used elastomeric matrix presents no significant hardening/softening with strain amplitude (see Figure A.1.a in Appendix). However, in accordance with other works in the literature [44], there is a strong effect of the strain amplitude when testing under external magnetic fields due to changes in the relative positions of the magnetized particles that modulate dipole-dipole interactions (see Figure A.1.b). Therefore, the amplitude of the harmonic oscillations is defined as 0.05 rad (∼30 % strain) to limit this effect (stronger at lower strain amplitudes). The results of these experiments are shown in Figure 3.10 and Figure 3.11, where the storage modulus, loss modulus and loss factor are plotted versus frequency for magnetic fields of 0 mT and 200 mT, and 500 mT and 1000 mT, respectively.

Diverse findings can be stated from these rotational frequency sweeps. For all the test conditions, the complex modulus increases with angular velocity, showing the strain rate dependency of the MREs under shear loading. The maximum stiffness increase of the material due to this effect is observed for MRE samples with $\phi = 0.3$ and a magnetic field of $B = 1000$ mT, presenting a value of $\Delta G^* = 71$ kPa with respect to the smallest oscillation frequency at these conditions. In addition, the loss factor provides relevant information about the viscoelastic behavior of the material. As for the compression mode tests, $\tan\delta$ decreases with larger B-field inductions, denoting that material stiffening due to magnetorheological effect brings it closer to a purely elastic and non-viscous behavior (see a quantitative comparison in Table 3.4). Another remark for high magnetic field (1000 mT) is related to the storage and loss moduli at low frequencies, where both present an abrupt decrease, see Figure 3.11.b. This tendency is more notable for the higher magnetic particles' volume fractions.

Table 3.4 gathers the results from the magneto-mechanical shear tests. A first look into these quantitative values suggests that the MR effect strongly depends on the deformation mode. The DMA frequency sweeps under the same magnetic fields shows a magnetorheological stiffening substantially smaller in shear mode than in axial compression mode (see Table 3.3). In this regard, in shear mode the stiffness of the MRE is improved within one order of magnitude, whereas in axial compression it increased up to two orders of magnitude. These observations must be carefully discussed as they are the result of different effects. On the one hand, it must be noted that the external magnetic field is axially applied (i.e., in compression direction) during both types of tests. This axial magnetic field promotes a strong interaction of the magnetic particles in axial direction which, apart from dipole-dipole

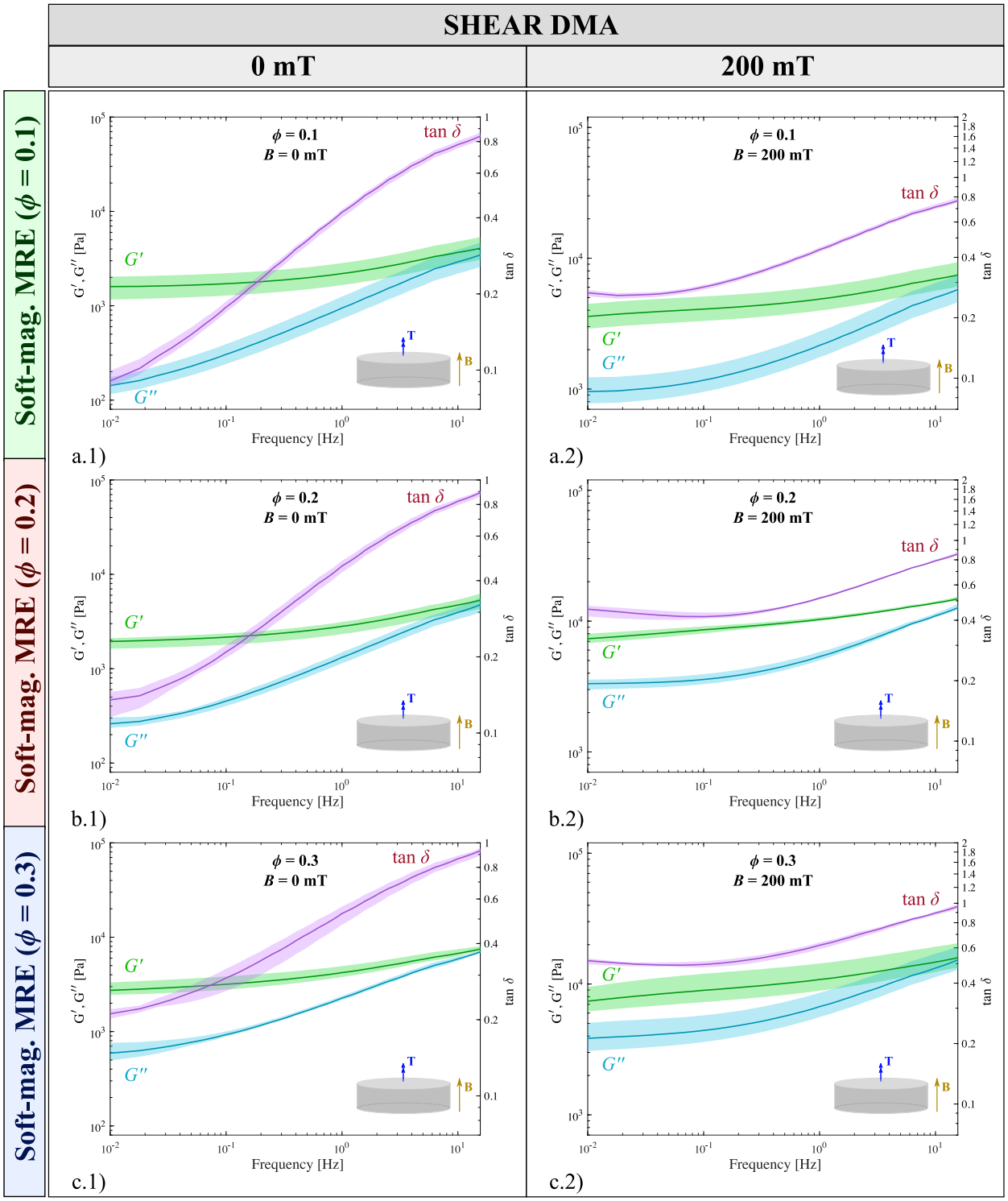

Figure 3.10: Experimental results for frequency sweeps from 0.01 to 16 Hz under shear mode on 1 mm height and 20 mm diameter cylindrical samples and with magnetic particles volume fractions of: (a) 0.1, (b) 0.2, and (c) 0.3. The storage modulus (G'), loss modulus (G'') and loss factor ($\tan\delta$) are plotted against the oscillation frequency. Magnetic fields of (a-c.1) 0 mT and (a-c.2) 200 mT are externally applied on the samples. Scatter areas around each mean curve are depicted to quantify the variability of experimental data sets.

interaction forces, results into particles alignment into chain-like microstructures (note that the extremely soft nature of the elastomer used allows this). Therefore, it seems reasonable

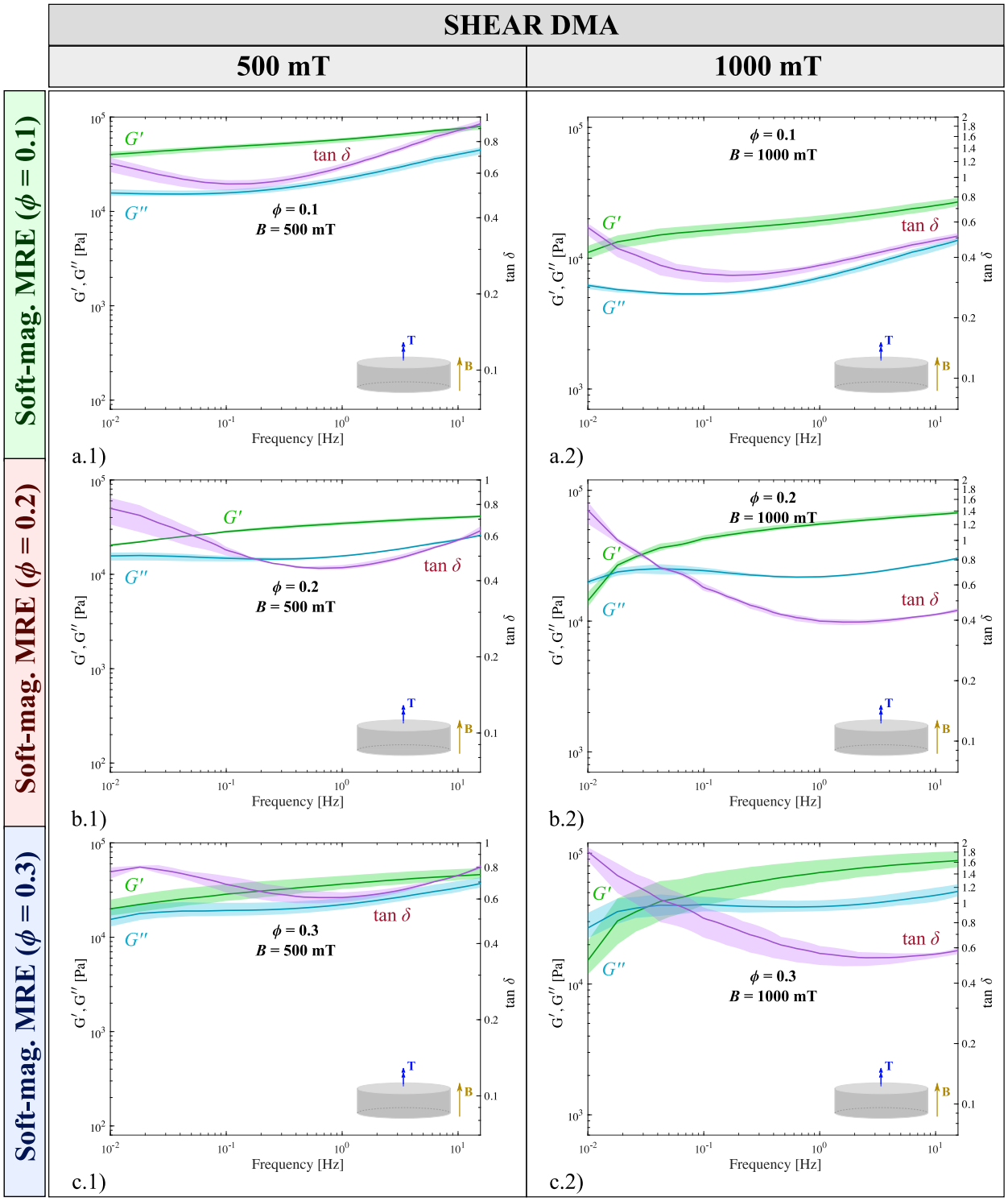

Figure 3.11: Experimental results for frequency sweeps from 0.01 to 16 Hz under shear mode on 1 mm height and 20 mm diameter cylindrical samples and with magnetic particles volume fractions of: (a) 0.1, (b) 0.2, and (c) 0.3. The storage modulus (G'), loss modulus (G'') and loss factor ($\tan\delta$) are plotted against the oscillation frequency. Magnetic fields of (a-c.1) 500 mT and (a-c.2) 1000 mT are externally applied on the samples. Scatter areas around each mean curve are depicted to quantify the variability of experimental data sets.

that external magnetic fields result in a higher resistance to deformation in axial than in shear mode. On the other hand, the application of the axial magnetic field while confining

the axial deformation of the sample leads to a pre-compression state. Thus, when analyzing the MREs under axial loading, a relevant increase in stiffness is observed due to not only magnetic interactive forces but also to such a pre-compression state. However, a thorough study of the effect of this axially induced stress states that it scarcely affects the magnetorheological stiffening. In this respect, Figure 3.12 compares the shear complex modulus obtained from a shear frequency sweep for three different frequencies and three representative conditions: i) MRE under null magnetic field and subjected to negligible axial force (i.e., pre-compression); ii) MRE under an externally applied magnetic field; iii) MRE under null magnetic field and subjected to an axial force equivalent to the one observed during the magneto-mechanical test performed in condition ii) (i.e., equivalent pre-compression state due to the applied magnetic field). These results show small change in stiffness due to the pre-compression arising from magnetic interactions, whereas a much more significant increase in stiffness due to the application of the external magnetic field is found.

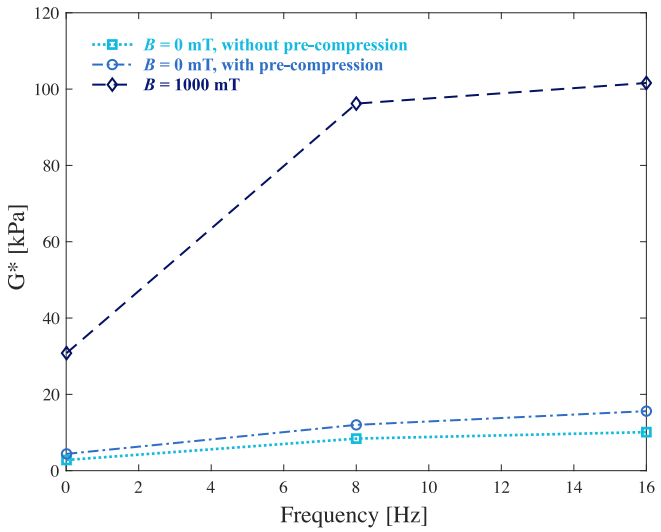

Figure 3.12: Experimental results comparing the effects of three different conditions on frequency sweep tests with frequencies of $f = \{0.01, 8, 16\}$ Hz, i.e., experiment with high magnetic field (1000 mT), experiment without magnetic field but with a pre-strain producing the same axial force as with magnetic field, and experiment without magnetic field and without pre-compression.

Table 3.4: Quantitative summary and comparison of the trends revealed by the mechanical and magneto-mechanical shear tests on MRE samples with magnetic particles' volume fractions of $\phi = \{0, 0.1, 0.2, 0.3\}$ and magnetic fields of $B = \{0, 200, 500, 1000\}$ mT. The results are given for three oscillation frequencies of 0.01 Hz (quasi-static), 8 Hz, and 16 Hz. All the results provided correspond to the mean values over the six experimental repetitions.

Case study: Magneto-mechanical tests - Shear		**CIPs amount (ϕ)**			
Parameter	**Test conditions**	**0**	**0.1**	**0.2**	**0.3**
Complex modulus G^* [kPa] for 0 mT	0.01 Hz	1.1	1.6	2.0	2.8
	8 Hz	3.6	4.4	5.7	8.4
	16 Hz	4.4	5.3	7.0	10.1
Complex modulus G^* [kPa] for 200 mT	0.01 Hz	-	3.7	8.1	8.3
	8 Hz	-	8.1	16.8	18.8
	16 Hz	-	9.3	19.3	21.6
Complex modulus G^* [kPa] for 500 mT	0.01 Hz	-	10.8	24.2	25.3
	8 Hz	-	20.8	45.5	54.3
	16 Hz	-	22.8	48.4	59.1
Complex modulus G^* [kPa] for 1000 mT	0.01 Hz	-	12.7	25.4	30.8
	8 Hz	-	27.2	69.8	96.2
	16 Hz	-	30.1	73.9	101.6
CIPs stiffening ratio, $G^*_{\phi=i}/G^*_{\phi=0}$ [-], for $B = 0$ mT	0.01 Hz	-	1.5	1.8	2.5
	8 Hz	-	1.2	1.6	2.3
	16 Hz	-	1.2	1.6	2.3
MR Effect, $\frac{G'_{B=200\text{mT}}}{G'_{B=0\text{mT}}}$ [-]	0.01 Hz	-	2.2	3.8	2.7
	8 Hz	-	1.9	3.0	2.2
	16 Hz	-	1.8	2.8	2.1
MR Effect, $\frac{G'_{B=500\text{mT}}}{G'_{B=0\text{mT}}}$ [-]	0.01 Hz	-	6.3	10.5	7.3
	8 Hz	-	5.3	8.9	6.8
	16 Hz	-	4.8	7.5	6.1
MR Effect, $\frac{G'_{B=1000\text{mT}}}{G'_{B=0\text{mT}}}$ [-]	0.01 Hz	-	6.9	7.4	5.5
	8 Hz	-	7.0	14.4	13.1
	16 Hz	-	6.4	12.4	11.5

3.2.4 Mechanically confined tests under magnetic actuation

This section introduces novel experiments where the MRE sample is mechanically confined in the axial direction. While keeping such a mechanical boundary condition, a magnetic field actuates in the axial direction at a given magnetic loading rate. Once a specific targeted magnetic field is reached, this magnetic field is kept constant during certain time in order to reach steady state. Note that these experiments have a motivation similar to relaxations tests (here the magnetic field acts as strain). Therefore, the main input in the experiment is the evolution of the magnetic flux density field along time and a mechanical boundary condition equivalent to a permanent unit axial stretch. Then, the upper plate of the rheometre, equipped with an axial load cell, provides the evolution of the axial force (suitably expressed

in engineering stress terms) as output. These tests are conducted for four different magnetic rates that are applied until reaching a magnetic field of 1000 mT, which is then kept constant, and for different MREs with magnetic particle's volume fractions of $\phi = \{0.1, 0.2, 0.3\}$. The results are shown in Figure 3.13 by means of engineering stress versus time showing average curves and experimental dispersion from a number of six tests per condition.

Applying a magnetic field with axially confined samples is equivalent to a relaxation test. However, instead of imposing uniaxial compression by external mechanical boundary conditions, the mechanical forces are imposed by internal interaction forces arising from the application of an external magnetic field. Liao et al. [294] worked on a similar idea by establishing relationships between the magnetic field induction and the pre-strain of MRE samples. These experiments enable in-detail studying the magneto-mechanical principles that originate at the micro-scale level and determine the macroscopic response. Therefore, despite constraining the macroscopic axial deformation, microstructural phenomena drive particles to new states of equilibrium while interacting with the viscoelastic matrix. In addition, under specific conditions (e.g., high particle concentrations, strong magnetic fields), these fillers can collide. In general terms, these magneto-mechanical interplays are difficult to detail and need to be addressed from macroscopic measurements.

Each sub-figure in Figure 3.13 corresponds to a magnetic field application rate $\dot{B} = \{2, 20, 200, 1000\}$ mT s^{-1} and compares the response of different particles' volume fractions. A thorough analysis of these results provides the following unexplored observations:

- The increase in engineering stress (and then in axial force) when applying the axial magnetic field indicates that the MREs tend to expand.
- As the magnetic field ramp begins, the axial force evolves in an initially parabolic fashion. However, this tendency is lost in favor of a sigmoidal fashion when larger values of the magnetic field are reached. These tendencies are related to an internal magnetic stress which depends on the magnetic field by a second order function (see modeling approaches in the literature [170, 295–298]). This relationship changes at higher magnetic fields due to a nonlinear relationship between particles' magnetization and magnetic field when approaching to magnetic saturation (see [182, 184]). Note that although the linear relationship between particles' magnetization and external magnetic field is lost, the particles do not saturate completely [299].
- There is a proportional relationship between the maximum stress reached and the magnetic particles content. This is explained by the higher macroscopic magnetization of the MRE and the increment of internal dipole-dipole interactions between particles pushing the elastomeric matrix to deform [49, 170].
- The maximum stress is reached exactly at the time point where the magnetic field reaches its maximum value at low magnetic rates. However, there is a delay in this peak when the magnetic rate is higher. Such a delay owes to a rate dependency on the particles' magnetization, which presents a limit rate to polarize due to magnetic viscosity [300–303]. This phenomenon is governed by the thermal activation of the magnetization over local energy barriers arising from varied sources, e.g., shape and anisotropy of the particles. The coefficient of magnetic viscosity has been widely used to take into account these mechanisms, being the temperature a major factor [304].

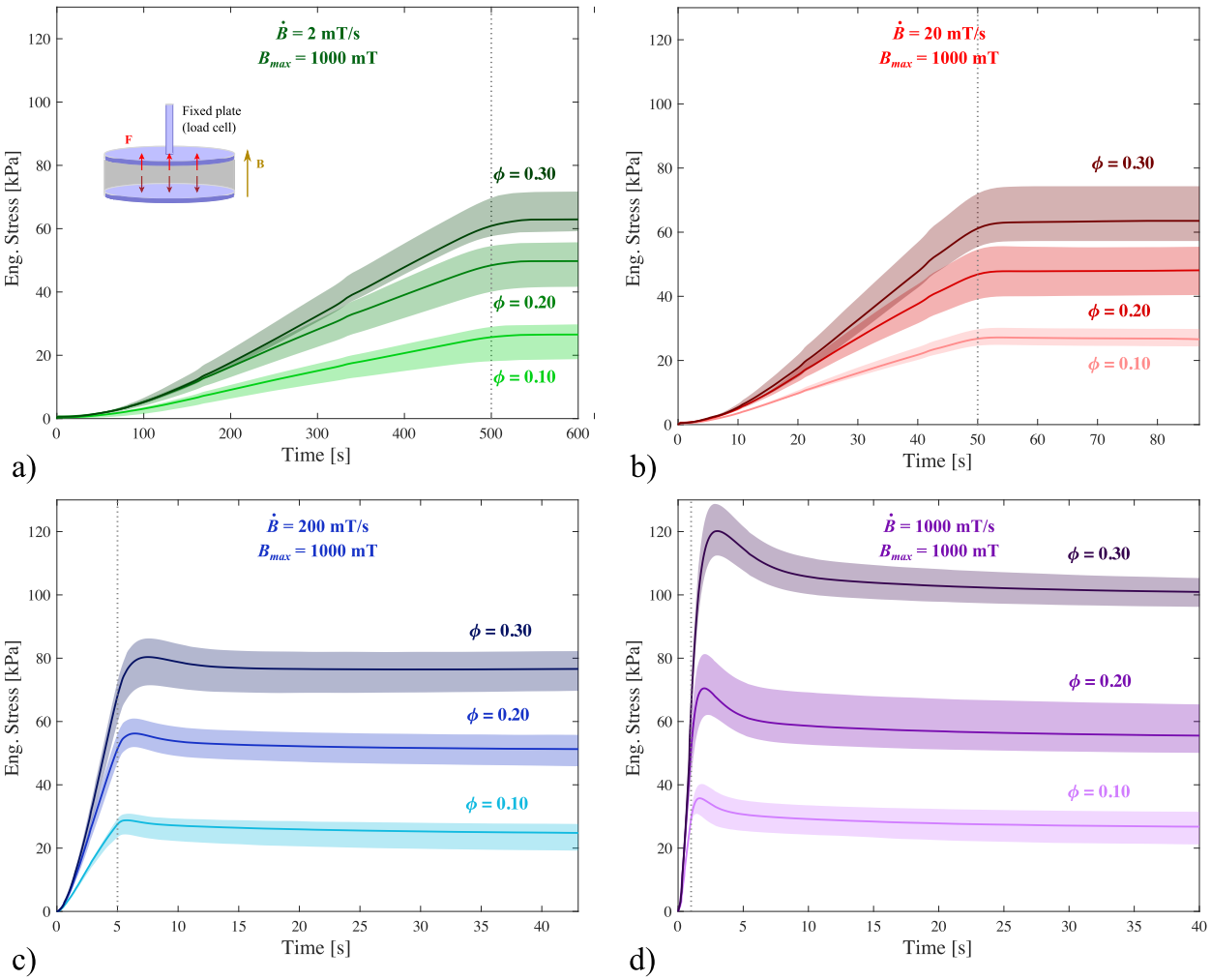

Figure 3.13: Experimental results for the application of a 1000 mT magnetic field in the form of temporal ramps with different application rates: (a) 2 mT s^{-1}, (b) 20 mT s^{-1}, (c) 200 mT s^{-1} and (d) 1000 mT s^{-1}. After reaching the targeted magnetic field, indicated by a dotted vertical line, the magnetic field is kept constant for a given time. Confined axial deformation is imposed during the whole experiment as mechanical boundary condition. The samples consist in cylindrical MREs with height 1 mm and diameter 20 mm, which are manufactured with different magnetic particles' volume fractions of $\phi = \{0.1, 0.2, 0.3\}$. Engineering stress is plotted against time covering the temporal application of the ramp plus an additional period where the field is held constant at 1000 mT. Scatter areas around each mean curve are depicted to quantify the variability of experimental data sets.

• At the lower magnetic rates, although mechanical strain rate effects were expected at these time scales, the maximum stress reached is the same. A recently developed microstructural-based model for soft magneto-active polymers helps understand these tendencies [170]. In this regard, the macroscopic stress is understood as the contribution of a magnetic stress due to dipole-dipole interactions between particles and the external magnetic field, and the contribution of a mechanical stress due to deformation of the polymeric matrix. Thus, when fixing the axial stretch and applying the external magnetic field, the particles magnetize leading to interaction forces and reaching an equilibrium state. In such a scenario, the device measures the magnetic forces transmitted within the MRE. The viscoelastic response is balanced, without relevant implications for the lower magnetic rates. In this regard, a recent co-authored work delves into the microstructural mechanisms

and viscoelastic response of these materials [291].

• For the largest magnetic rates (200 and 1000 mT s^{-1}) a magneto-mechanical relaxation process is observed. Provided that the magnetic particles require a certain amount of magnetic energy and time to reorganize from their initial positions to a new spatial arrangement, a microstructural blockage would occur for sufficiently high field rates. Since magnetic interactions between the magnetic particles are transmitted in the form of mechanical forces to the carrier matrix, this microstructural collapse is macroscopically detected by a larger axial force on the specimen, i.e., larger maximum stresses. This phenomenon requires further investigation by means of more advanced microstructural based models.

• After reaching the maximum stress value, while the stress is kept constant for tests at low magnetic rates, the MREs experience a relaxation response at higher magnetic rates. In other words, at slow enough magnetic rates the particles are able to reach the final equilibrium state (i.e., magnetic particles' distribution under the applied field). Therefore, the purely elastic and viscous contributions of the elastomeric matrix stress balance each other until full microstructural relaxation. Moreover, at higher magnetic rates, the previously mentioned microstructural blockage is followed by a mechanical relaxation of the elastomeric matrix relaxing such a state. Note that this statement is supported by the relaxation time scales observed in these experiments, which are in the same order than the characteristic times identified from the relaxation tests (Figure 3.6).

• The final observation relates to the long term stresses reached after complete relaxation (steady state). These values are notably larger at higher magnetic rates, suggesting that the MRE encounters alternative particles-rearrangement states (i.e., magnetic particles' distributions) attending to the historical evolution of the microstructural deformation. From a mechanical perspective, this effect can be understood as a yielding-like process where the particles and the matrix get blocked under the applied magnetic field. Ongoing efforts are being dedicated to unravel these mechanisms considering longer relaxation times.

3.2.5 Influence of the elastomeric matrix's stiffness

The stiffness of the matrix is another important factor affecting the magneto-mechanical coupling and the response of MREs. To elaborate on it, sMREs with twelve different combinations of elastomeric mixing ratio[10] (i.e., matrix's stiffness) and particles volume fraction were prepared. Note that, a priori, softer elastomeric matrices and higher particles content lead to higher magnetorheological effects (i.e., mechanical deformation under magnetic fields and/or stiffness changes). Figure 3.14 provides the results obtained with macroscopic mechanical compression experiments, i.e., monotonous compression and relaxation tests. Moreover, Table 3.5 contains quantitative values for the characteristic relaxation times. The mixing ratios of the elastomeric matrix are 6:5, 1:1, 9:10, 5:6 (for the softest to the stiffest) and the particles contents, 0, 0.15 and 0.3. Note that, here, no magnetic actuation is applied

[10]Note that the matrix is cured after mixing the two phases provided by the manufacturer, thus the stiffness can be tuned with a proper choice of the mixing ratio of the phases.

yet.

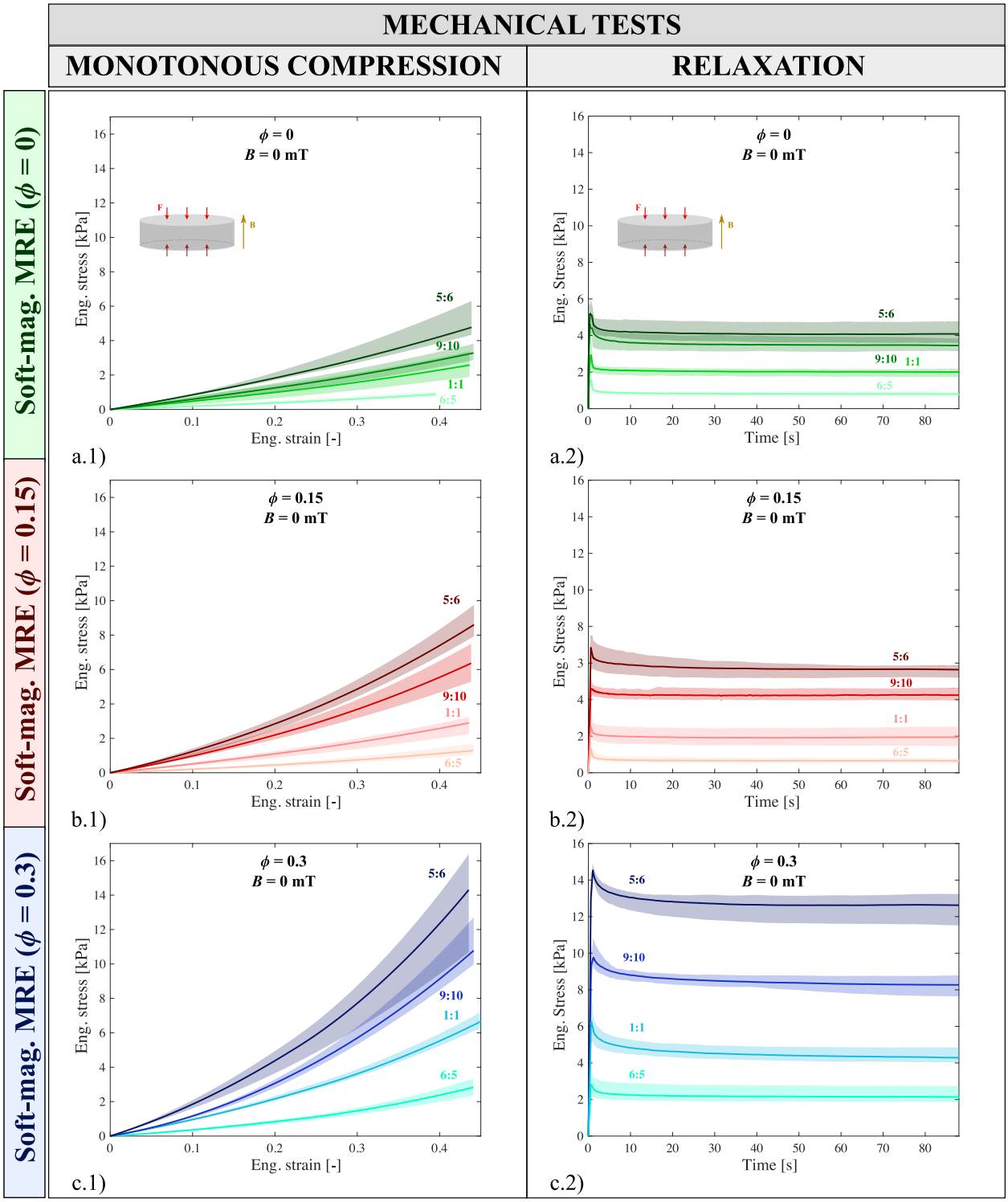

Figure 3.14: Macroscopic behavior of the sMRE under uniaxial compressive deformation and for different manufacturing conditions of the matrix. (a-c.1) The results for monotonous compression tests are depicted as plots of engineering stress against engineering strain for magnetic particles volume fractions of 0, 0.15, and 0.3; and for mixing ratios of the elastomeric matrix of 6:5, 1:1, 9:10, 5:6. The cylindrical samples are compressed at constant quasi-static rate. (a-c.2) Time-dependent behavior of the MRE for different manufacturing conditions. The experimental results from mechanical relaxation tests are presented as engineering stress versus time plots. A 40 % strain step is applied at a fast strain rate of 0.7 s^{-1} and kept constant for 90 s. Scatter areas are plotted around the mean curves computed from all data sets.

Table 3.5: Characteristic relaxation times from the macroscopic rheological experiments over the sMREs. The results are presented for two mixing ratios of 6:5, 1:1, 9:10, and 5:6 and magnetic particles volume fractions of 0, 0.15 and 30. The relaxation time is defined for a decay of 63.21 %.

RELAXATION TIMES [s]	**Mixing ratio**			
CIP concentration	**6:5**	**1:1**	**9:10**	**5:6**
$\phi = 0$ vol.%	1.01	1.02	2.27	1.63
$\phi = 15$ vol.%	1.10	1.28	2.88	2.73
$\phi = 30$ vol.%	2.54	5.61	9.74	4.99

Further results comprise magneto-mechanical DMA tests under compression mode (see Figures A.3 and A.4 in the Appendix) and shear load (Figures A.5 and A.6), for the magnetic particles content of 0.15 and 0.3 and the mixing ratios of the elastomeric matrix are 6:5, 1:1, 9:10, 5:6. To provide a clearer picture, Table 3.6 summarizes the values of the storage shear modulus for three oscillating frequencies (0.01 Hz, 8 Hz, and 16 Hz). Moreover, Figure 3.15 with 3D graphs synthesizes the results for the quasi-static storage axial and shear stiffness moduli (E' and G', respectively) as a function of the matrix mixing ratio and the external magnetic actuation. When subjected to an axial magnetic field (see Figure 3.15.a), the MREs experience a significant increase in stiffness that is stronger in compression than in shear loading. This effect is explained by the application of the magnetic field along the axial direction during compression loading, leading to the structural (macroscopic) response of the MRE to govern its behavior. Under shear loading (see Figure 3.15.b), the magnetic actuation plays a lower role on the MRE's mechanical performance. Although a direct relationship between the elastomeric mixing ratio and stiffness (under null magnetic fields) is observed in the former tests, the magneto-mechanical response under uniaxial compression loading reveals complex dependencies due to the complex multi-physical nature of the MRE system. However, under shear loading, the effect of the mixing ratio is consistent for all the different magneto-mechanical conditions [87]. Shear experiments show a MR effect of up to 1.7 times for 50 mT and 9.3 times for 200 mT. In this respect, note that the stiffening refers to a macrostructural effect and does not imply microstructural stiffening of the elastomeric matrix.

Table 3.6: Quantitative summary of the trends revealed by the shear DMA tests on sMREs with different matrix's mixing ratios. The results of the storage shear modulus G' are presented for the magnetic particles volume fractions of 0.15 and 0.3, mixing ratios of 6:5, 1:1, 9:10 and 5:6, and magnetic fields of 0 mT, 50 mT, 100 mT and 200 mT. Frequencies of 0.01 Hz, 8 Hz and 16 Hz are chosen as representative values. Note that these data correspond to the mean values over the three experimental repetitions.

Case study: Magneto-mechanical tests - Shear			**Matrix mixing ratio**			
CIP concentration	**Magnetic field**	**Frequency**	**6:5**	**1:1**	**9:10**	**5:6**
Storage modulus G' [kPa] for $\phi = 15$ vol.%	$B = 0$ mT	0.01 Hz	0.4	1.5	2.9	3.2
		8 Hz	1.2	3.8	6.0	6.4
		16 Hz	1.6	4.8	7.4	7.8
	$B = 50$ mT	0.01 Hz	0.7	1.8	3.2	3.4
		8 Hz	1.6	4.1	6.4	6.6
		16 Hz	2.1	5.1	7.8	8.0
	$B = 100$ mT	0.01 Hz	1.6	2.7	4.0	4.1
		8 Hz	2.9	5.4	7.5	7.6
		16 Hz	3.4	6.6	9.1	9.0
	$B = 200$ mT	0.01 Hz	4.1	5.7	6.7	6.6
		8 Hz	6.9	10	12	12
		16 Hz	7.8	12	14	14
Storage modulus G' [kPa] for $\phi = 30$ vol.%	$B = 0$ mT	0.01 Hz	0.6	2.7	4.6	5.8
		8 Hz	2.3	6.4	11	12
		16 Hz	3.0	7.7	13	14
	$B = 50$ mT	0.01 Hz	1.0	2.8	5.0	6.2
		8 Hz	2.9	5.6	12	13
		16 Hz	3.7	6.8	14	15
	$B = 100$ mT	0.01 Hz	2.0	4.1	6.1	7.4
		8 Hz	4.6	7.8	14	15
		16 Hz	5.9	9.4	16	17
	$B = 200$ mT	0.01 Hz	5.6	7.4	9.4	11
		8 Hz	10	14	20	22
		16 Hz	12	17	23	25

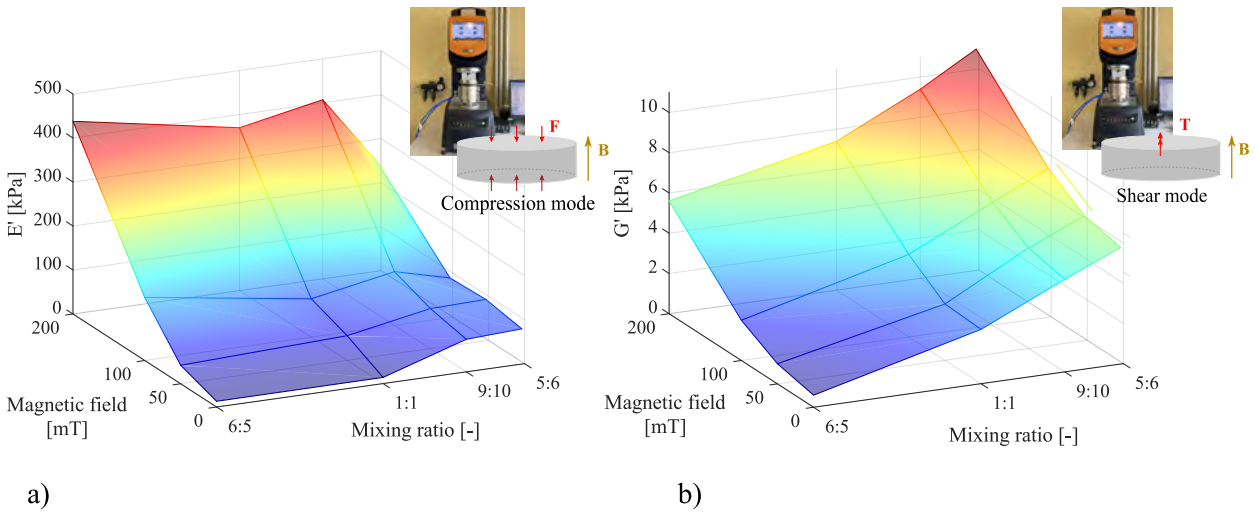

Figure 3.15: Summary of the quasi-static uniaxial and shear DMA results as 3D graphs for different mixing ratios of the elastomeric matrix on sMREs under magnetic actuation conditions. (a) Under uniaxial compression loading, storage Young's modulus (E') depending on the mixing ratio used for the polymeric matric of the MRE and on the magnetic field applied; (b) under shear loading, storage shear modulus (G') depending on the mixing ratio used for the polymeric matric of the MRE and on the magnetic field applied. These tests were performed under quasi-static conditions and for a magnetic particles volume ratio of 30 %. The entire set of results from the frequency sweep tests (i.e., DMA) can be found in Figures A.3, A.4, A.5, and A.6.

3.2.6 Microstructural characterization: nanoindentation tests

The former characterization at the macroscale provides insightful information not only about the material response, but also about structural effects of MREs. Usually, such structural effects are responsible of the multifunctional behavior of the material. However, to complete the experimental characterization, a microstructural characterization is still missing. Nanoindentation brings information about the surface stiffness of a sample at a local point. To this end, the micrometric spherical tip of the indenter presses the surface and measures the force required. The force-indentation curves are used to determine the stiffness according to the method described in the previous Section 3.1, which is based on the Hertz contact model.

The results for the microscopic stiffness, together with relaxation (load versus time) curves, are depicted in Figure 3.16. In addition, Table 3.7 summarizes the results with quantitative values. The local stiffness ranges from 4.1 kPa to 14.6 kPa depending on the mixing ratio of the elastomeric matrix, i.e., 6:5, 1:1, 9:10, and 5:6. Moreover, the characteristic relaxation time (calculated from the stress relaxation curves in Figure 3.16.b) is in the order of $\sim 0.5-1.5$ s. A crucial point is that the results were found to not depend on the magnetic particles content. This owes to the fact that the indentations were done locally on the matrix in between the particles. For that reason, the microscopic characterization of MREs is the same for all sMREs, hMREs and hybrid MREs. Consequently, the following sections focus solely on the rheological macroscopic characterization of hMREs and hybrid MREs.

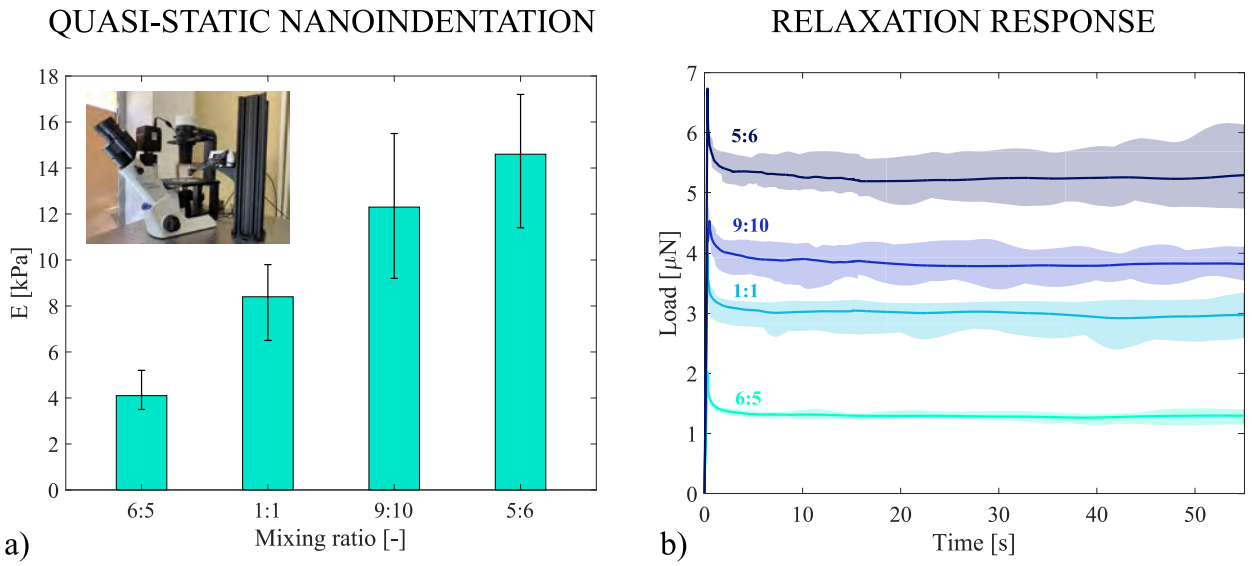

Figure 3.16: Magneto-mechanical characterization at the microscale using a nanoindentation equipment. (a) Young's modulus (E) depending on the mixing ratio used for the polymeric matric of the MRE; (b) load versus time relaxation curves depending on the mixing ratio used for the polymeric matrix of the sMRE. Note that the microscopic measurements were done on the polymeric phase, hence the they did not show significant changes when varying the particles content or when applying external magnetic fields.

Table 3.7: Characteristic relaxation times from the microscopic nanoindentation relaxation tests on the sMRE. The results are presented for elastomeric mixing ratios of 6:5, 1:1, 9:10, and 5:6 and magnetic particles volume fractions of 0, 0.15, and 0.3. The relaxation time is defined for a decay of 63.21 %. Note that the microscopic measurements were taken on the polymeric phase and the values measured did not show significant changes when varying the particles content or applying external magnetic fields.

Elastomeric mixing ratio	**6:5**	**1:1**	**9:10**	**5:6**
Microscopic stiffness E [kPa]	4.1	8.4	12.3	14.6
Relaxation time [s]	0.60	0.55	1.53	0.57

3.3 Hard-magnetic MREs

Since hMREs are able to sustain remanent magnetic fields, they are classified attending to two magnetic conditions, i.e., virgin and pre-magnetized states. This allows to determine the influence of remanent magnetic fields on their mechanical behavior. Moreover, the reader may note that this section focuses on shear deformation mode and not compression. This provides sufficient information of the rheological performance of hMREs. Besides, mechanically confined tests under magnetic actuation are performed in the same manner as for sMREs, but here the direction of the magnetic actuation with respect to the permanent magnetization of the sample plays an important role. Finally, additional free deformation experiments allow to delve into the remarkable shape-morphing capability of hMREs.

3.3.1 Materials and synthesis

The proposed hMRE is composed of an ultra-soft elastomer for the continuous phase (carrier matrix) and hard-magnetic powder for the discontinuous phase. The same extremely soft elastomer used in the previous section for sMREs, i.e., Dowsil CY52-276 (DowSil, Midland, MI, USA) (PDMS), was chosen to achieve large magnetorheological stiffening and shape-morphing capability with small external magnetic fields. Following the manufacturer recommendations, the phases were blended at the volume ratio 1:1. Note that the influence of this mixing ratio was already studied in the previous Section 3.2.5 for sMREs. In what concerns the magnetic phase, this is made of NdFeB, with hard-magnetic properties, provided by Magnequench (MQP-S-11-9-grade powder, Neo Materials Technology Inc., Greenwood Village, Colorado, United States). The median diameter of the spherical-shaped particles conforming the powder is 35 - 55 µm. The magnetic powder was added to the matrix according to the volume fractions $\phi = \{0.1, 0.2, 0.3\}$. To prevent sedimentation of the fillers, the elastomeric phases and the mold were pre-heated at 80 °C for 2 min. Increasing the initial viscosity of the mixture during the addition of the magnetic powder guaranteed that its homogeneous distribution within the elastomeric matrix was preserved without deposition issues. Note that this is a main difference with the manufacturing methodology of sMREs, where the smaller size of the fillers (radius of $3.9 - 5$ µm) does not cause sedimentation phenomenon. The reader can find more detail on the methodology used for sMREs in the previous Section 3.2.1. Afterwards, the blend was cured in an oven at 80 °C for 2 h, as for sMREs. Then, 1 mm height and 20 mm diameter-wise cylindrical samples were cut with a die. As a final step, to produce pre-magnetized samples, virgin ones were exposed to an axial homogeneous magnetic field of 1000 mT. Figure 3.17 summarizes the procedure followed. Provided that the focus of the present study is to understand the response during the magnetization process, and not only the behavior after reaching full permanent magnetization at saturation, partial remanent magnetization rather than fully saturation magnetization was intentionally pursued. This was done by the application of maximum fields under the value of 1600 kA/m (fully magnetizing field given by the manufacturer). See [305, 306] for a deeper characterization of the magnetic powder.

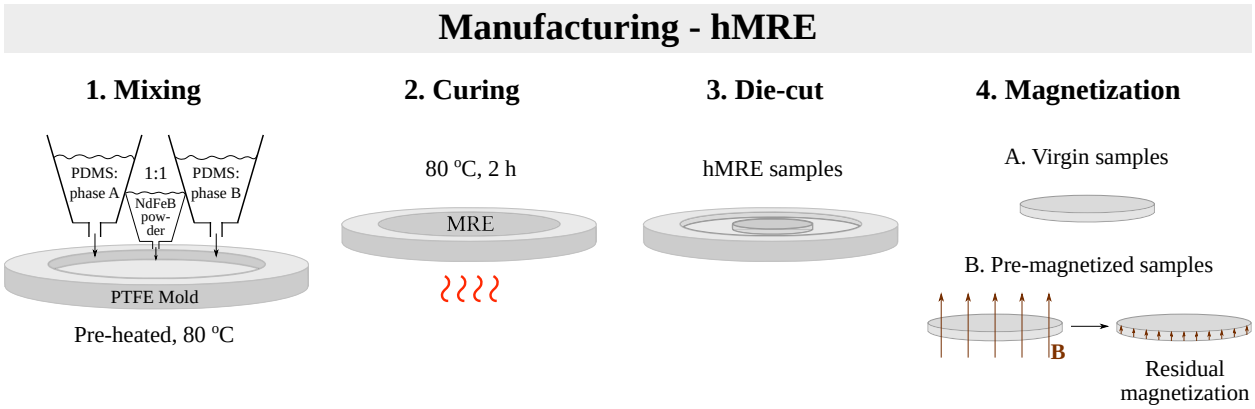

Figure 3.17: A scheme of the hMRE synthesis. The manufacturing methodology is composed of four steps: (1) blending of the components, i.e., the two phases of the pre-heated elastomeric matrix (phases A and B) and the hard-magnetic powder, previously poured into a pre-heated mold; (2) curing in an oven; (3) die-cutting 1 mm height and 20 mm diameter samples; (4) the magnetization of samples with homogeneous magnetic fields.

The micrograph for the resulting virgin (i.e., non pre-magnetized) hMRE is shown in Figure 3.18.

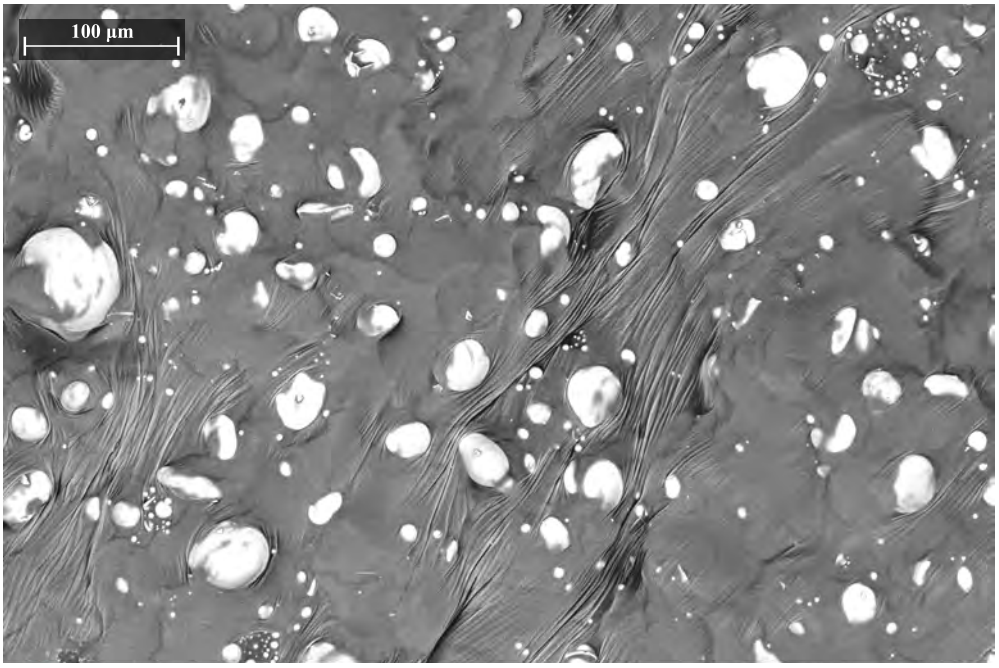

Figure 3.18: Field emission scanning electron microscopy (FESEM) images of the microstructural arrangement before magnetic actuation of hard-magnetic MREs for a particles content of 30 vol.%.

3.3.2 Magneto-mechanical characterization under shear loading

To explore the material behavior along the magnetization process, constant oscillatory tests and frequency sweeps were performed under magnetic fields of 0 mT, 200 mT, 500 mT, and 1000 mT on both virgin and pre-magnetized samples. The same methodological considerations as in Section 3.2.3 for sMREs apply here.

Constant oscillatory shear

A first array of experiments was designed for an angular amplitude of 0.05 rad. The angular velocity of the oscillations is 2 rad s^{-1}. In addition, the sticky nature of the sample prevents slippage at the sample-machine interfaces [292, 293, 305]. Figure 3.19 contains the results of the tests.

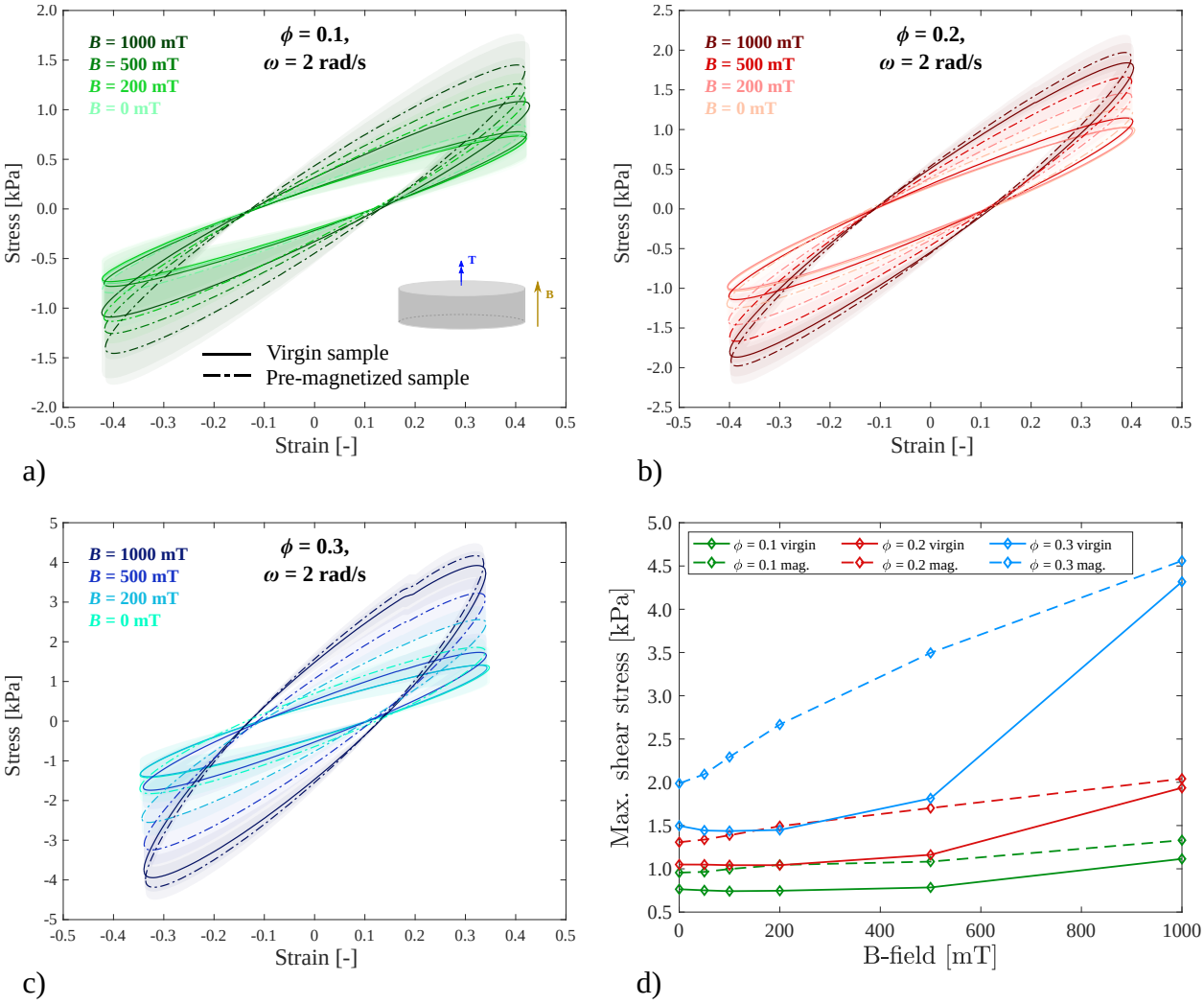

Figure 3.19: Mechanical response of hMREs under shear deformation. The experimental results from constant oscillatory shear tests are depicted for magnetic particles' volume fractions (ϕ) of (a) 0.1, (b) 0.2, and (c) 0.3 and magnetic fields of $B = \{0, 200, 500, 1000\}$ mT. To consider the magnetic remanence, hard-magnetic MREs are tested twice: virgin samples and magnetized samples after a permanent magnetization at 1000 mT (continuous and dashed line, respectively). Scatter areas are plotted around the mean curves computed from the three data sets obtained for the same testing conditions. (d) Curves for tests with magnetic particles' volume fractions of 0.1, 0.2 and 0.3 are plotted against the magnetic field intensity to illustrate the effects of the permanent magnetization of hMREs on the maximum shear stress of the hysteresis loops from the constant oscillatory shear experiments. Two curves for each volume fraction stand for the behavior of virgin samples (continuous line) and pre-magnetized samples (abbreviated as "mag.") after experiencing pre-magnetization at 1000 mT (dashed line).

These results lead to relevant findings. First, the MR effect is less pronounced when using hard-magnetic particles than soft-magnetic ones, with maximum values of approximately 4 times versus 30 times, respectively. hMREs, however, are able to keep this effect even in

the absence of magnetic stimulation and, as it will be discussed in following sections, they are able to perform functional deformation modes. When actuating on virgin samples with external magnetic fields below 200 mT, hysteresis loops do not display any remarkable MR effect, even for the largest volume ratio of magnetic particles of 0.3. Figure 3.20 clarifies the results from the loops in Figure 3.19.a, by showing an initial range where the maximum shear stress does not depend on the magnetic field. From 500 mT on, however, the specimens reach larger maximum shear stresses (i.e., for 500 mT and 1000 mT fields). Such a threshold was not encountered when using soft-magnetic particles, i.e., the MR effect was noticeable for the smallest fields too, see Figure 3.19.b. On the contrary, pre-magnetized hMRE samples display a different behavior. In the absence of magnetic actuation, they reach larger stresses than virgin samples, and for fields below 200 mT, the MR effect is also noticeable, see Figure 3.20. As a final general remark, the more magnetic fillers added to the matrix, the stronger the magneto-mechanical effects are.

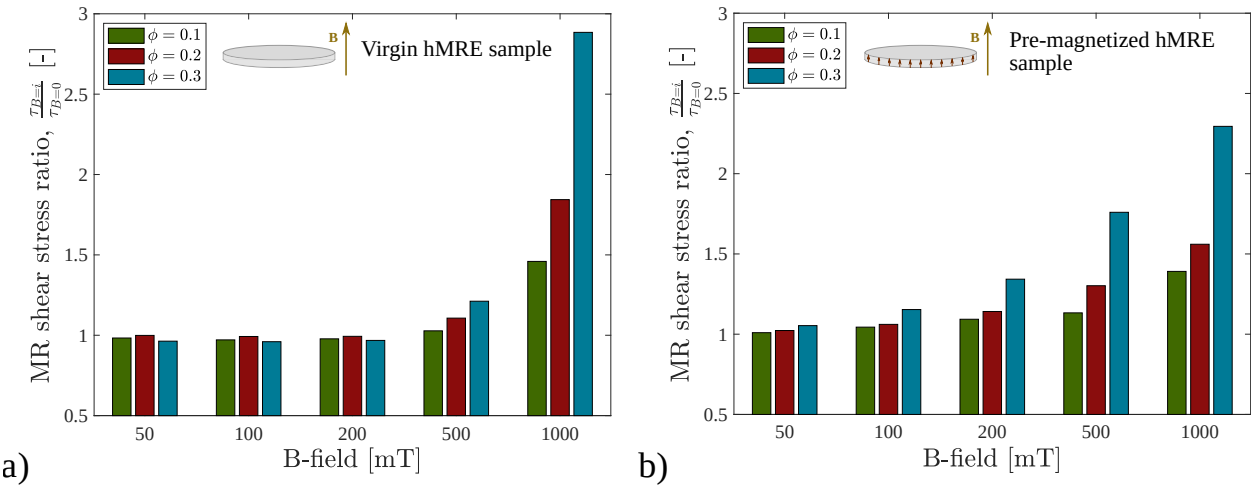

Figure 3.20: Effects of the permanent magnetization of hMREs on the maximum shear stress of the hysteresis loops from the constant oscillatory shear experiments. Magnetorheological shear stress ratio, defined as the quotient between the maximum stress under magnetic actuation and the stress in the absence of external magnetic actuation, for (a) a virgin sample and for (b) a pre-magnetized sample.

Dynamic mechanical analysis (DMA) under shear loading

To explore the relation between the viscoelastic response of hMREs and the mechanical excitation frequency, a second set of experiments was performed as frequency sweeps from 0.01 Hz to 10 Hz. Here, the shear storage modulus (G'), shear loss modulus (G'') and loss factor $\tan\delta = \frac{G''}{G'}$ provide measures of the macrostructural stiffness, see Figure 3.21 for magnetic actuations of 0 mT and 200 mT, and Figure 3.22 for 500 mT and 1000 mT. The magnetic actuation was applied on both virgin and pre-magnetized hMREs samples. As a result, the curves for pre-magnetized samples (i.e., initial pre-magnetization with a 1000 mT magnetic field) uncover the effect of the non-zero magnetic coercivity of the hard-magnetic particles on the structural response of hMREs.

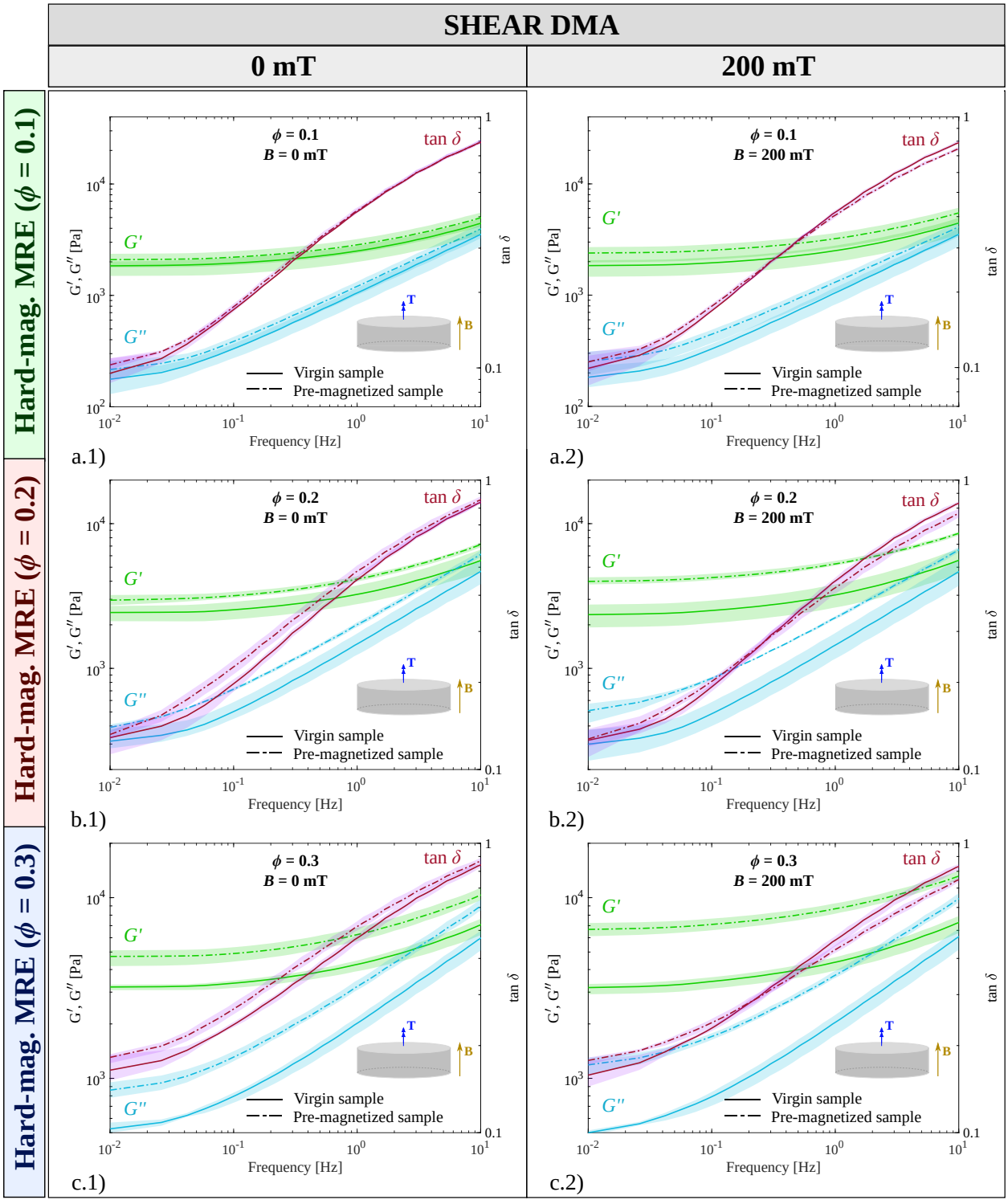

Figure 3.21: Dependence of the mechanical responses of MREs with the harmonic shear mechanical deformation for magnetic fields of $B = \{0, 200\}$ mT and magnetic particles' volume fraction of $\phi = \{0.1, 0.2, 0.3\}$. Shear storage moduli (G'), loss moduli (G''), and loss factors ($\tan\delta$) obtained from frequency sweeps from 0.01 Hz to 10 Hz are presented for virgin samples and pre-magnetized samples after permanent magnetization at 1000 mT (continuous and dashed lines, respectively). Scatter areas representing the variability of the experimental data sets are depicted around each mean curve.

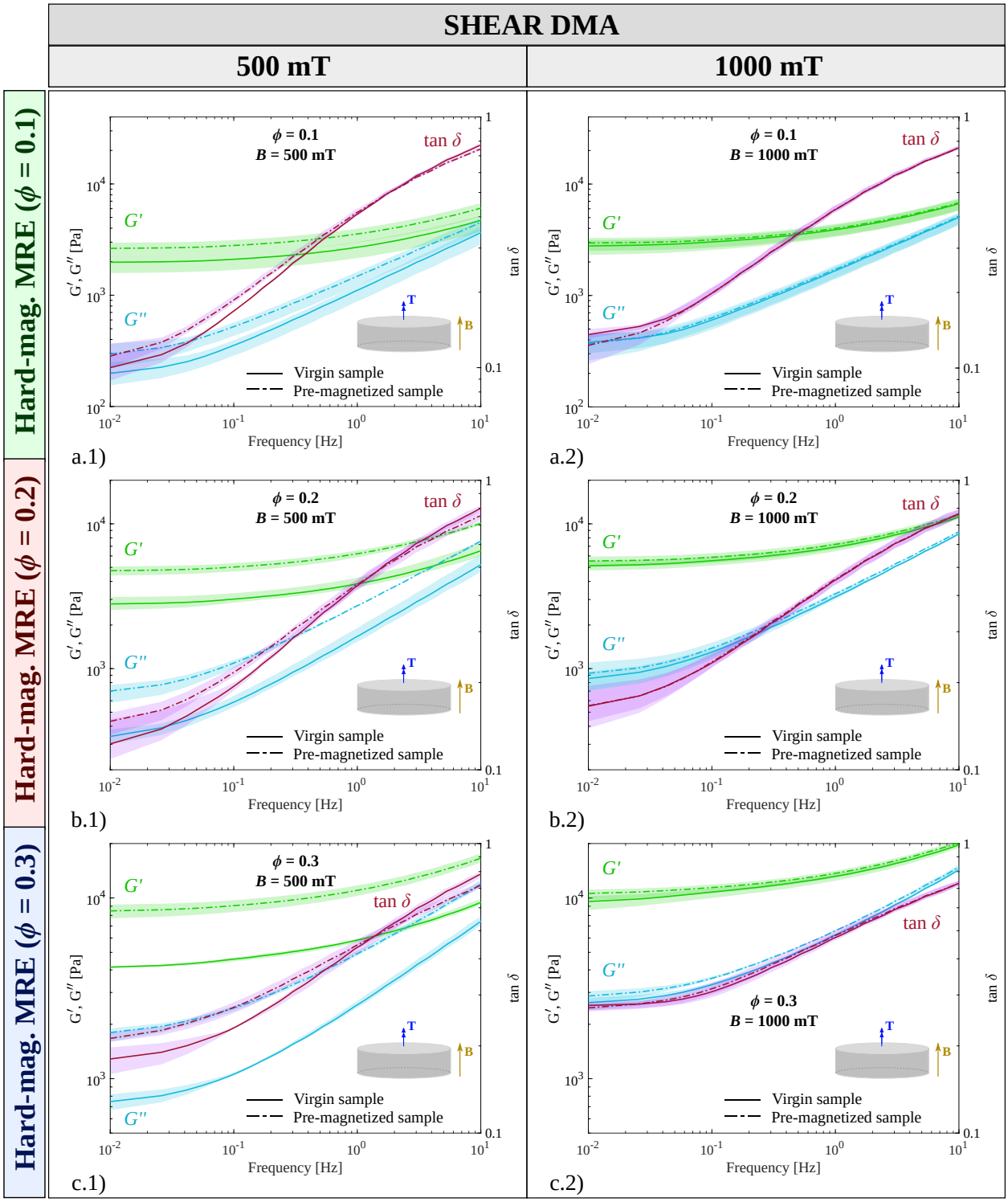

Figure 3.22: Dependence of the mechanical responses of MREs with the harmonic shear mechanical deformation for magnetic fields of $B = \{500, 1000\}$ mT and magnetic particles' volume fraction of $\phi = \{0.1, 0.2, 0.3\}$. Shear storage moduli (G'), loss moduli (G''), and loss factors ($\tan\delta$) obtained from frequency sweeps from 0.01 Hz to 10 Hz are presented for virgin samples and pre-magnetized samples after permanent magnetization at 1000 mT (continuous and dashed lines, respectively). Scatter areas representing the variability of the experimental data sets are depicted around each mean curve.

The main findings are the following ones. First, the MR effect is stronger for increasing amounts of hard-magnetic particles. For a magnetic actuation of 1000 mT, mechanical oscillation at 0.1 Hz, hMRE virgin samples, and particles contents of $\phi = \{0.1, 0.2, 0.3\}$,

the MRE effect is 1.5, 2.1 and 3.0, respectively. For the pre-magnetized samples and for the different particles content, the MR effect is 1.5, 1.9 and 2.2, respectively. For a faster deformation, i.e., 10 Hz, the MR effect for the virgin samples is 1.5, 2.0 and 2.8, and for the pre-magnetized ones it is 1.4, 1.6 and 1.9, respectively for the particle contents considered. Second, for the intermediate fields of 200 mT and 500 mT, the MR effect for pre-magnetized samples significantly increases with respect to the MR effect of virgin samples. For 200 mT and quasi-static mechanical deformation, the MR effect of the virgin hMRE sample with 30 vol.% particles is 1.0, and 1.4 for the pre-magnetized sample. For 500 mT, the MR effect of the virgin hMRE sample is 1.3, and 1.8 for the pre-magnetized sample. This tendency can be better visualized in Figure 3.23, in which the shear storage modulus is plotted against magnetic field for a quasi-static (0.01 Hz) and a fast angular velocity (10 Hz). In this regard, the moduli of both virgin and pre-magnetized samples merge to the same value when the field approaches 1000 mT.

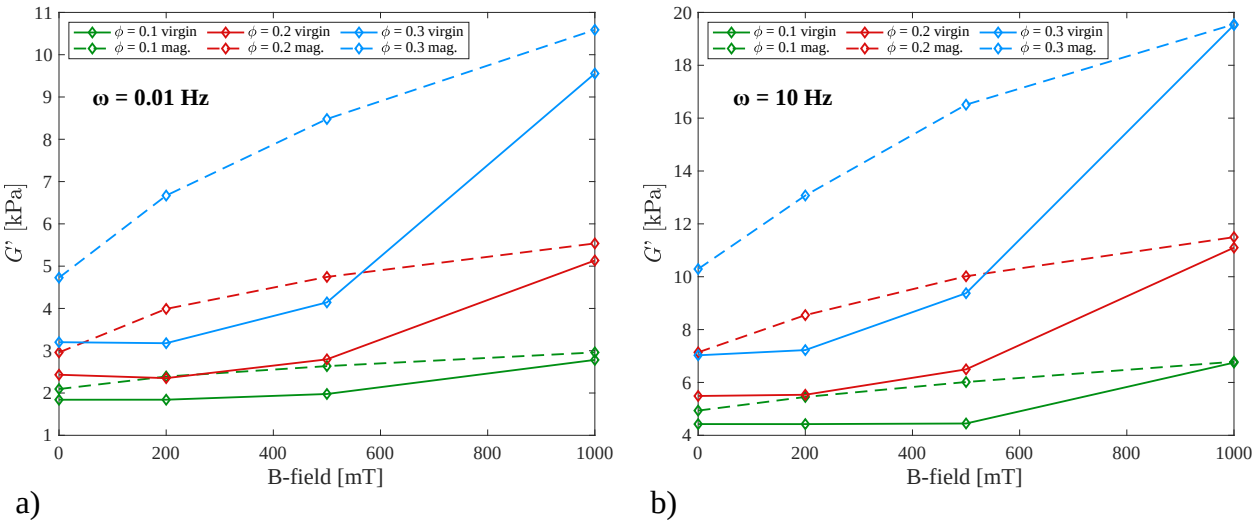

Figure 3.23: Effects of the permanent magnetization of hMREs on the shear storage modulus for two extreme harmonic deformation velocities of (a) 0.01 Hz (quasi-static case) and (b) 10 Hz. Curves for tests with magnetic particles' volume fractions of 0.1, 0.2 and 0.3 are plotted against the magnetic field intensity. Two curves for each volume fraction stand for the behavior of virgin samples (continuous line) and pre-magnetized samples (abbreviated as "mag.") after experiencing re-magnetization at 1000 mT (dashed line).

When comparing the response of the hMREs with that of the sMREs (see Table 3.6 for sMREs), the MR effect is higher for the second ones. Overall, hMREs present a maximum MR effect of 3, whereas sMREs show a maximum of 12. Furthermore, for all the manufacturing and testing conditions of the hMRE, the loss factor monotonously increases with frequency, whereas for sMREs it is less dependent on the frequency. The response of hMREs is quite expectable, i.e., activation of viscoelastic mechanisms of the matrix at increasing deformation rates. For sMREs, however, the interactions between particles are much stronger (i.e., dipole-to-dipole interplays) due to their higher magnetization and magnetic permeability. Such interactions lead to significant rearrangements in the particles' distribution and the generation of strong links between them, which eventually affect the viscoelastic response.

Regarding the rheological behavior of extremely soft hMREs, permanent magnetization leads to increased stiffness in the absence of external magnetic stimulation. To clearly under-

stand the effects of the permanent magnetization, Figures 3.20 and 3.23 show, respectively, curves with the evolution of the maximum shear stresses of the hysteresis loops and the quasi-static storage modulus for different magnetic particles' volume fractions and magnetic fields, for both virgin and pre-magnetized hMRE samples. When the external magnetic field is turned off, internal magnetic interactions between the magnetic particles and the elastomeric matrix still remain. Also, the more magnetic particles, the larger the apparent (homogenized) permanent magnetization. This fact explains the relative stiffness increase between virgin and pre-magnetized samples with increasing particles volume fraction, both under the action of external magnetic fields or in the absence of them. In addition, the relative stiffness increase reduces to zero at 1000 mT, expectable as the MRE got magnetized at 1000 mT. When comparing the results between hMREs and sMREs, see Figures 3.19 and 3.9, it is clear that the MR effect is larger for the soft-magnetic version (around 7 times larger). This is so because the saturation magnetization and magnetic susceptibility of hard-magnetic MQP-S-11-9-grade powder are smaller than those of CIPs, see the magnetization curves in the Appendix (Figure A.7, adapted from [307]). Overall, hMREs lose the intense MR stiffening of sMREs but gain the capability to achieve it in the absence of magnetic fields.

3.3.3 Mechanically confined tests under magnetic actuation

In what concerns the confined expansion experiments, magnetic field ramps were performed on virgin hMRE samples at the rate of 20 mT s^{-1} up to 1000 mT (direct magnetic actuation). Then, the field was kept constant for 75 s. Finally, the field was turned off for 50 s. In the meanwhile, the evolution of the axial force exerted on the upper plate of the rheometer was monitored. These experiments were done following the methodology reported for sMREs in Section 3.2.4. The pre-magnetized samples were tested following the same procedure but limiting the maximum magnetic field to 500 mT. The residual of the macroscopic samples after applying an external magnetic field of 1000 mT is 3 mT. Recalling the extremely soft nature of the matrix ($\sim$ 1 kPa), a consequence is that such small magnetization is enough to drive significant mechanical changes in the hMRE under external magnetic actuation. The use of the 500 mT is justified as it is sufficiently large to induce significant mechanical actuation, but small enough to not alter the residual magnetization. Moreover, the magnetic actuation was performed in a reversed manner up to -500 mT (reverse magnetic actuation). To keep positive the axial force and prevent stretching the sample, an initial pre-compression of 0.5 N was imposed on every test.

The results are grouped according to the magnetic profile applied and magnetization state of the hMRE samples: magnetic field ramp up to 1000 mT on virgin samples in Figure 3.24.a, and ramps up to +/-500 mT (direct and reverse fields) on pre-magnetized samples in Figure 3.24.b. Differences of the axial stress during the loading ramp can be found when comparing both the virgin and pre-magnetized samples. While for the virgin sample the curve is parabolic, for the magnetized specimen the loading region is more linear. Another remark, when the magnetic actuation stops, is that the axial force decreases and becomes even smaller than the pre-compression at the beginning of the experiment. Then,

it slightly increases. This is observed for the cases where the field is applied along the same direction as the magnetization (i.e., "direct" fields). For the case of reverse magnetic actuation, almost no jump in the axial force occurs.

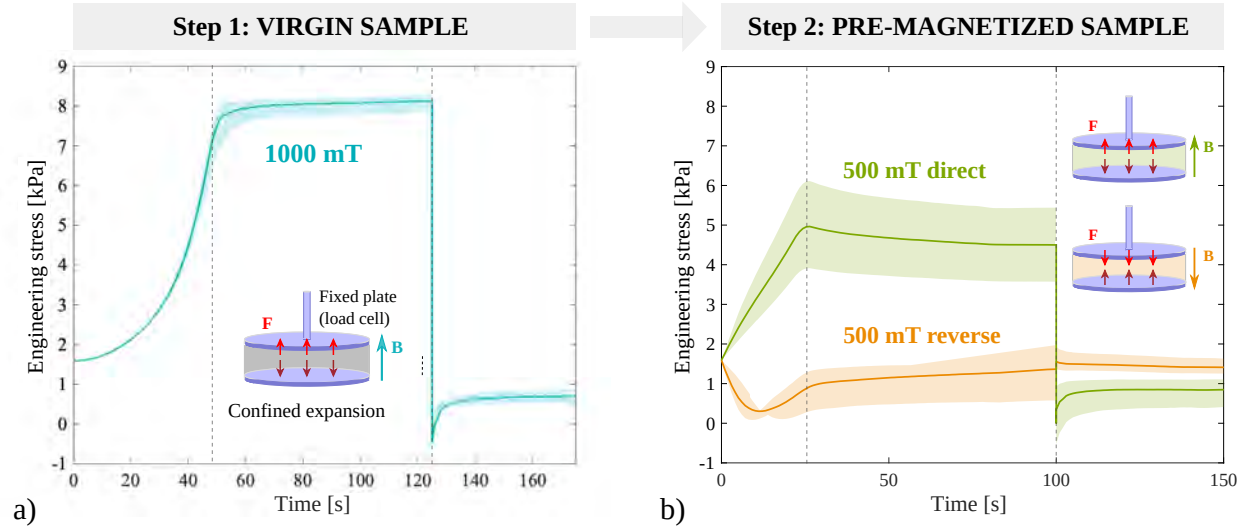

Figure 3.24: Time evolution of the axial stress of mechanically confined hMREs during magnetic ramps. (a) The magnetic actuation event of virgin samples, which undergo a magnetic field ramp at a rate of 20 mT s^{-1} up to 1000 mT, that is then held until stabilization and, finally, the magnetic actuation is turned off. (b) Pre-magnetized samples were tested under the same procedure, but limiting the maximum magnetic field to 500 mT for both direct and reverse fields. Note that the same initial pre-compression of 0.5 N is applied for all the experiments to prevent that the axial force becomes negative, i.e., contraction of the sample.

Non-symmetric macrostructural responses are observed for direct (along magnetization direction) and reverse (contrary to magnetization direction) magnetic fields on pre-magnetized hMRE samples tested in confined deformation experiments. Following the evolution of the axial force exerted by the sample on the fixed plates, see Figure 3.24, valuable information about the magnetization process is harvested. The initial magnetic actuation up to 1000 mT yields an initial parabolic increase in the stress. This can be explained by the quadratic dependence of internal magnetic stress on the externally applied magnetic field [162, 295]. The abrupt decrease in the stress when stopping the magnetic actuation and the subsequent relaxation unveils internal viscous mechanisms. As these stresses go below the initial axial force, we believe that the internal deformation mechanisms are not reversible. In other words, the microscopic configuration of virgin and pre-magnetized hMREs would be different. When observing the results for the second stimulation step (i.e., direct and reverse fields up to 500 mT) the same finding can be reported. Hence, this behavior is not due to the permanent magnetization of the magnetic powder but due to varying microstructural arrangements also under weaker magnetic actuation. Finally, regarding the effect of the magnetization direction, the non-symmetrical curves for the direct and reverse fields suggest that reversing the magnetic field produces a decrease of the axial force (i.e., confined compression) rather than an increase. In addition, such a decrease is smaller in magnitude than the increase for the direct field. A further finding related to such a reverse stimulation is that the evolution of the axial force during the application of the magnetic field ramp is not monotonous. Such findings under reverse magnetic actuation can be understood as

the result of local rearrangements of the particles that were aligned with the magnetization field (direct magnetic actuation). When the sense of the field changes, we believe that local rearrangements of the particles occur until they align with the new field. This transient mechanism would end in a microstructural stabilization where interactions between different domains of the hMRE structure govern the structural response.

Related to the latter discussion, another important observation from Figure 3.24 relates to the transient stress evolution that occurs once the maximum magnetic field is reached. On virgin samples, the steady state is quickly reached, suggesting negligible relaxation effects. However, the tests conducted on pre-magnetized samples unveil a transient stress response indicating significant relaxation within the MRE. To explain these results, we suggest the existence of two main microstructural deformation mechanisms. First, the application of an external magnetic field on virgin samples results in dipole-to-dipole interactions leading to the formation of chain-like microstructures and the subsequent expansion of the MRE (i.e., increase in confined stress). Then, when switching off the external magnetic field, the dipole-to-dipole interactions are relaxed leading to a re-accommodation of the particles within the MRE, which present a given residual magnetization. Second, when applying a magnetic field on pre-magnetized samples, the previously mentioned dipole-to-dipole interactions are combined with micro-torques due to Zeeman effect [162]. These torques induce high local deformations around the particles resulting in a stronger relaxation response. In addition, the orientation of the residual magnetization of the particles follows the rotation of the particles during such micro-relaxations, introducing time-varying microstructural equilibrium states. To elaborate on this behavior, deformation tests under free boundary conditions are discussed hereafter.

3.3.4 Shape-morphing tests

Even though the magnetorheological characterization is vital to obtain valuable information about the modulation of the mechanical properties of hMREs, the interest in extremely soft hMREs goes beyond the actuation on their mechanical properties [308, 309]. The geometrical effects of these structures and their remarkable micromechanics (i.e., interplays between the magnetic particles and the matrix) enable them to perform complex deformations via magnetic actuation. To provide novel insights into the magnetostrictive behavior of hMREs, this section presents free deformation tests on samples with different geometries unveiling qualitative structural responses.

Free deformation experiments were performed to analyze local-to-structural effects (i.e., geometrical effects) and the influence of rate dependences on them, see Figure 3.25. Special attention has been paid along the deformation processes to identify such local and structural mechanisms and to establish potential links with microstructural deformations. The tests were performed on different samples with bottom-up magnetization (see the magnetization procedure in Figure 3.17). Figure 3.25 depicts the results according to the morphology of the hMRE specimens and the magnetic actuation conditions. These are shown as a collection of frames taken from the recorded videos. The time event was recorded using a CCD camera (Alvium, Allied Vision Technologies GmbH, Germany) with 25 mm focal length lens (Ed-

mund Optics, Germany). Furthermore, to shed light on the shape-morphing capability of hMREs, the findings are additionally classified as microstructural and macrostructural-based mechanisms.

First, small cylindrical samples of 4 mm diameter were prepared and tested under alternating magnetic fields (oscillatory fields with amplitude of 300 mT and null bias) at frequencies of 1 Hz and 10 Hz, see Figure 3.25.a. The small dimension of the sample allowed the magnetic field to be homogeneous through all the specimen (the homogeneity of the field was checked by making use of a teslameter in vacuum conditions; thus, small heterogeneities are expected at the sample edges). When actuating on the hMRE samples at 1 Hz, two effects are observed. On the one hand, when the field starts increasing in the reverse manner, the upper and lower edges of the specimen start twisting towards the middle plane of the sample. On the other hand, when the field becomes large enough, macrostructural effects become sufficiently strong to make the sample turn and align with the magnetic field. The process starts again as the field goes in the other direction. When increasing the oscillation frequency of the field to 10 Hz, however, weaker local deformations were observed. Afterwards, two larger structures were tested to study geometrical effects, i.e., a bending disk with 20 mm diameter and a rectangular cantilever-shaped torsion beam (20 mm length and 5 mm width), see Figure 3.25.b. For the bending disk, the heterogeneous magnetic field reaches maximum values in the center of the sample and a macrostructural response governs the deformation of its peripheral regions, i.e., these outer domains tend to macroscopically align with the central axial magnetic lines. Note that we refer as heterogeneous fields to those generated by the coil system when its upper yoke is not used. On the contrary, homogeneous magnetic fields are those achieved with the use of the upper yoke, as done in the previous sections for the rheological characterization. In what respect to the cantilever beam, it performs a structural rotation via torsion along its longitudinal axis and following the external field.

The macrostructural response of hMREs is determined by the nature of the mechanisms that develop at the microscale, namely the magnetic interactions between the magnetic particles and the mechanical interactions between these and the carrier matrix. In this regard, Figure 3.26 illustrates the connection between the macrostructural functional deformation mode and the underlying microstructural mechanisms for a pre-magnetized hMRE. Three cases are described. First, when the structure is magnetically actuated in the same direction that it is pre-magnetized, the particles tend to align forming chain-like structures. This mechanism produces the macrostructural expansion of the hMRE, and it relates to the results in Figure 3.24 for the confined expansion experiments under direct magnetic actuation. Second, a perpendicular magnetic actuation with respect to the pre-magnetization leads to macrostructural bending. At the microscale, the particles try to rotate and align its magnetization with the external field. The results for the bending disk and torsion beam under free deformation in Figure 3.25.b relate to this mechanism. Finally, co-linear but reverse magnetic actuation produces symmetric twisting of the structure. Due to the extremely soft nature of the matrix, the particles tend to rotate and align with the external field, introducing microstructural torques in the hMRE. Such a mechanism is observed on the multifunctional structure in Figure 3.25.a.

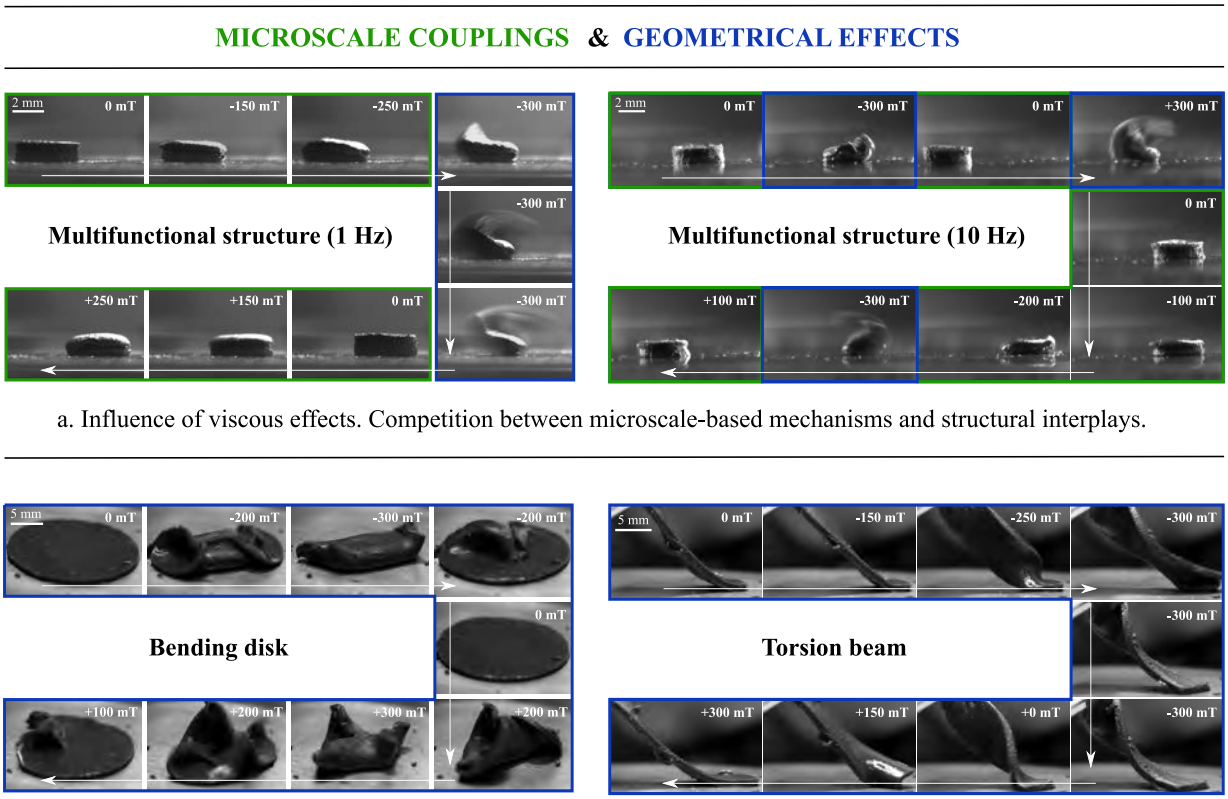

a. Influence of viscous effects. Competition between microscale-based mechanisms and structural interplays.

b. Influence of geometrical effects. Illustration of two functional applications of hMREs.

Figure 3.25: Tuning the shape-morphing behavior of hMRE samples by means of oscillatory magnetic stimulation and different initial geometries. The deformation modes that pre-magnetized hMRE samples undergo have been controlled by the application of harmonically-alternating magnetic fields. Low-diameter samples (i.e., 4 mm) were tested under field stimulation at (a.left) 1 Hz and (a.right) 10 Hz. Nine frames from recorded videos are shown for each case. In (b.left), the deformation scene of a larger (i.e., diameter of 20 mm) unveils macrostructural deformation modes. Finally, in (b.right), an alternative beam-shaped specimen undergoes torsion deformation.

Overall, free deformations of hMRE specimens unveil the underlying mechanisms that govern the interaction between the elastomeric and magnetic particles phases. In Figure 3.25.a, it can be seen that, when the reverse magnetic field is applied, the upper edges get twisted in a symmetric fashion. This suggests that the structural response is initiated at the microstructural level by translating microscopic deformation mechanisms into synergistic effect at the macroscale. We believe that such a complex morphological change unveils microscale transmission mechanisms of the magnetic torques on the particles to the matrix (this latter balances such mechanical actions). From a microstructural point of view, the magnetic particles are embedded in the carrier matrix. Under the application of a magnetic field, they can respond alternatively by: i) rotating and orientating along the direction of the field or ii) re-magnetizing by reversion of the orientation of the magnetization. Which phenomenon occurs is determined by the stiffness of the matrix. For soft matrices and small magnetic fields, the particles turn after the field, and for larger fields and stiffer matrices, they get re-magnetized [306, 310]. Figure 3.26 provides an illustration of the twisting deformation mechanism governed by the transmission of torques form the particles to the matrix.

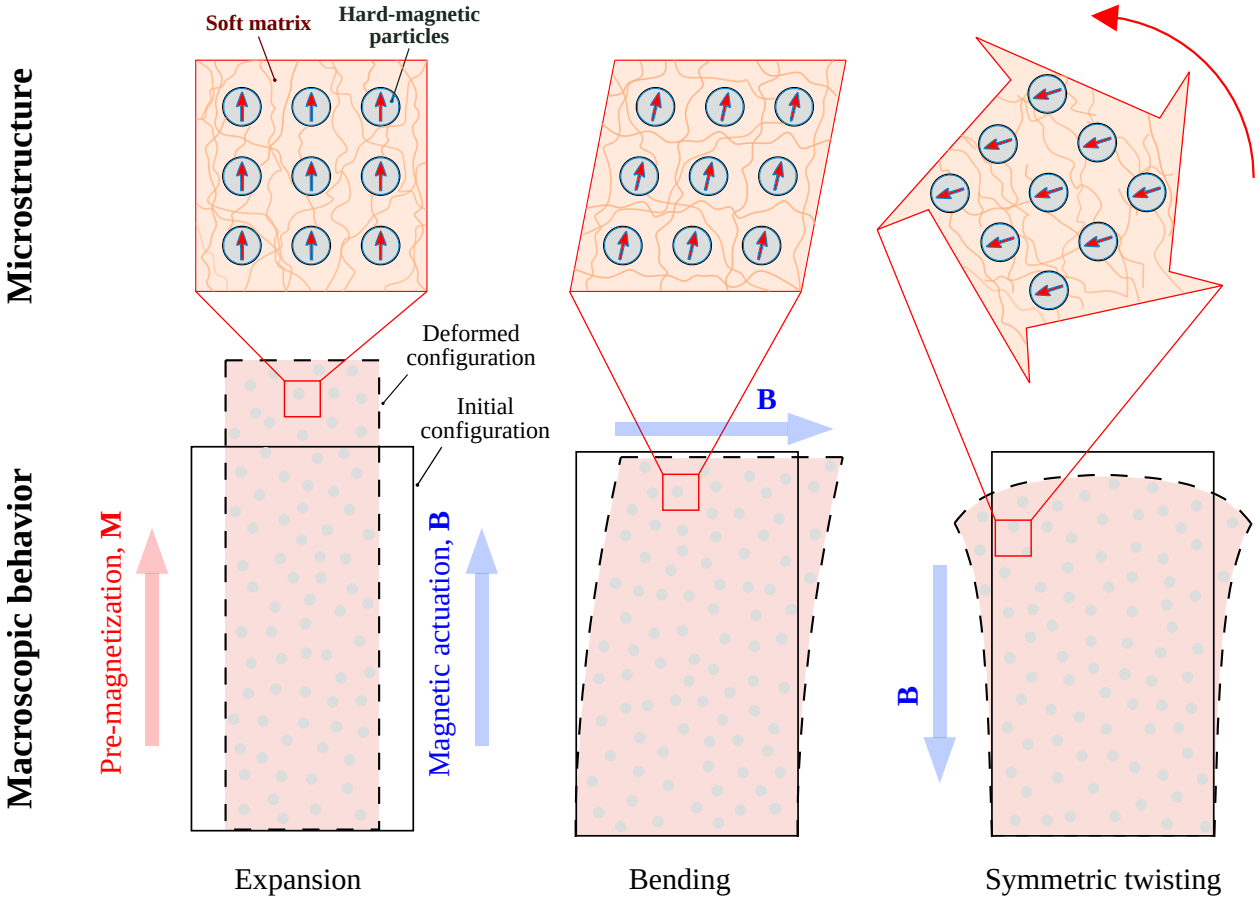

Figure 3.26: Schematic representation of the microscopic and macroscopic magneto-mechanical deformation mechanisms in hMREs under different magnetic actuation scenarios. (Left) Structural response under magnetic actuation parallel to the remanent magnetization and with the same orientation (direct actuation). Under this condition, the particles tend to align forming chain-like structures, leading to an overall expansion. (Center) Structural response under magnetic actuation perpendicular to the remanent magnetization. Under this condition the particles try to rotate and align its magnetization with the external field. This leads to overall bending. (Right) Structural response under magnetic actuation parallel to the remanent magnetization and opposite orientation. Under this condition, and due to the extremely soft nature of the matrix, the particles try to rotate and align with the external field introducing microstructural torque in the hMRE.

Moreover, the deformation rate determines the response of the sample. When the oscillation of the magnetic field is increased, local deformation of the sample (i.e., twist of the edges) plays a minor role. This is so because the faster the actuation, the stiffer the sample becomes and, therefore, the more difficult for the particles to turn and orient. Such an effect could lead to an eventual microstructural collapse, as reported for sMREs in Section 3.2.4.

When the geometry of the samples is larger, see the bending disk and torsion beam in Figure 3.25.b, instead of being local deformation the governing mechanisms, macrostructural changes in the shape appear as major effect on the material. Attending to the geometry of the specimen, the interaction between local domains of the hMRE can be tuned to achieve different complex deformation modes. Note that this type of deformation for homogeneously pre-magnetized samples is only achievable by means of heterogeneous magnetic fields. For the case of the disk, bending of the outer regions occurs, and for the case of the torsion

beam, the entire structure tends to turn 180 degrees to align with the imposed external field. Figure 3.26 provides an illustration of the bending deformation mode. These non-trivial deformation modes can relate to classifications reported in the literature, according to the movements, as deflections, elongations, contractions, coiling, crawling and jumping [234]. As a general concern, note that full saturation magnetization of the hMRE instead of partial magnetization (i.e., according to the manufacturer, fully magnetization is reached for a field of intensity 1600 kA/m) would yield permanent deformations larger than the ones obtained in Figure 3.25. We accept the maximum field of 1000 mT to be large enough for the activation of magneto-mechanical couplings and the functional application of the hMRE.

3.4 Hybrid MREs

The great advances on both sMREs and hMREs to date pose a timely question on whether the combination of both types of particles may optimize the multifunctional response of these active structures. sMREs undergo remarkable stiffening under a magnetic actuation, while hMREs perform intricate morphological changes. The macroscopic response of such hybrid MREs is not obvious as it results from complex interactions at the microscale. Some works in the literature provide manufacturing methodologies and some characterization data on hybrid MREs [12, 59, 299, 307, 311, 312]. However, a comprehensive characterization of the magneto-mechanical behavior of these materials and its dependency on the particle content is still missing. Consequently, further experimental works are required to determine how the relative mixing ratio between soft- and hard-particles modulates, in a combined fashion, both material property changes and shape actuation modes.

This section extends the rheological characterization methodology to hybrid MREs to demonstrate that hybrid MREs combining both soft- and hard-magnetic particles exhibit both functional behaviors. In other words, the goal is to modulate the individual features of sMREs and hMREs within a hybrid sample. Moreover, the results show that the choice of an adequate mixing ratio between soft- and hard-magnetic particles allows to optimize the magneto-mechanical performance of MREs. In addition, the use of an extremely soft elastomeric matrix allows the activation of such couplings even with very low magnetic fields.

3.4.1 Materials and synthesis

Ultra-soft hybrid MREs are manufactured combining three components: an elastomeric matrix, soft-magnetic particles and hard-magnetic particles. The volume ratio between both types of particles (soft-to-hard-magnetic particles volume ratio in the following) is modified according to the values of 1:0, 2:1, 1:1, 1:2 and 0:1. The total amount of magnetic particles, however, is fixed at 30 % volume ratio for all the samples. Table 3.8 summarizes the manufacturing conditions of the MREs. The soft-magnetic particles consist of soft SQ carbonyl iron powder (CIP) (BASF, Germany). The hard-magnetic particles consist of NdFeB powder (MQP-S-11-9-grade powder, Neo Materials Technology Inc., Greenwood Village, Colorado, United States). Both types of particles are spherical-shaped, but they differ in size. While the CIP has a mean diameter of 3.9 - 5 µm, NdFeB particles are larger with a mean diameter of 35 - 55 µm. For the matrix, an extremely soft elastomer Dowsil CY52-276 (DowSil, Midland, MI, USA) (PDMS with stiffness below 10 kPa) is used. In the previous sections, such soft matrices have been shown to be ideal to activate the magneto-mechanical response with small magnetic fields. To initiate the crosslinking, the two elastomeric phases are mixed at the ratio 1:1. Figure 3.27 shows the steps followed to manufacture the samples. Note that the initial blend is pre-heated to prevent the sedimentation of the NdFeB powder. A final step allows for the pre-magnetization of the specimens, defining virgin and pre-magnetized states as for hMREs in the previous section.

Table 3.8: Manufacturing conditions of the hybrid MRE samples depending on the soft-to-hard-magnetic particles volume ratio.

Soft-hard particles ratio [-]	$\alpha_{\text{soft-mag}}$ [vol.%]	$\alpha_{\text{hard-mag}}$ [vol.%]	α_{total} [vol.%]
1:0	30	0	
2:1	20	10	
1:1	15	15	30
1:2	20	10	
0:1	0	30	

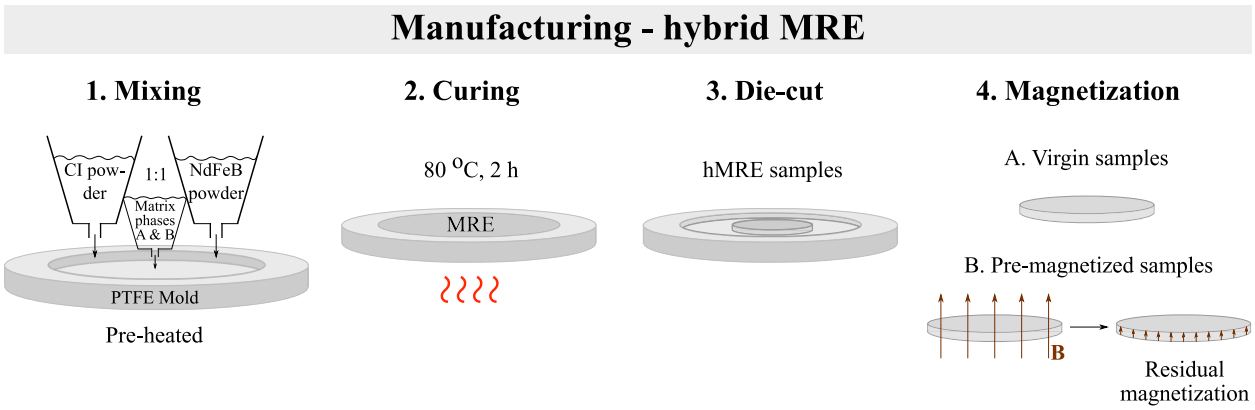

Figure 3.27: Scheme of the synthesis process of the hybrid MREs. The manufacturing process is composed of: (1) mixing of the components; (2) curing in oven; (3) die-cutting 1 mm height and 20 mm diameter geometries; (4) pre-magnetization of specimens with homogeneous magnetic fields.

The micrograph for the resulting virgin hybrid MRE is shown in Figure 3.28.

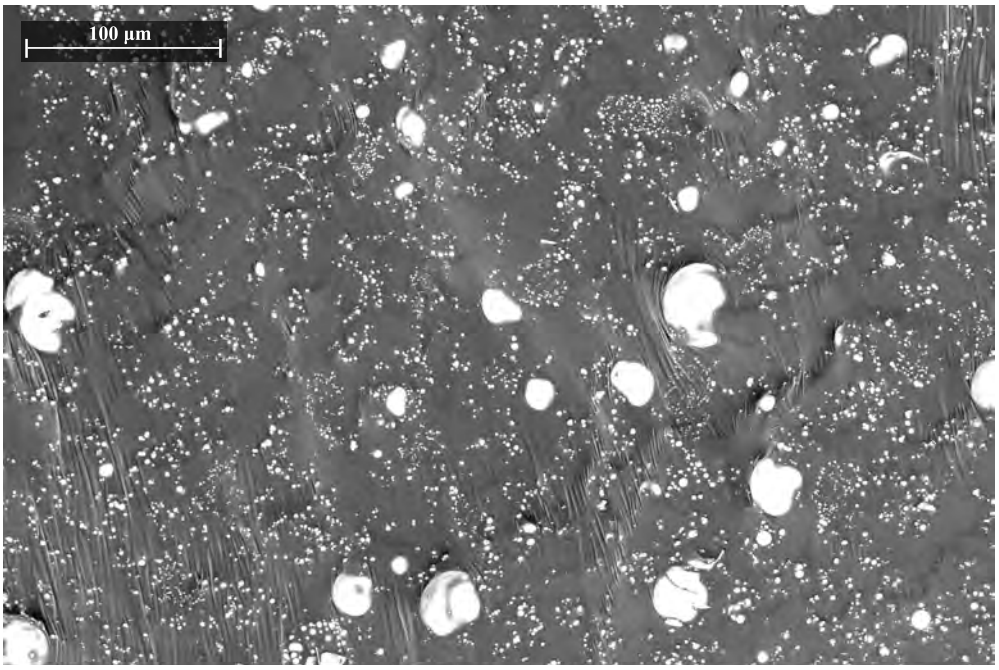

Figure 3.28: Field emission scanning electron microscopy (FESEM) images of the microstructural arrangement before magnetic actuation of hybrid MREs for a particles content of 30 vol.%.

3.4.2 Magneto-mechanical characterization under shear loading

To explore the material behavior along the magnetization process, constant oscillatory tests and frequency sweeps were performed under magnetic fields of 0 mT, 200 mT, 500 mT and 1000 mT on both virgin and pre-magnetized samples. Overall, the same methodology as for hMREs is applied here.

Constant oscillatory shear

A first array of experiments was designed for an angular amplitude of 0.05 rad. The angular velocity of the oscillations was chosen as 2 rad s^{-1}. Figures 3.29.a,b,c show hysteresis loops of the evolution of the shear stress with respect to the shear strain. In addition, Figure 3.29.d synthesizes the results as plots of the maximum shear stress against the external magnetic field. It compares the response for all the soft-to-hard-magnetic mixing ratios (including the extreme cases of pure soft- and hard-magnetic MREs) and for virgin and pre-magnetized samples. These results indicate that the magnetorheological stiffening increases with the amount of soft-magnetic particles. While maximum stresses of 26 kPa are reached in sMREs under 1000 mT, only a maximum of 5 kPa is reached in hMREs. In this regard, hybrid MREs stand in the middle with values of 21, 15 and 13 kPa for mixing ratios of 2:1, 1:1 and 1:2, respectively.

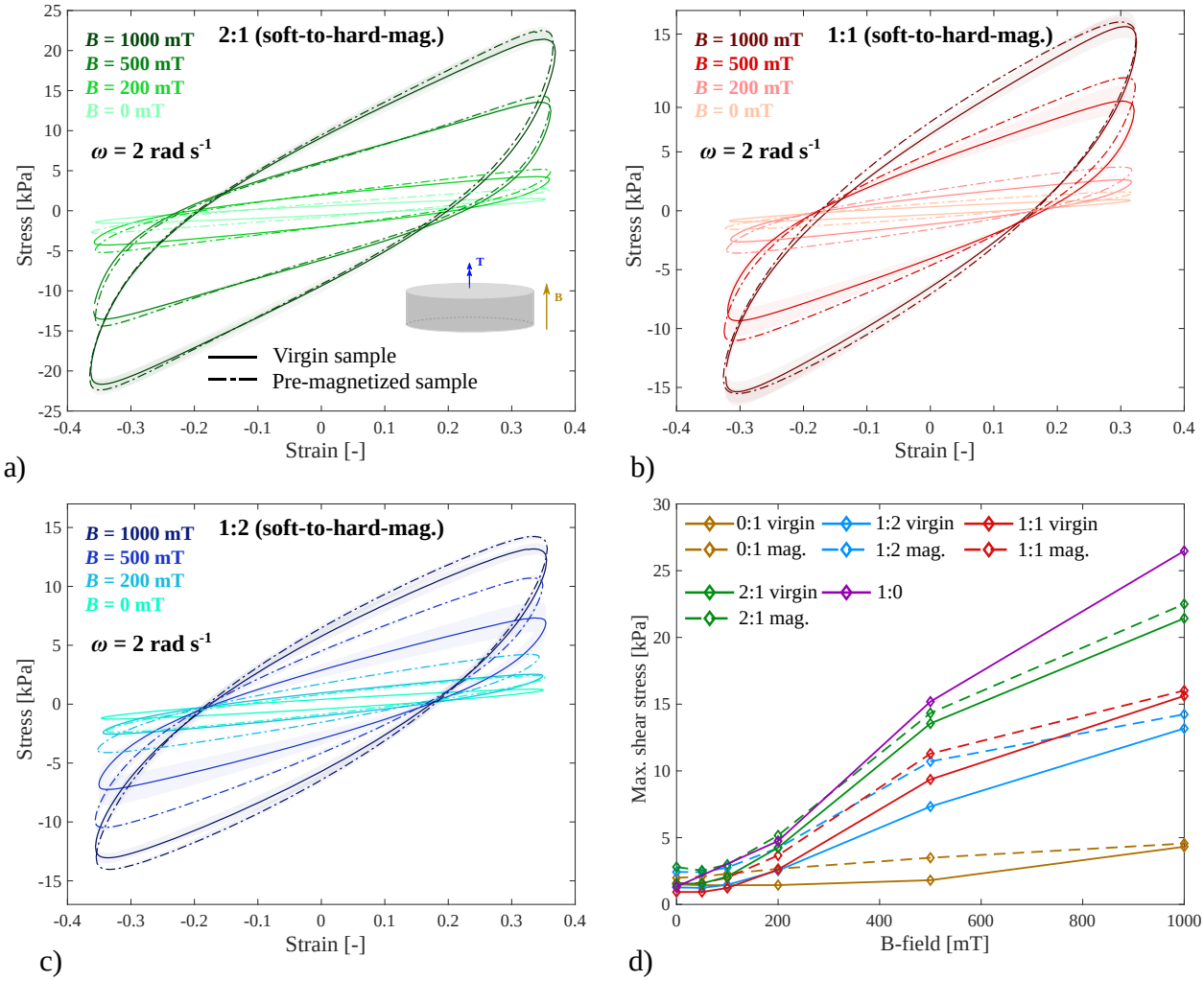

Figure 3.29: Experimental characterization of the magnetorheological and magnetic remanence effects depending on the mixing ratio between soft- and hard-magnetic particles on hybrid MREs. Results from constant oscillatory shear loops for particles mixing ratios of (a) 2:1, (b) 1:1 and (c) 1:2. The total amount of particles is 30 vol.%. The experiments are performed on both virgin and pre-magnetized samples (i.e., previously exposed to 1000 mT axial magnetic field). (d) Maximum shear stress of the hysteresis loops as a function of the magnetic field and for the same particles mixing ratios. The solid lines denote experimental results on virgin samples and dashed lines denote experimental results on pre-magnetized samples.

Dynamic mechanical analysis (DMA) under shear loading

As for sMREs and hMREs, frequency sweep tests under shear loading and different external magnetic conditions provide insights into the rate-dependent behavior of hybrid MREs. For all soft-to-hard-magnetic particles volume ratios, Figures 3.30 and 3.31 provide the evolution of the shear storage modulus (G'), shear loss modulus (G'') and loss factor ($\tan\delta$) for magnetic magnetic actuations of 0 mT, 200 mT, 500 mT, and 1000 mT. All samples, irrespective of the particles mixing ratio or magnetic field applied, show a stiffening response with the strain-rate (i.e., frequency here) due to the viscoelastic nature of the elastomeric matrix. In addition, all samples present a clear magnetorheological stiffening with the applied magnetic field. This effect, together with the effect of the magnetic remanence due to the hard-magnetic particles, is analyzed in-detail in the following paragraphs, where an intricate synergistic effect between both types of particles is to be uncovered.

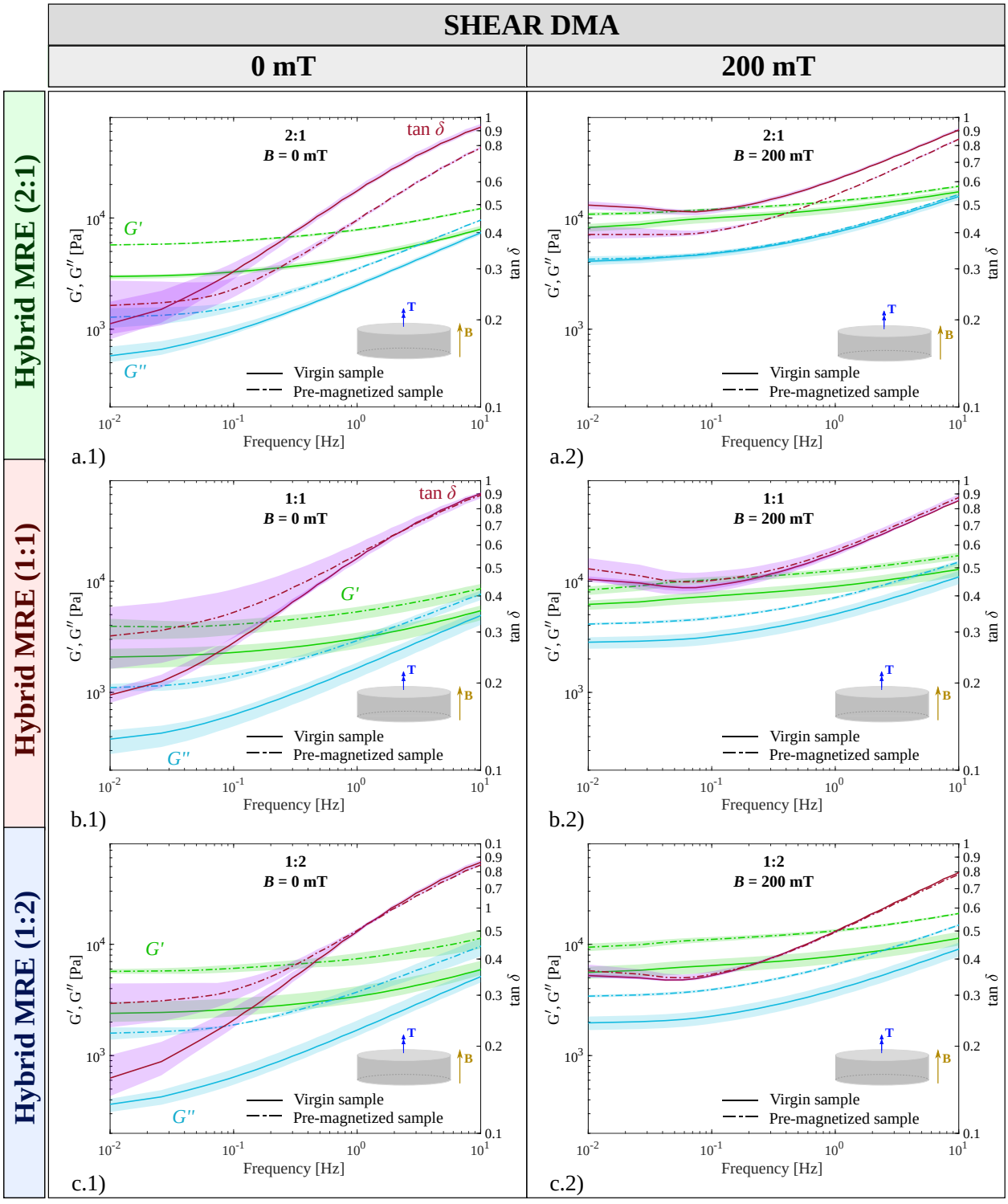

Figure 3.30: Experimental results for the frequency sweeps of hybrid MREs under shear mode. Curves for the storage modulus (G'), loss modulus (G'') and loss factor ($\tan\delta$) for soft-to-hard-magnetic particles mixing ratios of (a) 2:1, (b) 1:1 and (c) 1:2. The total amount of magnetic particles is 30 vol.%. The experiments are performed on both virgin and pre-magnetized samples under magnetic actuation of (a-c.1) 0 mT and (a-c.2) 200 mT.

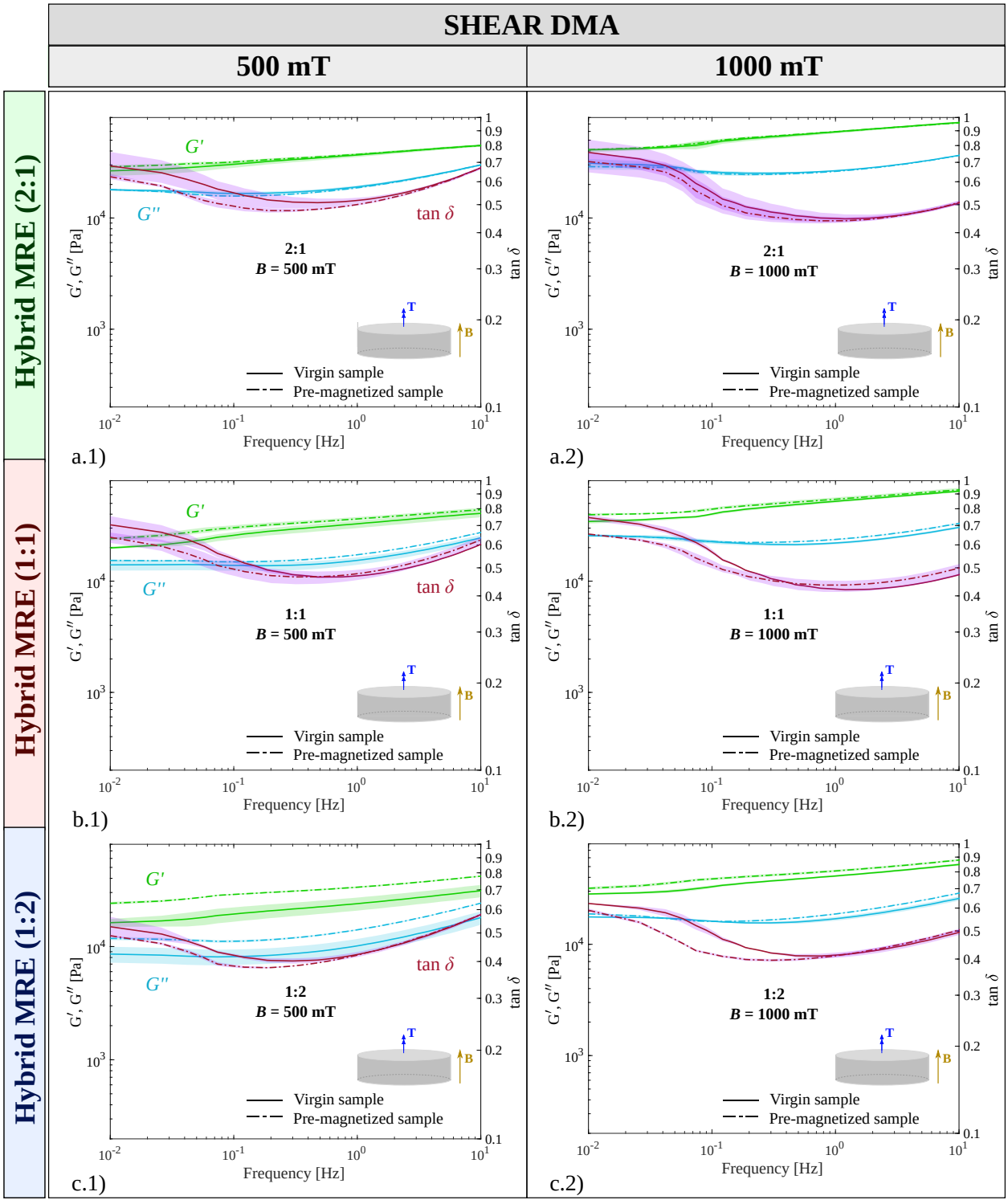

Figure 3.31: Experimental results for the frequency sweeps of hybrid MREs under shear mode. Curves for the storage modulus (G'), loss modulus (G'') and loss factor ($\tan\delta$) for soft-to-hard-magnetic particles mixing ratios of (a) 2:1, (b) 1:1 and (c) 1:2. The total amount of magnetic particles is 30 vol.%. The experiments are performed on both virgin and pre-magnetized samples under magnetic actuation of (a-c.1) 500 mT and (a-c.2) 1000 mT.

The magnetorheological effect is an insightful parameter to understand the results. Figure 3.32.a collects these data in the form of barplots for the different soft-to-hard-magnetic particles volume ratios and external magnetic actuations. As expected, sMREs present much higher effects than hMREs due to the higher relative magnetic permeability and the subsequent more intense particle magnetic interactions. However, surprisingly, the maximum magnetorheological effect is found for a soft-to-hard particles ratio of 1:1. These results suggest that the combination of soft- and hard-magnetic particles enhances the effective magnetic field within an MRE and increases the magnitude of the dipole-to-dipole magnetic interactions. In this regard, the reader may note that internal forces between particles not only depend on their magnetization (higher in the soft particles) but also on their volume (larger for the hard particles).

Moreover, the results for null magnetic actuation on virgin (solid lines) and pre-magnetized (dashed lines) hybrid MREs in Figures 3.30 and 3.31 unveil remarkable differences in terms of storage and loss moduli between virgin and pre-magnetized samples. To elaborate on this, the magnetic remanence effect, understood as the magnetorheological stiffening sustained after removing the magnetic field, is demonstrated in Figure 3.32.b. As expected, pure sMREs do not present any remanence effect due to the low magnetic coercivity of the soft-magnetic particles. One would expect such a remanence effect to be maximum for pure hMREs. However, the results indicate that the maximum corresponds to hybrid MREs with a mixing ratio of 1:2. This observation can be explained by the interaction between soft- and hard-magnetic particles during and after the pre-magnetization processes. In this regard, during the pre-magnetization, the externally applied field of 1000 mT is internally amplified by the soft-magnetic particles, favored by their high relative magnetic permeability (30 times higher than in hard-magnetic particles). Such an amplified magnetic field promotes a higher remanent magnetization in the hard-magnetic particles. Moreover, when the external field is switched off, the hard particles sustain residual magnetization. Due to dipole-to-dipole interactions, this magnetization influences the surrounding soft particles forming magnetic bridges.[11] The magnetic field generated by the hard particles is amplified by the soft ones, thus enhancing the interactions between particles at the microscale. These interactions create a higher resistance of the composite to deform, resulting in a remanent stiffening effect. Consequently, mixing soft-hard particles optimizes the magneto-mechanical coupling.

[11]Note that the magnetic bridges created by the soft-magnetic particles surrounding the hard-magnetic ones will be addressed later in the numerical application of hybrid MREs to design versatile soft actuators with capabilities to enhance their mechanical properties and perform complex shape changes at the same time.

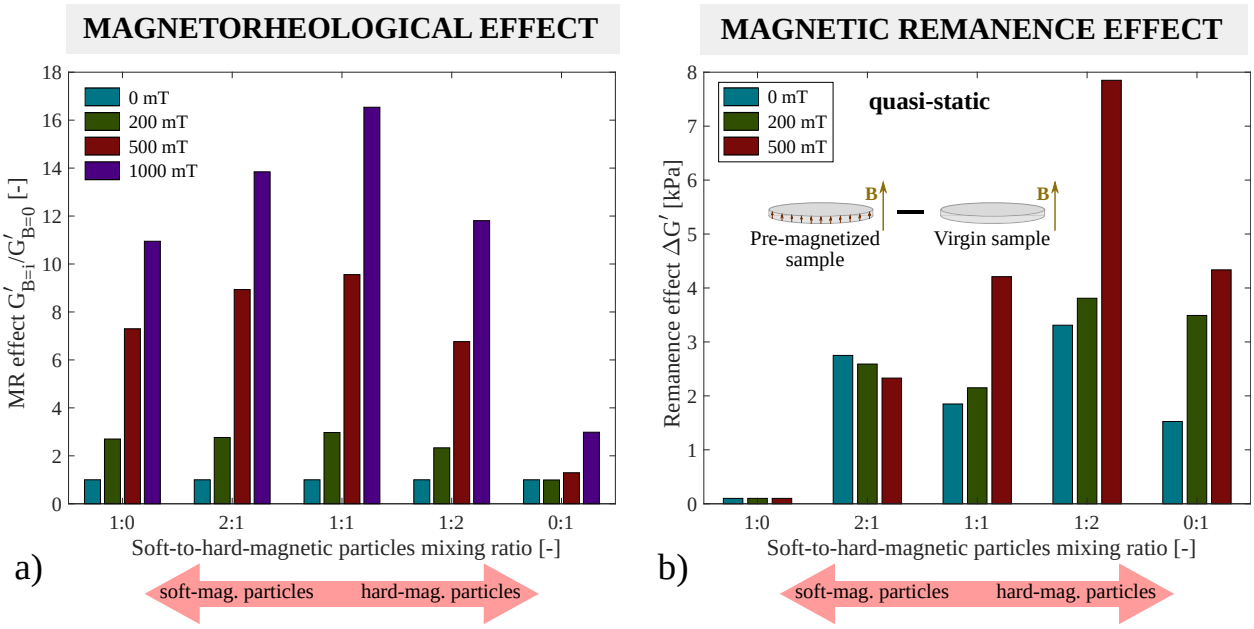

Figure 3.32: Magnetorheological effect and magnetic remanence effect as a function of the soft-to-hard-magnetic particles ratio and external magnetic actuation. (a) Magnetorheological effect, i.e., ratio between the storage shear moduli under magnetic actuation and under null magnetic actuation, for hybrid MREs with soft-to-hard-magnetic particles' mixing ratios of 1:0, 2:1, 1:1, 1:2, 0:1 and external magnetic fields of 0 mT, 200 mT, 500 mT and 1000 mT. (b) Magnetic remanence effect, i.e., difference between the storage shear moduli of pre-magnetized and virgin samples, for the same hybrid MREs and magnetic conditions.

3.4.3 Mechanically confined tests under magnetic actuation

Under the application of an external magnetic field, MREs respond mechanically by deforming and/or changing their mechanical and rheological properties. This behavior is the result of balancing the pure mechanical stresses and magnetically induced stresses within the sample. On the one hand, pure mechanical stresses are related to the passive deformation of the material and the mechanical properties of both elastomeric matrix and particles. They can be easily measured by a traditional experimental testing. On the other hand, magnetically induced stresses relate to magnetic particle interactions at the microstructural level. Such interactions result in attractive and repulsive forces that contribute to macroscopic deformations. Although these interactions are difficult to analyze experimentally, we evaluate them from the macroscopic magnetic stress induced in the MRE samples. This stress state is an excellent indicator of the physics governing internal processes as it is the direct result of microstructural interplays within the composite.

To conduct the experiments, the magneto-mechanical rheometer was used according to the methodology previously described for hMREs with mechanically confined conditions. The magnetic actuation leads to particles interactions within the sample that produce a macroscopic confined expansion. The system measures the axial force due to the unique contribution of magnetic stresses. The tests were first conducted on virgin samples applying magnetic ramps of 20 mT s^{-1} until reaching 1000 mT, then keeping the field constant for 75 s. Afterwards, the field was turned off for 75 s. The results are collected in Figure 3.33.(a-c).1 for the different hybrid MREs tested. The same tests were performed on pre-magnetized

samples until reaching 500 mT and under two different actuation modes: i) direct actuation, i.e., applying the magnetic field in the same direction as the pre-magnetization; and ii) reverse actuation, i.e., applying the magnetic field in the opposite direction to the pre-magnetization. Figures 3.33.(a-c).2 show the results for the different hybrid MREs tested. Note that these results are the counterparts of those for pure sMREs and hMREs in Figures 3.13 and 3.24, respectively.

The magnetic stress is modulated by the soft-to-hard-magnetic particles' mixing ratio. The response of sMREs is found to be independent of the direction of the applied magnetic field, and shows strong magnetically induced stresses. This can be explained by their low magnetic coercivity, which allows them to magnetize in the direction of the applied magnetic field without sustaining significant remanent fields. The larger stresses with respect to hybrid and hMREs may be explained by the higher magnetic permeability of soft-magnetic particles that enhances particle interactions. On the contrary, hMREs show lower induced stresses but their overall response highly differs for direct to reverse actuations. This is explained by the residual magnetization of the hard particles. Under a direct actuation, they tend to form chain-like structures leading to the expansion of the sample. For a reverse actuation, however, they tend to rotate and compress the sample. Regarding the response of hybrid MREs, it seems clear that the presence of soft particles is the main modulator under these conditions, tending all these samples to expand irrespective of the actuation mode (direct or reverse). In addition, the maximum stresses induced directly correlate with the amount of soft particles, i.e., 22 kPa, 18 kPa and 15 kPa for mixing ratios of 2:1, 1:1 and 1:2, respectively. Under confined conditions, the effect of the hard particles in the hybrid MREs can be noted by a jump in the maximum stresses for direct and reverse actuation modes.

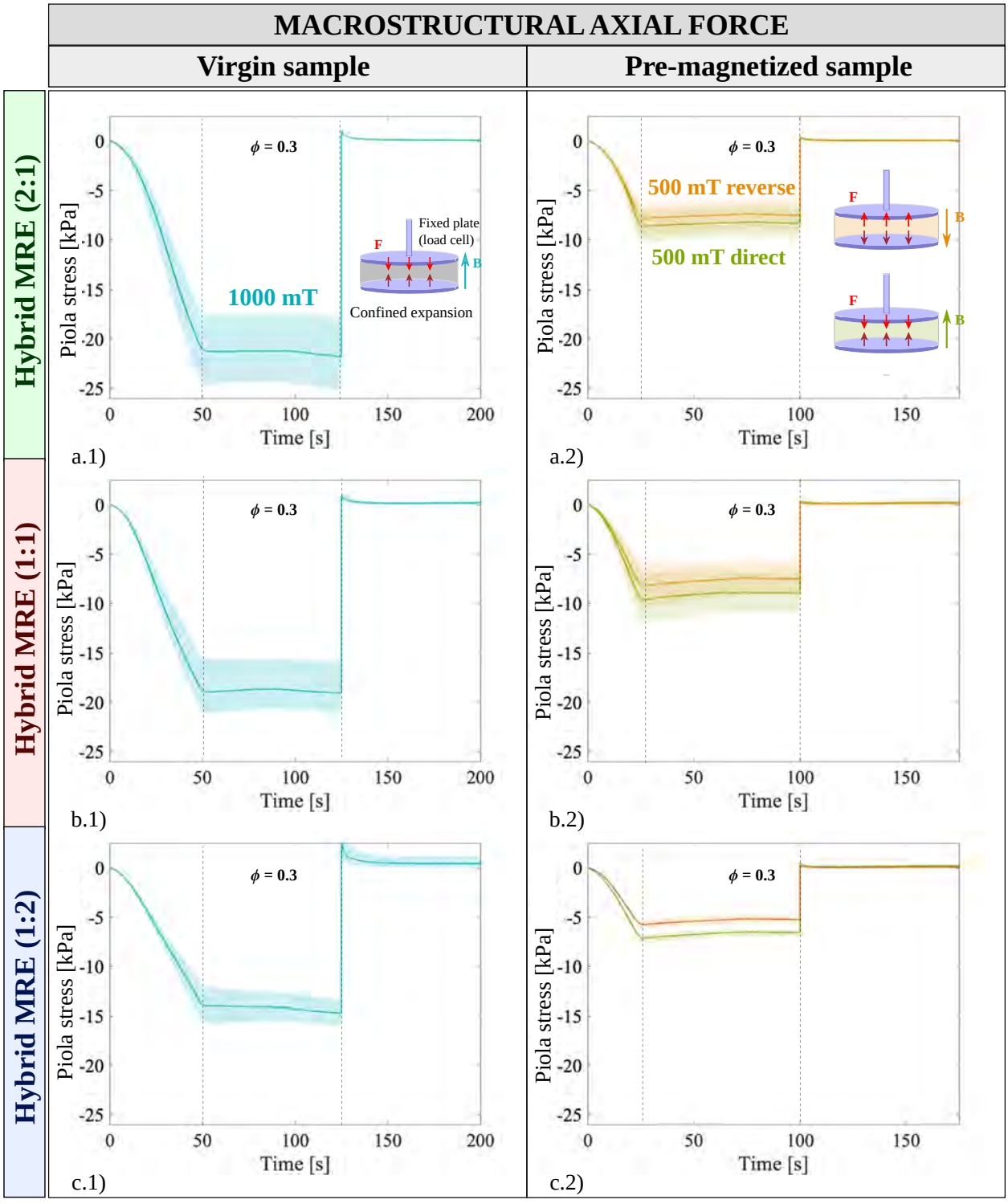

Figure 3.33: Macrostructural evaluation of microstructural magneto-mechanical interactions on hybrid MREs. Time evolution of the axial stress (Piola stress) exerted by mechanically confined samples on the upper plate of the rheometer for multiple soft-to-hard-magnetic particles mixing ratios of (a) 2:1, (b) 1:1, (c) 1:2. The experiments are conducted on virgin and pre-magnetized samples. The magnetic field on virgin samples is applied until reaching a maximum of 1000 mT, then kept constant for 75 s and finally switched off. On the pre-magnetized samples, the experiments include direct and reverse magnetic actuations following the same procedure but limiting the actuating magnetic field up to 500 mT.

3.5 Discussion

This chapter has provided a comprehensive characterization of sMREs, hMREs and, eventually, hybrid MREs combining soft- and hard-magnetic particles. On the one hand, DMA results for sMREs uncover a remarkable MR effect up to 200 in compression mode, and up to 15 under shear loading. Moreover, mechanically confined tests under magnetic actuation reveal that the microstructure may reach alternative particle-rearrangement states depending on the rate of the magnetic loading. In addition, the stiffness of the matrix has been shown to be a crucial design factor to tune the effective mechanical behavior of ultra-soft MREs. The combination of macroscopic and microscopic characterization techniques allows to isolate the deformation resistance due to the matrix deformation and due to the magnetic interactions. In this regard, the use of an elastomeric matrix with negligible strain hardening (see Figures 3.16.a and A.1.a) leads to constant stiffness measurements via nanoindentation under different magnetic field conditions. However, the macroscopic stiffness measured by rheological tests shows a significant increase, suggesting a strong influence of the magnetic microstructural interactions. On the other hand, hMREs present a MR effect in shear deformation mode five times smaller. However, they are able to retain the MR effect in the absence of magnetic actuation and to perform functional morphological changes, e.g., bending and twisting. Finally, hybrid MREs combine the features of sMREs and hMREs in a single material. The hybrid magnetic powder not only enables the composite to provide both functional responses (magnetorheological and magnetostriction effects), but also to outdo the performance of pure sMREs and hMREs, as shown in Figure 3.32. Synergistic effects enhance the MR effect above pure sMREs and the remanence effect above pure hMREs.

Even though the experimental results suggest interesting synergistic effects and complex interactions between soft- and hard-magnetic particles at the microscale, the study is restricted to overall structural observations. In this respect, *in silico* approaches would help unveil the microstructural mechanisms and provide guidance for the design of functional applications based on MREs. Hereafter such a theoretical-numerical approach is addressed. The following chapter provides the constitutive framework to model sMREs, hMREs and hybrid MREs. The constitutive models must consider the coupled effects of soft- and hard-magnetic particles and properly adjust to both microstructural and macrostructural scopes.

4 Modeling

This chapter addresses the constitutive framework for sMREs, hMREs and hybrid MREs, from the microscale to the macroscale. On the one hand, a material law for sMREs is introduced and particularized for each of the phases. The model encompasses the coupled magneto-mechanical physics based on the interactions between the highly stretchable matrix and the highly magnetizable soft-magnetic particles. Then, the model is extended to include the effect of remanent magnetization in hMREs. Hybrid MREs inherit a model that results from a combination of the former ones. Finally, a multi-scale homogenization transition scheme permits to transfer microscopic details of the MRE composition to the macroscopic scale. On the other hand, two macroscopic models allow to mimic the behavior of sMREs and hMREs from a continuum point of view. Note that the models are related to the numerical applications developed in the following chapter.[12] The first one reproduces the magneto-mechanical sMRE substrate designed for the stimulation of biological matter. The second one addresses for the first time the fracture mechanics of MREs, namely the fracture performance of hMREs with remanent magnetic fields. To this end, it combines the multi-physics framework with a phase-field approach to model cracks propagation. The well-posedness of the model is guaranteed through its thermodynamic derivation.

4.1 Microscopic modeling

The structural response of MREs is the outcome of microstructural interactions between the soft- and hard-magnetic particles and the carrier matrix. In order to encompass such interplays and, eventually, to obtain the homogenized material response, a constitutive description of each phase (i.e., matrix, soft-magnetic and hard-magnetic particles) is necessary.

[12] The constitutive models within this chapter are to be implemented in ad-hoc numerical frameworks (FE Boundary Value Problems). These numerical models will help understand and develop the applications presented in the next chapter. These applications comprise: i) the sMRE substrate to stimulate biological matter (i.e., deform and align cell cultures by the transmission of complex strain patterns from the substrate to the culture) in further Section 5.1 and ii) the conceptualization of hMREs with remanent magnetic fields as extremely tough materials with enhanced fracture performance, in Section 5.2. In addition, iii) the combination of both enables hybrid MREs with superior magneto-rheological stiffening and shape-morphing capability in Section 5.3. The values for all the model parameters will be provided in such sections.

4.1.1 Constitutive formulation for soft-magnetic MREs

Kinematics and balance laws

The constitutive framework is formulated considering finite deformations due to the ability of the MREs used in this work to undergo large strains. A deformation map $\mathbf{x} = \boldsymbol{\varphi}(\mathbf{X})$ links the continuum coordinates in the reference or material configuration $\mathbf{X} \in \Omega_0$ with the deformed or spatial configuration $\mathbf{x} \in \Omega$. Therefore, the displacement field is defined as $\mathbf{u} = \boldsymbol{\varphi}(\mathbf{X}) - \mathbf{X}$. The gradient of this primary field yields the deformation gradient as

$$\mathbf{F} = \boldsymbol{\nabla}_0 \boldsymbol{\varphi} = \boldsymbol{\nabla}_0 \mathbf{u} + \mathbf{I}, \quad J := \det \mathbf{F} \geq 0, \tag{4.1}$$

where $\boldsymbol{\nabla}_0$ is the gradient operator with respect to the reference configuration and $\mathbf{I}$ is the second-order identity tensor. Alternatively, one may use rotation-free strain tensors, namely the left and right Cauchy-Green tensors, respectively

$$\mathbf{b} := \mathbf{F} \cdot \mathbf{F}^{\mathrm{T}}, \quad \mathbf{C} := \mathbf{F}^{\mathrm{T}} \cdot \mathbf{F}. \tag{4.2}$$

The conjugate fields $\mathbf{P}$ and $\boldsymbol{\sigma}$ are the Piola and Cauchy stress tensors, respectively referred to the reference and current configurations. These are related according to

$$\boldsymbol{\sigma} = J^{-1} \mathbf{P} \cdot \mathbf{F}^{\mathrm{T}}. \tag{4.3}$$

The magnetic problem incorporates three main additional variables. These are the magnetic field intensity $\mathbb{H}$, the magnetization $\mathbb{M}$ and the magnetic induction $\mathbb{B}$ in the reference configuration, and their counterparts $\mathbb{h}$, $\mathbb{m}$ and $\mathbb{b}$ in the current configuration. Let us relate the variables in both configurations by

$$\mathbb{h} = \mathbf{F}^{-\mathrm{T}} \cdot \mathbb{H}, \quad \mathbb{b} = J^{-1} \mathbf{F} \cdot \mathbb{B}. \tag{4.4}$$

The magnetic vectors are related through the standard constitutive relation

$$\mathbb{b} = \mu_0 \left[\mathbb{h} + \mathbb{m} \right]. \tag{4.5}$$

Alternatively, Equation 4.5 can be written in the spatial configuration

$$\mathbb{B} = J \mu_0 \mathbf{C}^{-1} \left[\mathbb{H} + \mathbb{M} \right]. \tag{4.6}$$

The field equation for the mechanical displacement, neglecting inertial terms and external body forces, is

$$\boldsymbol{\nabla}_0 \cdot \mathbf{P} = \mathbf{0}. \tag{4.7}$$

For the magnetic problem, the Maxwell equations for the magnetostatic case state that

$$\boldsymbol{\nabla}_0 \times \mathbb{H} = \mathbf{0}, \quad \boldsymbol{\nabla}_0 \cdot \mathbb{B} = 0. \tag{4.8}$$

Note that 4.8_1 is automatically satisfied when $\mathbb{H}$ is derived from a magnetic scalar potential field ϕ as

$$\mathbb{H} = -\boldsymbol{\nabla}_0 \, \phi, \quad \text{in } \Omega_0. \tag{4.9}$$

Considering isothermal conditions, we define an energy density function that depends on the deformation gradient $\mathbf{F}$ and the magnetic field $\mathbb{H}$ as $\Psi(\mathbf{F}, \mathbb{H})$. The second law of thermodynamics in the form of Clausius-Duhem inequality becomes

$$\mathbf{P} : \dot{\mathbf{F}} - \mathbb{B} \cdot \dot{\mathbb{H}} - \frac{\partial \Psi}{\partial \mathbf{F}} : \dot{\mathbf{F}} - \frac{\partial \Psi}{\partial \mathbb{H}} \cdot \dot{\mathbb{H}} \geq 0, \tag{4.10}$$

The constitutive equations can be consistently derived, applying the Coleman-Noll framework as

$$\mathbf{P} = \frac{\partial \Psi}{\partial \mathbf{F}} - p\mathbf{F}^{-\mathrm{T}}, \quad \mathbb{B} = -\frac{\partial \Psi}{\partial \mathbb{H}}. \tag{4.11}$$

where the term $-p\mathbf{F}^{-\mathrm{T}}$ has been included to impose incompressibility, with p the Lagrange multiplier associated to the pressure.

Constitutive equations

The constitutive behavior at a local point, for the matrix and the particles, is defined by the energy density function Ψ to account for mechanical and magnetic responses. Following standard knowledge of such materials, we consider both the polymer matrix and particle phases as incompressible[13]. Here, the energy density is decomposed into three contributions, i.e., the mechanical energy, Maxwell energy and magnetization energy as

$$\Psi(\mathbf{F}, \mathbb{H}) = \Psi_{\mathrm{mech}}(\mathbf{F}) + \Psi_{\mathrm{maxw}}(\mathbf{F}, \mathbb{H}) + \Psi_{\mathrm{mag}}(\mathbf{F}, \mathbb{H}). \tag{4.12}$$

Let us define the mechanical energetic contributions following a Generalized neo-Hookean formulation as

$$\Psi_{\mathrm{mech}}(\mathbf{F}) = \frac{G}{2b}\left[\left[1 + \frac{b}{n}[I_1 - 3]\right]^n - 1\right], \tag{4.13}$$

with $I_1 = \mathrm{tr}\left(\mathbf{F} \cdot \mathbf{F}^{\mathrm{T}}\right)$ and G the small strain shear modulus of the considered phase and b and n material parameters. From this energetic definition, the mechanical part of the Piola stress tensor can be derived as

$$\mathbf{P}_{\mathrm{mech}}(\mathbf{F}, p) = \frac{\partial \Psi_{\mathrm{mech}}}{\partial \mathbf{F}} - p\mathbf{F}^{-\mathrm{T}}, \tag{4.14}$$

where the term arising from incompressibility (addressed later in Section 4.1.4) has been incorporated into this definition. Regarding the magnetic contributions, the background Maxwell energy in its standard expression for the material configuration reads as

$$\Psi_{\mathrm{maxw}}(\mathbf{F}, \mathbb{H}) = -\frac{\mu_0}{2} I_5, \tag{4.15}$$

where $I_5 = \left[\mathbf{F}^{-\mathrm{T}} \cdot \mathbb{H}\right] \cdot \left[\mathbf{F}^{-\mathrm{T}} \cdot \mathbb{H}\right]$ and the term J has been removed due to the incompressibility assumption. Moreover, let us define the magnetization by the hyperbolic tangent

[13] In reality, the particles exhibit a finite bulk modulus. Nonetheless, given their very large stiffness compared to that of the polymer, the effect of the actual value of the bulk modulus is of little importance provided that it is much larger than that of the matrix as is their shear modulus. This simplifies the numerical implementations.

type magnetization relation. The magnetic energy density function reads, in the reference configuration, as

$$\Psi_{\text{mag}}\left(\mathbf{F},\mathbb{H}\right)=-\mu_0\left[\frac{m_{\text{s}}^2}{\chi_{\text{e}}}\ln\left(\cosh\left(\frac{\chi_{\text{e}}}{m_{\text{s}}}\sqrt{I_5}\right)\right)\right]. \tag{4.16}$$

Here, χ_{e} is the magnetic susceptibility and m_{s} is the magnetic saturation of the magnetization curve of the corresponding phase, with $\chi_{\text{e}}=0$ for the non-magnetic matrix. Moreover, for the particles $\mu_0 m_{\text{s}}=2.5$ T. See Figure A.7 for the magnetic behavior of the soft- and hard-magnetic particles.

Then, the definition of the total Piola stress can be derived from the total energy density by adding the magnetic components to the mechanical one, i.e.,

$$\begin{aligned}\mathbf{P}\left(\mathbf{F},\mathbb{H},p\right)&=\frac{\partial\Psi}{\partial\mathbf{F}}-p\mathbf{F}^{-\text{T}}= \\ &=G\,\mathbf{F}\left[1+\frac{b}{n}\left[I_1-3\right]\right]^{n-1}-p\mathbf{F}^{-\text{T}}-\frac{\mu_0}{2}\frac{\partial I_5}{\partial\mathbf{F}}-\mu_0\frac{m_{\text{s}}}{2\sqrt{I_5}}\tanh\left(\frac{\chi_{\text{e}}}{m_{\text{s}}}\sqrt{I_5}\right)\frac{\partial I_5}{\partial\mathbf{F}},\end{aligned} \tag{4.17}$$

with $\frac{\partial I_5}{\partial\mathbf{F}}=-2\,\left[\mathbf{F}^{-\text{T}}\cdot\mathbb{H}\right]\otimes\left[\left[\mathbb{H}\cdot\mathbf{F}^{-1}\right]\cdot\mathbf{F}^{-\text{T}}\right]$. Note that in Equation (4.17) the terms of the partial derivatives arising form Maxwell and magnetization energy density functions appear, leading to magnetically induced forces.

Remark. The choice of the energy functions leads to an uncoupled magneto-mechanical response for each phase, i.e., the matrix and the particles (see a more detailed discussion in [175, 184]). The resulting magneto-mechanical coupling is an outcome of the complex interactions between the particles and their rearrangements subject to the mechanical constraints imposed by the surrounding matrix phase. The Maxwell energy in the otherwise non-magnetic matrix phase serves to describe the background magnetic energy due to the presence of a non-zero magnetic permeability, that of vacuum.

In a similar fashion and making use of Equation (4.11), the resulting definition of the magnetic flux as a function of the magnetic field yields into

$$\mathbb{B}\left(\mathbf{F},\mathbb{H}\right)=-\frac{\partial\Psi}{\partial\mathbb{H}}=\mu_0\left[1+\frac{m_{\text{s}}}{\sqrt{I_5}}\tanh\left(\frac{\chi_{\text{e}}}{m_{\text{s}}}\sqrt{I_5}\right)\right]\mathbf{F}^{-1}\cdot\left[\mathbf{F}^{-\text{T}}\cdot\mathbb{H}\right], \tag{4.18}$$

where it can be differentiated the addition of the linear term proportional to the magnetic field vector (Maxwell) and a magnetization term described as a hyperbolic tangent profile. The resulting Eulerian magnetization function reads as

$$\mathbb{m}\left(\mathbb{h}\right)=m_{\text{s}}\tanh\left(\frac{\chi_{\text{e}}}{m_{\text{s}}}\left|\mathbb{h}\right|\right)\frac{\mathbb{h}}{\left|\mathbb{h}\right|}, \tag{4.19}$$

where $|\mathbb{h}|$ represents the magnitude of the Eulerian magnetic field vector $\mathbb{h}$.

Remark. Setting $\chi_{\text{e}}=0$ in Equation 4.18 to recover a non-magnetic material (e.g. the polymer incompressible matrix phase), $\mathbb{B}$ yields

$$\mathbb{B}\left(\mathbf{F},\mathbb{H}\right)=\mu_0\,\mathbf{F}^{-1}\cdot\left[\mathbf{F}^{-\text{T}}\cdot\mathbb{H}\right], \tag{4.20}$$

or simply $\mathbb{b}=\mu_0\mathbb{h}$ by use of 4.4. This implies that the magnetization is $\mathbb{m}=\mathbf{0}$ in that case.

4.1.2 Constitutive formulation for hard-magnetic MREs

For the conceptualization of the model for hMREs, the formulation proposed in the previous Section 4.1.1 is extended to encompass the magnetic remanence of the particles. The model is postulated according to a non-dissipative simplification of the framework reported by Rambausek et al. [166]. A single total energy density function Ψ describes the magneto-mechanical constitutive behavior of both the matrix and magnetic fillers at the microstructural level.

Kinematics and balance laws

The deformation gradient and stress tensors are defined according to Equation 4.1 and 4.3. The magnetic problem is formulated on a primary scalar potential field ϕ. Let us define the magnetic field vector $\mathbb{H}$ as

$$\mathbb{H} = -\boldsymbol{\nabla}_0 \phi = \mathbb{H}_\mathrm{e} + \mathbb{H}_\mathrm{r}. \tag{4.21}$$

Unlike sMREs, here the magnetic field is split into an energetic contribution $\mathbb{H}_\mathrm{e}$ due to the magnetic susceptibility of the medium and a remanent contribution $\mathbb{H}_\mathrm{r}$ related to the permanent magnetization of the hMRE [164]. The last one is prescribed as a constant vector to capture the permanent magnetization of the medium. For the calibration procedure of the residual magnetization from experimental evidence, the reader can consult Section A.2.2. Moreover, the model for hMREs recalls the standard constitutive equation for the magnetic fields in Equation 4.6. The field equations are Equation 4.7 and Equation 4.8.

Constitutive equations

As for the model for sMREs, given the nearly incompressible nature of the polymeric matrix, and the larger stiffness of the magnetic particles with respect to the matrix, both phases are considered fully incompressible. The energy function is based on three contributions, i.e., mechanical, Maxwell and magnetization energies, according to

$$\Psi\left(\mathbf{F}, \mathbb{H}\right) = \Psi_\mathrm{mech}\left(\mathbf{F}\right) + \Psi_\mathrm{maxw}\left(\mathbf{F}, \mathbb{H}\right) + \Psi_\mathrm{mag}\left(\mathbf{F}, \mathbb{H}\right). \tag{4.22}$$

For the description of the elastic energetic contribution, the Generalized neo-Hookean formulation is chosen

$$\Psi_\mathrm{mech}\left(\mathbf{F}\right) = \frac{G}{2b}\left[\left[1 + \frac{b}{n}\left[I_1 - 3\right]\right]^n - 1\right], \tag{4.23}$$

with $I_1 = \mathrm{tr}\left(\mathbf{F}\cdot\mathbf{F}^\mathrm{T}\right)$ and G the small strain shear modulus of the considered phase and b and n material parameters.

With respect to the magnetic contributions, the Maxwell energy describes the background magnetic energy due to the non-zero magnetic permeability of the vacuum as

$$\Psi_\mathrm{maxw}\left(\mathbf{F}, \mathbb{H}\right) = -\frac{\mu_0}{2} I_5^\mathrm{e}, \tag{4.24}$$

with the energetic magnetic invariant[14] defined as

$$I_5^{\mathrm{e}} = \mathbb{h} \cdot \mathbb{h} = \left[\mathbf{F}^{-\mathrm{T}} \cdot \mathbb{H}\right] \cdot \left[\mathbf{F}^{-\mathrm{T}} \cdot \mathbb{H}\right]. \tag{4.25}$$

The contribution of the magnetizable media is additively decomposed in an energetic term $\Psi_{\mathrm{mag,e}}$ and a remanent contribution $\Psi_{\mathrm{mag,r}}$ as

$$\Psi_{\mathrm{mag}}\left(\mathbf{F}, \mathbb{H}\right) = \Psi_{\mathrm{mag,e}} + \Psi_{\mathrm{mag,r}} = -\mu_0 \left[\frac{m_{\mathrm{s}}^2}{\chi_{\mathrm{e}}} \ln\left(\cosh\left(\frac{\chi_{\mathrm{e}}}{m_{\mathrm{s}}}\sqrt{I_5^{\mathrm{e}}}\right)\right)\right] + \mu_0\left[1+\chi_{\mathrm{e}}\right] I_5^{\mathrm{er}} + \frac{\mu_0}{2\chi_{\mathrm{r}}} I_5^{\mathrm{r}}, \tag{4.26}$$

where χ_{e} and χ_{r} are the energetic and remanent magnetic susceptibilities, respectively, and m_{s} is the magnetic saturation of the magnetization curve of the corresponding phase.

Remark. The last term of Equation 4.26 vanishes when differentiating with respect to $\mathbf{F}$ and $\mathbb{H}$. It would be necessary to define a dissipative magnetic response (i.e., evolution of $\mathbb{H}_{\mathrm{r}}$ as an internal variable) to get the contribution of this term. In this work, we take the residual magnetization constant and, therefore, such an energetic term is negligible. Consequently, the parameter χ_{r} does not affect the simulations.

I_5^{er} is the magnetic invariant reported in [164]. It accounts for the energetic and remanent magnetic fields in the Eulerian configuration of the medium and it is defined as

$$I_5^{\mathrm{er}} = \mathbb{h} \cdot \mathbb{h}_{\mathrm{r}} = \mathbb{H} \cdot \mathbf{C}^{-1/2} \cdot \mathbb{H}_{\mathrm{r}}. \tag{4.27}$$

Finally, the invariant I_5^{r} only considers the remanent field, reading as

$$I_5^{\mathrm{r}} = \mathbb{h}_{\mathrm{r}} \cdot \mathbb{h}_{\mathrm{r}} = \mathbb{H}_{\mathrm{r}} \cdot \mathbb{H}_{\mathrm{r}}. \tag{4.28}$$

The Piola stress tensor can be derived from the total energy potential and the incompressibility condition as

$$\begin{aligned}\mathbf{P}\left(\mathbf{F}, \mathbb{H}, p\right) = \frac{\partial \Psi}{\partial \mathbf{F}} - p\mathbf{F}^{-\mathrm{T}} = \mathbf{P}_{\mathrm{mech}} + \mathbf{P}_{\mathrm{maxw}} + \mathbf{P}_{\mathrm{mag,e}} + \mathbf{P}_{\mathrm{mag,r}} = \\ = G\,\mathbf{F}\left[1 + \frac{b}{n}\left[I_1 - 3\right]\right]^{n-1} - p\mathbf{F}^{-\mathrm{T}} - \frac{\mu_0}{2}\frac{\partial I_5^{\mathrm{e}}}{\partial \mathbf{F}} - \mu_0 \frac{m_{\mathrm{s}}}{2\sqrt{I_5^{\mathrm{e}}}} \tanh\left(\frac{\chi_{\mathrm{e}}}{m_{\mathrm{s}}}\sqrt{I_5^{\mathrm{e}}}\right)\frac{\partial I_5^{\mathrm{e}}}{\partial \mathbf{F}} \\ + \mu_0\left[1+\chi_{\mathrm{e}}\right]\frac{\partial I_5^{\mathrm{er}}}{\partial \mathbf{C}} : \frac{\partial \mathbf{C}}{\partial \mathbf{F}},\end{aligned} \tag{4.29}$$

with $\frac{\partial I_5^{\mathrm{e}}}{\partial \mathbf{F}} = -2\,\left[\mathbf{F}^{-\mathrm{T}} \cdot \mathbb{H}\right] \otimes \left[\left[\mathbb{H} \cdot \mathbf{F}^{-1}\right] \cdot \mathbf{F}^{-\mathrm{T}}\right]$.

The variable p in the term $-p\mathbf{F}^{-\mathrm{T}}$ is the Lagrange multiplier that accounts for the incompressibility condition.

[14] The superscript "e" means that the invariant depends only on the energetic magnetic field $\mathbb{h}$, and not on the remanent contribution $\mathbb{h}_{\mathrm{r}}$.

In turn, the derivative of I_5^{er} [164] reads as

$$\frac{\partial I_5^{\mathrm{er}}}{\partial \mathbf{C}} = -\frac{4}{\Delta}\Big[I_1^{\mathrm{U}}\mathbf{C}^{1/2}\,\mathrm{sym}\left(\mathbb{H}\otimes\mathbb{H}_{\mathrm{r}}\right)\mathbf{C}^{1/2} - \left(I_1^{\mathrm{U}}\right)^2\left[\mathbf{C}^{1/2}\,\mathrm{sym}\left(\mathbb{H}\otimes\mathbb{H}_{\mathrm{r}}\right) + \mathrm{sym}\left(\mathbb{H}\otimes\mathbb{H}_{\mathrm{r}}\right)\mathbf{C}^{1/2}\right] + \left[I_1^{\mathrm{U}}I_2^{\mathrm{U}} - I_3^{\mathrm{U}}\right]\left[\mathbf{C}^{1/2}\,\mathrm{sym}\left(\mathbb{H}\otimes\mathbb{H}_{\mathrm{r}}\right)\mathbf{C}^{-1/2} + \mathbf{C}^{-1/2}\,\mathrm{sym}\left(\mathbb{H}\otimes\mathbb{H}_{\mathrm{r}}\right)\mathbf{C}^{1/2}\right] + \Big[\left(I_1^{\mathrm{U}}\right)^3 + I_3^{\mathrm{U}}\Big]\,\mathrm{sym}\left(\mathbb{H}\otimes\mathbb{H}_{\mathrm{r}}\right) - \left(I_1^{\mathrm{U}}\right)^2 I_2^{\mathrm{U}}\left[\mathrm{sym}\left(\mathbb{H}\otimes\mathbb{H}_{\mathrm{r}}\right)\mathbf{C}^{-1/2} + \mathbf{C}^{-1/2}\,\mathrm{sym}\left(\mathbb{H}\otimes\mathbb{H}_{\mathrm{r}}\right)\right] + \Big[\left(I_1^{\mathrm{U}}\right)^2 I_3^{\mathrm{U}} + \left[I_1^{\mathrm{U}}I_2^{\mathrm{U}} - I_3^{\mathrm{U}}\right]I_2^{\mathrm{U}}\Big]\mathbf{C}^{-1/2}\,\mathrm{sym}\left(\mathbb{H}\otimes\mathbb{H}_{\mathrm{r}}\right)\mathbf{C}^{-1/2}\Big], \tag{4.30}$$

and $\Delta = 8\left[I_1^{\mathrm{U}}I_2^{\mathrm{U}} - I_3^{\mathrm{U}}\right]I_3^{\mathrm{U}}$. Note that I_1^{U}, I_2^{U} and I_3^{U} are the three principal invariants of $\mathbf{U} = \mathbf{C}^{1/2}$.

Likewise, the magnetic induction is obtained from the energy density function as

$$\mathbb{B}\left(\mathbf{F},\mathbb{H}\right) = -\frac{\partial\Psi}{\partial\mathbb{H}} = \mu_0\left[1 + \frac{m_{\mathrm{s}}}{\sqrt{I_5^{\mathrm{e}}}}\tanh\left(\frac{\chi_{\mathrm{e}}}{m_{\mathrm{s}}}\sqrt{I_5^{\mathrm{e}}}\right)\right]\mathbf{F}^{-1}\cdot\mathbf{F}^{-\mathrm{T}}\cdot\mathbb{H} - \mu_0\left[1+\chi_{\mathrm{e}}\right]\mathbb{H}_{\mathrm{r}}\mathbf{C}^{-1/2}. \tag{4.31}$$

Remark. In the above expression, one can read the contribution of a linear term proportional to the magnetic intensity vector (background Maxwell contribution) and a term due to the magnetization of the medium by the hyperbolic tangent profile. Note that the remanent magnetic field vector $\mathbb{H}_{\mathrm{r}}$ is imposed as a constant within the hard-magnetic particles. It can be straightforwardly understood that the prescription of $\mathbb{H}_{\mathrm{r}}$ leads to a permanent magnetization with opposite sign.

4.1.3 Constitutive formulation for hybrid MREs

The constitutive model for hybrid MREs is straightforwardly formulated from the model for hMREs in the previous Section 4.1.2. To this end, the energy functions need to be defined for an additional domain, i.e., the soft-magnetic particles. In total, three domains stand for the microstructure (i.e., matrix, soft-magnetic particles and hard-magnetic particles. In this case, soft- and hard-magnetic particles have different magnetic properties. Moreover, the remanent magnetic field ($\mathbb{H}_{\mathrm{r}}$) is prescribed only on the hard-magnetic particles (see Section A.2.2 for the calibration procedure of the residual magnetization from experimental evidence).

4.1.4 Homogenization fundamentals

The homogenization framework solves the magneto-mechanical equilibrium at the microscale and homogenizes the results to macroscale variables. To this end, the RVE is created to be periodic at the boundaries of the domain Ω_0. However, inside the domain the arrangement of the phases is random. This idealizes a infinite random arrangement of particles by a repetition of the RVE.

The primary variables of the homogenization problem are the microscopic displacement field $\mathbf{u}(\mathbf{X})$ and the microscopic magnetic potential field $\phi(\mathbf{X})$, which yield into the definition

of the microscopic deformation gradient $\mathbf{F}(\mathbf{X}) = \mathbf{I} + \boldsymbol{\nabla}_0 \mathbf{u}(\mathbf{X})$ and the microscopic magnetic field $\mathbb{H}(\mathbf{X}) = -\boldsymbol{\nabla}_0 \phi(\mathbf{X})$. Let us define the macroscopic deformation gradient $\overline{\mathbf{F}}$ and the macroscopic magnetic field $\overline{\mathbb{H}}$ as the volume average of the microscopic counterparts as

$$\overline{\mathbf{F}} = \frac{1}{|\Omega_0|} \int_{\Omega_0} \mathbf{F}(\mathbf{X}) \, \mathrm{d}\Omega_0, \qquad \overline{\mathbb{H}} = \frac{1}{|\Omega_0|} \int_{\Omega_0} \mathbb{H}(\mathbf{X}) \, \mathrm{d}\Omega_0, \tag{4.32}$$

respectively.

The microscopic (local) displacement vector $\mathbf{u}(\mathbf{X})$ and magnetic scalar potential $\phi(\mathbf{X})$ are additively decomposed into a linear contribution (macroscopic) and a higher order contribution (microscopic fluctuation) as

$$\mathbf{u}(\mathbf{X}) = \left[\overline{\mathbf{F}} - \mathbf{I}\right] \cdot \mathbf{X} + \widetilde{\mathbf{u}}(\mathbf{X}) \qquad \text{and} \qquad \phi(\mathbf{X}) = -\overline{\mathbb{H}} \cdot \mathbf{X} + \widetilde{\phi}(\mathbf{X}), \qquad \forall \, \mathbf{X} \in \Omega_0, \tag{4.33}$$

with $\widetilde{\mathbf{u}}(\mathbf{X})$ and $\widetilde{\phi}(\mathbf{X})$ the fluctuation fields. Note that the average of the fluctuation fields over the RVE domain Ω_0 must vanish to satisfy (4.32). This requirement is automatically fulfilled with the imposition of periodic fluctuation fields on the boundaries of Ω_0.

Given the constitutive equations of the different phases and the local incompressibility constraint, the admissible sets of solution spaces $\mathcal{K}$ and $\mathcal{G}$ for $\mathbf{u}$ and ϕ are, respectively,

$$\mathcal{K}(\overline{\mathbf{F}}) = \left\{\mathbf{F} = \mathbf{I} + \boldsymbol{\nabla}_0 \mathbf{u}, \ \det \mathbf{F} = 1, \mathbf{u} = (\overline{\mathbf{F}} - \mathbf{I}) \cdot \mathbf{X} + \widetilde{\mathbf{u}}, \ \widetilde{\mathbf{u}} \text{ periodic in } \Omega_0\right\}, \tag{4.34}$$

$$\mathcal{G}(\overline{\mathbb{H}}) = \left\{\mathbb{H} = -\boldsymbol{\nabla}_0 \phi, \ \phi = -\overline{\mathbb{H}} \cdot \mathbf{X} + \widetilde{\phi}, \ \widetilde{\phi} \text{ periodic in } \Omega_0\right\}. \tag{4.35}$$

Here, the fluctuation fields $\widetilde{\mathbf{u}}(\mathbf{X})$ and $\widetilde{\phi}(\mathbf{X})$ are the unknowns of the problem.

After imposing the incompressibility condition by a Lagrange multiplier p, the following homogenized energy potential $\overline{\mathcal{W}}$ is posed for the homogenization problem

$$\overline{\mathcal{W}}(\overline{\mathbf{F}}, \overline{\mathbb{H}}, \overline{p}) = \inf_{\mathbf{u} \in \mathcal{K}(\overline{\mathbf{F}})} \sup_{\phi \in \mathcal{G}(\overline{\mathbb{H}})} \sup_{p} \left[\frac{1}{|\Omega_0|} \int_{\Omega_0} \left[\Psi\left(\mathbf{F}, \mathbb{H}, \mathbf{X}\right) - p \left[\det \mathbf{F} - 1\right]\right] \mathrm{d}\Omega_0 \right]. \tag{4.36}$$

The balance equations of the homogenization problem are obtained by optimization of the homogenized potential energy $\overline{\mathcal{W}}$ in Equation (4.36). In the absence of body forces and under periodic boundary conditions, they result in

$$\begin{aligned} \frac{\partial \overline{\mathcal{W}}}{\partial \widetilde{\mathbf{u}}} &= \boldsymbol{\nabla}_0 \cdot \mathbf{P}\left(\mathbf{F}, \mathbb{H}, p, \mathbf{X}\right) = 0, \\ \frac{\partial \overline{\mathcal{W}}}{\partial \widetilde{\phi}} &= \boldsymbol{\nabla}_0 \cdot \mathbb{B}\left(\mathbf{F}, \mathbb{H}, \mathbf{X}\right) = 0, \\ \frac{\partial \overline{\mathcal{W}}}{\partial p} &= \det \mathbf{F} - 1 = 0. \end{aligned} \tag{4.37}$$

Remark. The proposed computational framework enables controlling mixed boundary conditions by means of macroscopic mechanical stress/strain and magnetic induction/intensity in the current or reference configurations. This means controlling either the independent macroscopic (average) fields $(\overline{\mathbf{F}}^{\text{app}}, \overline{\mathbb{H}}^{\text{app}})$, and the conjugate macroscopic fields $(\overline{\mathbf{P}}^{\text{app}}, \overline{\mathbb{B}}^{\text{app}})$, or a combination of them by imposing certain components of the primary fields and certain components of the conjugate fields. It is important to note that the macroscopic magnetic

induction to be prescribed as boundary conditions (BCs) of the homogenization problem contains both the energetic and remanent contributions according to Equation 4.31. An alternative approach is to prescribe just the energetic part of the magnetic induction $\mathbb{B}_e$. Results illustrating this last approach are shown in a following section.

Remark. The average Maxwell (magnetic) stresses are automatically equilibrated by imposing continuity of the magnetic fields in neighboring RVEs. Thus, only the average Maxwell stress contribution needs to be neglected at the macroscopic boundary conditions.

When one controls the conjugate fields $\overline{\mathbf{P}}$ and $\overline{\mathbb{B}}$, the average potential energy for the RVE is defined as

$$\mathcal{P}(\overline{\mathbf{F}}, \overline{\mathbb{H}}) = \overline{\mathcal{W}}(\overline{\mathbf{F}}, \overline{\mathbb{H}}) - \overline{\mathbf{P}}^{\text{app}} \cdot \left[\overline{\mathbf{F}} - \mathbf{I}\right] - \overline{\mathbb{H}} \cdot \overline{\mathbb{B}}^{\text{app}}. \tag{4.38}$$

In Equation (4.38) the first term stands for the internal energy and the two last terms, for the work of the external "force" loads. These last terms vanish if the primary fields $\overline{\mathbf{F}}$ and $\overline{\mathbb{H}}$ are prescribed instead. Note that $\overline{\mathbf{P}}^{\text{app}}$ refers to the stress including both mechanical and magnetization average stresses applied (not the Maxwell component). If a combination of components of the primary and conjugate average fields is imposed, the potential energy $\mathcal{P}$ needs to be amended accordingly just for such components. To prescribe such loading conditions on the conjugate macroscopic fields, it is necessary to additionally fulfill

$$\begin{aligned} \frac{\partial \mathcal{P}}{\partial \overline{\mathbf{F}}} &= \int_{\Omega_0} \mathbf{P}\left(\mathbf{F}, p, \mathbf{X}\right) \, \mathrm{d}\Omega_0 - \overline{\mathbf{P}}^{\text{app}} = 0, \\ \frac{\partial \mathcal{P}}{\partial \overline{\mathbb{H}}} &= \int_{\Omega_0} \mathbb{B}\left(\mathbf{F}, \mathbb{H}, \mathbf{X}\right) \, \mathrm{d}\Omega_0 - \overline{\mathbb{B}}^{\text{app}} = 0, \end{aligned} \tag{4.39}$$

which are derived from (4.38).

To solve the non-linear equilibrium state, Equations (4.37), (4.39) are formulated in their integral weak form to be solved in the discretized Ω_0 domain. A Newton-Raphson scheme implemented in the open source code FEniCS is used to solve the non-linear problem under the prescribed boundary conditions. To enhance the convergence, the loading conditions are progressively applied via a time discretization.

Hereafter, it follows a list of specific BCs to be imposed for ad-hoc actuation modes:

- Mechanical uniaxial compression:

$$\overline{\mathbf{F}}(t) = \begin{bmatrix} * & * & * \\ 0 & * & * \\ 0 & 0 & 1 + \Delta F_{end} t / t_{end} \end{bmatrix}, \quad \overline{\mathbf{P}}_{mech}(t) = \begin{bmatrix} 0 & 0 & 0 \\ * & 0 & 0 \\ * & * & * \end{bmatrix}. \tag{4.40}$$

- Mechanical compression relaxation test:

$$\overline{\mathbb{B}}(t) = \begin{Bmatrix} 0 \\ 0 \\ b_{end} t / t_{ramp} \end{Bmatrix}, \quad \overline{\mathbf{P}}_{mech}(t) = \begin{bmatrix} 0 & 0 & 0 \\ * & 0 & 0 \\ * & * & 0 \end{bmatrix}, \quad \overline{\mathbf{F}}(t) = \begin{bmatrix} * & * & * \\ 0 & * & * \\ 0 & 0 & * \end{bmatrix}. \tag{4.41}$$

- Magnetostriction test (free deformation):

$$\overline{\mathbb{B}}(t) = \begin{Bmatrix} 0 \\ 0 \\ b_{end}t/t_{ramp} \end{Bmatrix}, \quad \overline{\mathbf{P}}_{mech}(t) = \begin{bmatrix} 0 & 0 & 0 \\ * & 0 & 0 \\ * & * & 0 \end{bmatrix}, \quad \overline{\mathbf{F}}(t) = \begin{bmatrix} * & * & * \\ 0 & * & * \\ 0 & 0 & * \end{bmatrix}. \tag{4.42}$$

- Magnetic ramp on mechanically confined MRE:

$$\overline{\mathbb{B}}(t) = \begin{Bmatrix} 0 \\ 0 \\ b_{end}t/t_{ramp} \end{Bmatrix}, \quad \overline{\mathbf{F}}(t) = \begin{bmatrix} 1 & 0 & 0 \\ 0 & 1 & 0 \\ 0 & 0 & 1 \end{bmatrix}. \tag{4.43}$$

- Shear test under magnetic actuation:

$$\overline{\mathbb{B}}(t) = \begin{Bmatrix} 0 \\ 0 \\ b_{end} \end{Bmatrix}, \quad \overline{\mathbf{F}}(t) = \begin{bmatrix} * & * & 0 \\ 0 & * & F_{max}t/t_{ramp} \\ 0 & 0 & 1 \end{bmatrix}, \quad \overline{\mathbf{P}}_{mech}(t) = \begin{bmatrix} 0 & 0 & * \\ * & 0 & * \\ * & * & * \end{bmatrix}. \tag{4.44}$$

The computational model allows to link macroscopic measurements with material properties of the phases at the microscale. In this regard, a crucial parameter is the residual magnetization at the single particle level, defined by the variable $\mathbb{H}_{\mathrm{r}}$. The evaluation of this variable is experimentally unapproachable, being limited to macroscopic measurements of the apparent magnetic remanence (i.e., using a Teslameter on the pre-magnetized samples). However, the computational framework developed herein allows to estimate the residual magnetization of the hard particles that leads to a given experimental macroscopic value.

4.2 Macroscopic modeling

Macroscopic formulations or phenomenological approaches provide an efficient approach to model complex structures. They model the composite as a homogeneous and continuum medium. Consequently, and unlike microstructural approaches, a single definition of the energy function holds for the entire MRE. This constitutive law has to reproduce the overall material behavior. In addition, numerical boundary value problems (BVP) usually consist of several domains, e.g., the homogeneous MRE and the air, each with its individual constitutive definition.

As mentioned previously, the models in this chapter are to be implemented in ad-hoc numerical frameworks that will help understand and develop the applications presented in the next chapter. These applications comprise the sMRE substrate to stimulate biological matter (further Section 5.1) and the conceptualization of hMREs with remanent magnetic fields as extremely tough materials with enhanced fracture performance (Section 5.2).

4.2.1 Phenomenological model for sMRE samples

The magneto-mechanical problem is formulated on the deformation gradient tensor ($\mathbf{F}$) and the magnetic variables: magnetic field ($\mathbb{H}$), magnetization ($\mathbb{M}$), and magnetic induction ($\mathbb{B}$). These variables are related according to Equation 4.6.

Let us define the constitutive formulation for the MRE within a thermodynamic consistent framework deriving the stress and magnetic components from a total energetic potential as

$$\Psi\left(\mathbf{F},\mathbb{H}\right)=\Psi_{\text{mech}}\left(\mathbf{F}\right)+\Psi_{\text{maxw}}\left(\mathbf{F},\mathbb{H}\right)+\Psi_{\text{mag}}\left(\mathbf{F},\mathbb{H}\right), \tag{4.45}$$

where Ψ_{mech}, Ψ_{maxw} and Ψ_{mag} are, respectively, the mechanical (Gent model formulation), the Maxwell and the magnetization energetic contributions, defined as

$$\Psi_{\text{mech}}\left(\mathbf{F}\right)=-\frac{GJ_{\text{m}}}{2}\ln\left(1-\frac{\text{tr}\left(\mathbf{F}^{\text{T}}\cdot\mathbf{F}\right)-3}{J_{\text{m}}}\right), \tag{4.46}$$

$$\Psi_{\text{maxw}}\left(\mathbf{F},\mathbb{H}\right)=-\frac{\mu_0}{2}I_5, \tag{4.47}$$

$$\Psi_{\text{mag}}\left(\mathbf{F},\mathbb{H}\right)=-\mu_0\left[\frac{m_{\text{s}}^2}{\chi_{\text{e}}}\ln\left(\cosh\left[\frac{\chi_{\text{e}}}{m_{\text{s}}}\sqrt{I_5}\right]\right)\right], \tag{4.48}$$

where G, m_{s} and χ_{e} are the shear modulus, the magnetic saturation, and the magnetic susceptibility of the MRE, respectively. Moreover, the parameter J_{m} defines a stretching threshold associated with the extensibility limit of the material and the invariant $I_5=\left[\mathbf{F}^{-\text{T}}\cdot\mathbb{H}\right]\cdot\left[\mathbf{F}^{-\text{T}}\cdot\mathbb{H}\right]$.

Similarly to the calculation of the stress tensors from thermodynamic principles in hyperelasticity, the mechanical and magnetic constitutive equations can be derived from the total energy potential as

$$\begin{aligned}\mathbf{P}\left(\mathbf{F},\mathbb{H},p\right)&=\frac{\partial\Psi\left(\mathbf{F},\mathbb{H}\right)}{\partial\mathbf{F}}-p\mathbf{F}^{-\text{T}}=\\&=\frac{G\,J_{\text{m}}}{J_{\text{m}}-\text{tr}\left(\mathbf{F}^{\text{T}}\cdot\mathbf{F}\right)+3}\mathbf{F}-p\mathbf{F}^{-\text{T}}-\frac{\mu_0}{2}\frac{\partial I_5}{\partial\mathbf{F}}-\mu_0\frac{m_{\text{s}}}{2\sqrt{I_5}}\tanh\left(\frac{\chi_{\text{e}}}{m_{\text{s}}}\sqrt{I_5}\right)\frac{\partial I_5}{\partial\mathbf{F}},\end{aligned} \tag{4.49}$$

and

$$\mathbb{B}\left(\mathbf{F},\mathbb{H}\right)=-\frac{\partial\Psi\left(\mathbf{F},\mathbb{H}\right)}{\partial\mathbb{H}}=\mu_0\left[1+\frac{m_{\text{s}}}{\sqrt{I_5}}\tanh\left(\frac{\chi_{\text{e}}}{m_{\text{s}}}\sqrt{I_5}\right)\right]\mathbf{F}^{-1}\cdot\left[\mathbf{F}^{-\text{T}}\cdot\mathbb{H}\right], \tag{4.50}$$

with $\frac{\partial I_5}{\partial\mathbf{F}}=-2\ \left[\mathbf{F}^{-\text{T}}\cdot\mathbb{H}\right]\otimes\left[\left[\mathbb{H}\cdot\mathbf{F}^{-1}\right]\cdot\mathbf{F}^{-\text{T}}\right]$.

Remark. A Lagrange multiplier (p) appears in the definition of the stress to impose incompressibility condition within the MRE. It is worth mentioning that the magnetic problem allows to take any magnetic variable as the independent one. Namely, the choice will be determined by the specific application. These constitutive equations, along with the corresponding governing equations, provide the computational framework for the magneto-mechanical problem.

The main governing equations are the mechanical balance and the magnetostatics Maxwell's equations, i.e., Equations 4.7 and 4.8.

4.2.2 Phase-field model for hMREs undergoing fracture

The deformation of the ultra-soft, i.e., brain-like stiffness, hMRE is formulated in a finite strain framework. The displacement field, i.e., unknown field of the mechanical problem, is $\mathbf{u} = \boldsymbol{\varphi}(\mathbf{X}) - \mathbf{X}$. Let us define the deformation gradient as

$$\mathbf{F} = \boldsymbol{\nabla}_0 \boldsymbol{\varphi} = \boldsymbol{\nabla}_0 \mathbf{u} + \mathbf{I}, \tag{4.51}$$

where $\boldsymbol{\nabla}_0$ is the gradient with respect to the material configuration and $\mathbf{I}$ the second-order identity tensor.

The magnetic problem is formulated on a primary scalar potential field ϕ. The magnetic field vector $\mathbb{H}$ is defined as

$$\mathbb{H} = -\boldsymbol{\nabla}_0 \phi = \mathbb{H}_\mathrm{e} + \mathbb{H}_\mathrm{r}. \tag{4.52}$$

The magnetic field is split into an energetic contribution $\mathbb{H}_\mathrm{e}$ due to the magnetic susceptibility of the medium and a remanent contribution $\mathbb{H}_\mathrm{r}$ related to the permanent magnetization of the hMRE [164]. The last one is prescribed as a constant vector to capture the permanent magnetization of the medium, as done in the microstructural formulation for hMREs in Section 4.1.2.

Finally, the damage field d is a scalar order parameter that describes whether a continuum point is damaged or not. This non-local strategy allows to model crack growth and the consequent degradation of the properties in damaged areas. As reported by Kumar and co-authors [313], compressibility of the medium is paramount to avoid non physical behavior. A non-local field equation governs the evolution of damage. To this end, the crack surface energy is regularized and transformed to a volumetric energy. Thereby, let us define the continuous crack surface density function per unit volume according to Ambrosio et al. [314] as

$$\gamma(d, \boldsymbol{\nabla} d) = \frac{3}{8}\left[\frac{d}{l} + l|\boldsymbol{\nabla} d|^2\right], \tag{4.53}$$

with $\boldsymbol{\nabla} = \boldsymbol{\nabla}_0 \cdot \mathbf{F}^{-1}$ the gradient with respect to the spatial configuration and l the length scale parameter. Note that Equation 4.53 considers d as alternative to d^2 as often used alternatively.[15]

Furthermore, $g_1(d)$ is a degradation function

$$g_1(d) = [1 - d]^2. \tag{4.54}$$

Remark. The second order expression in Equation 4.54 for the degradation function is a free constitutive choice. Alternative mathematical functions could also be implemented and tested.

[15] There exist two common options for the definition of the crack surface density function [314–321], i.e., AT1: $\gamma(d, \boldsymbol{\nabla} d) = \frac{3}{8}\left[\frac{d}{l} + l|\boldsymbol{\nabla} d|^2\right]$ and AT2: $\gamma(d, \boldsymbol{\nabla} d) = \frac{1}{2}\left[\frac{d^2}{l} + l|\boldsymbol{\nabla} d|^2\right]$. Throughout this thesis we focus on the AT1 model.

The constitutive formulation is based on an additive decomposition of the total energy density into mechanical, Maxwell (i.e., magnetic vacuum), matter magnetization and magneto-mechanical coupling contributions as

$$\Psi\left(\mathbf{F},\mathbb{H}\right)=g_2\left(d\right)\Psi_{\text{mech}}\left(\mathbf{F}\right)+\Psi_{\text{maxw}}\left(\mathbf{F},\mathbb{H}\right)+g_1\left(d\right)\Psi_{\text{mag}}\left(\mathbf{F},\mathbb{H}\right)+g_1\left(d\right)\Psi_{\text{coup}}\left(\mathbf{F},\mathbb{H}\right). \quad (4.55)$$

The degradation of all the components except for the Maxwell one guarantees the continuity of the magnetic problem as fully damaged domains are treated as air (i.e., vacuum magnetic properties). Note that $g_2\left(d\right)=\left[\left[1-d\right]^2+k\right]$ is a second degradation function, which is essentially the same as $g_1\left(d\right)$, but incorporates a parameter $k=1\cdot10^{-3}$ to introduce a residual mechanical stiffness on damaged areas and ensure numerical convergence [322].

Let us pose a total rate potential functional of the solid as

$$\dot{\Pi}=\dot{\Pi}_{\text{int}}+\dot{D}_{\text{crack}}+\dot{D}_{\text{crack,visc}}-\dot{\Pi}_{\text{ext}}. \quad (4.56)$$

Therein, the internal power is

$$\dot{\Pi}_{\text{int}}=\int_{\Omega_0}\left[\partial_{\mathbf{F}}\Psi:\dot{\mathbf{F}}+\partial_{\mathbb{H}}\Psi\cdot\dot{\mathbb{H}}+\Psi_{\text{mat}}\partial_d\, g_1\dot{d}\right]\mathrm{d}V, \quad (4.57)$$

with $\Psi_{\text{mat}}=\Psi_{\text{mech}}+\Psi_{\text{mag}}+\Psi_{\text{coup}}$ the material energy density.

The dissipation rate potential functional due to crack formation $\dot{D}_{\text{crack}}$ is

$$\dot{D}_{\text{crack}}=\int_{\Omega}G_{\text{c}}\dot{\gamma}\,\mathrm{d}V=\int_{\Omega}\frac{3G_{\text{c}}}{8}\left[\frac{\dot{d}}{l}+2l\boldsymbol{\nabla}d\boldsymbol{\nabla}\dot{d}\right]\mathrm{d}V, \quad (4.58)$$

the rate-dependent crack growth dissipation potential $\dot{D}_{\text{crack,visc}}$ is as in [323, 324]

$$\dot{D}_{\text{crack,visc}}=\int_{\Omega}\frac{\eta}{2}\dot{d}^2\,\mathrm{d}V, \quad (4.59)$$

and the external power $\dot{\Pi}_{\text{ext}}$ reads

$$\dot{\Pi}_{\text{ext}}=\int_{\Omega_0}\mathbf{b}_0\cdot\dot{\mathbf{u}}\,\mathrm{d}V+\int_{\partial\Omega_0}\mathbf{t}_0\cdot\dot{\mathbf{u}}\,\mathrm{d}A, \quad (4.60)$$

with $\mathbf{b}_0$ and $\mathbf{t}_0$ the body and traction force vectors, respectively, in the material configuration.

The fracture parameters are the critical energy release rate G_c and the length scale parameter l. In addition, the viscosity parameter η allows the rate dependent formation of cracks. In this work, it is used as a numerical viscous regularization to improve the robustness of the numerical results.

From the rate potential, an incremental potential can be integrated as

$$\Pi=\int_{t}^{t+\Delta t}\dot{\Pi}\,\mathrm{d}t. \quad (4.61)$$

The optimization of the potential[16] in Equation 4.61 with respect to d, or alternatively the variation of the rate potential in Equation 4.56 with respect to $\dot{d}$, yields the local phase-field equation. Recent works have studied the implications of pre-existing flaws and material strength [317, 325]. To reconcile crack nucleation with the current approaches and keep the characteristic length l as a regularization parameter independent of the strength, an amended form of the phase-field equation incorporates an additional configurational force c_{e}. It reads as

$$\frac{\partial \overline{\Pi}}{\partial d} = \frac{3G_c}{8}\left[\frac{1}{l} - 2l\boldsymbol{\nabla}^2 d\right] + g_1'(d)\,\Psi^+_{\mathrm{mat}} + \eta\dot{d} + c_{\mathrm{e}} = 0, \tag{4.62}$$

where $g_1'(d)$ is the derivative with respect to the damage field. The thermodynamic consistency of the model is guaranteed when the viscous resistance term $\eta\dot{d} \geq 0$, i.e., $\dot{d} \geq 0$ and $\eta \geq 0$.

Let us include the configurational external force c_{e} following [317, 325] to include the hydrostatic strength of the material. It reads as

$$c_{\mathrm{e}} = -\left[1-d\right]\frac{3^{5/4}G_{\mathrm{c}}\kappa}{2l\sigma_{\mathrm{hs}}}\frac{\mathrm{tr}\left(\mathbf{H}\right)}{\left[3+\mathbf{H}:\mathbf{H}\right]^{5/4}}, \tag{4.63}$$

with $\mathbf{H} = \mathbf{F} - \mathbf{I}$, κ the bulk modulus and $\sigma_{\mathrm{hs}} = \frac{1}{3}\mathrm{tr}\left(\boldsymbol{\sigma}_{\mathrm{s}}\right) = 0.065$ MPa the spherical critical stress, determined from a tensile test to rupture of a bulk (i.e., uncut) hMRE sample (see Figure A.9).

In Equation 4.62 the positive energy density Ψ^+_{mat} is defined with the magnetic contribution that induces the expansion of the medium as

$$\Psi^+_{\mathrm{mat}} = \begin{cases} \Psi_{\mathrm{mech}}, & \text{if} \quad \alpha \geq 0 \\ \Psi_{\mathrm{mech}} + \Psi_{\mathrm{mag}} + \Psi_{\mathrm{coup}}, & \text{if} \quad \alpha < 0 \end{cases}, \tag{4.64}$$

where $\alpha = \frac{1}{3}\mathrm{tr}\left(\boldsymbol{\sigma}_{\mathrm{mag}} + \boldsymbol{\sigma}_{\mathrm{coup}} + \boldsymbol{\sigma}_{\mathrm{maxw}}\right)$ is the spherical component of the magnetic Cauchy stress tensor. Figure 5.14 shows the α field for different stages along the propagation of the crack.

Remark. Equation 4.64 is necessary since expansive magnetic volumetric contributions lead to mechanical compression of the hMRE. Therefore, only compressive contributions should favor material damage.

Moreover, to include the constraint $0 \leq d \leq 1$, penalty energy functions are included to the potential energy as

$$\Pi_{\mathrm{penalty}} = \begin{cases} 10^4 G_c d^2, & \text{if} \quad d < 0 \\ 10^4 G_c \left[d-1\right]^2, & \text{if} \quad d > 1 \end{cases}. \tag{4.65}$$

[16] Without loss of consistency, the governing equation for the phase-field problem derives from an amended internal potential $\overline{\Pi}_{\mathrm{int}}$. This potential differs from Π_{int} in the effective energetic material contribution. In this regard, the framework requires the definition of an amended material energy Ψ^+_{mat} since expansive magnetic volumetric contributions lead to mechanical compression of the MRE. Therefore, only compressive contributions should favor material damage.

The optimization of Equation 4.61 with respect to the primary field $\mathbf{u}$ and in the absence of body forces yields the mechanical field equation

$$\frac{\partial \Pi}{\partial \mathbf{u}} = \boldsymbol{\nabla}_0 \cdot \mathbf{P} = \mathbf{0}. \tag{4.66}$$

Finally, the optimization of the potential in Equation 4.61 with respect to the primary field ϕ yields the magnetic field equation, i.e., Maxwell's equation for the magnetic induction

$$\frac{\partial \Pi}{\partial \phi} = -\boldsymbol{\nabla}_0 \cdot \mathbb{B} = 0. \tag{4.67}$$

The magnetic induction $\mathbb{B}$, magnetic field $\mathbb{H}$ and magnetization $\mathbb{M}$, satisfy the following standard constitutive relation

$$\mathbb{B} = J\mu_0 \mathbf{C}^{-1} \left[\mathbb{H} + \mathbb{M}\right], \tag{4.68}$$

with $\mathbf{C} = \mathbf{F}^{\mathrm{T}} \cdot \mathbf{F}$ the right Cauchy-Green deformation tensor, μ_0 the magnetic permeability of vacuum and $J = \det(\mathbf{F})$ the Jacobian of the deformation gradient.

The constitutive formulation is based on the additive decomposition of the total energy density in Equation 4.55. The mechanical contribution consists in two parts: isochoric and volumetric energy densities $\Psi_{\mathrm{mech,iso}}$ and $\Psi_{\mathrm{mech,vol}}$, respectively. For the isochoric one, let us choose the Generalized neo-Hookean (GNH)

$$\Psi_{\mathrm{mech,iso}}(\mathbf{F}) = \frac{G}{2b}\left[\left[1 + \frac{b}{n}\left[I_1 - 3\right]\right]^n - 1\right], \tag{4.69}$$

with $I_1 = \mathrm{tr}\left(\mathbf{F} \cdot \mathbf{F}^{\mathrm{T}}\right)$ and G the small strain shear modulus of the considered phase, and b and n material parameters.

The volumetric contribution is taken from [324] as

$$\Psi_{\mathrm{mech,vol}}(\mathbf{F}) = \frac{G}{\beta}\left[J^{-\beta} - 1\right], \tag{4.70}$$

with $\beta = \frac{2\nu}{1-2\nu}$ and ν the Poisson's ratio. To allow for larger deformation of the damaged material, the framework adopts an approach similar to the one reported by Li et al. [326] where the bulk modulus is degraded faster than the shear modulus. In this way, ν depends on the damage variable according to $\nu(d) = \left[1 - d^2\right]\nu_1 + \left[1 - \left[1 - d\right]^2\right]\nu_2$, with ν_1 the material Poisson's ratio and $\nu_2 = 0.2\,\nu_1$ a degraded Poisson's ratio.

The magnetic Maxwell energy describes the background magnetic energy due to the non-zero magnetic permeability of the vacuum as

$$\Psi_{\mathrm{maxw}}(\mathbf{F}, \mathbb{H}) = -\frac{\mu_0}{2} J I_5^{\mathrm{e}}, \tag{4.71}$$

with the energetic magnetic invariant $I_5^{\mathrm{e}} = \left[\mathbf{F}^{-\mathrm{T}} \cdot \mathbb{H}\right] \cdot \left[\mathbf{F}^{-\mathrm{T}} \cdot \mathbb{H}\right]$.

Let us additively decompose the magnetic contribution into an energetic term $\Psi_{\mathrm{mag,e}}$ and a remanent contribution $\Psi_{\mathrm{mag,r}}$ as

$$\Psi_{\mathrm{mag}}(\mathbf{F}, \mathbb{H}) = \Psi_{\mathrm{mag,e}} + \Psi_{\mathrm{mag,r}} = -\frac{\mu_0}{2} J \chi_{\mathrm{e}} I_5^{\mathrm{e}} + \mu_0 J\left[1 + \chi_{\mathrm{e}}\right] I_5^{\mathrm{er}} + \frac{\mu_0}{2\chi_{\mathrm{r}}} J I_5^{\mathrm{r}}, \tag{4.72}$$

where χ_e and χ_r are the energetic and remanent magnetic susceptibility, respectively, as in [164]. In the simulations, the remanent magnetic field is assumed to be constant. Therefore, the parameter χ_r does not affect the results.

The invariant $I_5^{er} = \mathbb{h} \cdot \mathbb{h}_r = \mathbb{H} \cdot \mathbf{C}^{-1/2} \cdot \mathbb{H}_r$ is uncoupled to the displacement field and accounts for the energetic and remanent magnetic fields in the Eulerian configuration of the medium.

An additional coupling term is included to include the effect of the microstructural attraction forces between the particles, as reported in [164]

$$\Psi_{coup} = \beta_{coup}\mu_0 J \left[[I_4^r - I_5^r] - 2\chi_e \left[I_4^{er} - I_5^{er} \right] \right], \tag{4.73}$$

with the coupled invariants $I_4^r = \mathbb{H}_r \cdot \mathbf{C} \cdot \mathbb{H}_r$ and $I_4^{er} = \mathbb{H} \cdot \mathbf{C}^{1/2} \cdot \mathbb{H}_r$, the uncoupled invariant $I_5^r = \mathbb{H}_r \cdot \mathbb{H}_r$, and the coupling parameter β_{coup}.

The total Piola stress is derived from the total energy potential in Equation 4.55 according to

$$\begin{aligned} \mathbf{P}(\mathbf{F}, \mathbb{H}) = \frac{\partial \Psi}{\partial \mathbf{F}} &= g_2 \mathbf{P}_{mech,iso} + g_2 \mathbf{P}_{mech,vol} + \mathbf{P}_{maxw} + g_1 \mathbf{P}_{mag,e} + g_1 \mathbf{P}_{mag,r} + g_1 \mathbf{P}_{coup} = \\ &= g_2 G \, \mathbf{F} \left[1 + \frac{b}{n} [I_1 - 3] \right]^{n-1} - g_2 G J^{-\beta} \mathbf{F}^{-T} - \frac{1}{2}\mu_0 J \frac{\partial I_5^e}{\partial \mathbf{F}} - g_1 \frac{1}{2}\mu_0 J \chi_e \frac{\partial I_5^e}{\partial \mathbf{F}} \\ &+ g_1 \mu_0 J [1 + \chi_e] \frac{\partial I_5^{er}}{\partial \mathbf{C}} : \frac{\partial \mathbf{C}}{\partial \mathbf{F}} + g_1 \mu_0 \beta_{coup} J \left[\mathbb{H}_r : \frac{\partial \mathbf{C}}{\partial \mathbf{F}} : \mathbb{H}_r - 2\chi_e \left[\frac{\partial I_4^{er}}{\partial \mathbf{F}} - \frac{\partial I_5^{er}}{\partial \mathbf{F}} \right] \right], \end{aligned} \tag{4.74}$$

with the derivative of the invariant I_5^e

$$\frac{\partial I_5^e}{\partial \mathbf{F}} = -2 \left[\mathbf{F}^{-T} \cdot \mathbb{H} \right] \otimes \left[\left[\mathbb{H} \cdot \mathbf{F}^{-1} \right] \cdot \mathbf{F}^{-T} \right]. \tag{4.75}$$

The derivative of I_4^{er} is taken from [164]

$$\begin{aligned} \frac{\partial I_4^{er}}{\partial \mathbf{C}} = \frac{4}{\Delta} \Big[& I_1^U \mathbf{C} \, \mathrm{sym}(\mathbb{H} \otimes \mathbb{H}_r) \, \mathbf{C} - \left(I_1^U\right)^2 \left[\mathbf{C} \, \mathrm{sym}(\mathbb{H} \otimes \mathbb{H}_r) \, \mathbf{C}^{1/2} + \mathbf{C}^{1/2} \mathrm{sym}(\mathbb{H} \otimes \mathbb{H}_r) \, \mathbf{C} \right] + \\ & \left[I_1^U I_2^U - I_3^U \right] \left[\mathbf{C} \, \mathrm{sym}(\mathbb{H} \otimes \mathbb{H}_r) + \mathrm{sym}(\mathbb{H} \otimes \mathbb{H}_r) \, \mathbf{C} \right] + \left[\left(I_1^U\right)^3 + I_3^U \right] \mathbf{C}^{1/2} \, \mathrm{sym}(\mathbb{H} \otimes \mathbb{H}_r) \, \mathbf{C}^{1/2} - \\ & \left(I_1^U\right)^2 I_2^U \left[\mathbf{C}^{1/2} \mathrm{sym}(\mathbb{H} \otimes \mathbb{H}_r) + \mathrm{sym}(\mathbb{H} \otimes \mathbb{H}_r) \, \mathbf{C}^{1/2} \right] + \\ & \left[\left(I_1^U\right)^2 I_3^U + \left[I_1^U I_2^U - I_3^U \right] I_2^U \right] \mathrm{sym}(\mathbb{H} \otimes \mathbb{H}_r) \Big], \end{aligned} \tag{4.76}$$

with $\Delta = 8 \left[I_1^U I_2^U - I_3^U \right] I_3^U$. Note that I_1^U, I_2^U and I_3^U are the three principal invariants of $\mathbf{U} = \mathbf{C}^{1/2}$.

Similarly, the derivative of I_4^{er} is

$$\begin{aligned} \frac{\partial I_5^{er}}{\partial \mathbf{C}} = -\frac{4}{\Delta} \Big[& I_1^U \mathbf{C}^{1/2} \, \mathrm{sym}(\mathbb{H} \otimes \mathbb{H}_r) \, \mathbf{C}^{1/2} - \left(I_1^U\right)^2 \left[\mathbf{C}^{1/2} \, \mathrm{sym}(\mathbb{H} \otimes \mathbb{H}_r) + \mathrm{sym}(\mathbb{H} \otimes \mathbb{H}_r) \, \mathbf{C}^{1/2} \right] + \\ & \left[I_1^U I_2^U - I_3^U \right] \left[\mathbf{C}^{1/2} \, \mathrm{sym}(\mathbb{H} \otimes \mathbb{H}_r) \, \mathbf{C}^{-1/2} + \mathbf{C}^{-1/2} \, \mathrm{sym}(\mathbb{H} \otimes \mathbb{H}_r) \, \mathbf{C}^{1/2} \right] + \left[\left(I_1^U\right)^3 + I_3^U \right] \mathrm{sym}(\mathbb{H} \otimes \mathbb{H}_r) - \\ & \left(I_1^U\right)^2 I_2^U \left[\mathrm{sym}(\mathbb{H} \otimes \mathbb{H}_r) \, \mathbf{C}^{-1/2} + \mathbf{C}^{-1/2} \, \mathrm{sym}(\mathbb{H} \otimes \mathbb{H}_r) \right] + \\ & \left[\left(I_1^U\right)^2 I_3^U + \left[I_1^U I_2^U - I_3^U \right] I_2^U \right] \mathbf{C}^{-1/2} \, \mathrm{sym}(\mathbb{H} \otimes \mathbb{H}_r) \, \mathbf{C}^{-1/2} \Big]. \end{aligned} \tag{4.77}$$

Likewise, let us obtain the magnetic induction from the energy density function through constitutive arguments as

$$\begin{aligned}\mathbb{B}\left(\mathbf{F},\mathbb{H}\right) &= -\frac{\partial\Psi}{\partial\mathbb{H}} = \mathbb{B}_{\text{maxw}} + g_1\mathbb{B}_{\text{mag,e}} + g_1\mathbb{B}_{\text{mag,r}} + g_1\mathbb{B}_{\text{coup}} = \\ &= \mu_0 J\mathbf{F}^{-1}\cdot\mathbf{F}^{-\text{T}}\cdot\mathbb{H} + g_1\mu_0 J\chi_{\text{e}}\mathbf{F}^{-1}\cdot\mathbf{F}^{-\text{T}}\cdot\mathbb{H} - g_1\mu_0 J\left[1+\chi_{\text{e}}\right]\mathbb{H}_{\text{r}}\cdot\mathbf{C}^{-1/2} \\ &- g_1 2\mu_0\beta_{\text{coup}}J\chi_{\text{e}}\left[\mathbf{C}^{-1/2}-\mathbf{C}^{1/2}\right]\cdot\mathbb{H}_{\text{r}}.\end{aligned} \tag{4.78}$$

4.3 Discussion

This chapter has provided a complete vision of the constitutive framework to be used in the present thesis. Starting with a constitutive description of the phases (matrix, soft- and hard-magnetic particles), going through a homogenization framework for extremely soft hybrid MREs and ending with two macroscopic models. The first macroscopic model is a continuum phenomenological model for sMREs to be used as smart substrates for mechanobiology studies. The second model consists in a fracture phase-field framework for hMREs.

A critical aspect of the microscopic modeling concerns the huge contrast in the mechanical stiffness between the magnetic particles and the ultra-soft matrix (81.78 GPa and 1.00 kPa, respectively). Given the viscohyperelastic nature of the soft nature, note that ongoing works consider modeling the time-dependent mechanisms [291]. In addition, the homogenization framework not only has to work across domains with stiffness that differ in several orders, but also with different magnetic behaviors. Whereas the matrix is paramagnetic ($\chi_{\text{e}} = 0$), the soft-magnetic particles have a much larger magnetic susceptibility (χ_{e}) of 30. This will lead to considerable contrasts also in the magnetic field.

On the one hand, the continuum model for the sMRE smart substrate accounts for incompressibility, macroscopic mechanical strain hardening (Gent hyperelastic model) and magnetic saturation. The model is calibrated for four mixing ratios of the matrix, i.e., four stiffness values of the matrix. The macroscopic magnetic permeability is determined from the homogenization framework, and the mechanical parameters are obtained from calibration of the hyperelastic model with the experimental data from Figure 3.14.(a-c).1. On the other hand, the model for fracture of hMREs addresses the influence of remanent magnetic fields in the propagation of cracks. Here, the Generalized neo-Hookean model allows for an accurate calibration with the experimental results. Moreover, the coupling term introduces the effect of microstructural particles interactions.

5 Applications

This chapter explores three ground-breaking applications of ultra-soft sMREs, hMREs and hybrid MREs. First, sMREs are used to design a functional substrate to stimulate biological material. Under remote actuation with permanent magnets, the surface of the substrate deforms reproducing complex strain patterns found in biological tissues. With an adequate arrangement of the magnets, the substrate is able to tune its deformation and transmit it to cell cultures attached to the surface. This enables studies on mechanobiological processes, such as traumatic brain injury and cell migration processes. Digital image correlation provides measures of the surface deformation, whereas a numerical model allows to guide the design of the stimulation framework. Second, hMREs with remanent magnetic fields are demonstrated to have superior toughness and enhanced fracture behavior. In this regard, permanently magnetized hMREs increase their fracture energy density up to a 50 % with respect to the non pre-magnetized ones, delay crack propagation and decrease stress concentration at the crack tip. Tensile tests and digital image correlation are used to study the fracture performance of pre-cut samples. Moreover, a fracture phase-field model for MREs unveils that the stress concentration at the crack is also benefited from remanent magnetic fields. Finally, hybrid MREs are proposed as an ideal material to design versatile soft actuators outdoing pure sMREs and hMREs. Such structures enhance their mechanical properties under magnetic actuation and, at the same time, they have the shape-morphing capability endemic of hMREs. Moreover, the functional behavior is enhanced due to synergistic effects from the combination of soft- and hard-magnetic particles within the same matrix. A homogenization model helps delve into such a behavior. Besides, the *in silico* design of a bimorph cantilever actuator demonstrates the potential benefits when used for smart structures, e.g., soft-robots.

5.1 Magneto-mechanical sMRE substrate to reproduce and transmit complex strain patterns to biological materials

Research efforts are dedicated to unravel the effects of mechanics in biology such as alterations in functional responses, morphological changes and the influence on migration, growth or healing processes [327–332]. However, there are still significant limitations to evaluating biomechanical effects and applying defined mechanical stimuli for quantitative

analysis. Critical limitations are related to the isolation, combination and non-invasive control of the aimed mechanical actions affecting the biological structure of interest. Current approaches are based on polymeric substrates for cell culture and the direct application of mechanical loading on them [333–337]. However, this kind of system is limited to rather simple deformation modes and rarely allows for a combination of them (neither sequentially nor simultaneously). This limitation hinders the analysis and deep understanding of mechanical scenarios where complex deformation states evolve over time. See relevant physiological scenarios in the literature [338–341]. Among these, closed-head impacts lead to heterogeneous strain distributions that rapidly evolve resulting in significant alterations in physiological behavior [342, 343]. Scarring processes (e.g., cardiac, glial, or dermal) inducing stiffness gradients within the tissue also lead to heterogeneous strain patterns resulting in temporal-varying interaction forces between the extracellular matrix (ECM) and the cellular systems [344, 345]. Moreover, other relevant biological processes such as neural crest cell migration during development are also highly influenced by tissue stiffening and complex deformation modes associated with a gradual organization and enrichment of collagen fibers [346–348]. Another limitation of most of the current mechanical-stimulation systems is that they require direct (invasive) contact with the cellular substrate, hence risking to contaminate and introduce local damage to the matter.

More sophisticated solutions include photo-activation of changes in material properties [349], but are limited by the low penetration depth of visible light in the material and surrounding medium. To overcome these issues, some authors have proposed the use of magneto-responsive substrates [281, 282]. However, these approaches were limited to overall stiffness changes and the control of different deformation modes was not allowed. Uslu and co-authors have recently developed a wireless microactuator to study mechanobiology, which is based on a hydrogel substrate connected to a permanent magnet [283]. This has provided a novel in vitro system but whose mechanical stimulation is constrained to a specific deformation mode. Another recent use of magneto-mechanical coupling is the development of soft robots, driven by external magnetic fields, to interact with biological tissues [22, 350]. However, to the best of the authors' knowledge, there is no available methodology to conduct mechanobiological studies under controlled complex and time-varying deformation scenarios.

The 4D-BIOMAP project aims at changing the paradigm by developing a novel experimental-computational framework that allows for non-invasive and real-time control of complex deformation modes within the cellular substrates. The system allows for instantaneous evaluation of mechanical effects and for influencing different biological responses while recording the whole temporal event. The non-invasive stimulation is possible thanks to the ability of MREs to respond mechanically to external magnetic fields [57, 351]. This thesis provides the basis for the integration and use of ultra-soft MREs in such a novel system. Within these materials, the magnetic particles magnetize leading to internal forces in the form of particles interactions. These forces are transmitted to the elastomeric matrix causing a mechanical deformation and/or changes in the rheological properties of the MRE (i.e., stiffness). Therefore, the overall response of the MRE depends on different factors: the nature of the elastomeric matrix and magnetic particles, distribution of the particles within the matrix, mechanical boundary conditions (BCs) and external magnetic fields.

A special remark relates to the mechanical BCs, as these define the coupled response of the composite: (i) if fixed BCs are imposed, the sample does not deform but experiences internal stress. Thus, if the elastomeric matrix presents a nonlinear mechanical behavior, the result of the magnetic field application is a variation in apparent material stiffness; (ii) if free BCs are imposed, the internal stresses within the MRE due to the application of the magnetic field result in mechanical deformation (i.e., change in shape).

The stimulation framework uses the multifunctional properties of MREs to control cellular substrates' mechanical deformation (allowing for the temporal programming of complex deformation modes) in a non-invasive manner. To carry out the work, different MREs varying their stiffness and the intensity of their magneto-mechanical coupling (see the previous Section 3.2.5 for the experimental characterization of the influence of the stiffness of the matrix). Motivated on these factors, a multi-physics *in silico* framework was developed to act as guidance for the experimental stimulation setup. This provides the controlling parameters to induce desired magnetic fields on the MRE-cellular substrate, and the subsequent mechanical deformation to be transmitted to the biological matter. Then, the ability of the system to reproduce complex mechanical scenarios is demonstrated by simulating a set of local strain patterns occurring within the brain tissue during a head impact. Overall, this framework opens doors for novel stimulation capabilities of biological matter.

5.1.1 Magneto-mechanical stimulation device

A magneto-stimulation device was designed to fit in an incubator allowing for the application of magnetic fields on the MRE substrate along time.[17] The device was conceived to allow for real-time application of semi-uniform magnetic fields (reasonably uniform near the center area with magnitudes, ranging from 0 to 20 mT in vacuum and not compromising cell viability). The system is externally bounded by the incubator in the microscope. To impose the magnetic conditions, our stimulation system is comprised of four independently controllable sets of permanent magnets surrounding the sample, with two sets aligned along each axis (Figure 5.1). By moving the magnets closer or further from each other, the resulting field over the region of interest can be adjusted. The two axes lie orthogonal to control the field in each direction, with the final field obtained by superposition. The resultant mechanical deformation of the MRE substrate will be determined by the final field and macroscopic particle interactions due to the presence of the magnets, with the magnitude determined by their relative position to the MRE sample. The whole framework shown in Figure 5.1 allows to measure cellular dynamics by means of morphological changes, proliferation or migration processes, among others.

[17] The development of the stimulation device was carried out in collaboration with the members of the 4D-BIOMAP project, and its viability with living systems has been demonstrated.

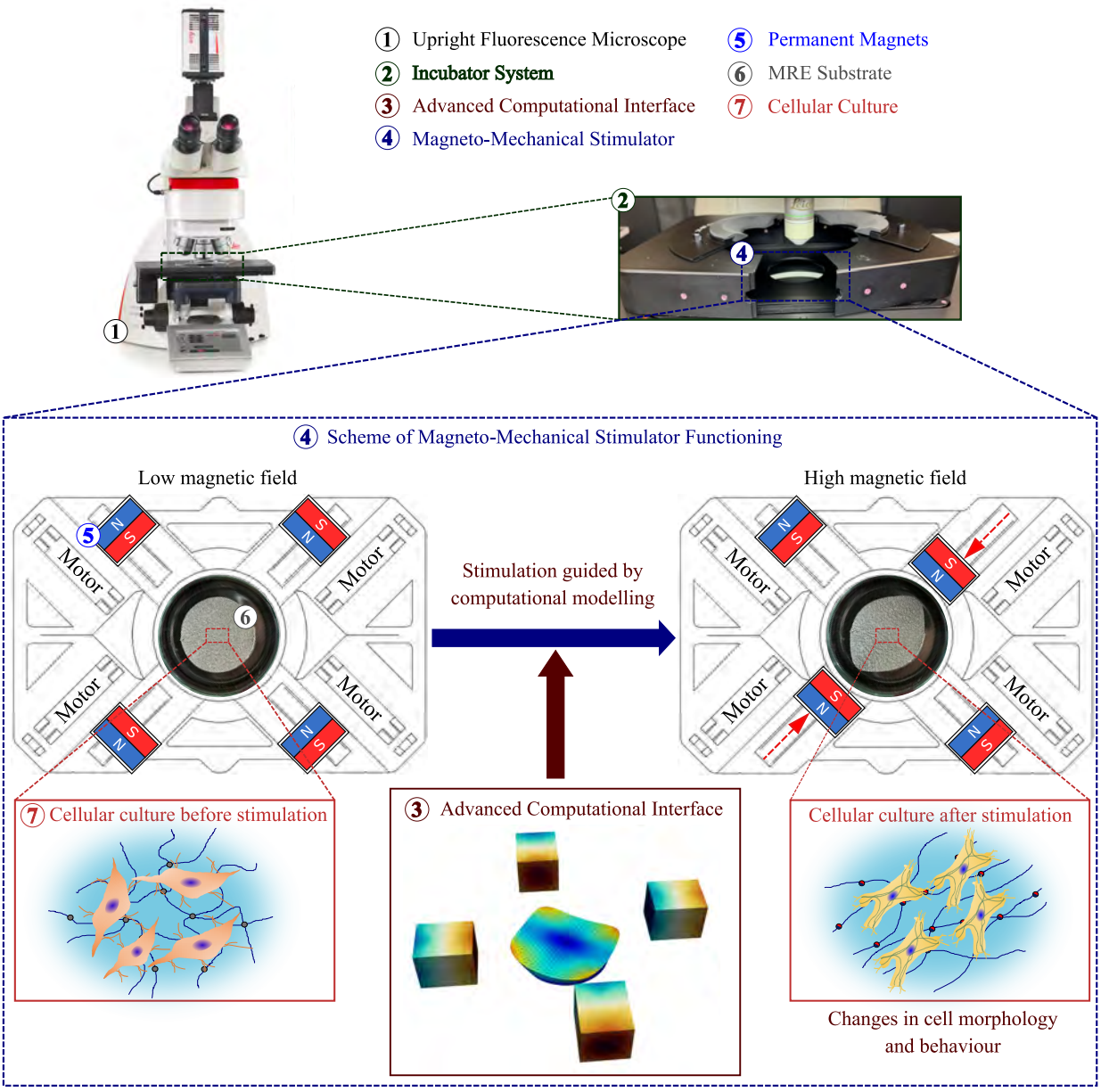

Figure 5.1: Magneto-mechanical stimulation device coupled to the multidimensional imaging system. Multidimensional imaging system LEICA LAS X with an upright fluorescence microscope (with ceramic objectives) coupled to a non-ferromagnetic incubator system. The incubator system hosts a magneto-mechanical stimulation device that actuates on a magnetorheological elastomer (MRE) sample that serves as the substrate for the cellular system. The device is equipped with permanent magnets that are moved by small motors controlled by a computational-experimental interface. Based on computational simulations, the controlling system computes the permanent magnets' relative positions to generate a given magnitude and direction of the magnetic field within the MRE. The targeted magnetic field is estimated by multi-physical computational modeling to induce deformation patterns within the MRE substrate that are transmitted to the biological system cultured.

5.1.2 Digital image correlation analysis

The upper side was treated to prepare the samples by applying a white speckle (characteristic dimension of 100 ± 50 µm) with an airbrush over the grey MRE, see Figure 3A. A CCD

camera (Alvium, Allied Vision Technologies GmbH, Germany) with a 25 mm focal length lens (Edmund Optics, Germany) was set perpendicular to the surface so that geometric distortion of the imaging system is negligible. After acquiring the images, the NCorr open-source software package, implemented in MATLAB [352], was used to compute the displacement fields and derive the Euler-Almansi strain fields. To this end, a constant subset radius of 500 µm and subset spacing of 60 µm were used. For the smoothing of the strain fields, a plane fit radius of 250 µm was chosen. The resulting fields have a resolution of 60 µm/pixel. Moreover, to cope with large displacement, the correlation algorithm updates the reference image. Moreover, the analysis was done in a backwards manner to properly deal with the discontinuity of the crack. To this end, the final deformed image was taken as the reference one, and the correlations of all the others with smaller deformation were done with respect to that one.

To correct the rigid body motion of the sample during image acquisition, a postprocessing algorithm was implemented in MATLAB. It operates directly on the displacement fields and accounts for both translational and rotational motions. Principal strain lines are numerically computed with a given point and the tangent as

$$y_{i+1} = y_i + \frac{\mathrm{d}y}{\mathrm{d}x}\mathrm{d}x, \tag{5.1}$$

$$\frac{\mathrm{d}y}{\mathrm{d}x} = -\frac{\epsilon_{\mathrm{xx}} - \epsilon_{\mathrm{yy}}}{2\epsilon_{\mathrm{xy}}} \pm \sqrt{\left[\frac{\epsilon_{\mathrm{xx}} - \epsilon_{\mathrm{yy}}}{2\epsilon_{\mathrm{xy}}}\right]^2 + 1}, \tag{5.2}$$

with an increment $\mathrm{d}x$ of 0.0001. Here, x and y refer to cartesian coordinates, subscripts refer to time points, and ϵ refers to Euler-Almansi strain components. To perform this implementation, the discrete strain field must be interpolated to any arbitrary coordinate to evaluate the tangent. The resulting curves are plotted on the Frobenius norm of the strain field.

5.1.3 FE model: Numerical details

The numerical simulations compute, in the presence of a given MRE sample, the effective magnetic field magnitude and direction depending on the position of the permanent magnets. Then, the subsequent deformation state within the MRE is estimated by multi-physical computational modeling taking as input the material substrate characteristics, according to the constitutive framework in Section 4.2.1 and the values for the parameters in Table 5.1. To this end, the simulations model the magneto-mechanical problem and replicate the experimental testing conditions of the stimulation device when actuating within the imaging system. In this regard, a finite element (FE) model considering the cylindrical MRE sample, the four permanent magnets and the surrounding air was defined. The model accounts for the magneto-mechanical coupling within the MRE due to magnetic field lines going through and for the macroscopic interactions between the MRE and the magnets. The domains representing the different phases are discretized in FE meshes of quadratic tetrahedral elements (Figure 5.2). An adaptive meshing strategy has been used to provide finer element size in the MRE sample. After spatial convergence analysis, the full mesh comprises 32 112

elements: 12 171 for the MRE, 395 for each permanent magnet and 18 361 for the surrounding air. For the incompressibility condition associated with the Lagrangian multiplier in Equation 4.49, the discretization is reduced to the points corresponding to the centers of the tetrahedral elements. The numerical implementation of the problem consists in the integration of the equilibrium equations (Equations 4.7 and 4.8) along with the penalty term for incompressibility. The problem was implemented in the python Finite Element module FEniCS by symbolically indicating the weak form of those equations. The non-linear problem was solved monolithically with a Newton-Raphson scheme.

Table 5.1: Model parameters used in the computational simulations depending on the matrix's mixing ratio. Description of the model parameters used in the macroscopic simulations to predict the magneto-mechanical response of the MREs (for 30 % particles volume ratio) when using the stimulation device. The mechanical properties are obtained from calibration of the Gent model using the uniaxial compression tests shown in Figure 3.14.(a-c).1. During the calibration, the shear moduli were found defining value-ranges around the experimental measurements obtained from the macroscopic shear tests. The macroscopic magnetic parameters are obtained from the homogenization approach using a magnetic susceptibility (χ_e) of 0 and 30 for the elastomeric and magnetic particles phases, respectively; and a magnetic saturation of $\mu_0 m_s = 2.5$ T.

	Elastomeric mixing ratio			
$\phi = 0.3$	**6:5**	**1:1**	**9:10**	**5:6**
μ [kPa]	1.1	2.9	5.0	6.5
J_m [-]	1.4	1.7	1.5	1.7
χ_e [-]	2.1	2.1	2.1	2.1
$\mu_0 m_s$ [T]	0.7	0.7	0.7	0.7

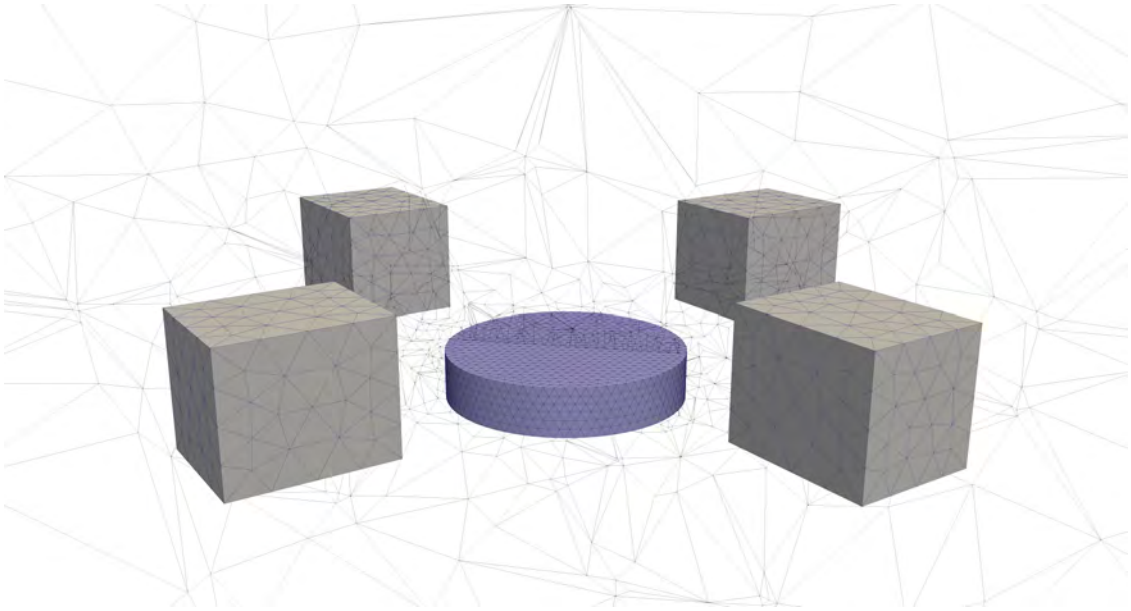

Figure 5.2: Finite element mesh of the magneto-mechanical stimulation setup used in the computational simulation. A detail of the discretized domain including the MRE substrate, the four magnets and the surrounding air. The meshing of the MRE sub-domain is refined to enhance the accuracy in the MRE substrate, whereas a courser meshing strategy is chosen for the magnets and further air. Note that to facilitate the visualization, the mesh of the air is depicted by means of a two-dimensional clip in the middle plane.

The coupled problem requires the definition of certain boundary conditions. In this regard, the permanent magnets were fixed (all mechanical degrees of freedom) in the target position according to the experimental condition simulated. In addition, the base of the MRE sample was mechanically fixed reproducing the experimental conditions, i.e., the MRE sample stuck to the Petri dish. To overcome convergence difficulties associated with the highly nonlinear nature of the coupled problem, the permanent magnetization of the magnets was imposed in the form of a temporal ramp until reaching the real value. Finally, the boundary of the air phase was also mechanically fixed. Note that the outer domain boundary is sufficiently remote from the volume occupied by the MRE and magnets such that the magnetic field perturbations caused by the latter practically vanish at the air boundary. As the Maxwell stress contribution is present in all domains, it was neglected in the implementation following previous works [61, 95, 353].

Moreover, note that permanent magnets need to be modeled in the FE model. These magnets are responsible to deform the substrate in a remote way. The constitutive law defines them as quasi-rigid solids, i.e., stiffness of $G = 1$ GPa, various orders of magnitude higher than the MRE. Their magnetic behavior is defined by a constant magnetization $\mu_0|\mathbb{M}| = 1.1$ T, equal to their residual magnetization and added to the magnetic intensity vector ($\mathbb{H}$). Note that the remanent field was calibrated from experiments using a Wuntronic, KOSHAVA5-USB Tesla/Gauss Meter. This calibration was validated by un-coupled magnetic FE modeling, simulating cases without MRE sample and comparing computational values of the field B with experimental measurements at different positions. In addition, from the magnetic field $\mathbb{H}$, the magnetic flux density vector $\mathbb{B}$ can be computed using Equation 4.6. Note that the material parameters that describe the magnetic behavior of the MRE (m_s and χ_e) correspond to homogenized variables that encompass both the elastomeric matrix and the magnetic particles. These were estimated from the homogenization approach, where only mechanical and magnetic parameters with clear physical meaning were used.[18] The mechanical parameters (G and J_m) were directly taken from experimental characterization data.

For the description of the surrounding air,[19] null magnetization $\mathbb{M}$ was defined along with vacuum magnetic permeability. The mechanical response of the surrounding air was defined as a compressible material with a very low stiffness of $G = 1$ Pa so that no mechanical constraints were imposed on the MRE sample [61, 95, 353, 354]. Note that both the air and the permanent magnets phases lack of strain hardening (i.e., $J_m = 2000$). Moreover, their magnetic susceptibility is $\chi_e = 0$. To prevent excessive element distortion of the air in the regions in contact with the MRE and enhance the convergence of the model, the auxiliary energy density approach reported by Dorn et al. [61, 166] was implemented. To this end, a weighting function was directly applied to the energy function on such sub-domain to balance

[18] The reader can consult the phases' parameters of the microscopic model in Table 5.4 in the following Section 5.3.1, where the microstructural homogenization model is thoroughly applied for hybrid MREs.

[19] Coupled magneto-mechanical BVPs require modeling the free space surrounding the magnetizable medium [61].

its stiffness. This modification is suitable when the air is modeled as a mesh that becomes coarser at larger distances from the magnetic body. A further alternative to deal with large MRE deformations would require the use of multipoint constraints or more sophisticated approaches [143, 164, 355].

5.1.4 Mechanical deformation patterns within the cellular substrate

If the device is used under free mechanical BCs, it allows to evaluate the mechanical deformation of the MRE due to the applied magnetic field. These experiments showed significant mechanical deformations within the MRE, see Figure 5.3. Digital image correlation (DIC) was used to compute local deformation values on the top MRE surface. The plots in Figure 5.4 present the magnitude of the local deformations according to the legend, and principal strain lines to indicate the effective force direction that the cells sense. In this regard, the magnetic-stimulation system can introduce deformation patterns in different directions of up to > 30 %. It must be noted that the free-deformation tests showed significant variability when exposed to high magnetic fields with maximum relative errors of 15 %. However, these errors corresponded to the peripheral regions. Within the internal region of the MRE (up to 7.5 mm radial distance from the center), the errors were below 5 %. This behavior is explained by the strong influence of the distance to the permanent magnets on the local magneto-mechanical response of the MRE (i.e., the larger the distance, the more reproducible the deformation is).

An important feature when using the magnetic stimulation device (Figure 5.1) is that the external magnetic field cannot be controlled homogeneously due to fringing effects and heterogeneous magnetic permeability, hindering the analysis of the experiments. Another issue is the nonlinear coupling between magnetic fields and mechanical deformation. A bespoke 3D finite element (FE) model was developed to help control and predict the deformation patterns transmitted to the cells during the experimental assays. The model takes the MRE material composition and geometry, as well as the position of the permanent magnets to provide: i) the spatial distribution of the magnetic fields; and ii) the resultant local deformations within the MRE. It consists of a FE model that explicitly accounts for the permanent magnets, MRE sample and surrounding air, and it couples nonlinear magnetics with nonlinear mechanics. The complete constitutive formulation and details of the integration algorithm were provided in the previous Sections 4.2.1 and 5.1.3, while a validation against experimental data by means of displacement fields at the upper MRE surface is provided in Figures 5.3B. This computational tool is essential to design experiments on biological systems.

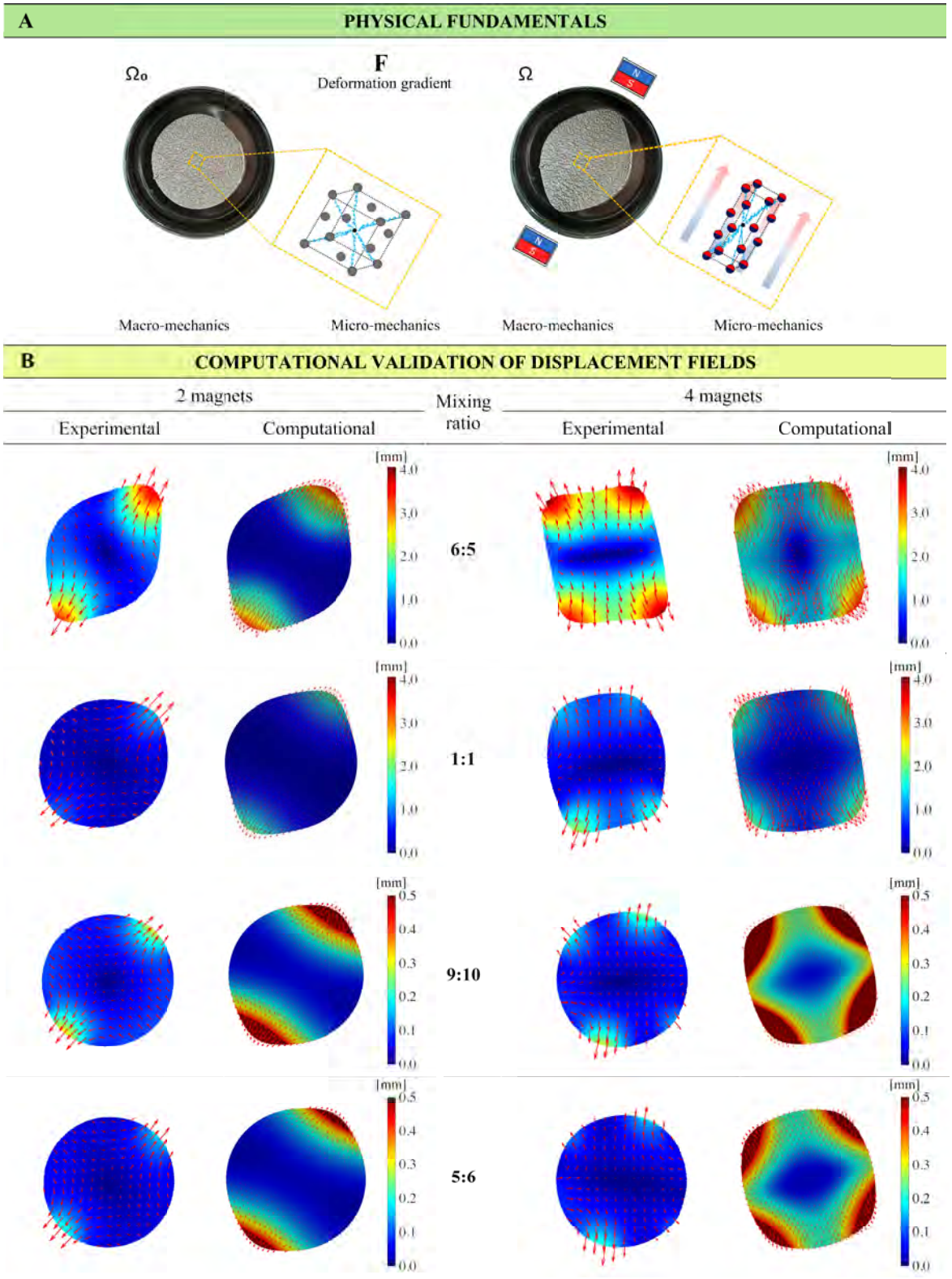

Figure 5.3: Multifunctional response and complex strain patterns of MRE samples under magnetic stimulation conditions. (A) Scheme of the micro-mechanical mechanisms and the resultant macro-mechanical deformation of the MRE samples when subjected to an external magnetic field generated by permanent magnets. (B) Comparison of experimental data and computational predictions by means of displacement fields, for two different magnetic conditions (i.e., approach of two and four magnets, see Figure 5.1) and the mixing ratios of the MRE's matrix of 6:5, 1:1, 9:10, and 5:6. Note that the position of the permanent magnets corresponds to the maximum magnetic and mechanical deformation fields that can be reached with the current system. All these experiments and computational results correspond to MREs with a particles volume fraction of 30 %.

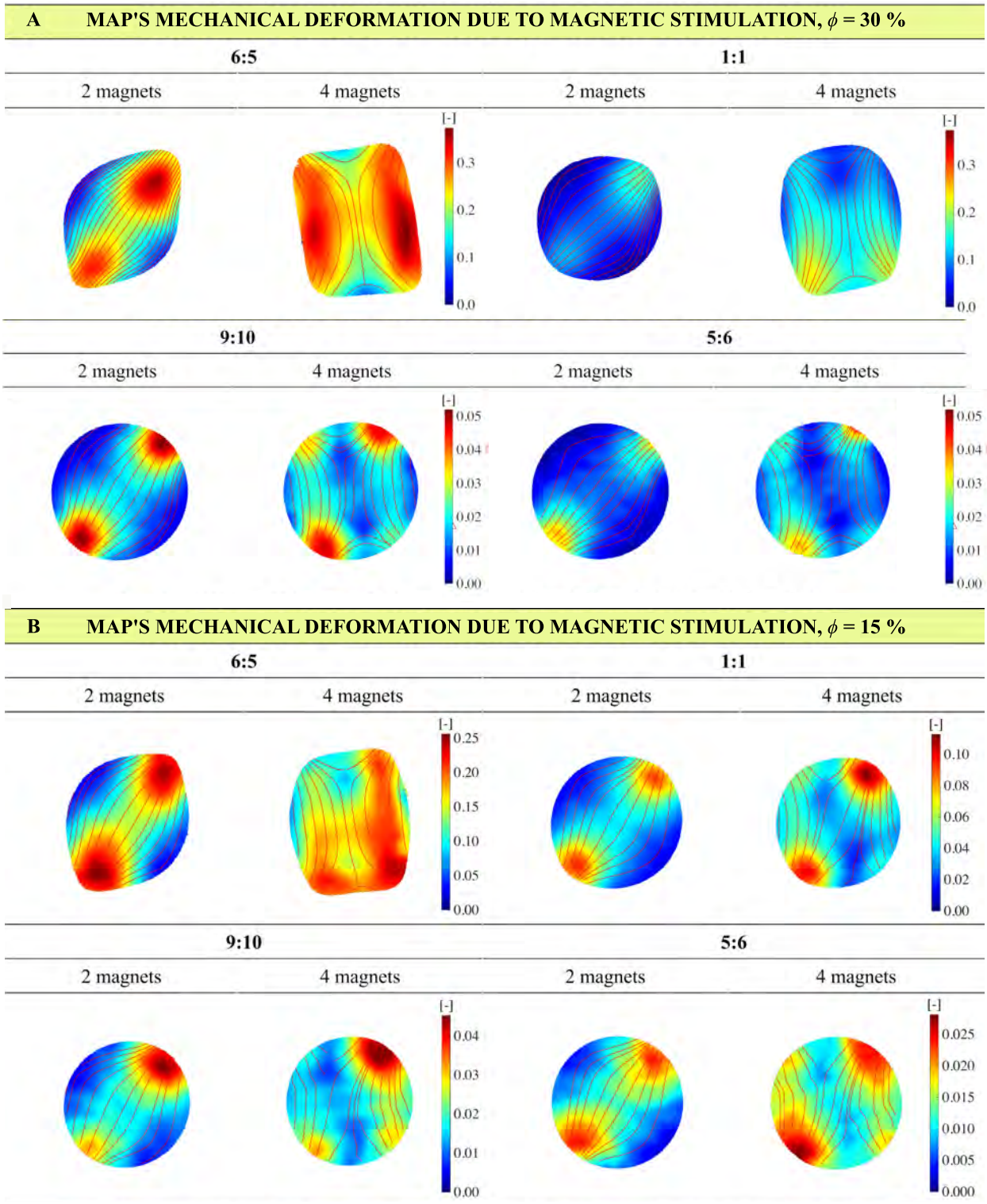

Figure 5.4: Mechanical strain fields of the (A) 30 % and (B) 15 % magnetic particles ratio MRE substrates and matrix mixing ratios of 6:5, 1:1, 9:10, and 5:6. Norm of the strain fields of the upper surface of the substrate are computed from DIC displacement fields. In addition, principal strain lines are depicted to show the force lines that the cell culture senses. The two mixing ratios of the elastomeric matrix and amount of magnetic fillers presented lead to the stiffest MRE structures. The experimental results are shown for two different magnetic conditions, i.e., approach of two and four magnets.

Considering the (microstructural and macrostructural) experimental and computational data altogether, the deformations were found to develop as stretching along the main field direction (see an illustration of the primary mechanism governing such a response in Figure 5.3A). When the permanent magnets approach the MRE, the magnetic particles start to magnetize leading to three main magneto-mechanical couplings: (i) dipole-dipole interaction between particles that result in attraction forces [170]; (ii) paramagnetic torques that lead to the formation of chain-like particles distributions and their reorientation along the external magnetic field [356]; and (iii) a strong attraction force between the particles and the magnet itself. The extremely soft nature of the elastomeric matrix facilitates the rearrangement of particles favoring the latter mechanisms and, therefore, the resulting expansion of the MRE towards the permanent magnet's location. Overall, the experimental-computational results from this section and the previous one provide the stiffness and deformation ranges that can be reached with the magnetic stimulation system as a function of the manufacturing conditions of the MRE substrate (see Table 5.2).

Table 5.2: Local mechanical deformations within the sMRE region occupied by cells when using the stimulation device. These values represent the magneto-mechanical scenarios that occur when using the developed stimulation framework during the cellular assays.

	Multifunctional response of MRE samples					
	Magnetic conditions	Particles' volume fractions	Elastomeric mixing ratio 6:5	1:1	9:10	5:6
Local deformation at MRE center [%]	2 magnets	15 %	14.3	4.0	1.7	1.2
		30 %	21.4	8.5	1.8	1.2
	4 magnets	15 %	16.4	3.4	1.4	1.1
		30 %	24.8	13.3	1.5	1.0

The results provided in Figure 3.15 (experimental chapter) unveil a promising magnetostrictive response of the MREs (i.e., mechanical deformation under an external magnetic field), but a slight increase in microstructural stiffness (i.e., stiffening of the elastomeric phase, see Sec. 3.2.6) due to low strain-hardening (low nonlinear response). Note that, for the proposed biomechanical stimulation framework, these features must be evaluated at a microscale level (i.e., cell characteristic length) [286]. To assess the micro-magnetorheological effect, the nanoindentation system was coupled to the magnetic-stimulation device depicted in Figure 5.1. This allows for measuring changes in stiffness due to the application of an external magnetic field. The nanoindentation results within the central region showed negligible stiffness changes due to the external magnetic fields (as expected owing to the low strain-hardening of the elastomeric matrix), Figure 3.16.

Finally, Figure 5.5 shows the three-dimensional deformation of the MRE sample on the computational framework. A clip allows to visualize a cross-section area of the substrate.

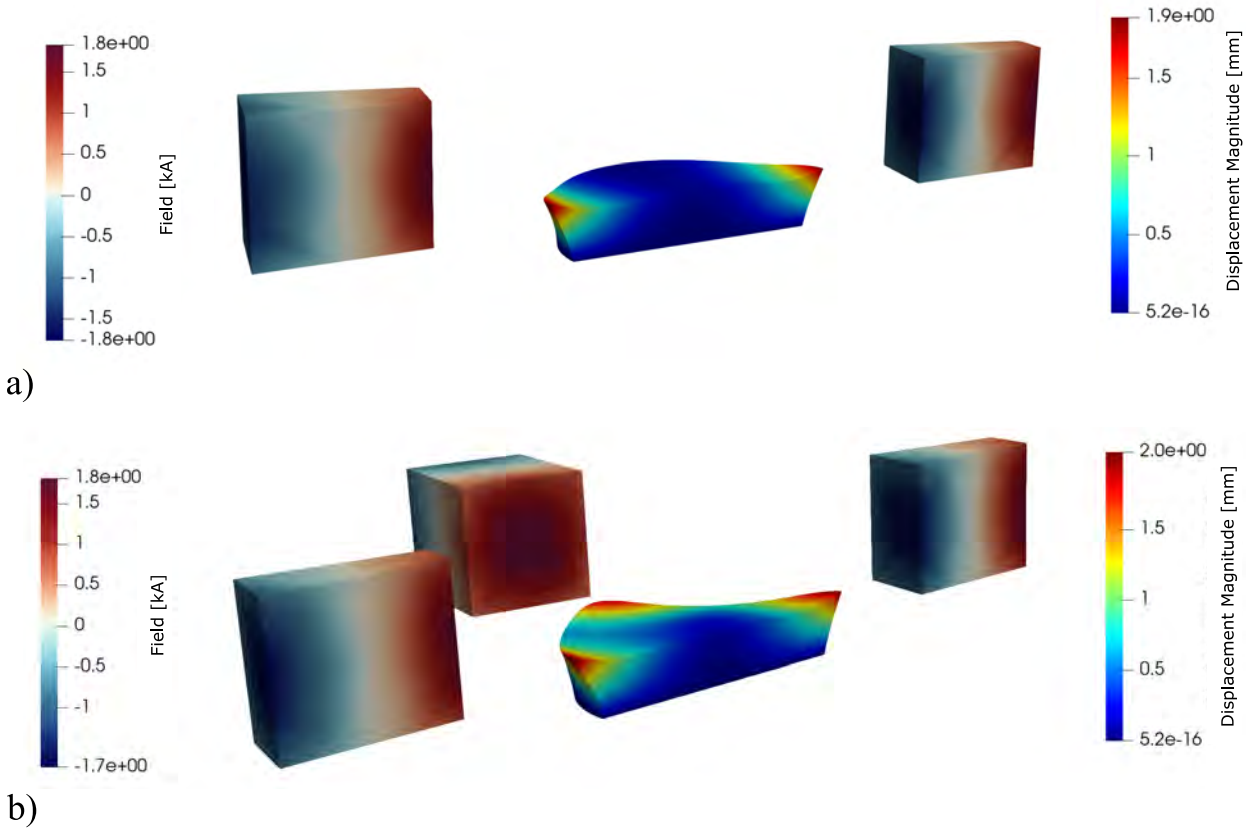

Figure 5.5: Three-dimensional numerical results of a 30 % magnetic particles ratio MRE substrate with mixing ratio 1:1, under stimulation with: (a) two permanent magnets; (b) four permanent magnets. The plots show the magnitude of the displacement fields within the MRE sample, and the scalar magnetic potential within the permanent magnets. For visualization purposes, a perpendicular clip is applied to all the domains and the free space is removed.

5.1.5 Application of the stimulation system to reproduce complex brain strain distributions from experimental data

Regarding a direct application of mechanical loads on a substrate, some authors have reported pure and simple mechanical stimulation frameworks [334, 336, 337]. Intricate physiological strain patterns, such as myocardial tissue contractions, skin Langer lines and deformations on the brain due to closed head impact, however, require novel experimental frameworks. They need not only to reproduce these patterns, but also to control and adapt them over time [330]. This section introduces a demonstration of the versatility of our system to, fed by in vivo experimental strain distributions, reproduce a real mechanical event along time.

The capability of the system to reproduce brain strain patterns during closed head impact is evaluated here. Such an event is one of the most complex mechanical scenarios as strain distributions evolve leading to complex non-symmetric strain distributions. To this end, we take the experimental results recently published by Knutsen et al. [357], where the authors presented *in vivo* mechanical deformations of the brain tissue when subjected to a head impact scenario (neck abrupt rotation). Figure 5.6.A shows different maximum

principal strain heterogeneous distributions from an axial view of the brain of a volunteer during repeatable mild head rotations. Despite being ground-breaking, the study mentioned above was limited to low strains to avoid volunteer injury. Thus, the challenge addressed here is to reproduce the complex strain distributions of a local brain region (Figure 5.6.B) while amplifying the strain magnitudes so actual injury-scenarios could be simulated in vitro, i.e., local strains above 21 %. Note that this adds complexity as it requires larger nonlinear deformation patterns [343]. Unlike already existing stimulation frameworks in the literature, our system enables reproducing dynamic heterogeneous deformation patterns on cells in a non-invasive manner. This mechanical control can be imposed on-the-fly mimicking realistic physiological and pathological processes observed in nature.

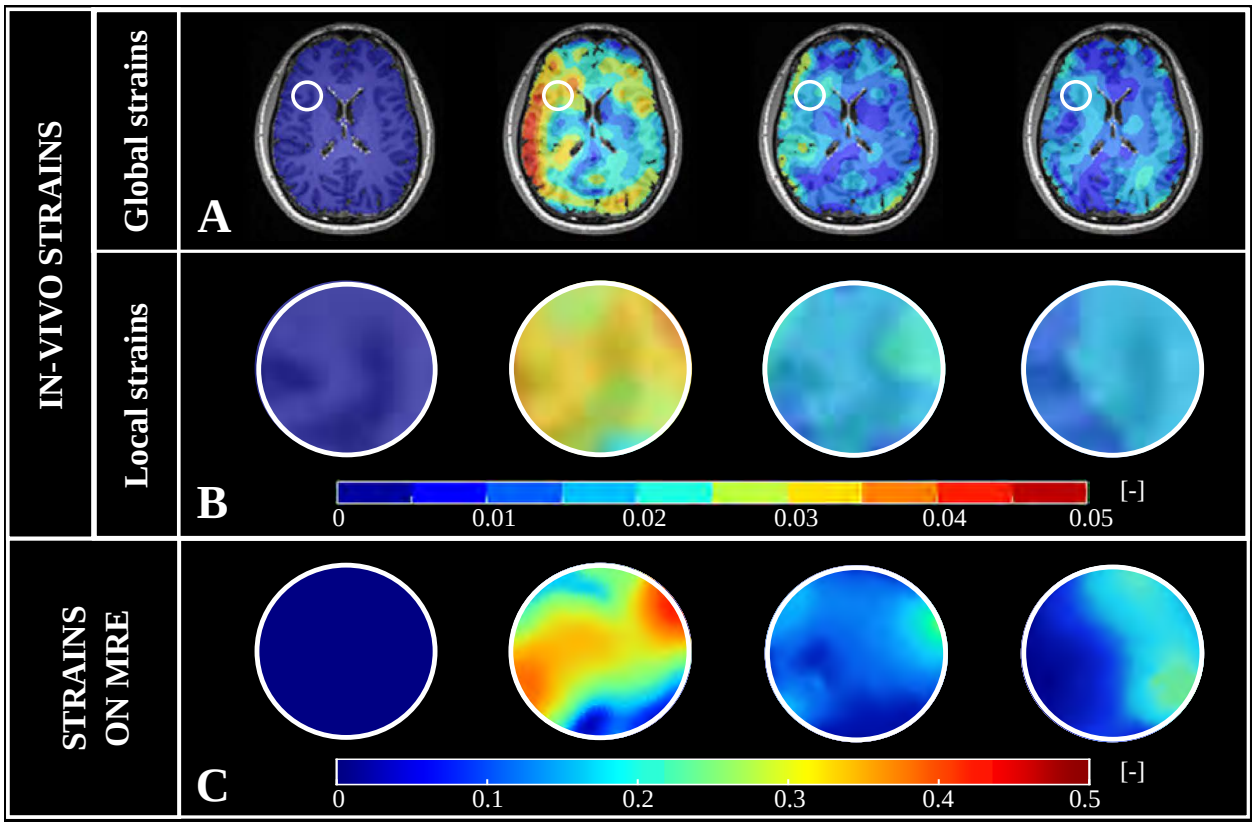

Figure 5.6: Evaluation of the versatility of the framework to simulate the complex heterogeneous strain distributions found in the brain. (A) In vivo strain distribution within an axial view of a human volunteer brain tissue subjected to an abrupt neck rotation, at different impact (deformation) stages. (B) Detail of local strain distributions of the region indicated in (A) with a white circle. The experimental data shown for (A) and (B) are taken from [357]. (C) Experimental strain distribution computed by digital image correlation and plotted on the undeformed configuration of the MRE substrates. Note that the experiments on the MREs (C) aim at reproducing the in vivo strain patterns (B) but with an amplification of ten times their magnitude to reach strain values above injury thresholds in traumatic brain injury ($\approx$ 21 %).

5.1.6 Discussion

The stimulation framework presented opens the possibility of novel *in vitro* fundamental studies to evaluate the effects of mechanics on mechanistic-mediated biological processes. The experimental system, guided by the computational framework, allows for remote modulation of complex strain conditions on the cellular substrate by applying (non-invasive) external magnetic fields. In the near future, relevant problems within the bioengineering field such as the study of scarring processes [330], wound healing [358, 359], cell polarization of immune cells [360, 361], proliferation and migration processes in cancer progression [332, 362, 363], axonal damage due to mechanical impact [328] or neural crest cell migration [328, 347], among others, may take advantage of this system. In the recent work by the authors and other members of the research group [364], the system has been applied to develop experiments with fibroblasts.

With the current solution, large deformation states can be imposed on cellular substrates of around 0.5 to 3 kPa stiffness (in terms of shear modulus). Although this stiffness range is ideal for several biological studies, softer or stiffer substrates may be needed in other scenarios. In this regard, the system allows for using magneto-active hydrogels instead of MRE if softer substrates are required [365]. Indeed, soft enough hydrogels would allow for manufacturing magneto-active substrates with low particles content allowing for the visualization of cellular systems within a confocal microscope, thus enabling the use of the stimulator system in 3D models. For the use of stiffer substrates, however, the main limitation would be the need for higher magnetic fields to reach significant mechanical deformation. This problem may be solved by opting for larger magnets or using experiment-specific designs optimizing (i.e., reducing) the size of the sample, resulting in much higher magnetic fields for the same magnets.

The main outcome of the computational model is to provide physical insights into the magneto-mechanical coupling and, more importantly, guidance during experimental designs to define the relative positions between permanent magnets and the MRE substrate leading to a specific mechanical deformation state. Within mechanical equilibrium, the model faithfully describes the magneto-mechanical coupled response but presents some deviations for the stiffer MRE substrates. This behavior is due to the smaller displacement fields reached in such conditions that lead to higher predictive errors. However, it is essential to mention that, in its current form, the model takes as inputs only material parameters with clear physical meaning and that can be controlled during the manufacturing process (note that the same model is applied for different MRE compositions). Adopting phenomenological approaches in the constitutive definition of the energy functions could improve the predictions for a specific MRE substrate. This would be an excellent approach for the use of a very specific MRE substrate. However, the aim of the proposed framework is to provide a computational tool that not only helps define the positions of the magnets to reach a given deformation for a specific MRE, but also helps at choosing the appropriate MRE composition.

5.2 Hard magnetics enable fracture-resistant MREs

The fast growing of ultra-soft polymers is accompanied with the study of their failure mechanisms. Recent applications, such as the development of skin patches based on soft polymers [366], meshes for wound closure [367] and bioadhesive skin sensors [368, 369] require understanding fracture mechanisms in soft matter to design materials with improved fracture behavior. A point of common interest concerns the strategies to enhance the fracture toughness, understood as the fracture energy density, of soft polymers [370, 371]. To accomplish this, Lin and co-authors reported chain entanglement of the polymeric matrix as a potential mechanism [372]. Moreover, time-delay in crack propagation is a factor that reduces fracture likelihood and benefits the design of such functional applications. In this regard, Li et. al [220] reported mesoscale phase contrast with tough mesophase structures to design self-healing, tough and fatigue-resistant soft materials. Strategies to modify the crack path and fiber reinforced composites have also been reported to arrest crack propagation [373, 374]. Overall, the fracture performance of multifunctional materials is determined by their constitutive behavior, which relies on an intricate coupling of several physical phenomena. For the case of hMREs, the structural response results from complex magneto-mechanical interactions at the microscale. Here, the interplay between the matrix and the magnetic particles affects functional material parameters, such as the macroscopic mechanical stiffness. In this respect, the advancement of MREs poses a question on whether the magnetization state may enhance the fracture behavior of soft hMREs under large deformations. To the best of the authors' knowledge, there is still no work that studies the fracture behavior of MREs, neither from the experimental nor from the computational point of view.

Although there are no studies on the fracture behavior of MREs, their passive mechanical contribution to fracture is related to the soft polymeric matrix and the effect of the fillers. In this regard, strategies to elaborate on the fracture performance of highly stretchable polymers rely on experimental and computational approaches. Experimental methods comprise peeling and tack experiments on soft adhesives and fracture mechanics tests on films, sheets or thick polymeric samples [375, 376]. While experimental tests mainly focus on a macroscopic viewpoint, *in silico* approaches provide further understanding of the underlying physics of the problem and allow for the consideration of the microstructural composition [377]. In the literature, the work by Miehe and co-authors [378] advocated a phase-field model for fracture. Kumar et al. [313] revisited the constitutive foundations accounting for crack nucleation, Loew et al. [323] conceptualized a phase-field framework to model the rate-dependent fracture of rubbers, Yu et al. [379] considered time-delayed fracture due to solvent diffusion and Li et al. [374] and Li et al. [220] elaborated on the fatigue resistance of soft elastomers and gels. Moreover, Ahmad et al. [380], Zhou et al. [381] and Chen et al. [382] studied the flaw-sensitivity of highly stretchable polymers. This study is of great importance as pre-existing flaws are an unavoidable consequence from manufacturing processes and determine the fracture performance. In addition, some authors have defined analytical expressions for the crack tip fields on highly stretchable elastomers [383, 384], which are useful for efficient analytical approaches to the deformation problem and strain concentration of soft polymers. More recently, Tan et al. [385] and Sridhar et al. [386]

developed phase-field models for multifunctional piezoelectric materials.

Here, a combination of experiments and theory helps uncover the fracture behavior of ultra-soft hMREs with remanent magnetic fields. For that, we take the ultra-soft hMREs manufactured in Section 3.3. Tensile tests are used to demonstrate, for the first time in the literature, that remanent magnetic fields increase the fracture toughness of pre-magnetized hMREs, i.e., the energy absorbed by the sample until complete rupture [381, 382]. Digital image correlation (DIC) allows to calculate the strain fields at the crack tip and estimate the J-integral according to the method previously described in Section 5.1.2. In addition, crack closure due to the magnetic field is reported as a phenomenon that delays the opening of cracks. To provide further understanding into the constitutive basis of such a behavior, this work conceptualizes for the first time a bespoke numerical phase-field framework for fracture of hMREs. The results suggest that remanent magnetic fields induce beneficial compressive stresses in the medium as they decrease the stress concentration at the crack tip. Overall, we unveil intriguing potential applications for functional actuators with enhanced fracture performance and better behavior under cyclic loading.

5.2.1 Materials and synthesis of the samples

Molds were filled with the blend (i.e., PDMS and NdFeB magnetic powder) to produce prismatic samples with 60 mm length, 10 mm width and 2 mm thickness. They were cured in the oven at 85 °C during 2 h. Hereafter, the following definition is important, i.e., virgin samples as those without remanent magnetic field and pre-magnetized samples with remanent magnetic field. For pre-magnetized samples, an impulse magnetizer (DX-MAG20C, Dexing Magnet Tech. Co, Xiamen, China) applied permanent magnetization in the longitudinal direction of the samples. The magnetizer was set at 1000 V, endowing the samples with an apparent macroscopic remanent magnetic induction of 40 mT (measured with a teslameter). Moreover, a blade was used to apply cuts on the samples of 1, 2, 3, 4, and 5 mm, which define crack-width ratios of $c/w = 0.2, 0.3, 0.4, 0.5$, with c the length of the initial crack and w the width of the sample.

5.2.2 Experimental estimation of J-integral

The J-integral is estimated from the displacement fields obtained with DIC and the analytical description of Long et al. [384] for the crack tip fields under large deformations. The analytical approach is based on the Generalized neo-Hookean model (GNH) to fit the vertical displacement fields. The parameters of the GNH model were independently calibrated from tensile tests on virgin and pre-magnetized hMRE specimens without initial cuts. For virgin and pre-magnetized samples, respectively, shear moduli G of 6.2 kPa and 11 kPa and strain-hardening exponents n of 1.18 and 1.10 were calibrated (see Figure A.9). An annular grid places the fitting points far enough from the crack tip to avoid the dissipative length scale [387], and far enough from the boundary to avoid boundary effects.

The analytical model relies on the method of asymptotic analysis and the Generalized neo-Hookean Model (GNH). Stephenson [388] established that the elastic potential near the

crack tip is governed by

$$\Psi = AI_1^n + BI_1^{n-1}, \tag{5.3}$$

with A, B and n material parameters and $I_1 = \mathrm{tr}\,(\mathbf{C})$, where $\mathbf{C} = \mathbf{F}^{\mathrm{T}} \cdot \mathbf{F}$ with $\mathbf{F}$ the deformation gradient.

Analytically, the vertical displacement field is described by

$$u_2 = ar^{1-\frac{1}{2n}} U(\theta, n), \tag{5.4}$$

with a an amplitude parameter, r the radial coordinate with respect to crack tip and $U\,(\theta, n)$ an odd function of the angular coordinate θ, defined as

$$U(\theta, n) = \sin\,(\theta/2) \sqrt{1 - \frac{2\kappa^2 \cos^2\,(\theta/2)}{1 + \omega\,(\theta, n)}} \left[\omega\,(\theta, n) + \kappa \cos\,(\theta)\right]^{\kappa/2}, \tag{5.5}$$

with

$$\kappa = 1 - \frac{1}{n}, \quad \omega\,(\theta, n) = \sqrt{1 - \kappa^2 \sin^2\,(\theta)}. \tag{5.6}$$

Finally, the amplitude parameter a, hence the displacement field u_2, is related to J according to

$$J = \frac{G\pi}{2} \left[\frac{b}{n}\right]^{n-1} \left[\frac{2n-1}{2n}\right]^{2n-1} n^{1-n} a^{2n}, \tag{5.7}$$

with G the shear modulus and b a material parameter of the GNH model. Detail on the calibration of these parameters is provided in Section A.2.3.

The fitting with the experimental and analytical displacement field is done at the i points defined by the annular grid in Figure 5.11.b.1, by taking J as unknown variable, and performing least squares fitting, according to

$$\min_{J \in \mathbb{R}^+} \sum_i^n \left[u_{2,theo}^{2n} - u_{2,exp}^{2n}\right]_i^2. \tag{5.8}$$

5.2.3 FE model: Numerical details

Here we recall the constitutive model in Section 4.2.2. The first variation of the field equations (mechanical, magnetic and damage field equations) yields the weak form of the problem, which is numerically solved in the open source finite element environment FEniCS using the NonLinearVariationalProblem library [389]. The magneto-mechanical problem and the phase-field problem are decoupled in a staggered scheme and the magneto-mechanical problem is solved monolithically. Iterations stop when the maximum difference of the fields between two consecutive iterations is smaller than a tolerance, here set to $tol_1 = 1 \cdot 10^{-2}$. This approach ensures computational efficiency and is more robust than the monolithic problem [378]. However, the staggered scheme requires small enough load steps. To decrease the calculation time, an adaptive load stepping increases and reduces the load step according to the growth of the damage variable [323]. For an increase larger than $tol_2 = 0.15$, the load increment is reduced by a factor of $1/1.2$ up to a minimum value of $\Delta_t = 1 \cdot 10^{-3}$. Otherwise, it is incremented by a factor of 1.2 up to a maximum value of $\Delta_t = 1.6 \cdot 10^{-2}$.

The finite element computation was performed on a two-dimensional mesh with 69444 triangular elements. The boundaries of the air sub-domain were mechanically fixed with null perpendicular displacements. Moreover, multipoint constraints were applied on the displacement field of the air to enhance the numerical convergence. To mimic a tensile test, the displacement of the upper and lower edges of the rectangular sample are constrained. A first stage allows for the pre-compression of the sample with the application of the remanent magnetic field. A second stage applies vertical displacements of the edges. With regard to the magnetic field, the magnetic potential was set to zero on a reference point and the background Maxwell stress contribution was subtracted from the stress as it is balanced by the stress from the surrounding air. Finally, initial damage representing the pre-existing crack is prescribed directly on the phase-field as $d = 1$. In addition, the contribution to the weak form due to the phase-field equation is restricted to the sub-domain of the hMRE. To this end, the contribution of the air is excluded from the residual and the phase-field is set to zero in the air.

The air (free space) is modeled as a compliant sub-domain that surrounds the hMRE and deforms with it [164, 166, 390]. To avoid interpenetration of the elements on the upper and lower edges of the hMRE sample, multipoint constraints prescribe the vertical displacement field on the regions of the air above and below the sample, see Figure 5.7 [165, 166]. A second-order polynomial is defined to be $u_{2,\text{hMRE}}$ (i.e., vertical displacement of the upper and lower edges of the hMRE sample) in the middle horizontal coordinate and zero on the left and right boundaries, and a first-order polynomial is defined to be $u_{2,\text{hMRE}}$ in the upper and lower edges of the hMRE sample and zero in the top and bottom boundaries.

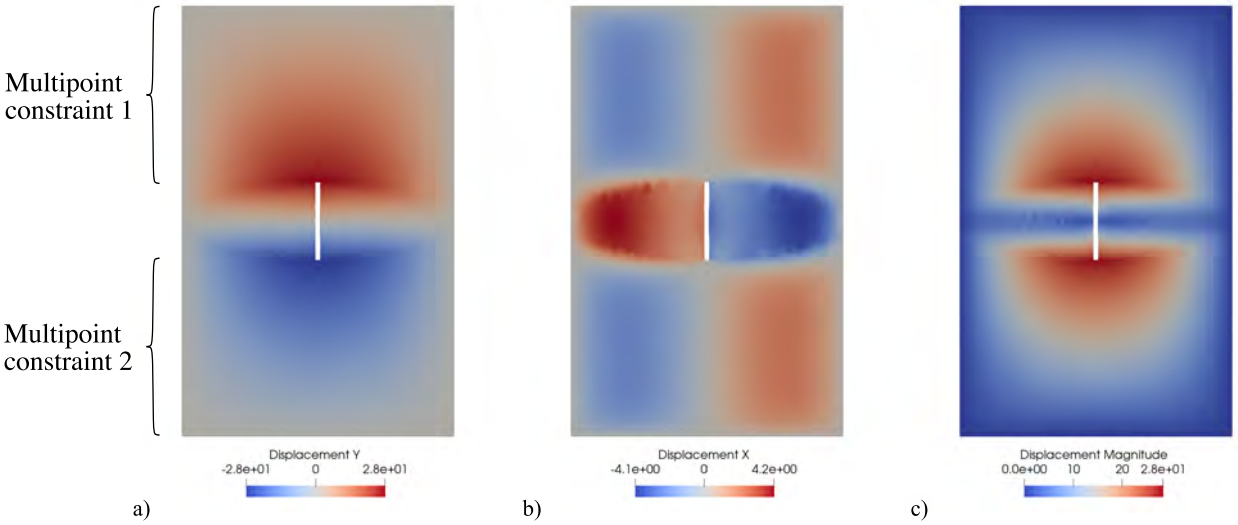

Figure 5.7: Multipoint constraints on the vertical displacement fields of the air sub-domain to improve numerical stability in the simulations for fracture of hMREs. A second-order polynomial is defined to be $u_{2,\text{hMRE}}$ in the middle horizontal coordinate and zero on the left and right boundaries, and a first-order polynomial is defined to be $u_{2,\text{hMRE}}$ in the upper and lower edges of the sample and zero in the top and bottom boundaries. (a) Vertical displacement field of the air sub-domain, (b) horizontal displacement field and (c) magnitude of the displacement field.

The parameters of the model are classified as mechanical, magnetic and fracture parameters, for both hMRE and free space (i.e., air) sub-domains. For the hMRE, the shear

modulus $G = 6.2$ kPa, the Poisson's ratio of the non-damaged hMRE $\nu_1 = 0.47$,[20] the strain hardening/softening exponent $n = 1.18$, and the correction parameter at low strain $b = 1$ (see the calibration in Section A.2.3 from tests on uncut virgin samples).[21] For the air, modeled as an extremely compliant domain [390], $G = 0.01$ kPa, $\upsilon = 0.4$, $n = 1.18$, and $b = 1$. With respect to the magnetic parameters, the experimental measure of the apparent (homogeneous) magnetic induction of a pre-magnetized hMRE with a teslameter provided a value of $\mu_0 \mathbb{H}_\mathrm{r} = 20$ mT. Besides, the coupling parameter was calibrated from the experimental results on an uncut pre-magnetized sample, whereby it was reduced to $\beta_\mathrm{coup} = 1$ to guarantee the numerical stability of the problem. Finally, the critical energy release rate $G_c = 4.9 \cdot 10^{-2}$ $\frac{\mathrm{N}}{\mathrm{mm}}$ and the length scale parameter $l = 0.1$ mm (see Figure A.10 for the experimental calibration of G_c). The latter is chosen small enough with respect to the dimensions of the sample. Furthermore, the viscosity parameter $\eta = 0.1$ allows the rate dependent formation of cracks and a numerical viscous regularization. Table 5.3 summarizes all the previous parameters.

Table 5.3: Mechanical, magnetic and fracture properties used in the phase-field model for hMREs undergoing fracture, for the hMRE and the air. Mechanical parameters: shear modulus G, Poisson's ratio of the non-damaged hMRE υ_1, strain hardening/softening exponent n_1, and correction parameter for low strain b. Magnetic parameters: remanent magnetic field $\mathbb{H}_\mathrm{r}$ and magneto-mechanical coupling parameter β_coup. Fracture parameters: critical energy release rate G_c and length scale parameter l.

Phase	**Mechanical**				**Magnetic**		**Fracture**	
	G [kPa]	υ [-]	n [-]	b [-]	$\mu_0 \mathbb{H}_\mathrm{r}$ [mT]	β_coup	G_c [N/mm]	l [mm]
hMRE	6.2	0.47	1.18	1	20	1	$4.9 \cdot 10^{-2}$	0.1
Air	0.01	0.40	1.18	1	0	0	-	-

5.2.4 Remanent magnetization enhances fracture toughness of hMREs

The constitutive behavior of MREs is highly influenced by the interaction between the magnetic particles, the soft matrix, and the external magnetic field. When MREs are manufactured with hard-magnetic particles, magneto-mechanical effects (e.g., structural stiffening) can be sustained even in the absence of magnetic fields. These premises suggest that also their fracture behavior must depend on the microstructural magneto-mechanical coupling. To delve into this, quasi-static uniaxial tensile tests were performed with a universal test-

[20] To allow for larger deformation of the damaged material, the bulk modulus is degraded faster than the shear modulus. In this way, ν depends on the damage variable according to $\nu(d) = \left[1 - d^2\right] \nu_1 + \left[1 - [1-d]^2\right] \nu_2$, with ν_1 the material Poisson's ratio and $\nu_2 = 0.2\,\nu_1$ a degraded Poisson's ratio.

[21] Note that the mechanical contribution in the numerical model is calibrated from experimental results for tensile tests on virgin samples and the magnetic fields for the pre-magnetization condition are included through a magnetic constitutive extension of the model. This differs from the material parameters used for the estimation of the J-integral, where the GNH parameters are calibrated to include the magnetorheological effect.

ing machine (Instron 34TM-5, Norwood, Massachusetts, United States) at a velocity of 0.003 mm s^{-1}. The initial separation of the grips was set at $l_0 = 30$ mm and $l_0 = 50$ mm to get results for two different sample lengths. Special grips for ultra-soft polymers with pneumatic actuation were used. The tests finish when the sample breaks and the load falls to zero. In the mean while, force-displacement data was recorded.

The force-displacement curves in Figure 5.8.a are used to calculate the fracture energy density, i.e., a measure of the fracture toughness [382], as the area under the curves divided by the volume of the samples. The results permit to compare the fracture toughness of hMREs with different cut lengths and remanent magnetic fields. For every condition, pre-magnetized hMREs are able to absorb more energy before fracture than virgin ones. For instance, the pre-magnetized sample with an initial length (l_0) of 30 mm and with a cut-width ratio (c/w) of 0.2 absorbs a 38 % more energy than the virgin counterpart. For the cut-width ratios of 0.3, 0.4, and 0.5, the increases in the energy absorbed are 46, 49, and 16 %, respectively. Moreover, the work of extension for uncut samples is 0.0551 and 0.0982 mJ mm^{-3}, respectively for virgin and pre-magnetized hMREs (see the results for the uncut case in Figure A.2.3). This gives an increase in the energy absorbed by pre-magnetized samples of 78 %. For the samples with initial length of 50 mm, the increases are 23, 51, 40, and 49 % for the same cut-width ratios. Overall, the pre-magnetized hMRE samples are tougher to fracture than virgin ones.

A further finding relates to the size of the initial cut and the stretch to failure. The larger the flaw, the smaller the displacement to failure. For the cut-width ratios of 0.2, 0.3, 0.4, and 0.5 and initial length $l_0 = 30$ mm, the displacement to failure of virgin samples is 51.9, 35.0, 34.4, and 31.4 mm, respectively. Chen and co-authors [382] elaborated on the dependency of the stretch to failure on the cut length of two stretch-stiffening highly stretchable elastomers: VHB and PU. For short cuts (i.e., below 0.1 mm length) the stretch to failure was insensitive to the length of the cut. Similarly, for long cuts (i.e., above 10 mm) it barely depended on the length. However, for intermediate lengths the dependency was maximum. Our results recover this tendency. For the largest cut ratios, the displacement to failure barely changes (35.0, 34.4, and 31.4 mm). For the smallest cut, the displacement to failure increases a 50 % (51.9 mm). Moreover, for an uncut sample, the displacement to failure increases to 100.5 mm (See Figure A.2.3). Note that the behavior for cuts smaller than 2 mm was not explored due to the large manufacturing error when applying small cuts in these sticky materials. Regarding the effect of the remanent magnetic fields, the results show that the stretch to failure barely depends on the pre-magnetization state. Just for the cut-width ratio of 0.2 there is an apparent difference, wherein the stretch to failure for the pre-magnetized sample is larger than for the virgin one. The larger manufacturing error explains such a discrepancy.

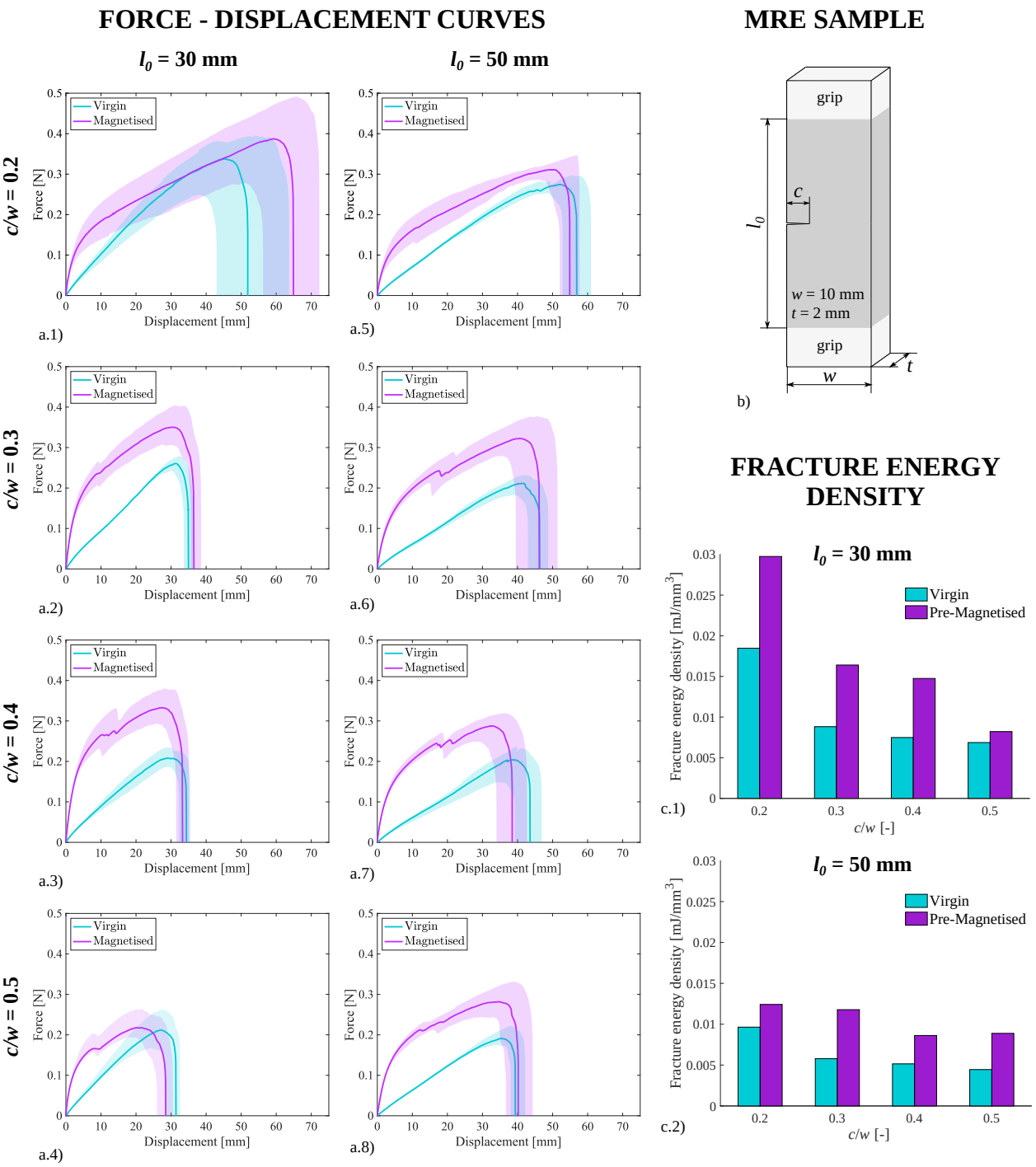

Figure 5.8: Experimental results from tensile tests to rupture on virgin and pre-magnetized hMRE samples and different pre-existing cuts. (a.1-4) Results for the force-displacement curves, cut-width ratios c/w of 0.2, 0.3, 0.4, and 0.5 and initial length of the sample of 30 mm. (a.5-8) Results for the force-displacement curves for samples with initial length of 50 mm. (b) Illustration of the geometry of the sample, dimensions and position of the grips for the experimental procedure, with l_0 the initial distance between grips, t the depth of the sample and c the length of the pre-cut. The initial crack of length c is placed at the middle of the heigh. (c.1) Barplot with the fracture energy density of virgin and pre-magnetized samples as a function of the cut length ratio for $l_0 = 30$ mm. (c.2) Barplot with the fracture energy density for $l_0 = 50$ mm.

5.2.5 Remanent magnetization delays the opening of pre-existing cracks

Pre-magnetized hMREs behave as permanent magnets from a macroscopic point of view. Consequently, the free surfaces of a crack attract each other, thus closing the discontinuity. Under tensile loading, the interface provides structural support up to a certain axial load. Eventually, the crack opens when the mechanical stress in the bulk material becomes larger than the magnetic attraction. Figure 5.9 provides pictures of the deformation process of a pre-magnetized hMRE sample during a tensile test. Three main stages characterize the process: i) the closed crack regime, ii) the crack opening phase, and iii) the eventual crack propagation. DIC on virgin and pre-magnetized samples with different pre-existing cuts, according to the method in Section 5.1.2, allows to provide a detailed study. The results consist in the surface displacement fields at the crack tip along quasi-static tensile tests.

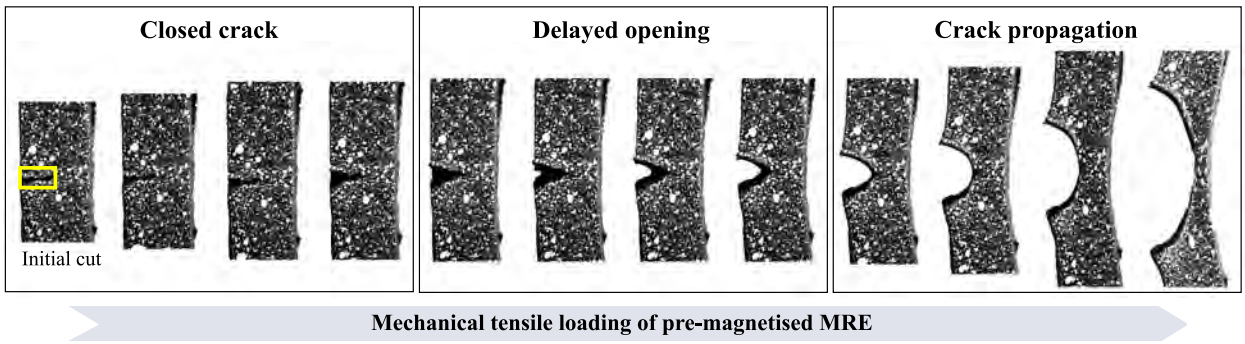

Figure 5.9: Stages along the stretching of a pre-magnetized hMRE with a 5 mm pre-existing crack: (left) closed crack, (center) delayed opening and (right) crack propagation.

For all tensile tests, two displacements are defined as control points: the first before the crack opens, i.e., “Displacement 1” of 10 mm, and the second after the opening of the crack, i.e., “Displacement 2” of 16 mm. Figure 5.11.a. illustrates the procedure and the closing mechanism. The results from the force-displacement curves in Figure 5.10.a show a drop in the force at the moment where the crack opens. In this regard, the longer the initial crack, the larger the drop in the force, with the maximum for the cut of 5 mm. Moreover, Figures 5.10.b.1-8 and 9-16 present the vertical strain fields at “Displacement 1” and “Displacement 2”, respectively. A first finding relates to the small values of the strain on the crack tip for a closed crack (Figure 5.10.b.5-8). Indeed, when the crack has not yet opened the structural behavior is close to that of a flawless sample. A second finding, after the opening of the crack (i.e., “Displacement 2”), is that strains at the crack tip are larger for pre-magnetized samples than for virgin ones, see Figure 5.10.b.13-16 and Figure 5.10.b.9-12, respectively. Although the strain fields do not provide a complete view of the constitutive behavior of the hMRE (i.e., stress response), they provide a measure of the deformation state.

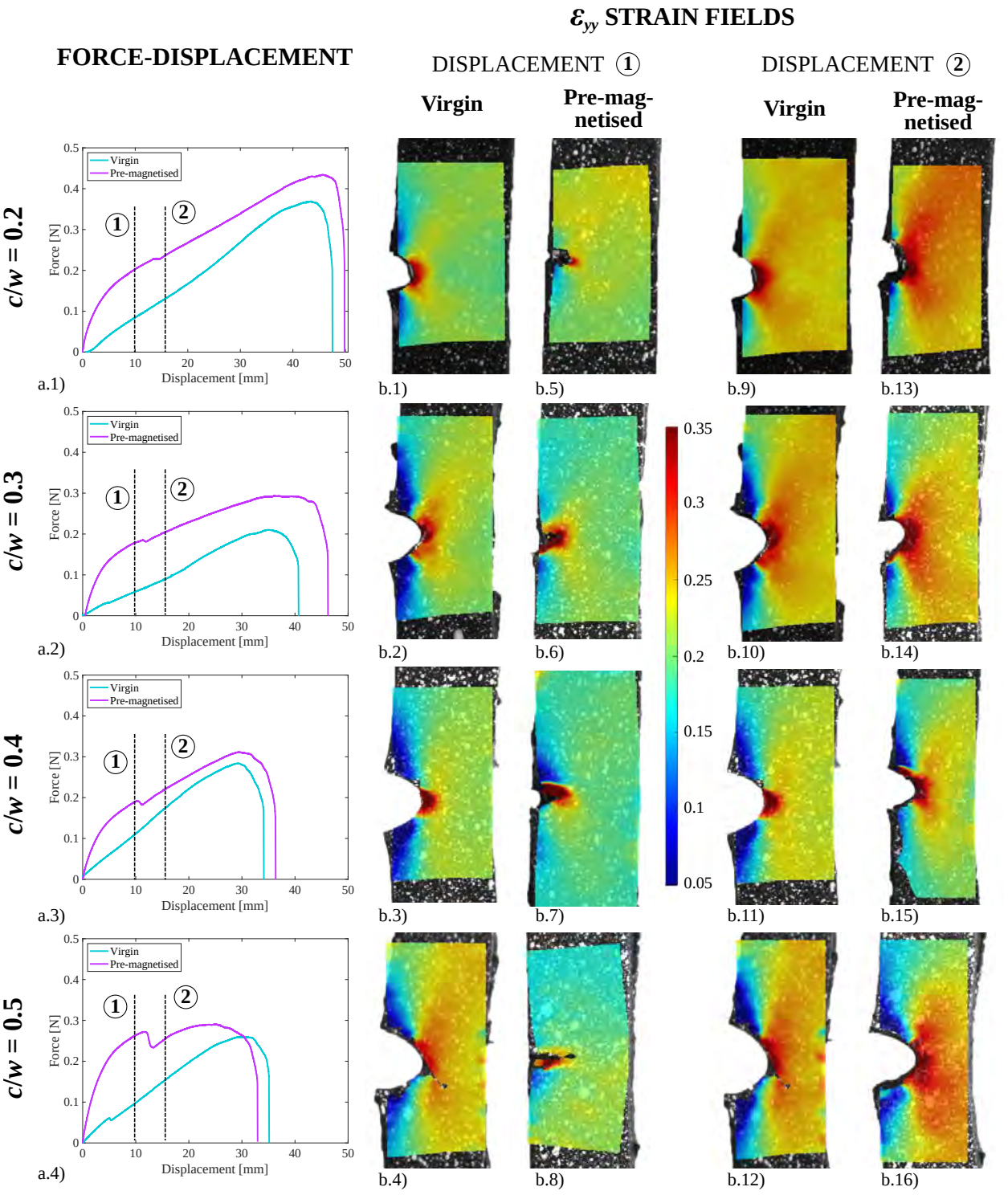

Figure 5.10: Experimental results for the surface deformation at the crack tip on virgin and pre-magnetized hMRE samples show the delay in the opening of the pre-existing crack. (a.1-4) Force-displacement curves for virgin and pre-magnetized hMREs with pre-existing cut-width ratios of 0.2, 0.3, 0.4, and 0.5. Two displacements (abscissa) are defined: "Displacement 1", equal to 10 mm, is defined for all the samples before the opening of the crack in the pre-magnetized samples; and "Displacement 2", equal to 16 mm, after the crack opening. In between these two reference displacements, and for pre-magnetized samples, the sides of the crack detach. (b.1-4) and (b.5-8) Vertical strain fields at "Displacement 1" of virgin and pre-magnetized samples, respectively. (b.9-12) and (b.13-16) Vertical strain fields at "Displacement 2" of virgin and pre-magnetized samples, respectively.

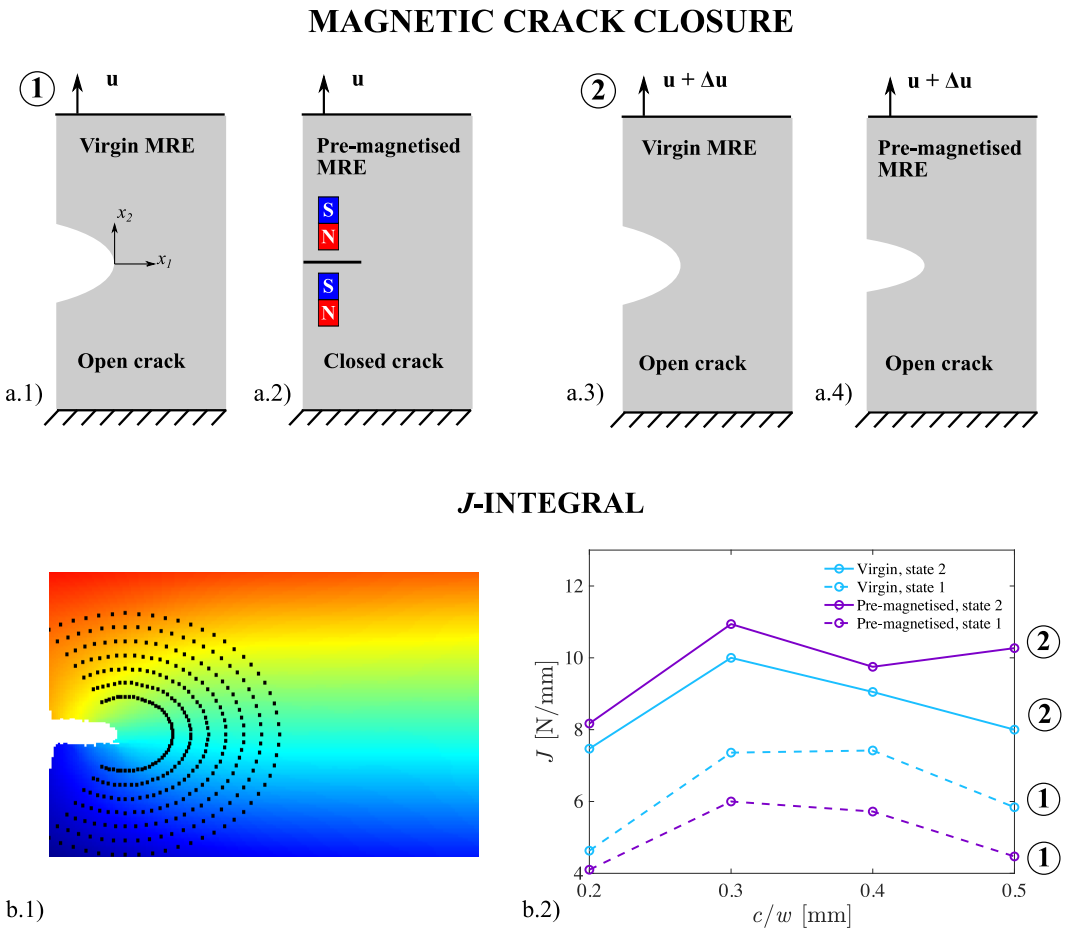

Figure 5.11: Magnetic crack closure mechanisms and estimation of the J-integral. (a.1-2) and (a.3-4) Illustration of the crack state (open/closed) of virgin and pre-magnetized state for Displacements 1 and 2, respectively. (b.1) Annular grid used for the fitting with the experimental and theoretical vertical displacement fields to estimate the J-integral. (b.2) Values of J for the virgin and pre-magnetized samples at Displacements 1 and 2 as a function of the crack-width ratio.

The J-integral provides a better quantification of the strain concentration at the crack tip. The estimation of this value is done with the analytical formulation in Section 5.2.2 for the crack tip fields under large deformations fitting the vertical displacement fields obtained with DIC. Moreover, the points used for the fitting are defined through an annular grid, see Figure 5.11.b.1. For further detail on the calibration of the model and the fitting procedure, see Section 5.2.2. In addition, Figure A.11 contains additional results for alternative annular grids. This confirms that the fitting grid does not influence the tendencies found. Figure 5.11.b.2 shows the results for all cut-width ratios, for "Displacement 1" and "Displacement 2" and for both virgin and pre-magnetized samples. A first finding relates to the crack closure phenomenon. The values of J are significantly smaller for pre-magnetized samples than for virgin hMREs at "Displacement 1". This result is explained by the crack closure due to remanent magnetic fields that provide material continuity through the crack region. The reduction is of approximately 11 %, 18 %, 23 %, and 23 % for the crack length ratios of 0.2, 0.3, 0.4, and 0.5, respectively. However, once the crack opens in the pre-magnetized hMRE, J is larger for the pre-magnetized sample than for the virgin one. It is 8.6 %, 9.4 %, 7.7 %, and 28 % larger, respectively for the crack length ratios.

An additional finding unveils that J shows a peak for cuts of intermediate lengths and, for short and long cracks, J is smaller. In other words, the shortest and longest cracks (2 mm and 5 mm, respectively) lead to smaller strain concentration at the crack tip. However, for the intermediate cut-width ratio of $c/w = 0.3$, increases between 35 % and 60 % with respect to the case for the shortest crack are shown in Figure 5.11.b.2. The smaller sensitivity of the hMRE to small flaws agrees with the work conducted by Chen and co-authors [382]. Regarding the large cuts, the smaller J would owe to a more homogeneous displacement field at the crack tip. Overall, although the experimental displacement fields can provide meaningful information, they miss constitutive information. Such additional information could be better considered through computational full-field models.

5.2.6 Remanent magnetization reduces stress concentration at the crack tip

The stress state at the crack tip drives crack growth. Given the complexity of the coupling between the mechanical and magnetic fields within pre-magnetized hMREs, experimental techniques are not enough to fully understand the constitutive response of hMREs. In this regard, DIC provides the displacement and strain fields of the deformed sample, but not the stress response. The highly complex behavior of hMREs requires constitutive models that consider the interactions between the magnetic particles and the soft elastomeric matrix. Such approaches, when implemented in a computational framework, provide deeper understanding of the underlying physics.

The present work conceptualizes a bespoke magneto-mechanical phase-field model to provide understanding on how remanent magnetic fields affect fracture mechanics of ultra-soft hMREs. More specifically, the framework explains the capacity of pre-magnetized hMREs to absorb more energy than virgin ones, as reported in the previous sections. The model is based on a continuum description of the hMRE within the finite strain framework [63, 165, 166, 184]. The Generalized neo-Hookean model (GNH) is used to model the mechanical mechanical behavior [384] (see Equation 4.69). Moreover, when the medium has remanent magnetization and/or is externally actuated, the coupling between the magnetic and mechanical fields modulates the overall stress in the bulk material. To properly model the interaction between magnetic particles at the microscale, an additional coupling term is added to the magnetic formulation. Furthermore, the air (free space) surrounding the hMRE is modeled as an extremely compliant mechanical medium [391]. On top of this, an order parameter field models the damage of the medium and crack propagation. The calibration of the critical energy release rate G_c is achieved from experimental force-displacement rupture curves for cracks of 2 and 5 mm. The area between both curves provides G_c, see Figure A.10. Note that this is an average estimation from the shortest crack to the largest one. The reader can find more detail on the calibration of the GNH model parameters in Section A.2.3 and on the constitutive model and numerical framework in Sections 4.2.2 and 5.2.3.

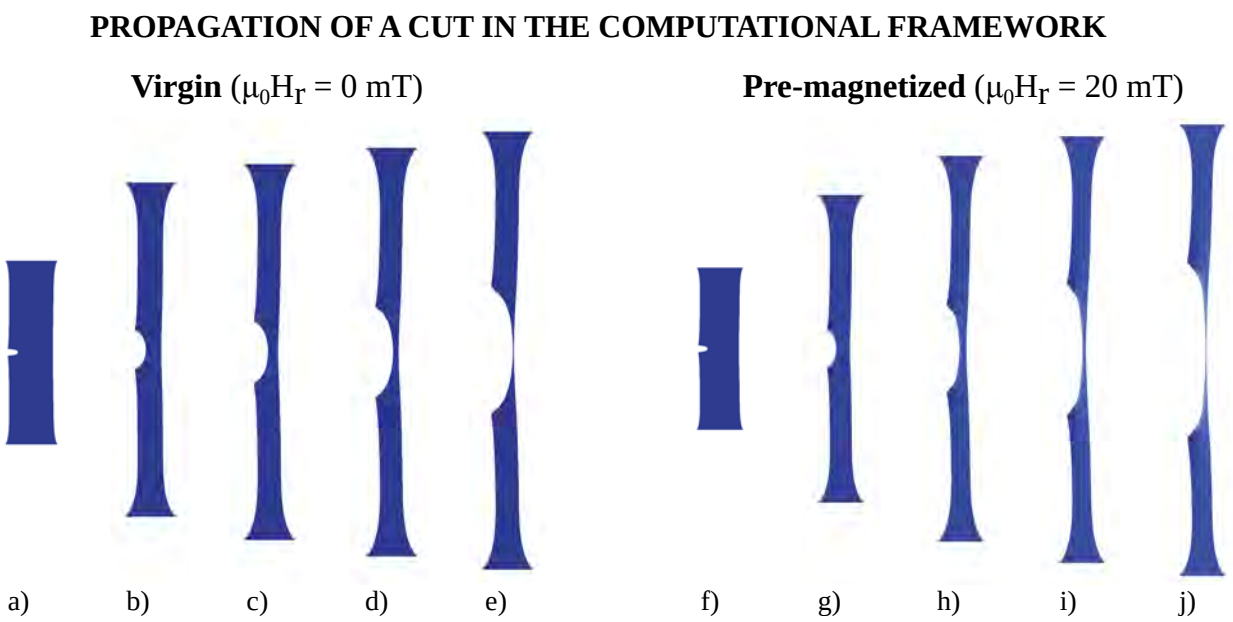

Figure 5.12: Computational stages along the stretching and crack propagation processes of a virgin and pre-magnetized hMRE. (a-e) Evolution of the morphology of the crack from an initial cut of 2 mm to final rupture of a virgin hMRE. The pictures correspond to deformed states for displacements of the edges of 3, 36, 53, 60, and 64 mm. (f-j) Crack patterns from an initial cut of 2 mm to final rupture of a pre-magnetized hMRE. The pictures correspond to deformed states for displacements of 5, 25, 35, 46, and 54 mm. The dimensions of the virtual samples are 10 mm width and 30 mm height.

The set of simulations comprises different magnetic remanent fields ($\mu_0 \mathbb{H}_r$) of 0, 5, 10, 15, and 20 mT and the cut-width ratios $c/w = 0.2, 0.3, 0.4, 0.5$. Figure 5.12 illustrates the morphology of the crack during its propagation in virgin and pre-magnetized hMREs, from the 2 mm initial cut to the eventual rupture of the sample. Force-displacement curves in Figure 5.13.a show increasing stiffness and stretch to failure for shorter cracks and larger remanent fields. Moreover, they allow to calculate the fracture energy from the area under the curve. In this regard, the barplots in Figure 5.13.b present the values of the fracture energy density, with increases of the fracture toughness above 50 % for the maximum 20 mT remanent field. Finally, Figure 5.13.c provides the vertical Cauchy stress fields (σ_{yy}) near the crack tip for virgin and pre-magnetized hMREs. For the pre-magnetized case, the stress concentration is smaller than for the virgin hMRE. This is a consequence of the coupled response of the hMRE, that results from a mechanical balance between the polymeric network deformation and magnetic stresses from particle dipole-to-dipole interactions. An isolated study of the magnetic stress contribution indicates that the magnetic stresses induce compression of the medium. In this regard, Figure 5.14 depicts the distribution of the spherical component of the magnetic contribution to the Cauchy stress tensor, where the positive values indicate magnetic compression of the medium.

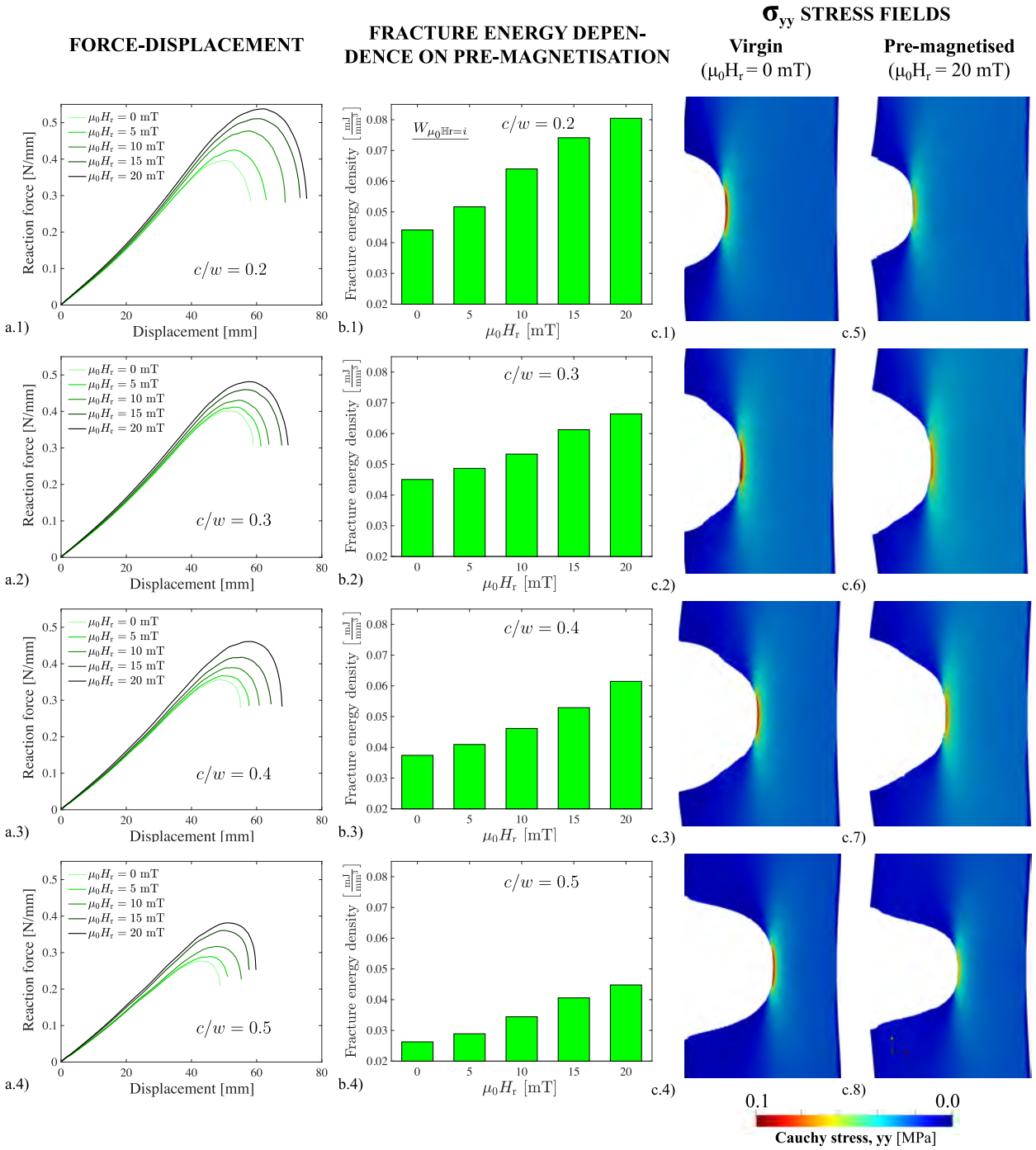

Figure 5.13: Numerical results from tensile tests to rupture performed in the virtual framework. (a.1-4) Force-displacement curves to rupture of rectangular hMRE specimens with initial crack-width ratios of 0.2, 0.3, 0.4, and 0.5, respectively, and remanent magnetic fields $\mu_0\mathbb{H}_\mathrm{r} = 0, 5, 10, 20$ mT. (b.1-4) Fracture energy density for the cut length ratios and remanent magnetic fields $\mu_0\mathbb{H}_\mathrm{r} = 0, 5, 10, 20$ mT. (c.1-4) and (c.5-8) Crack tip Cauchy vertical stress fields for virgin ($\mu_0\mathbb{H}_\mathrm{r} = 0$ mT) and pre-magnetized samples ($\mu_0\mathbb{H}_\mathrm{r} = 20$ mT). All pictures correspond to a displacement of 11.5 mm. Note that the fracture contours are obtained for $d < 0.85$, so that the regions of negligible stress contribution are not displayed.

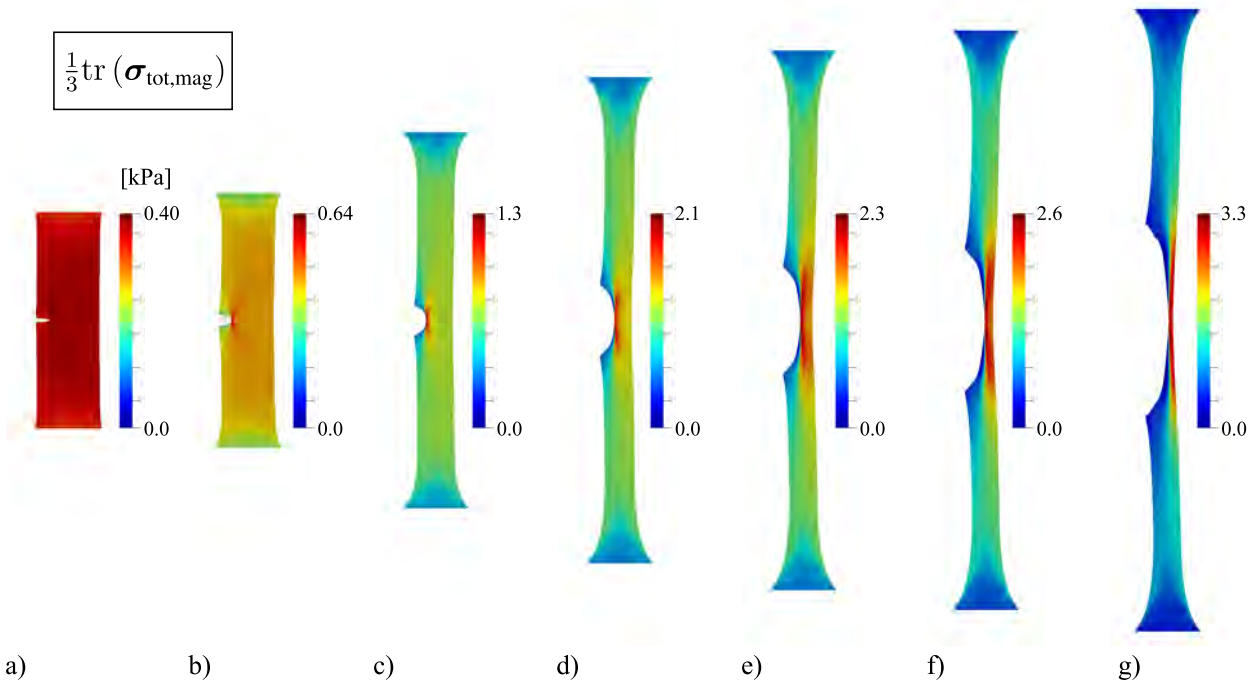

Figure 5.14: Spherical component of the magnetic Cauchy stress tensor along a virtual tensile test for the split of the energy driving crack propagation. Positive values relate to a compressive deformation of the pre-magnetized MRE in the direction of the magnetic field. (a-g) Deformed configuration for displacements of 5, 25, 35, 46 and 54 mm, respectively.

5.2.7 Discussion

The experimental and computational study shows that remanent magnetization of ultra-soft hMREs enhances their fracture performance. Our experimental approach demonstrates that pre-magnetized hMRE samples are tougher to fracture than virgin ones. In addition, crack closure due to a magnetic field delays the opening of cracks. The magnetic attraction between both sides of the crack acts as an artificial glue that heals the flaw. This ground-breaking capability suggests the application of pre-magnetized hMREs on smart structures less sensitive to pre-existing flaws. Furthermore, these ultra-soft structures would have the features to modify their mechanical properties and perform functional shape changes under external magnetic actuation. A comprehensive computational framework based on a bespoke phase-field approach allows to better understand how the magneto-mechanical coupling affects crack propagation. The virtual testbed, based on the constitutive description of hMREs at finite strains and magneto-mechanical coupling, allows to compare between magnetic conditions and pre-existing cuts of different lengths.

The concentration of the displacement, strain and stress fields at the crack tip are affected by the length of the pre-existing cut and permanent magnetization state. In this regard, the experimental strains at the crack tip in Figure 5.10.b are larger for pre-magnetized samples than for virgin ones. Moreover, according to the results for J, the fields are larger for cuts of intermediate lengths. However, strain fields are not enough to properly understand the constitutive behavior. Fracture mechanics is determined by the energy of the material and not only the strains. In this sense, the response of the material is given by a pure mechanical

contribution and a magnetic one. The former can be determined from the deformation of the material. The latter, however, actuates as a pre-stress and cannot be determined experimentally. In this respect, the computational framework provides more insightful information based on the intricate magneto-mechanical coupling of the medium. The framework allows for a detailed study of the stress response, which drives crack propagation, and reveals that the stress concentration at the crack tip is smaller for pre-magnetized hMREs than for virgin ones (see Figure 5.13.c). This justifies the slower crack growth rate observed from the virtual experiments on pre-magnetized hMREs and, overall, their enhanced fracture behavior.

As mentioned earlier in Section 5.2.4, pre-magnetized samples show higher fracture toughness. The computational framework clarifies this behavior. From the constitutive decomposition of the stress state into mechanical and magnetic contributions, one can verify that the magnetic stress contribution induces compressive deformation of the medium. The positive spherical component of the magnetic stress in Figure 5.14 quantifies this tendency. It unravels larger magnetic compression in front of the crack tip, a result that suggests that the magnetic fields homogenize the stress distribution within the medium. This is a consequence of the coupled response of the hMRE, that results from a mechanical balance between the polymeric network deformation and magnetic stresses from the particles' dipole-dipole interactions. The findings indicate that the particles' interactions oppose the elongation of the medium, hence increasing the fracture toughness of the hMRE. This would enable the design of structures with more complex geometries, diminishing the negative effect of stress concentrations around pre-existing flaws.

Overall, the experimental and computational evidence unveils that the magneto-mechanical coupling provided by hard magnetics enhance the fracture behavior of hMREs in an autonomous way. This feature opens doors to the design of self sufficient functional structures that can undergo large deformations minimizing fracture failure limitations. For example, skin patches based on soft polymers [366], meshes for wound closure [367] and bioadhesive skin sensors [368]. Moreover, the crack closure mechanism in pre-magnetized hMRE samples suggests the application of hMREs as a robust option to minimize fracture propensity. Here, the delay in the opening of the crack would reduce the amplitude of J during a load cycle, thus providing a better performance of hMREs under cyclic loading. The study of fatigue failure is out of the scope of this thesis, but the reader can consult the works by Sanoja et al. [371] and Li et al. [374] for further experimental considerations, the work by Loew et al. [392] for a computational approach and the work of Zheng et al. [393] for fatigue on hydrogels. Additional future efforts could focus on the computational study of crack nucleation and propagation from a microstructural viewpoint [394], e.g., via computational homogenization approaches. Furthermore, data-driven modeling could be a useful approach to account for unintended flaws resulting from actual manufacturing processes [395].

As a final remark, the combination of soft-magnetic and hard-magnetic particles within the same elastomeric matrix could additionally improve the fracture behavior of hMREs. Here, the soft-magnetic particles would create magnetic bridges around the hard-magnetic ones, enhancing the magneto-mechanical coupling. The next application elaborates on this hypothesis, where soft- and hard-magnetic particles are combined in the same ultra-soft

matrix. The results will uncover synergistic effects that enhance the functional response of the resulting composite, i.e., improvement in the mechanical properties and amplification of the shape-morphing capability.

5.3 Hybrid magnetorheological elastomers enable versatile soft actuators

Recent advances in magnetorheological elastomers (MREs) have posed the question on whether the combination of both soft- and hard-magnetic particles may open new routes to design versatile multifunctional actuators. The comprehensive experimental characterization in Section 3.4 unraveled that the magneto-mechanical performance of hybrid MREs can be optimized by selecting an adequate mixing ratio between particles. In the current section, a multi-physics computational framework provides insights into the synergistic magneto-mechanical interactions at the microscale. Soft-magnetic particles amplify the magnetization and hard-magnetic particles contribute to torsional actuations. Our numerical results suggest that the effective response of hybrid MREs emerges from these intricate interactions. Overall, this uncovers exciting possibilities to push the frontiers of MRE solutions. These are demonstrated by simulating a bimorph beam that provides actuation flexibility either enhancing mechanical bending or material stiffening, depending on the magnetic stimulation.

5.3.1 Microstructural homogenization model for hybrid MREs

The experimental results of hybrid MREs demonstrate a macroscopic stiffening of these materials under the application of external magnetic fields (Figure 3.29, 3.30, and 3.31). The mechanically confined tests in Figure 3.33, show that such a magneto-mechanical coupling is the result of internal stresses derived from the interactions between soft- and hard-magnetic particles that are, in turn, transmitted through the elastomeric matrix. Since these experimental data rely on the macroscopic realm, it is difficult to get insights into the microstructural mechanisms. The interactions between the particles and the matrix are of high complexity due to strong contrasts in the material properties of the different phases. Regarding the mechanical problem, there is an important stiffness contrast between the matrix (kPa) and particles (GPa). Moreover, the magnetic problem also presents an important phase contrast in terms of the relative magnetic permeability, with a value close to 1 for the matrix and hard particles whereas in the soft particles it is 31. These characteristics make the understanding of the problem non-intuitive, limiting the analysis to macrostructural measurements and hindering the identification of the links at the microscale. In the literature, there are only few works approaching the multifunctional interplays from microstructural approaches. Sanchez and co-authors [396] addressed the analysis from a molecular dynamics basis and, more recently, Becker and co-authors [397] proposed a mesoscopic constitutive model. Although the later work definitely provided relevant observations, it was performed under the assumption that the elastomeric matrix was rigid. To provide knowledge in this respect, a computational framework was designed as a numerical testbed for the evaluation of the magnetic interactions between particles and their influence on the mechanical response of the composite. The framework is based on a full-field computational model that explicitly accounts for the different phases, i.e., elastomeric matrix, soft- and hard-magnetic particles. Moreover, the model parameters have a clear physical meaning and their values are directly

taken either from the experiments reported herein or from the literature.

In the magneto-mechanical experiments, the extremely soft nature of the polymeric matrix allows the magnetic particles to rearrange forming chain-like structures within the MRE (see the discussion on the experimental results for hybrid MREs in Section 3.4). These deformation mechanisms imply very large deformations within the MRE that are not computationally reachable due to excessive element distortions. This fact, together with the need for explicitly simulating the magnetic sources, hinders a direct comparison between the experimental and computational results. However, the computational model enables simulating at the microscale, within a homogenization framework, the magneto-mechanical interactions between soft and hard particles depending on their mixing ratio. The simulations help explore the nature of such interactions and the main microstructural deformation mechanisms transmitted to the matrix. To this end, the simulations first applied the permanent magnetization of the hard-magnetic particles (positive along z-axis by the imposition of the variable $\mathbb{H}_{\mathrm{r}}$). Then, a second step applied an Eulerian (homogenized) magnetic induction up to 10 mT in the same direction as the magnetization (i.e., direct magnetic field) and in the opposite direction (i.e., reverse field). It is important to note that while the experiments analyzed the response of the macroscopic sample to an externally applied magnetic field, here a homogenized magnetic field within the RVE was directly prescribed. Thus, the computational framework allows to explore the intrinsic material behavior and microstructural interactions for such prescribed magnetic fields that are the result of external magnetic sources, residual magnetization in the hard particles and evolving fields within the soft particles. In other words, a null magnetic field in the RVE does not mean null external stimulation but an externally applied magnetic field that balances the residual magnetization within the RVE. This approach seems ideal for the purpose of these simulations, which is to evaluate the interactions between particles on a macroscopically constrained RVE. In addition, setting a common homogeneous magnetic induction to zero for all the RVEs and mixing ratios makes it possible to compare the response between all of them. More details about the boundary conditions and the residual homogeneous magnetic induction after pre-magnetization can be found in Sections 4.1.4 and A.2.2, respectively.

FE model: Numerical details

The complete computational framework was implemented in the open source FE software FEniCS to solve the non-linear magneto-mechanical problem by an implicit monolithic integration algorithm and the FEniCS standard UFL solver with independent tolerance criteria for each contribution to the residual. The remanent magnetization of hard magnetic particles and the macroscopic magnetic induction are applied consecutively and incrementally with the appropriate steps. Note that this implementation recalls the microscopic constitutive framework from Section 4.1. Then, a set of representative volume elements (RVEs) was created to match the particles mixing ratios from the MREs in the experimental section. These consist of multi-domain RVEs that explicitly consider the carrier matrix (continuous phase) and both soft- and hard-magnetic particles (dispersed phase). Every RVE was designed to have a total amount of magnetic particles of 30 vol.%. Meshes with tetrahedral

elements were defined to discretize the multiphase domain. The number of elements is comprised between 72 985 and 137 768, depending on the mixing ratio and other random factors. Moreover, Lagrange elements are chosen for a quadratic interpolation of the displacement and magnetic potential fields, and discontinuous Lagrange for the Lagrange multiplier for the incompressibility constraint. A Monte Carlo algorithm allowed to randomly distribute the magnetic particles within the RVE and simulate an isotropic distribution, also accounting for the difference in size between soft- and hard-magnetic fillers (Figure 5.15.left). The main macroscopic boundary conditions imposed in the homogenization framework for the confined deformation are

$$\overline{\mathbb{b}}(t) = \begin{Bmatrix} 0 \\ 0 \\ b_{\text{end}} t/t_{\text{ramp}} \end{Bmatrix}, \quad \overline{\mathbb{H}}_{\text{r}}(t) = \begin{Bmatrix} 0 \\ H_{\text{r}} \\ 0 \end{Bmatrix}, \quad \overline{\mathbf{F}}(t) = \begin{bmatrix} 1 & 0 & 0 \\ 0 & 1 & 0 \\ 0 & 0 & 1 \end{bmatrix}. \tag{5.9}$$

Note that the prescription of the Eulerian magnetic induction instead of its Lagrangian counterpart is just a mere modeling decision to better link to the real deformed state of the MRE [184].

Moreover, all the variables are taken directly from experimental data, either originated from this thesis or from the literature, see Table 5.4. Regarding the magnetic remanence, it has been evaluated measuring the apparent residual magnetic field in pre-magnetized hMRE samples (not fully magnetized but imposing a 1 T field). This experimental value has been taken to fit the residual magnetization of the particles comparing it with the homogenized residual magnetization under null external field conditions, see Section A.2.2 for further detail.

Table 5.4: Mechanical and magnetic properties used in the microstructural model for the matrix and the magnetic particles. Note that $n = 1$ and $b = 1$ to recover the Neo-Hookean behavior. Further non-linearities will arise after the homogenization of the microstructure. Therefore, and unlike further phenomenological models, the material laws of the phases need not include strain hardening.

Phase	**Mechanical**		
	Elastic shear modulus G [kPa]	**Hardening/ softening exp.** n [-]	**Correction at low strain** b [-]
Matrix	1.0	1	1
Soft-mag. particles	$81.78 \cdot 10^6$	1	1
Hard-mag. particles	$81.78 \cdot 10^6$	1	1

Phase	**Magnetic**		
	Magnetic susceptibility χ_{e} [-]	**Saturation magnetization** $\mu_0 m_{\text{s}}$ [T]	**Remanent magnetic field** $\mu_0 \mathbb{H}_{\text{r}}$ [T]
Matrix	0	-	-
Soft-mag. particles	30	2.5	-
Hard-mag. particles	0.05	0.5	0.015

Influence of the soft-to-hard-magnetic particles mixing ratio

Pre-magnetized hybrid MREs perform differently depending on the direction of the magnetic actuation. The computational results from the simulations are presented in Figure 5.15. The first column depicts representative RVEs for each soft-to-hard particles ratio. The second column shows plots of the homogenized stress in the RVEs against the homogenized magnetic field for direct and reverse actuations. Five different RVEs for each MRE type allow to characterize the variability related to the random distribution of the particles. Associated to these results, the last column shows the magnitude of the magnetic field for both direct and reverse actuations under a macroscopic field of 5 mT. As previously stated, note that the framework prescribes the total macroscopic magnetic induction. Besides, some simulations face convergence issues as the particles approach each other and try to form chains. These phenomena depend on the distances between particles and their soft or hard nature.

A first finding relates to the response of the MREs under direct and reverse actuations. In this regard, sMREs show exactly the same behavior irrespective of the direction of the external field, whereas the response of the hybrid and hMREs strongly differs depending on the direction of the magnetic actuation. The remanent magnetization of the hard-magnetic particles explains such a behavior. For sMREs, the particles magnetize along the applied magnetic direction leading to dipole-to-dipole interactions and a subsequent compression of the RVE. If larger magnetic fields are applied, the extremely soft matrix would allow the particles to rearrange forming chain-like structures. On the contrary, the residual magnetization within the hard-magnetic particles adds magnetic torques. These torques appear when the magnetization is not perfectly aligned with the external field. From the magnetic point of view, under direct magnetic fields, the magnetization within the hard particles is reinforced. However, for reverse fields, the total magnetization in the hard particles is diminished due to a balancing between energetic and residual terms in such a direction. In addition, the higher permeability of the soft particles results in a higher magnetization than for hard particles. The mixing of both types of particles leads to synergistic effects. In this case, as can be observed in Figure 5.15 from the magnetic field representations and the details in Figure 5.16, the soft particles create magnetic bridges between the hard ones, a phenomenon that amplifies the magnetization and enhances the magneto-mechanical coupling. This latter observation may explain the better performance of the hybrid MREs observed in the experiments. The following section will delve into these phenomena.

Regarding the values of the magnetic field, and for, e.g., a macroscopic magnetic induction of 5 mT, the microstructure has larger local fields of 20 mT in the soft magnetic particles, whereas the saturation magnetization is 2.5 T. Despite this fact, the extremely soft nature of the elastomeric matrix leads to significant macroscopic mechanical performance for magnetic fields in that range. Furthermore, when prescribing reverse magnetic actuation, the magneto-mechanical coupling is even stronger, which translates into a larger induced macroscopic stress. Moreover, the results from pure hMRE simulations (hMRE (0:1)) reach higher macroscopic inductions of up to 100 mT. The analysis of the results shows finite local deformations and high microstructural magnetic gradients. This provides insightful observations of the microstructural mechanisms that are influencing the macroscopic response of

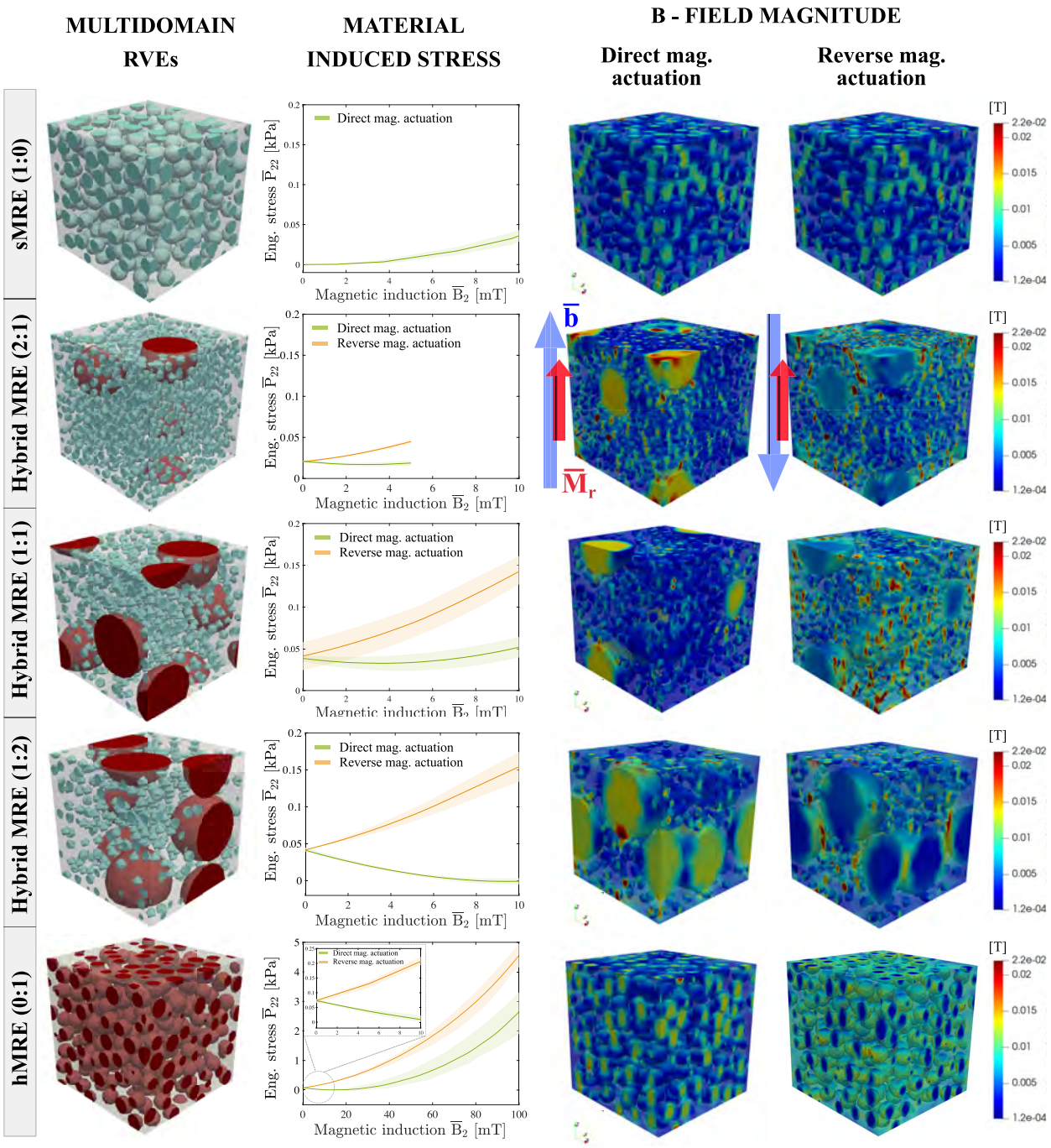

Figure 5.15: Computational results of the microstructural magneto-mechanical coupling in hybrid MREs using a homogenization model. Computational results for the homogenized framework when subjecting different representative volume elements (RVEs) to homogeneous magnetic inductions while applying mechanical confinement. The first column shows representative RVEs for the different particle mixing ratios analyzed. The second column shows the homogenized stress against the prescribed homogenized magnetic induction for the direct and reverse actuations. The last column shows the microstructural distribution of the magnetic induction within the RVEs for direct and reverse actuation for a macroscopic Eulerian magnetic induction of 5 mT. Note that a scheme with two collinear arrows illustrates the directions of the prescribed magnetic induction (blue) and permanent magnetization (red) vectors for the direct and reverse magnetic actuation. In addition, five RVEs have been considered for each particles mixing ratio. The stress versus magnetic induction curves include scatter areas to quantify the numerical variability. Also, note that a representative RVE has been chosen for each mixing ratio in the magnetic induction plots.

the MREs experimentally tested.

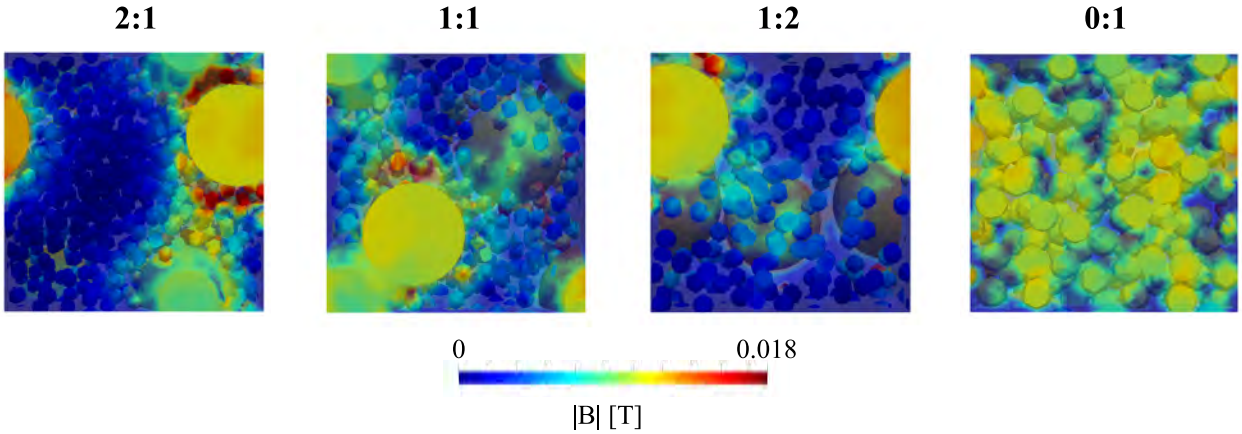

Figure 5.16: Magnetic bridges created by the soft-magnetic particles scattered along the space between the hard-magnetic particles. Clips to visualize the magnetic induction magnitude inside the RVE for soft-to-hard-magnetic particles mixing ratios of 2:1, 1:1, 1:2, and 0:1. Note that the opacity of the matrix has been reduced to visualize the particles in rear planes.

Influence of the soft-to-hard-magnetic particles size ratio

A further factor determining the mechanical behavior of hybrid MREs is the relative size ratio between soft- and hard-magnetic particles. In this regard, and in addition to the previous results, further simulations help understand how differences in the relative size between particles affect the microstructural magneto-mechanical coupling. Additional simulations were performed on RVEs of hybrid MREs with a soft-to-hard-magnetic particles' mixing ratio of 1:1. Then, different particles size ratios (soft:hard) were considered: 6:1, 3:1, 1:1, 1:3, 1:6. These results suggest a stronger magneto-mechanical coupling when using soft-magnetic particles smaller than the hard-magnetic ones. The effect is clearer when applying a reverse magnetic field (i.e., contrary to the initial magnetization direction). The bigger size of the hard-magnetic particles favors the transmission of the magnetic torque, whereas a lower size of the soft-magnetic particles contributes to generate magnetic bridges between the hard particles leading to synergistic effects. On the contrary, i.e., smaller hard-magnetic particles, the magnetic bounding between the big soft particles is much weaker and the overall magneto-mechanical coupling becomes smaller.

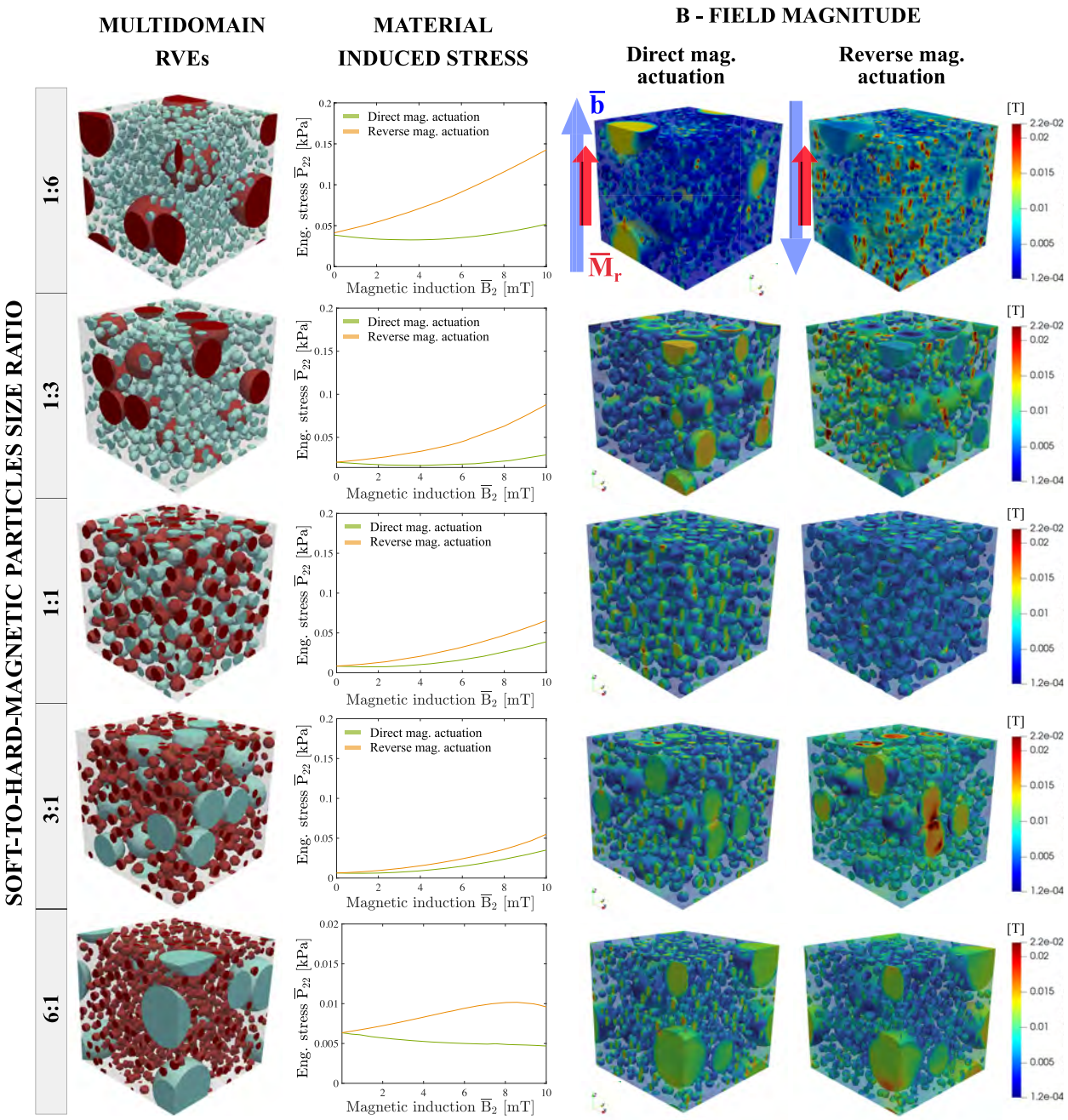

Figure 5.17: Influence of the particles' size ratio on the effective (homogeneous) behavior of hybrid MREs. The first column shows representative RVEs for the different soft-to-hard particles' size ratios. Red particles refer to hard magnetic and blue ones, to soft magnetic particles. The second column shows the homogenized stress against the prescribed homogenized magnetic induction for direct and reverse magnetic actuations. The last column shows the microstructural distribution of the magnetic induction within the RVEs for direct and reverse actuation for a macroscopic Eulerian magnetic induction of 5 mT. Note that a scheme with two collinear arrows illustrates the directions of the prescribed magnetic induction and permanent magnetization vectors for the direct and reverse magnetic actuation.

5.3.2 Virtual testing framework to design multifunctional actuators

The experimental and numerical results in Sections 3.4 and 5.3.1, respectively, suggest the possibility of mixing soft- and hard-magnetic particles to provide, at once, superior bending deformations and material stiffness enhancements under magnetic actuations. Recent advances in additive manufacturing (3D printing) techniques have made possible the design of micron-size actuators based on MREs [234, 398–400]. Ideally, the use of an extremely soft elastomeric matrix, as in this thesis, allows for magnetic stimulation with very low fields. These materials and micron-size structures have the potential to open new routes for the soft robotics community. However, the conceptualization and design of such systems present significant difficulties. For instance, the lack of proper experimental methods hinders the evaluation of magneto-mechanical coupling at this scale. The aim of this section is to demonstrate the capacity of the presented FE model as a virtual testing framework to overcome the bottlenecks impeding this advance. To this end, two micron-size beams are numerically designed to offer alternative actuation modes, i.e., depending on the direction of a low actuating magnetic field (below 50 mT), they react either by deflecting or by performing functional changes in their material properties (mechanical stiffening). Such a novel multifunctional behavior is achieved thanks to the multifunctional coupling that the combination of both soft- and hard-magnetic particles provides.

Numerical details

A FE model consisting of a beam surrounded by air is conceptualized, see Figure 5.19.a.1 for the case of a bimorph (i.e., bi-layered beam). The constitutive model of the beam layers relies on the microstructural description of the phases, i.e., matrix and particles, according to the formulation in Section 4.1.3. The top layer of the beam corresponds to a MRE component while the bottom layer is a purely elastomeric matrix. Meshes with triangular elements discretize the domains of the numerical model. Depending on the case, i.e., sMRE, hybrid MRE and hMRE, the meshes for the bimorph actuator have 87374, 94519 and 76234 elements, respectively. The constitutive model of the beam layers relies on the microstructural description of the phases, i.e., matrix and particles, as incompressible media according to the description in the previous sections. The air domain within the virtual testing framework is modeled as a rectangular box ten times larger than the beam. This enables the application of a homogeneous far-field imposing the magnetic potential on the external faces of this domain. The air is modeled as a Neo-Hookean compressible media with a negligible stiffness, i.e., shear modulus of $G = 80$ Pa. To model its compressible nature, the degrees of freedom due to the Lagrange multiplier p in the air domain are removed and, instead, a volumetric contribution is added to the mechanical contribution to the energy potential as

$$\Psi_{\text{mech}}(\mathbf{F}) = \Psi_{\text{mech,iso}} + \Psi_{\text{vol}} = G\mathbf{F} - G\mathbf{F}^{-\text{T}} + \lambda \ln(J)\mathbf{F}^{-\text{T}}, \tag{5.10}$$

with $\lambda = \kappa - \frac{2G}{3}$ as a function of the bulk modulus κ.

To minimize the additional stiffness posed by the air domain and to enhance its behavior, we implement the auxiliary energy function approach reported by Rambausek et al. [166]. The weight function gauges the mechanical contribution to the mechanical Piola stress tensor in the weak form. It takes values close to one in the smaller elements surrounding the beam, and smaller values for the larger elements further from the beam. The function reads as

$$w(\mathbf{X}) = \max\left[w_{min}, \min\left(\frac{V_{ref}}{V_0}, w_{max}\right)\right], \tag{5.11}$$

with $w_{min} = 1 \times 10^{-5}$, $w_{max} = 1$ and $V_{ref} = 2 \times 10^{-2}$. Figure 5.18 shows the values of the weight function in the air domain.

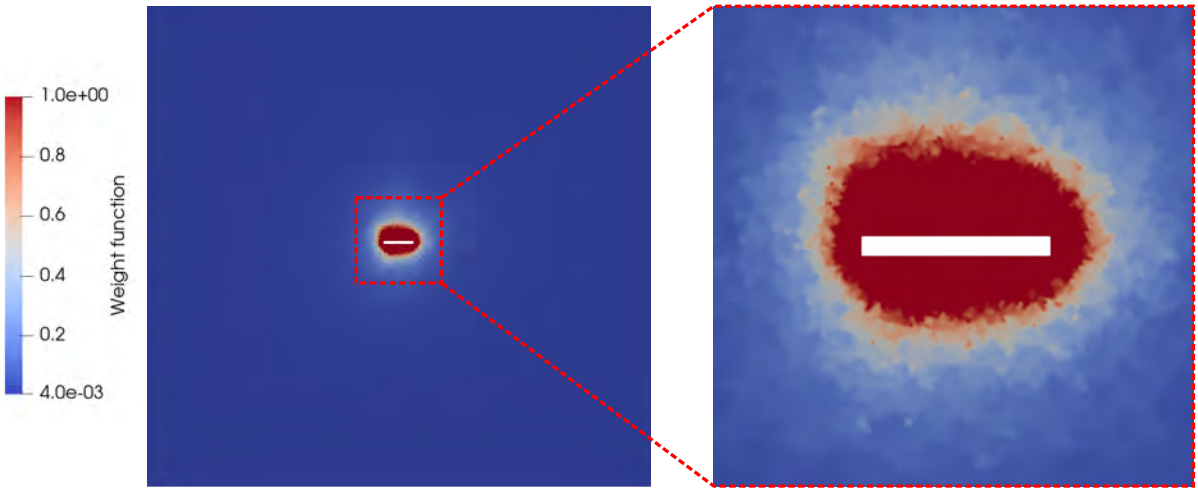

Figure 5.18: Distribution of the weight function in the air domain and a detail of the air domain in the proximity of the beam. The weight function takes values close to one in the smaller elements surrounding the beam, and smaller values for the larger elements further from the beam.

The NonlinearVariationalProblem library in FEniCS is used to numerically solve the model.

Cantilever actuator with perpendicular magnetic actuation

Figure 5.19 depicts the deflection, magnetic induction field and magnetization of a bimorph cantilever actuator under perpendicular magnetic actuation with respect to the pre-magnetization of the hard-magnetic particles. The main outcome is that, under a perpendicular magnetic actuation, the rightwards pre-magnetized hard particles lead to bending of the beam. Indeed, the transmission of torques from the particles to the matrix governs such a functional mechanism. Moreover, soft particles enhance the torques on hard ones in two ways: i) amplifying the magnetic field around the hard particles and ii) compressing the upper layer along the beam thickness. Regarding the former, the soft-magnetic particles, with a high magnetic permeability, create magnetic pathways around the hard-magnetic particles. Such a phenomenon increases the effective magnetic flux, which directly impacts the resultant microscopic torque transmitted from the hard particles to the matrix. Soft particles magnetize in the perpendicular direction, with the consequent dipole-to-dipole interactions and the perpendicular compression of the layer. With this contraction, the upper

layer expands, thus the structure bends. These features can be appreciated in Figure 5.19.d. Additionally, Figure 5.19.f depicts the evolution of the homogeneous magnetization of the hard, soft and hybrid beams in both perpendicular and parallel directions. Note that such magnetic pathways appear not only in the perpendicular (vertical) direction, but also in the longitudinal (horizontal) direction. Figure 5.19.f.2 clarifies this phenomenon. After the initial pre-magnetization, the homogeneous longitudinal magnetization slightly increases with the perpendicular magnetic actuation.

Figure 5.20 extends the study with additional results for the bimorph beam pre-magnetized in the opposite direction, i.e., leftwards pre-magnetization. Moreover, Figures 5.21 and 5.22 contain the results for perpendicular actuation on a homogeneous beam, i.e., the particles are scattered along all the beam without any passive layer.

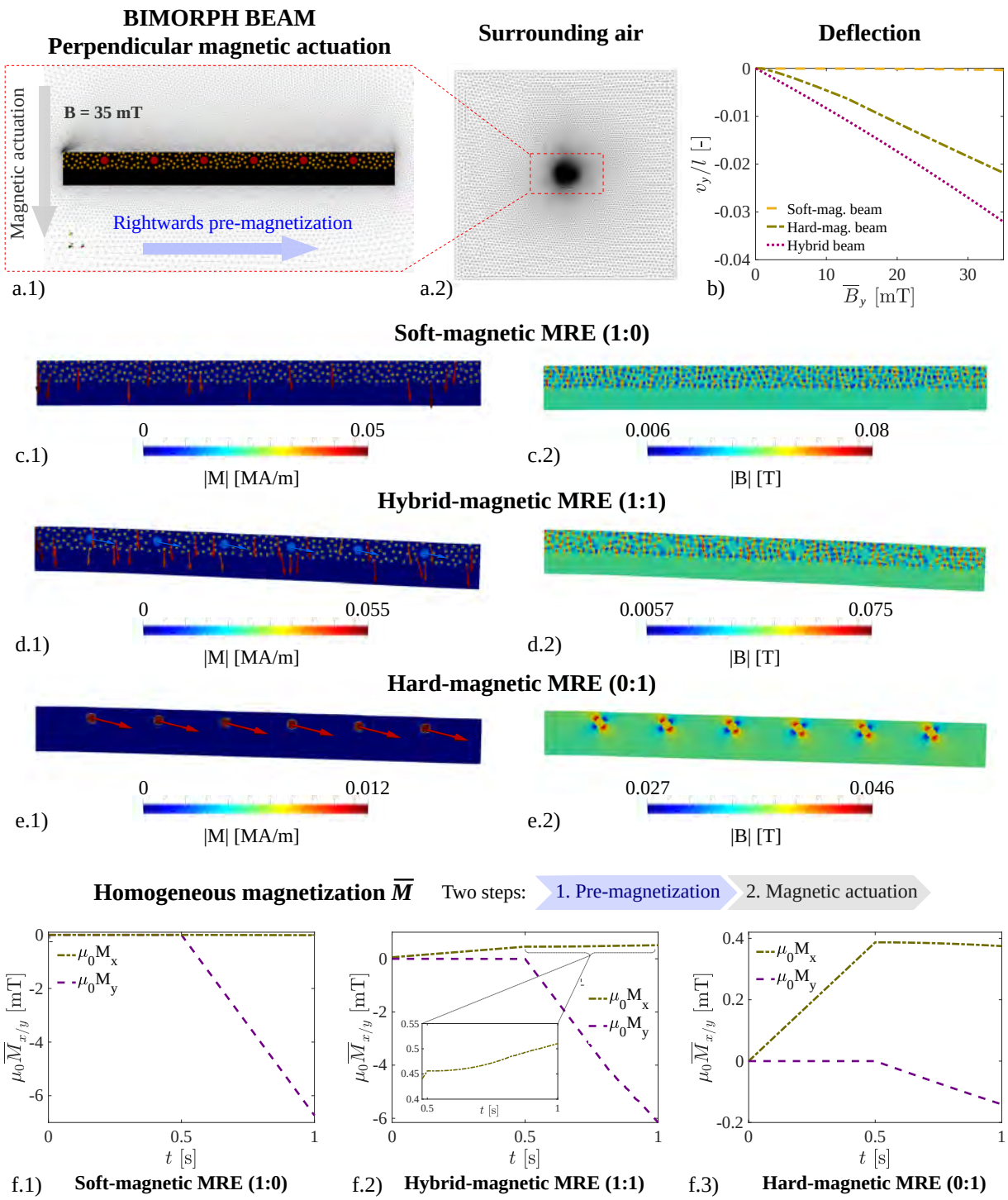

Figure 5.19: Numerical application of the microscopic model on a bimorph cantilever beam. (a.1) Perpendicular magnetic actuation conditions on a bi-layer cantilever beam with hybrid magnetic fillers (soft- and hard-magnetic particles) in the top layer and pure elastomeric matrix in the bottom layer. (a.2) Complete FE problem mesh including the air surrounding the beam to guarantee the proper application of the magnetic actuating field. (b) Normalized vertical beam deflection against the external applied magnetic field for sMRE, 1:1 hybrid MRE and hMRE. The hMRE beam and the hybrid beam bend under an external magnetic actuation as a consequence of the torque transmission from the hard-magnetic particles. (c.1) and (c.2) magnetization and magnetic induction fields within the sMRE beam after magnetic actuation (35 mT), respectively. (d.1) and (d.2) magnetization and magnetic induction fields within the hybrid MRE beam after the magnetic actuation (35 mT), respectively. (e.1) and (e.2) magnetization and magnetic induction fields within the hMRE beam after magnetic actuation (35 mT), respectively. (f.1-3) Evolution of the homogenized horizontal and vertical magnetization components of the sMRE, hybrid MRE and hMRE beams, respectively. Note that the arrows on the particles describe the Eulerian magnetization vector at their centers.

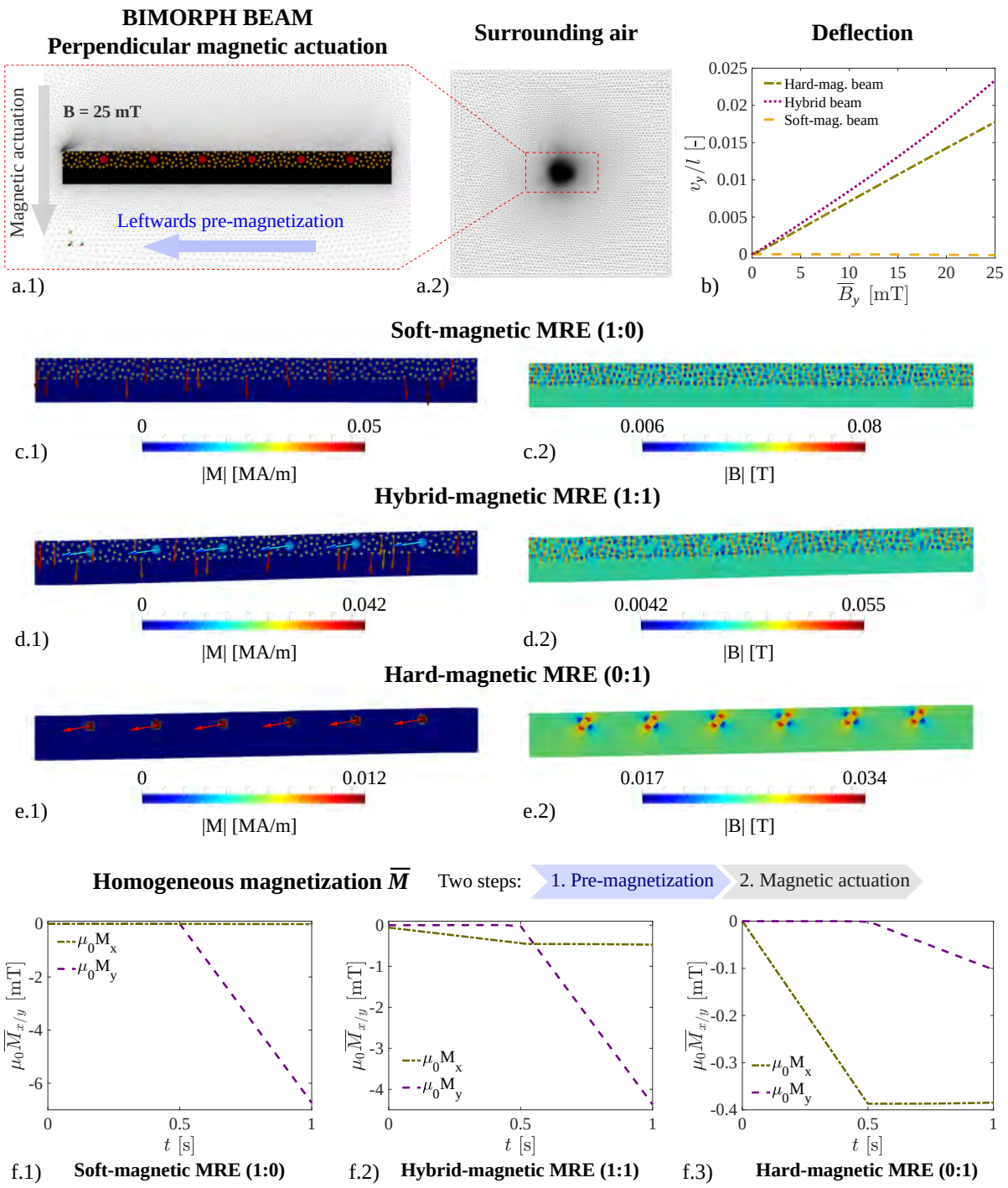

Figure 5.20: Numerical application of the microscopic model on a bimorph cantilever beam with leftwards pre-magnetization. (a.1) Magnetic actuation conditions on a bi-layered cantilever beam with hybrid magnetic fillers (soft- and hard-magnetic particles) in the top layer and pure elastomeric matrix in the bottom layer. Hard-magnetic particles are leftwards pre-magnetized with a remanent field of $\mathbb{H}_r = 0.015$ mT. (a.2) Complete FE problem meshed including the air surrounding the beam to guarantee the proper application of the magnetic actuating field. (b) Normalized vertical beam deflection against the external applied magnetic field for sMRE, 1:1 hybrid MRE and hMRE. The hMRE beam and the hybrid beam bend under external magnetic actuation as a consequence of the torque transmission from the hard-magnetic particles. (c.1) and (c.2) magnetization and magnetic induction fields within the sMRE beam after magnetic actuation (25 mT), respectively. (d.1) and (d.2) magnetization and magnetic induction fields within the hybrid MRE beam after magnetic actuation (25 mT), respectively. (e.1) and (e.2) magnetization and magnetic induction fields within the hMRE beam after magnetic actuation (25 mT), respectively. (f.1-3) Evolution of the homogenized horizontal and vertical magnetization components of the sMRE, hybrid MRE and hMRE beams, respectively.

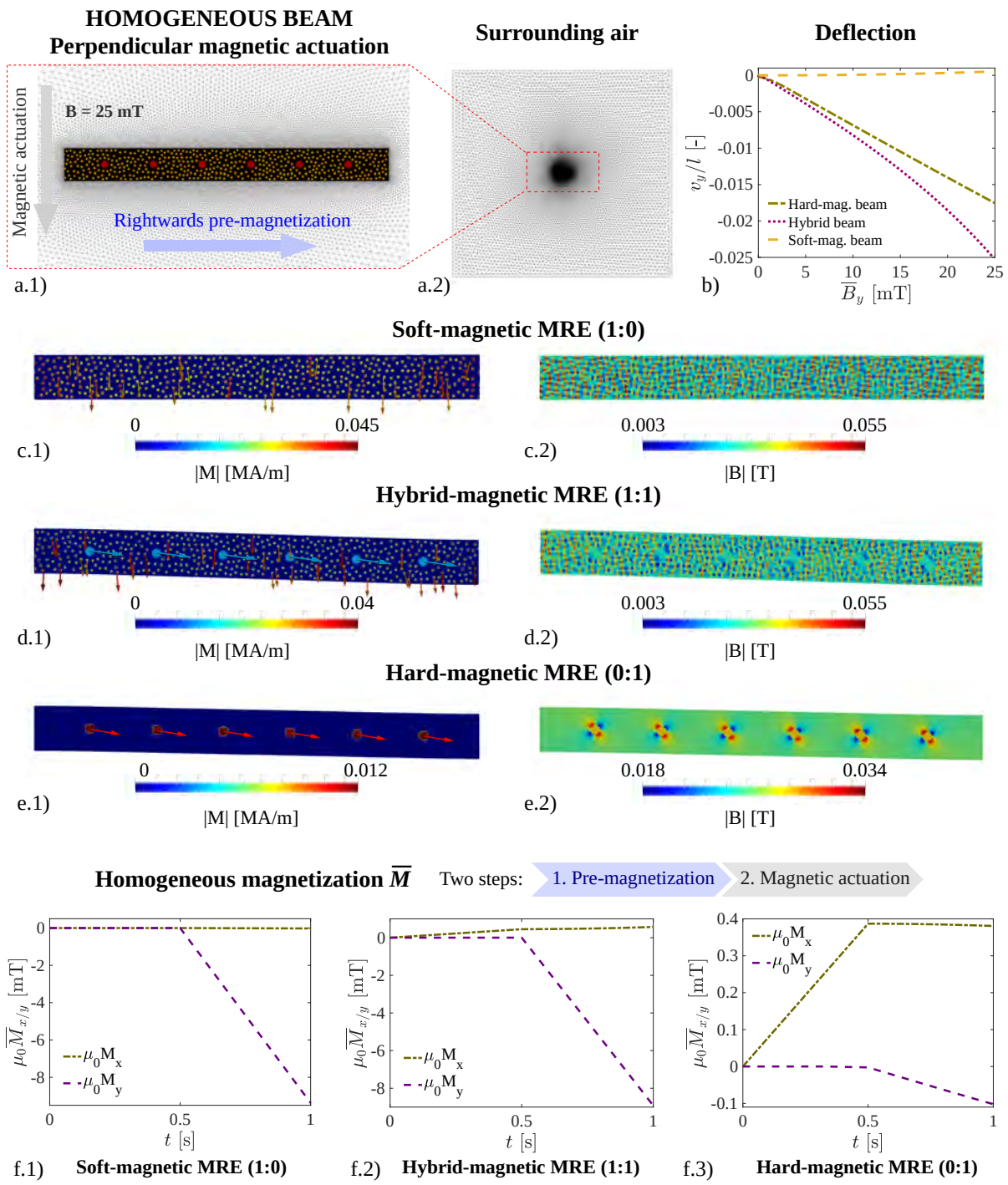

Figure 5.21: Numerical application of the microscopic model on a homogeneous cantilever beam with rightwards pre-magnetization. (a.1) Magnetic actuation conditions on a homogeneous cantilever beam with hybrid magnetic fillers (soft- and hard-magnetic particles). Hard-magnetic particles are rightwards pre-magnetized with a remanent field of $\mathbb{H}_r = -0.015$ mT. (a.2) Complete FE problem meshed including the air surrounding the beam to guarantee the proper application of the magnetic actuating field. (b) Normalized vertical beam deflection against the external applied magnetic field for sMRE, 1:1 hybrid MRE and hMRE. The hMRE beam and the hybrid beam bend under external magnetic actuation as a consequence of the torque transmission from the hard-magnetic particles. (c.1) and (c.2) magnetization and magnetic induction fields within the sMRE beam after magnetic actuation (25 mT), respectively. (d.1) and (d.2) magnetization and magnetic induction fields within the hybrid MRE beam after magnetic actuation (25 mT), respectively. (e.1) and (e.2) magnetization and magnetic induction fields within the hMRE beam after magnetic actuation (25 mT), respectively. (f.1-3) Evolution of the homogenized horizontal and vertical magnetization components of the sMRE, hybrid MRE and hMRE beams, respectively.

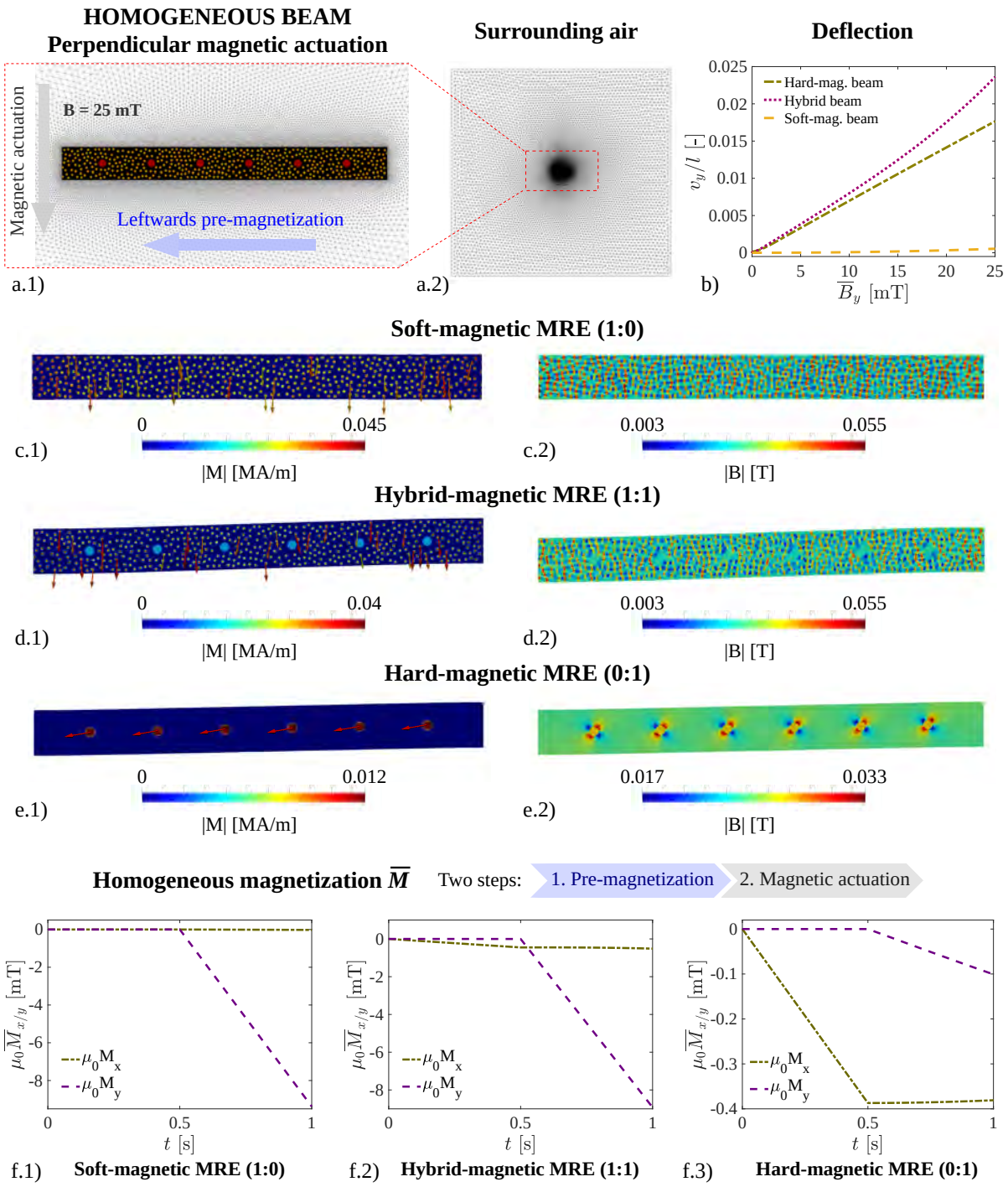

Figure 5.22: Numerical application of the microscopic model on a homogeneous cantilever beam with leftwards pre-magnetization. (a.1) Magnetic actuation conditions on a homogeneous cantilever beam with hybrid magnetic fillers (soft- and hard-magnetic particles). Hard-magnetic particles are leftwards pre-magnetized with a remanent field of $\mathbb{H}_r = 0.015$ mT. (a.2) Complete FE problem meshed including the air surrounding the beam to guarantee the proper application of the magnetic actuating field. (b) Normalized vertical beam deflection against the external applied magnetic field for sMRE, 1:1 hybrid MRE and hMRE. The hMRE beam and the hybrid beam bend under external magnetic actuation as a consequence of the torque transmission from the hard-magnetic particles. (c.1) and (c.2) magnetization and magnetic induction fields within the sMRE beam after magnetic actuation (25 mT), respectively. (d.1) and (d.2) magnetization and magnetic induction fields within the hybrid MRE beam after magnetic actuation (25 mT), respectively. (e.1) and (e.2) magnetization and magnetic induction fields within the hMRE beam after magnetic actuation (25 mT), respectively. (f.1-3) Evolution of the homogenized horizontal and vertical magnetization components of the sMRE, hybrid MRE and hMRE beams, respectively.

Cantilever actuator with parallel magnetic actuation

A completely different response is expected when the magnetic actuation is parallel to the beam, see Figure 5.23. For low external magnetic fields (25 mT), the hybrid MRE beam responds by increasing its apparent stiffness. Note that small enough fields prevent significant structural compression in the presence of soft particles, while being sufficient to functionally activate the structure. Figure 5.23 shows the results of these simulations. After the application of a parallel magnetic field on the pre-magnetized beam, a small stretch is applied in the same longitudinal direction. The apparent stiffness is computed as the homogenized axial Piola stress over the equivalent strain. In addition to the bimorph cantilever beam, Figure 5.23 includes the results for a homogeneous beam, i.e., particles scattered along all the matrix. This allows to directly compare the magneto-mechanical stiffening of both beams and extract insightful information.

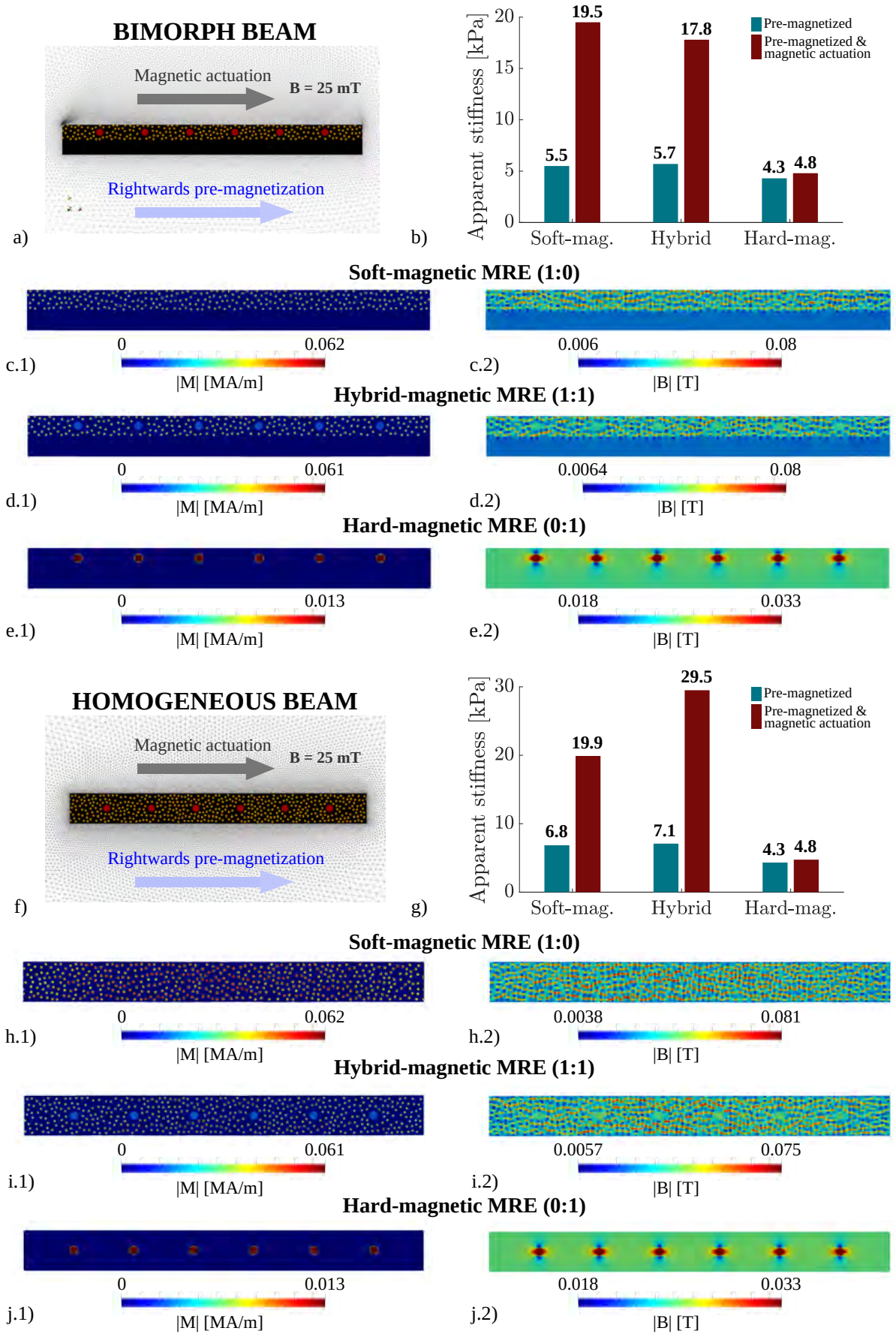

Figure 5.23: Numerical application of the microscopic model on a bimorph and homogeneous cantilever beams.

[Continues on next page]

[Continued from previous page]

(a) Parallel magnetic actuation conditions on a bi-layer cantilever beam with hybrid magnetic fillers (soft- and hard-magnetic particles) in the top layer and a pure elastomeric matrix in the bottom layer. (b) Apparent stiffness of the bimorph beam after pre-magnetization under null and magnetic actuations of 25 mT, depending on the filler content used in the upper layer: sMRE, 1:1 hybrid MRE and hMRE. (c.1) and (c.2) magnetization and magnetic induction fields within the sMRE beam after the magnetic actuation (25 mT), respectively. (d.1) and (d.2) magnetization and magnetic induction fields within the hybrid MRE beam after the magnetic actuation (25 mT), respectively. (e.1) and (e.2) magnetization and magnetic induction fields within the hMRE beam after magnetic actuation (25 mT), respectively. (f) Parallel magnetic actuation conditions on a homogeneous cantilever beam with the particles scattered along all the matrix. (g) Apparent stiffness of the homogeneous beam after the pre-magnetization under null and magnetic actuation of 25 mT, depending on the filler content used in the upper layer: sMRE, 1:1 hybrid MRE and hMRE. (h.1) and (h.2), (i.1) and (i.2), (j.1) and (j.2) magnetization and magnetic induction fields within the sMRE, hybrid MRE and hMRE beams, respectively, after the magnetic actuation.

5.3.3 Discussion

A glance over the results from Figures 5.19 and 5.23 shows that the use of hybrid MREs enables multi-actuation modes with a single structure. Note that we added the response of pure sMRE and hMRE beams in Figures 5.19 and 5.23. The hMRE provides bending actuation but almost negligible stiffening at low magnetic fields. On the contrary, the sMRE provides outstanding stiffening under applied magnetic fields but a negligible bending. Our proposed solution, i.e., hybrid MREs, provides an enhanced bending actuation beyond that of hMREs, whereas it keeps a similar material stiffening to that of sMREs for a low magnetic actuation. The results for the homogeneous beam in Figure 5.23.g indicate that the hybrid MRE beam provides a stronger stiffening effect than the pure sMRE and hMRE ones. These numerical results are supported by the experimental findings in Figure 3.32.a, which suggest the possibility of using hybrid MREs to combine enhanced mechanical actuation and change in the material properties.

The ultra-soft nature of the matrix allows to obtain functional responses with low magnetic actuation. Figure 5.24 shows additional results for the pure hard-magnetic bimorph under a larger magnetic actuation of 200 mT. This allows to see high local torsional deformations of the matrix in the particles' vicinity, which owes to the extremely soft nature of the matrix and explains the non-perfect parabolic macroscopic structural bending.

The present application may be useful in, for example, microfluidic systems to actuate in two modes. The beam bending can be activated via a perpendicular magnetic stimulation and a parallel fluid flow can be penalized. Alternatively, the parallel magnetic stimulation would increase its structural stiffness opposing to the fluid flow perpendicular to the beam. Another application area with great potential is bioengineering. The current hybrid MRE solutions are ideal candidates to push the advance in mechanobiological systems based on magneto-active polymers, e.g., for the sMRE substrate presented in Section 5.1.

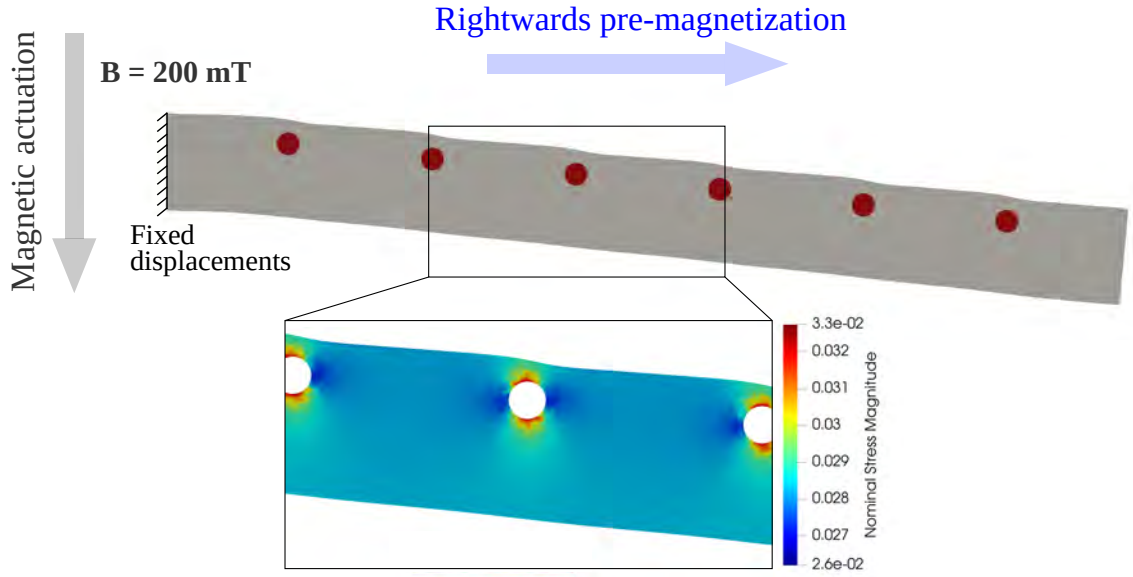

Figure 5.24: Numerical detail of local stress concentration in the bimorph beam. Applying a larger perpendicular magnetic field of 200 mT on the hard-magnetic bimorph cantilever beam allows to see high local torsional deformations of the matrix in the particles' vicinity. The particles are pre-magnetized in the horizontal direction and try to turn to align their magnetization with the external field. A detail shows the stress state of the matrix near the particles.

Moreover, the results for a homogeneous beam with the particles scattered along all the matrix confirm the experimental findings. The hybrid MRE actuator presents enhanced material stiffening with respect to the pure sMRE and hMRE counterparts. While the sMRE and hMRE stiffen 2.9 and 1.1 times with the magnetic field, respectively, the hybrid MRE stiffens 4.2 times. That makes the stiffening of the hybrid MRE almost a 150 % larger than that of pure sMREs. Such a finding is the result of the amplification effect of the local magnetic field due to the pre-magnetized hard particles surrounded by highly magnetizable soft particles. Even though this effect is less clear for the bi-layer actuator, it is still beneficial as its deflection under perpendicular magnetic actuation is larger than the pure sMRE and hMRE ones.

Another potential application of the bi-layer beam is to provide the same actuation mode independently of the external magnetic source. In this regard, sometimes it is difficult to control a specific magnetic field direction. However, under high enough magnetic fields, our bi-layer beam would deflect for both perpendicular and parallel actuations. A perpendicular field would activate the torques from the hard-magnetic particles, whereas a parallel field would activate compression/tensile deformation in the upper layer due to dipole-to-dipole interactions mainly arising from the soft particles. The axial deformation of the upper layer, in the presence of the lower passive layer, would also induce a mechanical bending.

The combination of the experimental and computational methods developed in this doctoral thesis would make possible the conceptualization of composite structures with superior performance. To this end, the microstructural modeling framework could be used to generate a large database considering different material properties for each phase (i.e., elastomeric matrix, soft and hard magnetic particles), differences in particle size, alternative microstructural arrangements of the particles, etc. Then, the optimal solutions from a microstructural

perspective could be obtained from such algorithms and tested experimentally to validate a superior multifunctional performance at the macrostructural level. The latter would benefit from machine learning or Bayesian optimization methods [401–404].

Conclusions and Future Works 6

This last chapter expands the original contributions and impact of the results obtained in the present doctoral thesis. Three main blocks classify the conclusions attending to the Experimental, Modeling and Applications chapters. Moreover, future works are included in a last section.

6.1 Conclusions

6.1.1 Experimental contributions

Identification and description of the deformation mechanisms of ultra-soft MREs

i. Conceiving MREs with an ultra-soft elastomeric matrix (stiffness ∼1 kPa) that allows large magnetostriction and magnetorheological effects of the composite under external magnetic actuation and/or internal remanent magnetic fields.

ii. The present thesis reports the largest experimental characterization of ultra-soft MREs to date, with more than 1 000 tests under more than 100 magneto-mechanical different rheology tests conditions. The experiments cover different deformation modes, i.e., monotonous uniaxial compression, magneto-mechanical DMA, relaxation tests, oscillatory shear for varying strain rates, frequency sweeps and mechanically confined tests under magnetic actuation.

iii. Conceptualization of a new methodology to describe microstructural deformation mechanisms unknown to date. The experiment enables isolating microstructural deformations of the material from macroscopic deformations. To this end, the sample is macroscopically confined while a homogeneous magnetic field is applied. The microstructural displacements of the magnetic particles lead to macroscopic stresses that can be measured. The results suggest that the microstructural configuration reaches alternative particles-arrangement states depending on the rate of application of the magnetic load.

iv. Comprehensive characterization of ultra-soft MREs with magnetic particles with high magnetic remanence (hMREs). The experimental methods were used to collect microstructural insights and macroscopic effects of the underlying deformation mechanisms of such materials. Consequently, the pre-magnetization of the composite allows to determine the impact of the remanent magnetization on the overall response.

Enhancing the magneto-mechanical performance with novel hybrid MREs

i. Conceptualization of novel ultra-soft hybrid MREs with soft- and hard-magnetic particles combined within the elastomeric matrix. The high magnetic coercivity of hard-magnetic particles endows pre-magnetized MREs with an improved shape-morphing capability under external magnetic actuation. Hard-magnetic particles transmit torques to the soft matrix. At the same time, soft-magnetic particles, with high magnetic susceptibility, amplify the magnetic field at the microscale providing an enhanced magnetorheological stiffening. Moreover, synergistic effects arise from the combination of both types of fillers due to strong magnetic bridges.

ii. Application of the experimental methods to provide a comprehensive characterization of the magneto-mechanical performance and deformation mechanisms of hybrid MREs. The soft-to-hard-magnetic particles mixing ratio is modified to characterize the combined effect of both types of magnetic fillers and to tune the structural response.

6.1.2 Modeling contributions

Development of a microstructural homogenization model for ultra-soft hybrid MREs

i. Development of a multi-physics computational framework at finite strains to homogenize the non-linear material behavior from the microscale. The representative volume elements consider the ultra-soft matrix (1 kPa) and the magnetic particles. These are soft-magnetic, hard-magnetic or a combination of both. In this last case, the size ratio of the different fillers is thoroughly considered. Moreover, the framework allows to impose macroscopic magneto-mechanical boundary conditions, enabling to understand the intricate physical interactions between the magnetic particles and the effects of remanent magnetic fields. Overall, the high contrast between the mechanical and magnetic properties of the phases poses an additional difficulty.

ii. The constitutive description of the phases can be easily modified and applied on different meshes designed *ad-hoc*.

Definition of a macroscopic constitutive framework suitable for functional sMREs for mechanobiological studies

i. Synthesis of a constitutive model based on the hyperelastic Gent formulation and mechanical incompressibility assumptions. The model is calibrated from experimental data for its eventual application to reproduce the sMRE substrate for mechanobiology studies. It considers different compositions of the carrier matrix (i.e., different stiffness).

Conceptualization of a macroscopic phase-field model for fracture of ultra-soft hMREs

i. Conceptualization for the first time of a phase-field model for fracture of hMREs. The numerical framework lies in the magneto-mechanical coupled problem together with a

damage parameter. A continuum approach to model the MRE considers its effective constitutive behavior and includes the remanent magnetization of the medium. The phase-field degrades the properties of the magnetizable medium towards that of the free space. Overall, the constitutive framework is derived from thermodynamic potentials and includes the surrounding free space.

ii. The constitutive framework can be easily adapted for other magnetizable media and pre-magnetization states. Moreover, external magnetic actuation could be easily included. Nevertheless, and for the sake of convenience and applicability of the actual material, the standalone magneto-mechanical coupling due to remanent magnetic fields may be more advantageous since no external magnetic actuation is needed.

6.1.3 Applications contributions

Contribution to the development of a new methodology for mechanobiology studies

i. Novel ultra-soft responsive materials, their characterization and modeling to be integrated into a new mechanobiology stimulation setup. The methodology enables reproducing *in vitro* mechanically dependent biological processes. The framework combines experimental and computational approaches to design MREs able to mimic complex strain patterns found in biological material. This allows researchers to control such strain patterns in a non-invasive manner and to transmit them to cell cultures. To this end, the computational framework is used to adjust the positions of four permanent magnets to get the desired deformation of the sMRE substrate. Consequently, the system allows for the instantaneous evaluation of the mechanical effects on cells and their different biological responses. Overall, the framework enables biomechanical studies, such as wound healing, cellular differentiation, neuroscience research and metastasis dynamics.

ii. *In vitro* simulation of the representative strains during a traumatic brain injury scenario, i.e., an impact on the head. Moreover, the system is able to modulate the magnitude of the strain patterns.

Conceptualization and characterization of fracture-resistant hMREs with remanent magnetization

i. First study of the fracture mechanics of MREs, uncovering remarkable mechanisms to enhance the fracture resistance of soft elastomers. Demonstration that hard magnetics enhance fracture toughness and arrest crack propagation in MREs. The experimental results show that remanent magnetic fields within the hMRE drastically increase the fracture energy (up to a 50 %). Applications in bioengineering based on highly stretchable elastomers may benefit from this characteristic.

ii. Introduction and characterization of a novel mechanism to arrest cracks propagation in MREs, i.e., magnetic crack closure due to the magneto-mechanical coupling. The

mechanism prevents the opening of pre-existing cracks and flaws under a certain load threshold. This suggests exiting possibilities for cyclic loading resistant and self-healing polymers.

iii. Application of the phase-field model for fracture of hMREs to explore the stress state at the crack tip. The results state that remanent magnetic fields decrease the stress concentration at the crack tip, hence delaying the propagation of cracks.

Conceptualization of soft actuators based on hybrid MREs

i. Application of the homogenization numerical framework to understand the synergistic magneto-mechanical interactions between soft- and hard-magnetic particles at the microscale. In addition, characterization of the effects resulting from the relative direction of the magnetic actuation with respect to the remanent magnetization of the hard-magnetic particles. The results indicate that the particles with low coercivity amplify the magnetization and the particles with high coercivity contribute to torsional actuation (i.e., transmission of torques to the elastomeric matrix). Overall, the numerical results suggest that the effective response of these materials arises from such complex interactions.

ii. Design of a virtual testbed to overcome the bottlenecks that hinder the advancement and testing of micron-sized multifunctional actuators. To this end, micron-sized cantilever beams (bimorph and homogeneous) are design to respond to low magnetic fields (below 50 mT) with morphological changes and with modifications of their mechanical properties, e.g., performing bending deformation and showing remarkable stiffening under external magnetic actuation.

iii. The results suggest interesting possibilities to open doors in the application of MREs. Both the experimental and numerical findings highlight the benefits of combining particles with low and high magnetic coercivity to provide, at the same time, enhanced bending deformations and improved magnetorheological stiffening under magnetic actuations.

6.2 Future works

During the development of the thesis, the following points have been identified as potential fields to further explore:

i. The current manufacturing methods are limited to simple geometries and spatial material distribution. New additive manufacturing solutions may overcome such limitations and provide higher flexibility.

ii. The mechanically confined tests under magnetic actuation suggest strong particles interactions and rearrangements when an ultra-soft elastomeric matrix is used. However, the specific mechanisms driving such relaxation processes remain still elusive. To better understand these phenomena, longer magnetic relaxation tests are needed. In addition, advanced microstructural computational frameworks would provide additional understanding.

iii. An *in silico* study of the visco-hyperelastic behavior of the carrier matrix and the additional viscous mechanisms arising from particle-particle and particle-matrix interactions. This problem must be addressed from both microstructural (i.e., full-field) and macrostructural (i.e., phenomenological) perspectives.

iv. Determination of the influence of magnetic boundary conditions on magneto-mechanical coupled problems. Along the manuscript and some previous works [61], the need to reproduce the complete experimental setup has been demonstrated to be essential.

v. Expand the magneto-mechanical stimulation capabilities of the mechanobiology system by improving the computational framework. Moreover, adapt additive manufacturing technologies to enhance the responsive substrates and the flexibility to reproduce complex strain patterns on cellular systems.

vi. Explore the benefits of fracture-resistant and hybrid MREs through new applications, e.g., autonomous self-healing structures.

Figure 6.1 illustrates the results of ongoing works related to the previous future works. These explore the visco-hyperelastic nature of ultra-soft MREs, determine the influence of the magnetic boundary conditions in real actuation setups, and conceptualize hMRE-based self-healing structures.

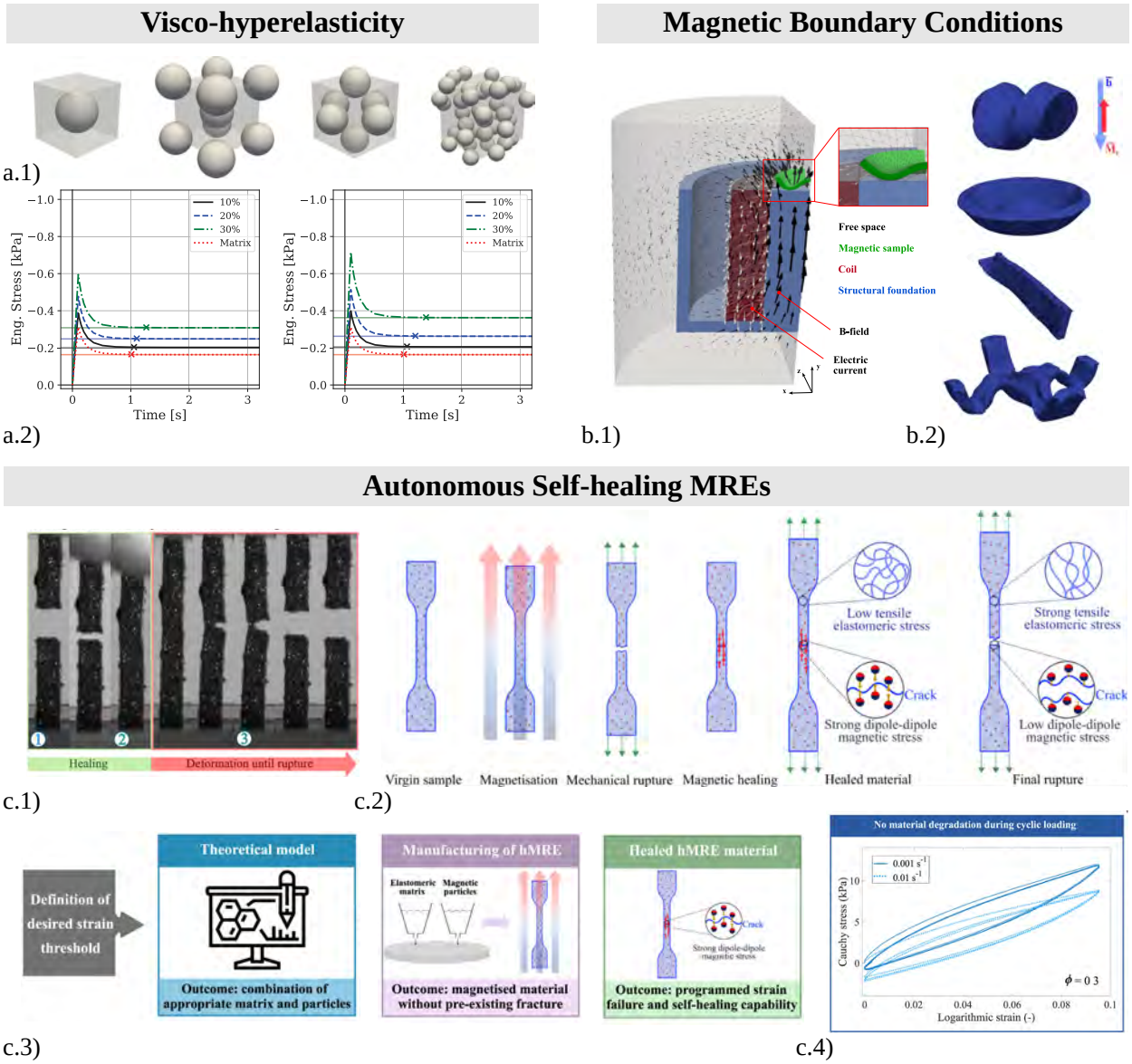

Figure 6.1: Ongoing works. Visco-hyperelasticity: computational homogenization to explore time-dependent mechanisms. (a.1) RVEs with four spatial arrangements of the particles, i.e., Simple Cubic (SC), Body Centered Cubic (BCC), Face Centered Cubic (FCC), and Random. (a.2) *In silico* relaxation tests for BCC (left) and Random (right) arrangement of the particles. Magnetic Boundary Conditions: modeling framework based on the reproduction of the entire boundary value problem of the rheometer setup. (b.1) It allows to reproduce the real magnetic boundary conditions of and adjust it to achieve (b.2) functional deformations of pre-magnetized hMRE structures, i.e., a 4 mm and 20 mm diameter disks, a bending beam and a four-arm soft robot. Autonomous Self-healing MREs: conceptualization of pre-magnetized hard-magnetic/hybrid MREs able to provide structural support even after complete rupture. (c.1) Experimental demonstration of the healing mechanism. (c.2) The healing mechanism is based on the magneto-mechanical coupling and allows an unlimited number of healing cycles. (c.3) Conceptualization and design of functional sensors based on strain thresholds. (c.4) No material degradation during cyclic loading.

Appendix

The Appendix contains three appendices with additional results for the Experimental, Modeling and Applications chapters.

A.1 Experimental

A.1.1 Amplitude sweep tests for soft-magnetic MREs

Amplitude sweep tests in the rheometer provide guidance to choose the constant strain amplitude for the oscillatory shear tests. Figure A.1 depicts the evolution of the shear moduli with the strain amplitude, for several deformation rates and magnetic field conditions. Under magnetic actuation (Figure A.1.b), note that the shear moduli become less sensitive to the strain amplitude for increasing strain values.

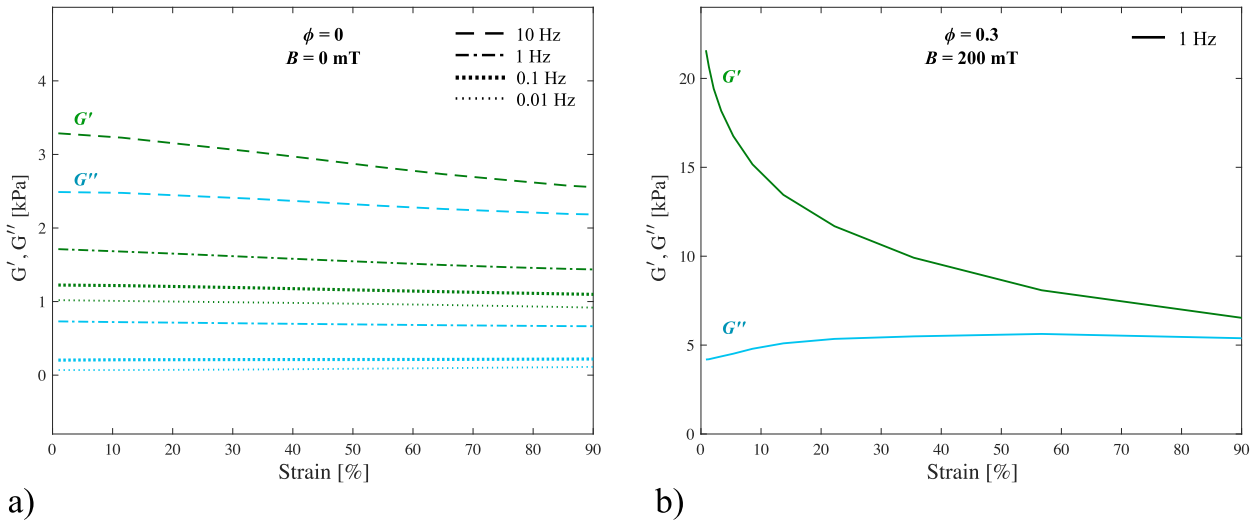

Figure A.1: Amplitude sweeps to determine the influence of the strain amplitude in shear deformation mode. (a) With null magnetic field and frequencies of $f = \{0.01, 0.1, 1, 10\}$ Hz; (b) with a magnetic field of 200 mT and angular velocity 1 Hz. The sensitivity of the shear moduli to the strain amplitude decreases at larger strain amplitudes.

A.1.2 Rheological characterization of the carrier matrix (ultra-soft PDMS)

This section contains the characterization of the PDMS matrix, i.e., no magnetic fillers, under oscillatory and axial frequency sweeps, see Figure A.2.

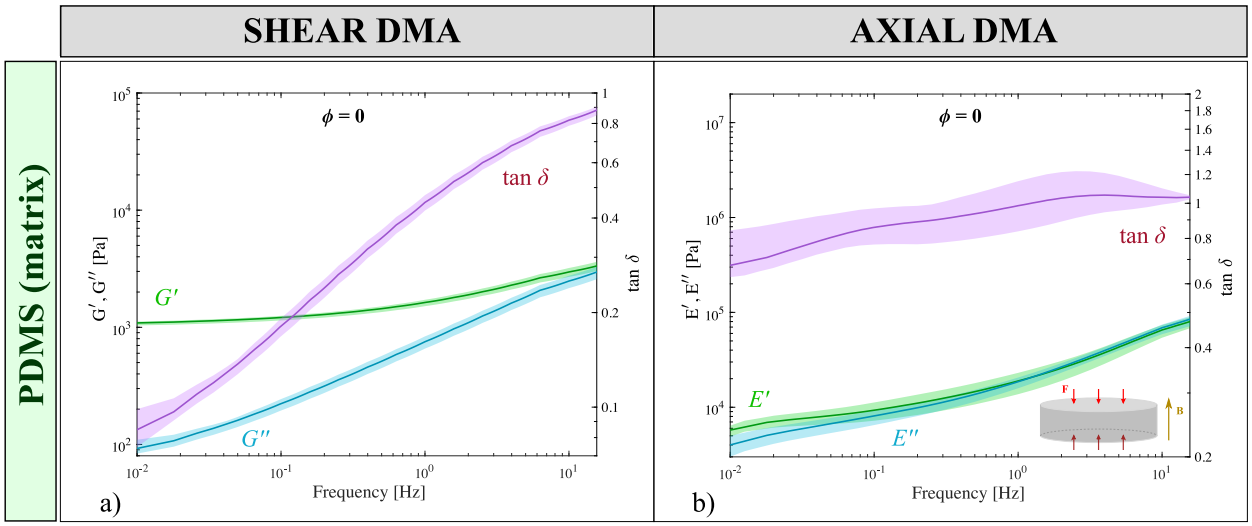

Figure A.2: Experimental results for frequency sweeps from 0.01 to 16 Hz under (a) shear and (b) uniaxial compressive DMA on 1 mm height and 20 mm diameter cylindrical PDMS samples, i.e., no magnetic particles. Storage shear/axial moduli (G', E'), loss moduli (G'', E'') and loss factor ($\tan\delta$) are plotted against the frequency. Scatter areas around each mean curve are depicted to quantify the variability of experimental data sets.

A.1.3 Results for DMA tests on sMREs with matrices of different stiffness

Figures A.3, A.4, A.5 and A.6 contain the raw results from the frequency sweeps in axial and oscillatory modes for the sMREs with matrices of different stiffness (i.e., different elastomeric mixing ratio).

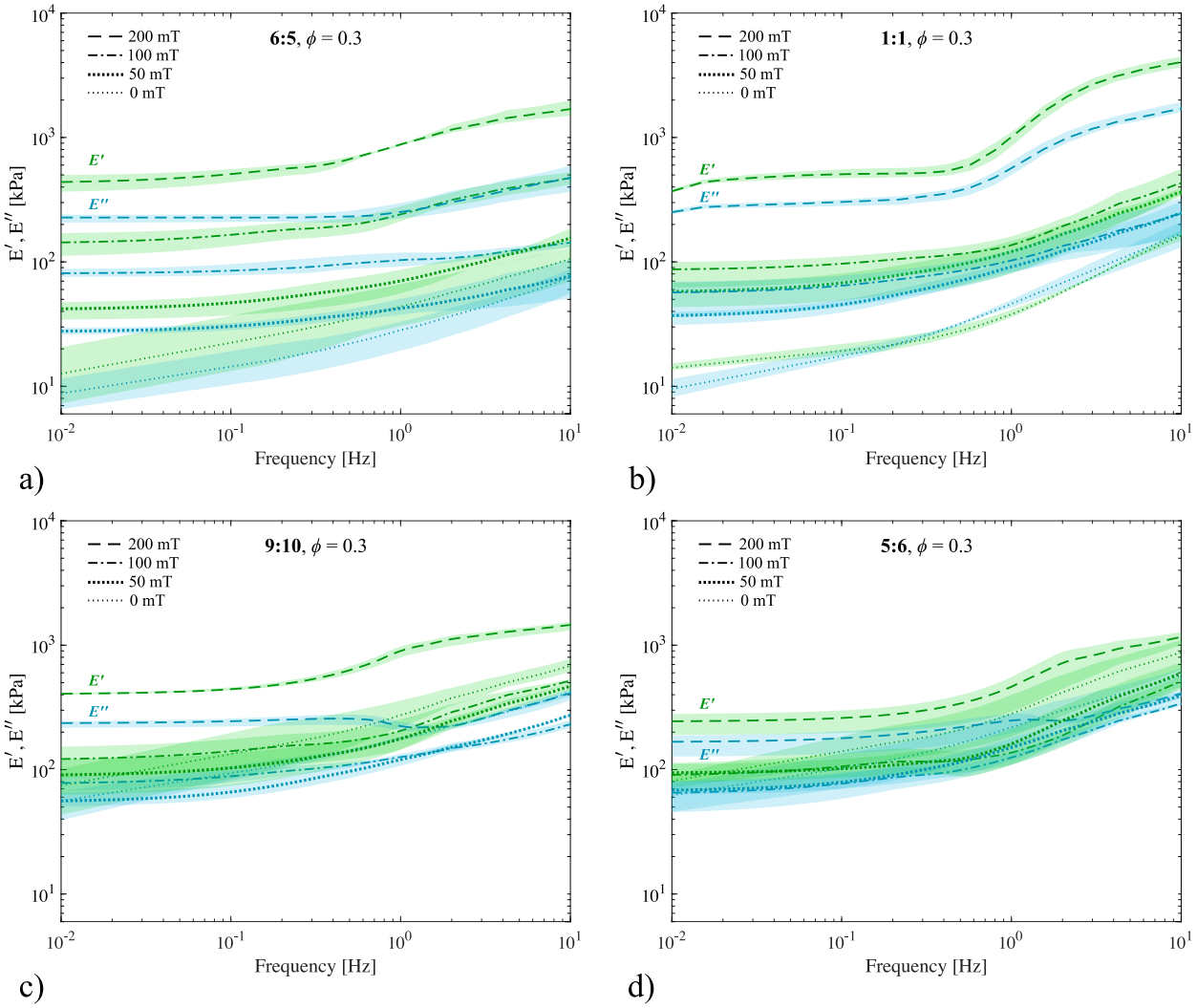

Figure A.3: Frequency-dependent behavior of the 30 % magnetic particles' ratio sMRE under macroscopic axial deformation for different manufacturing conditions and magnetic stimulation. The experimental results for frequency sweeps from 0.01 Hz to 10 Hz under compressive DMA and over MRE substrates with manufacturing mixing ratios of 6:5, 1:1, 9:10 and 5:6 are presented by means of the storage modulus (E') and loss modulus (E''). Magnetic fields of (a) 0 mT, (b) 50 mT, (c) 100 mT and (d) 200 mT are externally applied on the samples. Scatter areas are plotted around the mean curves computed from all data sets.

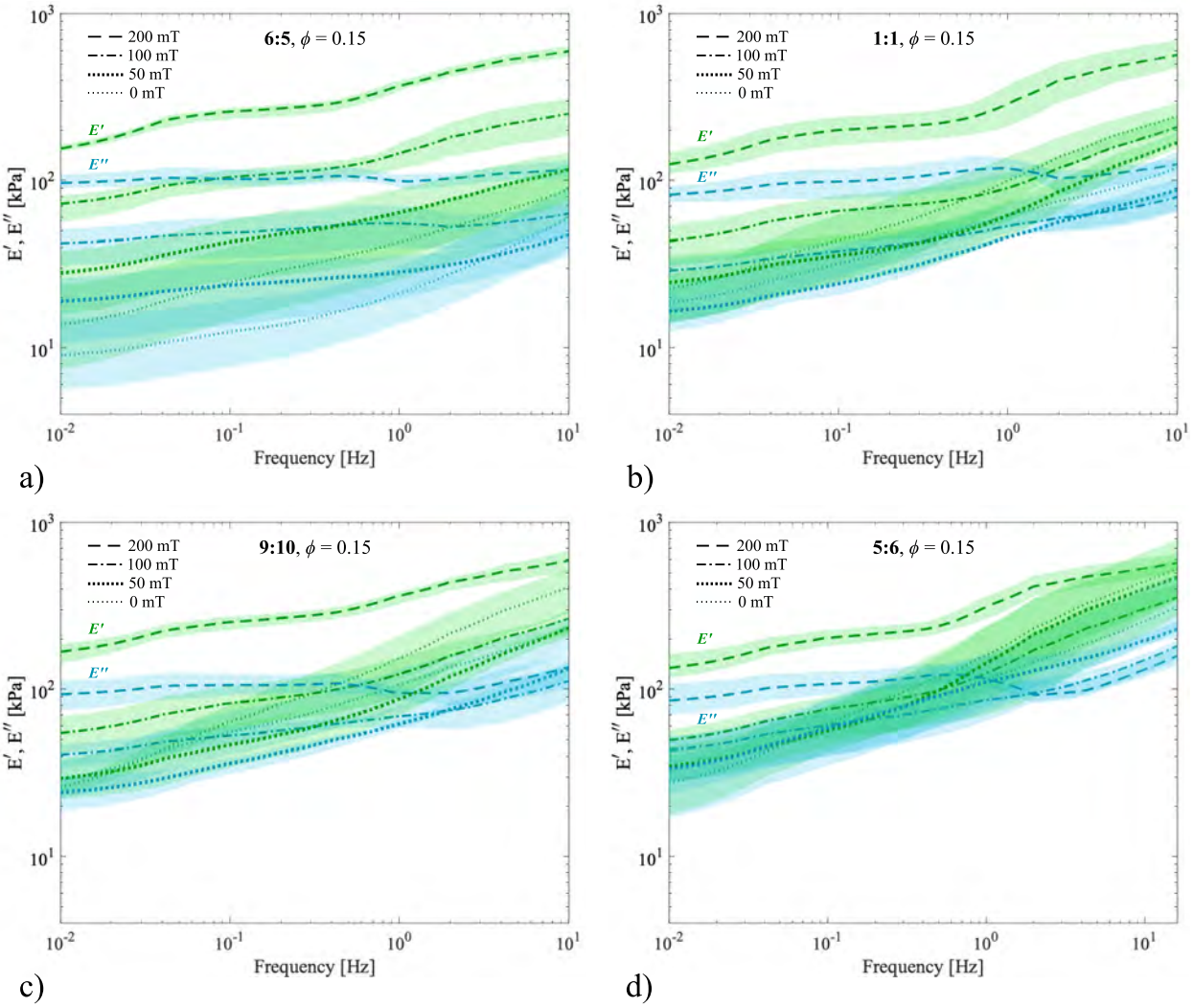

Figure A.4: Frequency-dependent behavior of the 15 % magnetic particles' ratio sMRE under macroscopic axial deformation for different manufacturing conditions and magnetic stimulation. The experimental results for frequency sweeps from 0.01 Hz to 10 Hz under compressive DMA and over MRE substrates with manufacturing mixing ratios of 6:5, 1:1, 9:10 and 5:6 are presented by means of the storage modulus (E') and loss modulus (E''). Magnetic fields of (a) 0 mT, (b) 50 mT, (c) 100 mT and (d) 200 mT are externally applied on the samples. Scatter areas are plotted around the mean curves computed from all data sets.

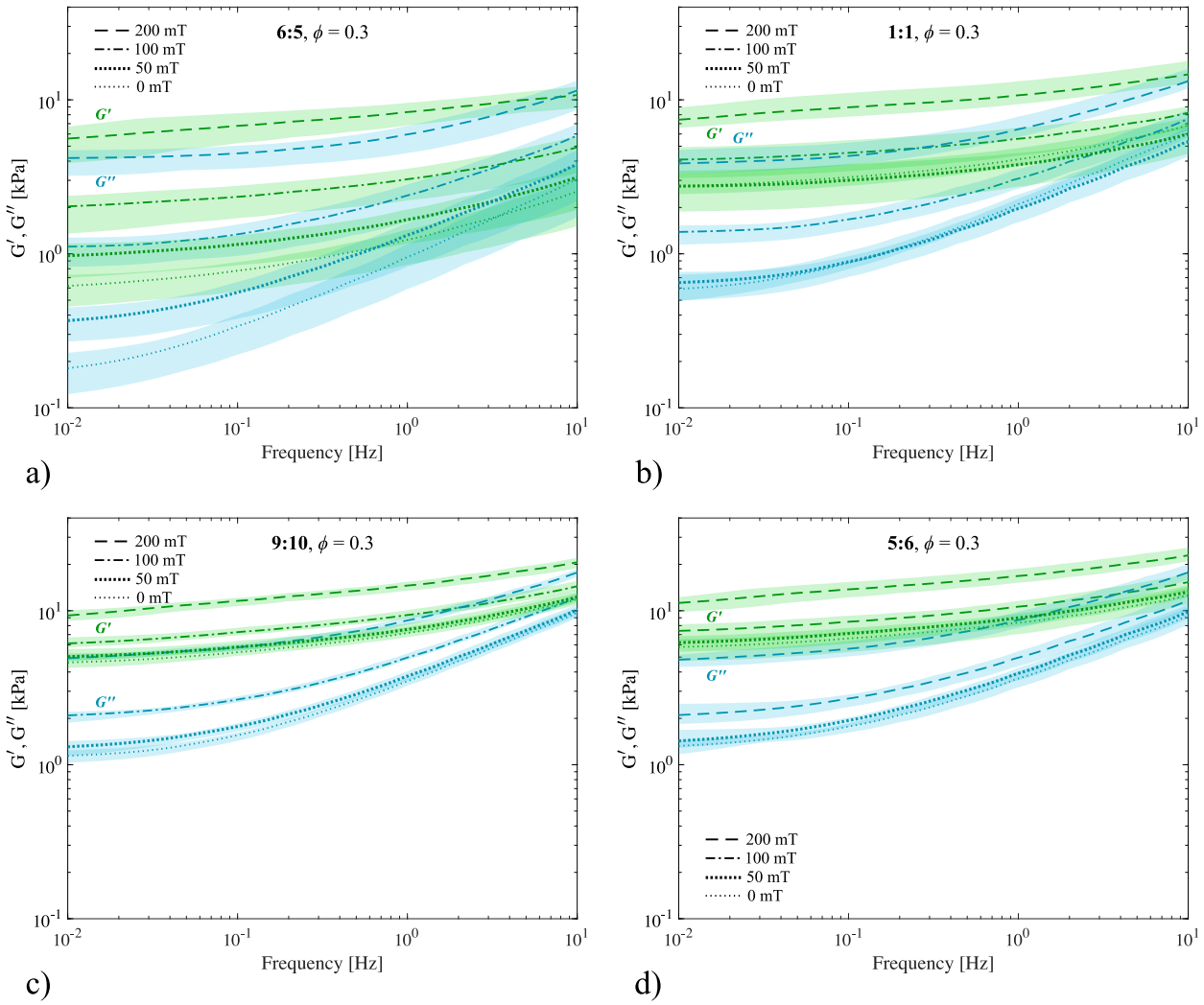

Figure A.5: Frequency-dependent behavior of the 30 % magnetic particles' ratio sMRE under macroscopic shear deformation for different manufacturing conditions and magnetic stimulation. The experimental results for frequency sweeps from 0.01 Hz to 10 Hz under compressive DMA and over MRE substrates with manufacturing mixing ratios of 6:5, 1:1, 9:10 and 5:6 are presented by means of the storage shear modulus (G') and loss shear modulus (G''). Magnetic fields of (a) 0 mT, (b) 50 mT, (c) 100 mT and (d) 200 mT are externally applied on the samples. Scatter areas are plotted around the mean curves computed from all data sets.

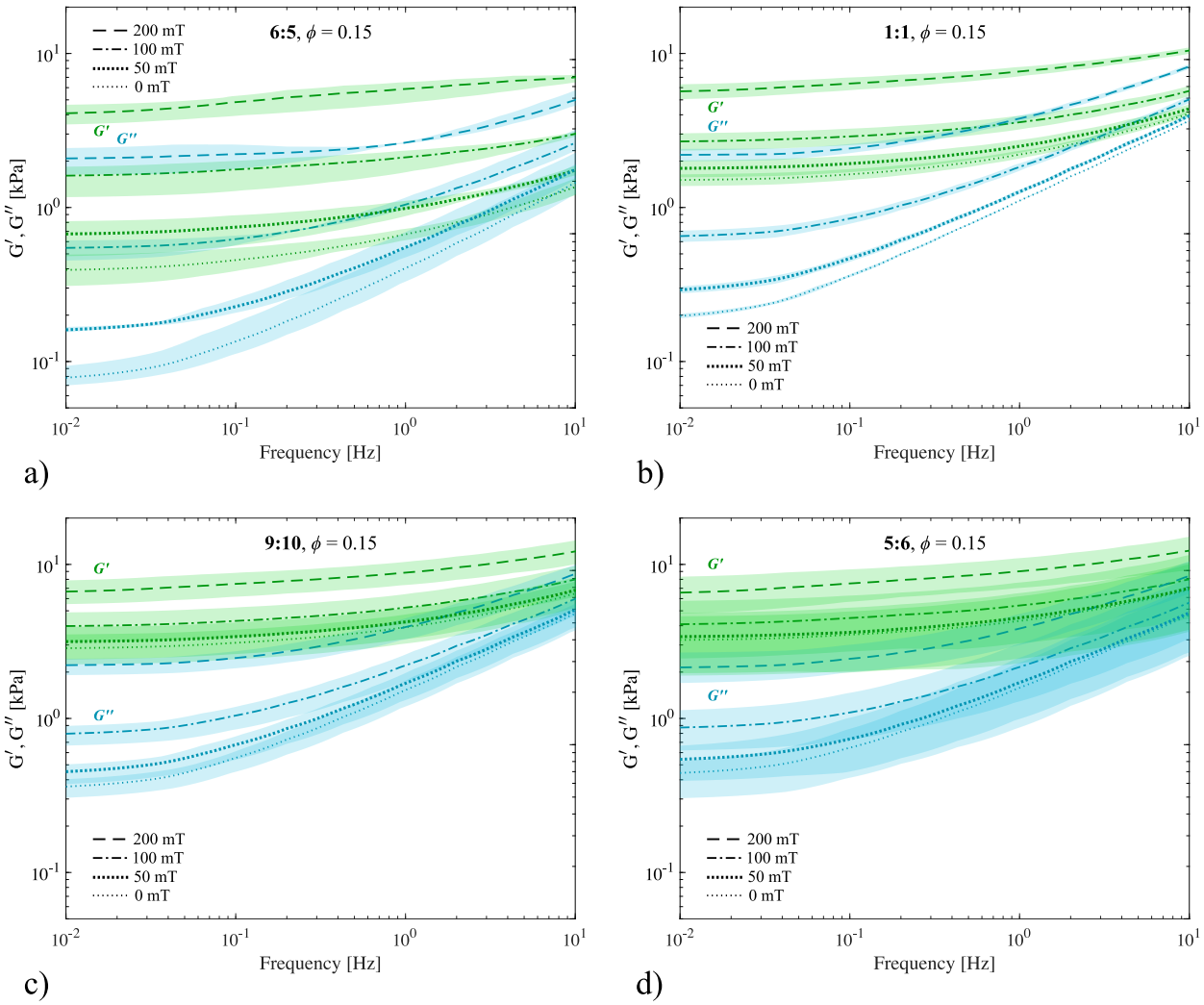

Figure A.6: Frequency-dependent behavior of the 15 % magnetic particles' ratio sMRE under macroscopic shear deformation for different manufacturing conditions and magnetic stimulation. The experimental results for frequency sweeps from 0.01 Hz to 10 Hz under compressive DMA and over MRE substrates with manufacturing mixing ratios of 6:5, 1:1, 9:10 and 5:6 are presented by means of the storage shear modulus (G') and loss shear modulus (G''). Magnetic fields of (a) 0 mT, (b) 50 mT, (c) 100 mT and (d) 200 mT are externally applied on the samples. Scatter areas are plotted around the mean curves computed from all data sets.

A.2 Modeling

A.2.1 Magnetic behavior of the soft-/hard-magnetic particles

Soft-magnetic particles have a large magnetic susceptibility but a low coercivity. On the contrary, hard-magnetic particles have a low magnetic susceptibility but a high magnetic coercivity. Figure A.7 illustrates such a magnetic behavior of both types of fillers.

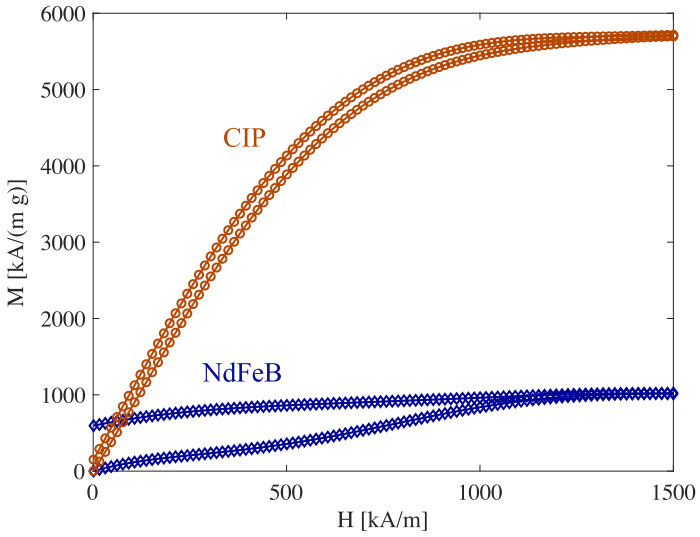

Figure A.7: Magnetization curves for BASF carbonyl iron powder (CIP) and Magnequench NdFeB MQP-S-11-9 (adapted from [307]).

A.2.2 Calibration of the residual magnetization ($\mathbb{H}_\mathbf{r}$)

The remanent magnetic field within hard-magnetic particles is prescribed as a constant value. To determine it, an inverse engineering approach is followed. After experimentally pre-magnetizing a hMRE sample under 1 T, we measured the magnetic induction on its surface. Then, the remanent field in the particles is adjusted so that the magnetization of the homogenization model fits the macroscopic experimental measurement. To this end, we take a representative sample of hMRE with 30 vol.%, according to the experiment. The sample is surrounded by air and uniquely subjected to the residual magnetization of the particles via $\mathbb{H}_\mathrm{r}$, see Figure A.8. Therefore, in this simulation, no external magnetization is applied, no periodic boundary conditions are set and no macroscopic fields are prescribed. In addition, this methodology allows for estimating the macroscopic remanent magnetization of hybrid MREs, see results in Figure A.8.

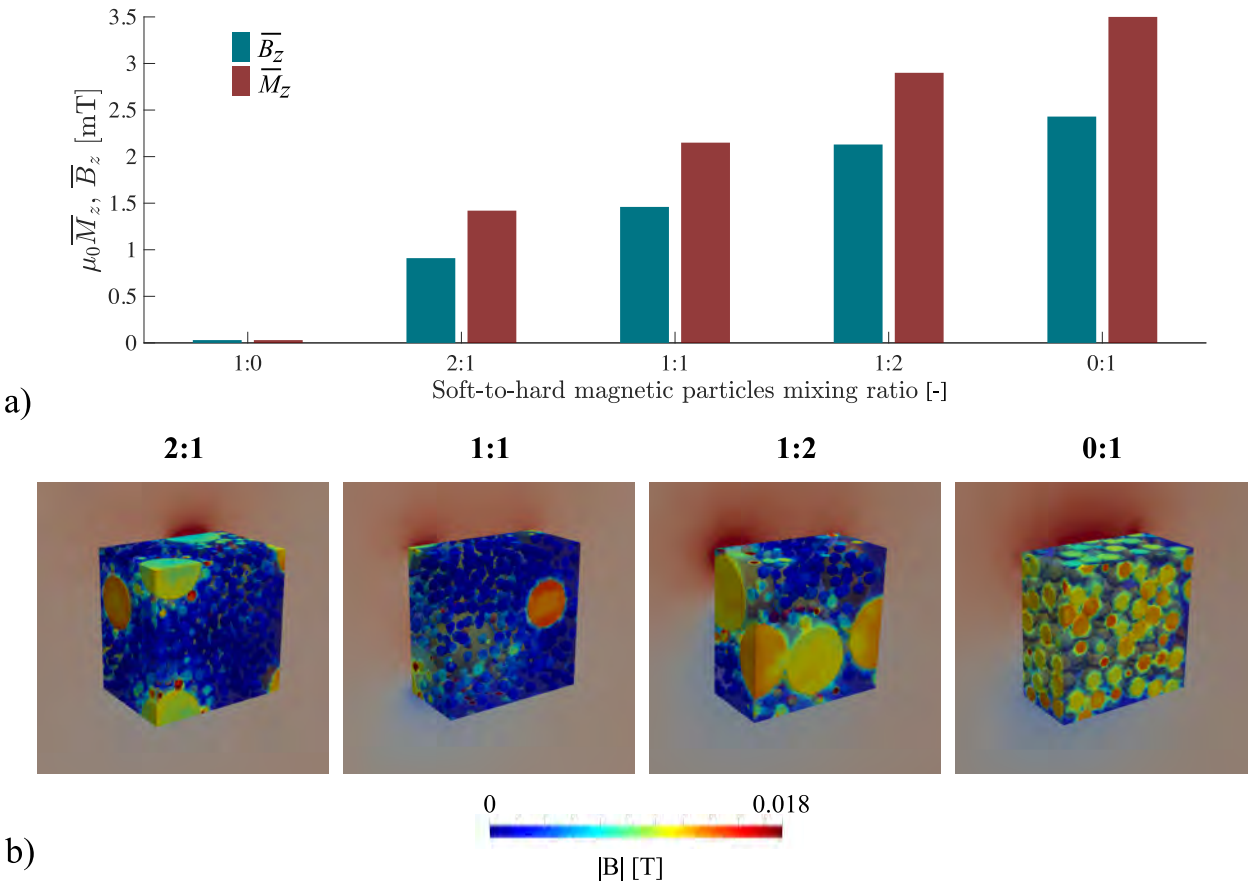

Figure A.8: Calibration procedure of the remanent magnetic field. In the absence of external magnetic actuation on a pre-magnetized MREs, the homogeneous magnetic induction within the pre-magnetized MREs is different than zero. (a) Homogeneous macroscopic magnetic induction and magnetization within the RVE in the direction of the pre-magnetization of the hard-magnetic particles and depending on the soft-to-hard particles mixing ratio. (b) Magnetic field magnitude in MRE samples for different mixing ratios. The sample is surrounded by air to model the experimental measuring of the remanent macroscopic field with the teslameter and perform the calibration.

A.2.3 Calibration of the Generalized neo-Hookean model with uncut samples

Tensile tests on uncut samples allowed the calibration of the mechanical material parameters. The parameter b was set to 1 to mimic, at small strains, a neo-Hookean material. Then, the shear modulus G and exponent n are obtained for virgin and for pre-magnetized hMREs by fitting the curve from the numerical model with the experimental ones. The mechanical contribution in the numerical model is calibrated from experimental results for tensile tests on virgin samples (blue curves in Figure A.9.a) and the magnetic fields for the pre-magnetization condition are included through a magnetic constitutive extension of the model. However, for the estimation of the J-integral on pre-magnetized specimens, the analytical GNH model is used without any magnetic extension, hence the GNH parameters are calibrated to include the magnetorheological effect (purple curves in Figure A.9.a). Note that the fitting is done up to 1.4 logarithmic strain. Moreover, the barplot in Figure A.9.b shows the fracture energy density as a function of the cut-width ratio, including the uncut case.

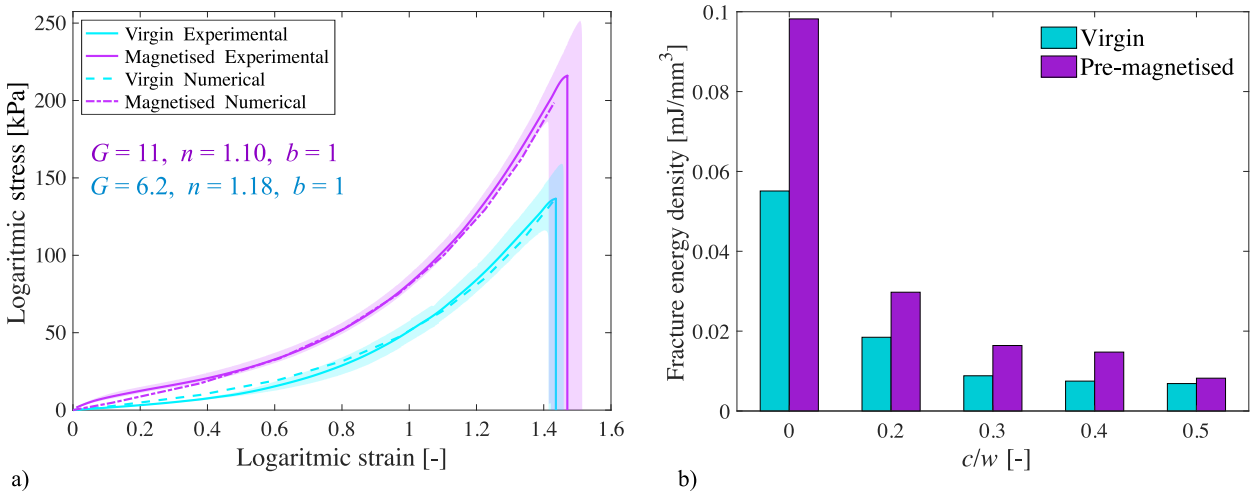

Figure A.9: Results for uncut virgin and pre-magnetized hMRE samples. (a) Calibration of the material parameters of the Generalized neo-Hookean model with uniaxial tensile tests on uncut samples. A numerical model without damage field provides the numerical stress-strain curve as a function of the material parameters. These are fitted so that the numerical curve fits the experimental ones for uncut virgin and pre-magnetized hMREs with initial length $l_0 = 30$ mm. (b) Barplot with the experimental fracture energy density of virgin and pre-magnetized samples as a function of the cut length ratio for $l_0 = 30$ mm, including the results for the uncut case for initial length $l_0 = 30$ mm.

A.2.4 Experimental estimation of the critical energy release rate (G_c)

The calibration of the critical energy release rate G_c is achieved from experimental force-displacement rupture curves for cracks of 2 and 5 mm. The area between both curves provides G_c, according to figure A.10. Note that this is an average estimation from the shortest crack to the largest one.

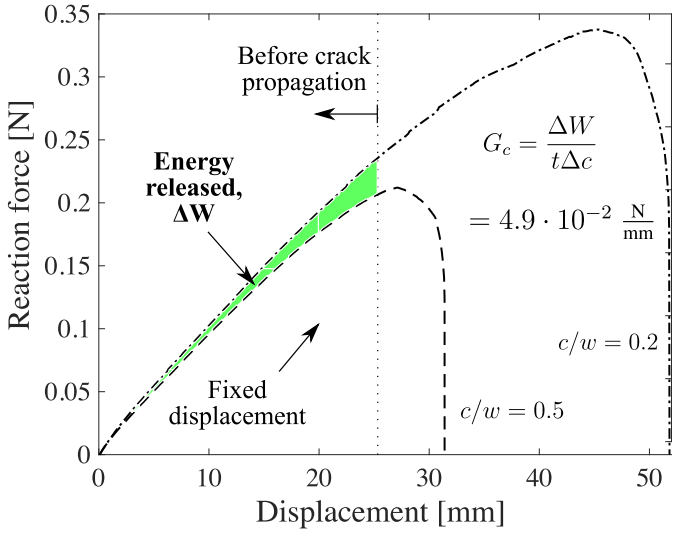

Figure A.10: Experimental estimation of the critical energy release rate to be used in the phase-field model. To provide an average estimation, it is calculated as the energy released between 2 mm and 5 mm cracks at a displacement of 25 mm.

A.3 Applications

A.3.1 Estimation of J-integral for alternative annular grids

Figure A.11 contains additional results for alternative annular grids. This confirms that the fitting grid to estimate the J-integral does not influence the tendencies found.

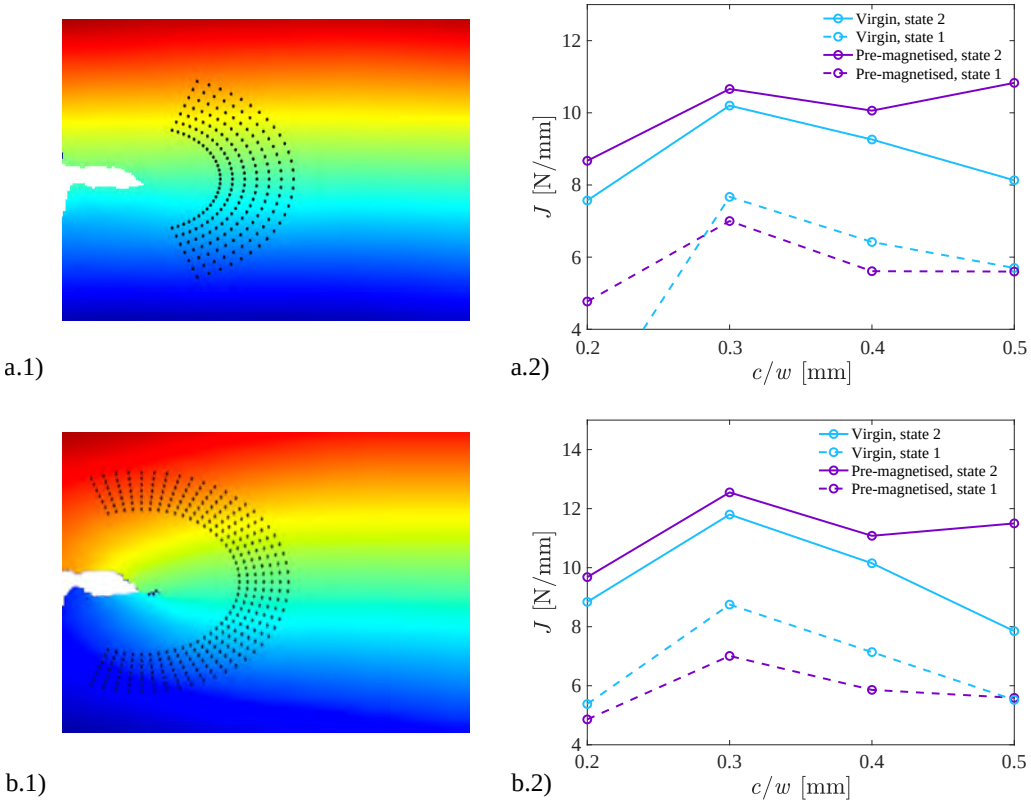

Figure A.11: Additional results for the estimation of the J-integral for two different annular grids. (a.1) Annular grid 1 with a smaller final angle and (b.1) annular grid 2 with a larger inner radius. (a.2), (b.2) Results for J-integral for the alternative fitting grids. The results prove the independence of J with the grid.

Bibliography

[1] Yu, K., Xin, A. & Wang, Q. Mechanics of light-activated self-healing polymer networks. *Journal of the Mechanics and Physics of Solids* **124**, 643–662 (2019).

[2] Jiao, P., Chen, T. & Xie, Y. Self-adaptive mechanical metamaterials (smm) using shape memory polymers for programmable postbuckling under thermal excitations. *Composite Structures* **256**, 113053 (2021).

[3] Zare, M., Prabhakaran, M. P., Parvin, N. & Ramakrishna, S. Thermally-induced two-way shape memory polymers: Mechanisms, structures, and applications. *Chemical Engineering Journal* **374**, 706–720 (2019).

[4] Tajeddini, V. & Muliana, A. Deformations of flexible and foldable electro-active composite structures. *Composite Structures* **160**, 280–291 (2017).

[5] dos Santos, C. R., Pacheco, D. R., Taha, H. E. & Zakaria, M. Y. Nonlinear modeling of electro-aeroelastic dynamics of composite beams with piezoelectric coupling. *Composite Structures* **255**, 112968 (2021).

[6] Zhang, C. *et al.* A ph-sensitive coordination polymer network-based nanoplatform for magnetic resonance imaging-guided cancer chemo-photothermal synergistic therapy. *Nanomedicine: Nanotechnology, Biology and Medicine* **23**, 102071 (2020).

[7] Kim, Y., Yuk, H., Zhao, R., Chester, S. A. & Zhao, X. *Printing ferromagnetic domains for untethered fast-transforming soft materials*, vol. 558 (Nature Publishing Group, 2018).

[8] Wang, T. *et al.* Adaptive wireless millirobotic locomotion into distal vasculature. *Nature Communications* **13**, 4465 (2022).

[9] Wu, S., Hu, W., Ze, Q., Sitti, M. & Zhao, R. Multifunctional magnetic soft composites: a review. *Multifunctional Materials* **3**, 042003 (2020).

[10] Stepanov, G. V. *et al.* Magnetoactive elastomer based on magnetically hard filler: Synthesis and study of viscoelastic and damping properties. *Polymer Science Series A* **56**, 603–613 (2014).

[11] Böse, H. Viscoelastic properties of silicone-based magnetorheological elastomers. *International Journal of Modern Physics B* **21**, 4790–4797 (2007).

[12] Becker, T., Zimmermann, K., Borin, D., Stepanov, G. & Storozhenko, P. Dynamic response of a sensor element made of magnetic hybrid elastomer with controllable properties. *Journal of Magnetism and Magnetic Materials* **449**, 77–82 (2018).

[13] Koo, J.-H., Dawson, A. & Jung, H.-J. Characterization of actuation properties of magnetorheological elastomers with embedded hard magnetic particles. *Journal of Intelligent Material Systems and Structures* **23**, 1049–1054 (2012).

[14] Lei, Y. *et al.* Building magnetoresponsive composite elastomers for bionic locomotion applications. *Journal of Bionic Engineering* **17**, 405–420 (2020).

[15] Lee, H. *et al.* 3d-printed programmable tensegrity for soft robotics. *Science Robotics* **5** (2020).

[16] Song, H. *et al.* Reprogrammable ferromagnetic domains for reconfigurable soft magnetic actuators. *Nano Letters* **20**, 5185–5192 (2020).

[17] Xu, C., Yang, Z. & Lum, G. Z. Small-scale magnetic actuators with optimal six degrees-of-freedom. *Advanced Materials* **33**, 2100170 (2021).

[18] Xu, T., Zhang, J., Salehizadeh, M., Onaizah, O. & Diller, E. Millimeter-scale flexible robots with programmable three-dimensional magnetization and motions. *Science Robotics* **4** (2019).

[19] Ze, Q. *et al.* Magnetic shape memory polymers with integrated multifunctional shape manipulation. *Advanced Materials* **32**, 1906657 (2020).

[20] Wallin, T. J., Pikul, J. & Shepherd, R. F. 3d printing of soft robotic systems. *Nature Reviews Materials* **3**, 84–100 (2018).

[21] Dong, X. *et al.* Bioinspired cilia arrays with programmable nonreciprocal motion and metachronal coordination. *Science Advances* **6** (2020).

[22] Son, D., Ugurlu, M. C. & Sitti, M. Permanent magnet array–driven navigation of wireless millirobots inside soft tissues. *Science Advances* **7** (2021).

[23] Eshaghi, M., Ghasemi, M. & Khorshidi, K. Design, manufacturing and applications of small-scale magnetic soft robots. *Extreme Mechanics Letters* **44**, 101268 (2021).

[24] Hu, W., Lum, G. Z., Mastrangeli, M. & Sitti, M. Small-scale soft-bodied robot with multimodal locomotion. *Nature* **554**, 81–85 (2018).

[25] Kim, Y., Parada, G. A., Liu, S. & Zhao, X. Ferromagnetic soft continuum robots. *Science Robotics* **4** (2019).

[26] Lu, H. *et al.* A bioinspired multilegged soft millirobot that functions in both dry and wet conditions. *Nature Communications* **9**, 3944 (2018).

[27] Lum, G. Z. *et al.* Shape-programmable magnetic soft matter. *Proceedings of the National Academy of Sciences* **113**, E6007–E6015 (2016).

[28] Ren, Z., Hu, W., Dong, X. & Sitti, M. Multi-functional soft-bodied jellyfish-like swimming. *Nature Communications* **10**, 2703 (2019).

[29] Cabanach, P. *et al.* Zwitterionic 3d-printed non-immunogenic stealth microrobots. *Advanced Materials* **32**, 2003013 (2020).

[30] Wang, L., Kim, Y., Guo, C. F. & Zhao, X. Hard-magnetic elastica. *Journal of the Mechanics and Physics of Solids* **142**, 104045 (2020).

[31] Wang, L. *et al.* Evolutionary design of magnetic soft continuum robots. *Proceedings of the National Academy of Sciences* **118**, e2021922118 (2021).

[32] Zhang, J. *et al.* Liquid crystal elastomer-based magnetic composite films for reconfigurable shape-morphing soft miniature machines. *Advanced Materials* **33**, 2006191 (2021).

[33] Hohlbein, N., Shaaban, A. & Schmidt, A. Remote-controlled activation of self-healing behavior in magneto-responsive ionomeric composites. *Polymer* **69**, 301–309 (2015).

[34] Gaddes, D. *et al.* Self-healing textile: Enzyme encapsulated layer-by-layer structural proteins. *ACS Applied Materials & Interfaces* **8**, 20371–20378 (2016).

[35] Novelino, L. S., Ze, Q., Wu, S., Paulino, G. H. & Zhao, R. Untethered control of functional origami microrobots with distributed actuation. *Proceedings of the National Academy of Sciences* **117**, 24096–24101 (2020).

[36] Pena-Francesch, A., Jung, H., Demirel, M. C. & Sitti, M. Biosynthetic self-healing materials for soft machines. *Nature Materials* **19**, 1230–1235 (2020).

[37] Montgomery, S. M. *et al.* Magneto-mechanical metamaterials with widely tunable mechanical properties and acoustic bandgaps. *Advanced Functional Materials* **31**, 2005319 (2021).

[38] Sun, C. *et al.* Unconventional deformation and sound absorption properties of anisotropic magnetorheological elastomers. *Smart Materials and Structures* **30**, 105022 (2021).

[39] Charles, A. D., Rider, A. N., Brown, S. A. & Wang, C. H. Multifunctional magneto-polymer matrix composites for electromagnetic interference suppression, sensors and actuators. *Progress in Materials Science* **115**, 100705 (2021).

[40] Yimyai, T., Pena-Francesch, A. & Crespy, D. Transparent and self-healing elastomers for reconfigurable 3d materials. *Macromolecular Rapid Communications* 2200554 (2022).

[41] Abramchuk, S. *et al.* Novel highly elastic magnetic materials for dampers and seals: part ii. material behavior in a magnetic field. *Polymers for Advanced Technologies* **18**, 513–518 (2007).

[42] Najgebauer, M. *et al.* Magnetic composites in electric motors (2018).

[43] Schümann, M. & Odenbach, S. In-situ observation of the particle microstructure of magnetorheological elastomers in presence of mechanical strain and magnetic fields. *Journal of Magnetism and Magnetic Materials* **441**, 88–92 (2017).

[44] Dargahi, A., Sedaghati, R. & Rakheja, S. On the properties of magnetorheological elastomers in shear mode: Design, fabrication and characterization. *Composites Part B: Engineering* **159**, 269–283 (2019).

[45] Vatandoost, H., Hemmatian, M., Sedaghati, R. & Rakheja, S. Dynamic characterization of isotropic and anisotropic magnetorheological elastomers in the oscillatory squeeze mode superimposed on large static pre-strain. *Composites Part B: Engineering* **182**, 107648 (2020).

[46] Stepanov, G., Chertovich, A. & Kramarenko, E. Magnetorheological and deformation properties of magnetically controlled elastomers with hard magnetic filler. *Journal of Magnetism and Magnetic Materials* **324**, 3448–3451 (2012).

[47] Stepanov, G. V., Borin, D. Y., Bakhtiiarov, A. V., Lobanov, D. A. & Storozhenko, P. A. Ring-like structures in magnetoactive elastomers based on magnetic hard powder. *Smart Materials and Structures* **30**, 015023 (2021).

[48] Morillas, J. R. & de Vicente, J. Magnetorheology: a review. *Soft Matter* **16**, 9614–9642 (2020).

[49] Danas, K., Kankanala, S. & Triantafyllidis, N. Experiments and modeling of iron-particle-filled magnetorheological elastomers. *Journal of the Mechanics and Physics of Solids* **60**, 120–138 (2012).

[50] Gordaninejad, F., Wang, X. & Mysore, P. Behavior of thick magnetorheological elastomers. *Journal of Intelligent Material Systems and Structures* **23**, 1033–1039 (2012).

[51] Kallio, M. The elastic and damping properties of magnetorheological elastomers. *VTT Publications* 3–146 (2005).

[52] Schubert, G. & Harrison, P. Large-strain behaviour of magneto-rheological elastomers tested under uniaxial compression and tension, and pure shear deformations. *Polymer Testing* **42**, 122–134 (2015).

[53] Schubert, G. & Harrison, P. Equi-biaxial tension tests on magneto-rheological elastomers. *Smart Materials and Structures* **25**, 015015 (2016).

[54] Burhannuddin, N. L. *et al.* Physicochemical characterization and rheological properties of magnetic elastomers containing different shapes of corroded carbonyl iron particles. *Scientific Reports* **11**, 868 (2021).

[55] Lucarini, S., Hossain, M. & Garcia-Gonzalez, D. Recent advances in hard-magnetic soft com-

posites: Synthesis, characterisation, computational modelling, and applications. *Composite Structures* **279**, 114800 (2022).

[56] Stepanov, G. *et al.* Effect of a homogeneous magnetic field on the viscoelastic behavior of magnetic elastomers. *Polymer* **48**, 488–495 (2007).

[57] Bastola, A. K. & Hossain, M. A review on magneto-mechanical characterizations of magnetorheological elastomers. *Composites Part B: Engineering* **200**, 108348 (2020).

[58] Kramarenko, E. Y. *et al.* Magnetic and viscoelastic response of elastomers with hard magnetic filler. *Smart Materials and Structures* **24**, 035002 (2015).

[59] Stepanov, G., Borin, D., Bakhtiiarov, A. & Storozhenko, P. Influence of the size of magnetic filler particles on the properties of hybrid magnetic elastomer with magnetically hard filler. *Journal of Magnetism and Magnetic Materials* **498**, 166071 (2020).

[60] Antonel, P. S. *et al.* Magnetic and elastic properties of cofe ¡sub¿2¡/sub¿ o ¡sub¿4¡/sub¿ - polydimethylsiloxane magnetically oriented elastomer nanocomposites. *Journal of Applied Physics* **110**, 043920 (2011).

[61] Dorn, C., Bodelot, L. & Danas, K. Experiments and numerical implementation of a boundary value problem involving a magnetorheological elastomer layer subjected to a nonuniform magnetic field. *Journal of Applied Mechanics* **88** (2021).

[62] Koo, J.-H., Khan, F., Jang, D.-D. & Jung, H.-J. Dynamic characterization and modeling of magneto-rheological elastomers under compressive loadings. *Smart Materials and Structures* **19**, 117002 (2010).

[63] Pelteret, J.-P. & Steinmann, P. *Magneto-Active Polymers: Fabrication, characterisation, modelling and simulation at the micro- and macro-scale* (De Gruyter, 2020).

[64] Agirre-Olabide, I., Berasategui, J., Elejabarrieta, M. J. & Bou-Ali, M. M. Characterization of the linear viscoelastic region of magnetorheological elastomers. *Journal of Intelligent Material Systems and Structures* **25**, 2074–2081 (2014).

[65] Hemmatian, M., Sedaghati, R. & Rakheja, S. Characterization and modeling of temperature effect on the shear mode properties of magnetorheological elastomers. *Smart Materials and Structures* **29**, 115001 (2020).

[66] Nam, T. H., Petríková, I. & Marvalová, B. Experimental characterization and viscoelastic modeling of isotropic and anisotropic magnetorheological elastomers. *Polymer Testing* **81**, 106272 (2020).

[67] Narayan, S. A. & Palade, L. I. Modeling payne effect with a framework of multiple natural configurations. *International Journal of Engineering Science* **157**, 103396 (2020).

[68] Laun, H. M., Schmidt, G., Gabriel, C. & Kieburg, C. Reliable plate–plate mrf magnetorheometry based on validated radial magnetic flux density profile simulations. *Rheologica Acta* **47**, 1049–1059 (2008).

[69] MacManus, D. B., Murphy, J. G. & Gilchrist, M. D. Mechanical characterisation of brain tissue up to 35strain at 1, 10, and 100/s using a custom-built micro-indentation apparatus. *Journal of the Mechanical Behavior of Biomedical Materials* **87**, 256–266 (2018).

[70] Qian, L. *et al.* Influence of strain rate on indentation response of porcine brain. *Journal of the Mechanical Behavior of Biomedical Materials* **82**, 210–217 (2018).

[71] Pei, S. *et al.* Instrumented nanoindentation in musculoskeletal research. *Progress in Biophysics and Molecular Biology* (2022).

[72] Xu, D. *et al.* Measuring the elastic modulus of soft biomaterials using nanoindentation. *Journal of the Mechanical Behavior of Biomedical Materials* **133**, 105329 (2022).

[73] Hamm, E., Reis, P., LeBlanc, M., Roman, B. & Cerda, E. Tearing as a test for mechanical characterization of thin adhesive films. *Nature Materials* **7**, 386–390 (2008).

[74] Han, G., Marimuthu, K. P. & Lee, H. Evaluation of thin film material properties using a deep nanoindentation and ann. *Materials & Design* **221**, 111000 (2022).

[75] Liu, T., Gaillard, Y., Butaud, P., Placet, V. & Ouisse, M. In situ damping identification of plant fiber composites using dynamic grid nanoindentation. *Composites Part A: Applied Science and Manufacturing* 107158 (2022).

[76] Wang, K., Gao, W., Wang, X. & He, H. Quasi-static and dynamic nanoindentation of particle-reinforced soft composites. *Journal of Applied Polymer Science* **134** (2017).

[77] Gorodkin, S. R., James, R. O. & Kordonski, W. I. Magnetic properties of carbonyl iron particles in magnetorheological fluids. *Journal of Physics: Conference Series* **149**, 012051 (2009).

[78] Liu, T.-Y., Hu, S.-H., Liu, D.-M., Chen, S.-Y. & Chen, I.-W. Biomedical nanoparticle carriers with combined thermal and magnetic responses. *Nano Today* **4**, 52–65 (2009).

[79] Khairi, M. H. A. *et al.* Role of additives in enhancing the rheological properties of magnetorheological solids: A review. *Advanced Engineering Materials* **21**, 1800696 (2019).

[80] Chen, L. *et al.* Investigation on magnetorheological elastomers based on natural rubber. *Journal of Materials Science* **42**, 5483–5489 (2007).

[81] Cvek, M., Kracalik, M., Sedlacik, M., Mrlik, M. & Sedlarik, V. Reprocessing of injection-molded magnetorheological elastomers based on tpe matrix. *Composites Part B: Engineering* **172**, 253–261 (2019).

[82] Kallio, M. *et al.* Dynamic compression testing of a tunable spring element consisting of a magnetorheological elastomer. *Smart Materials and Structures* **16**, 506–514 (2007).

[83] Li, Y., Li, J., Li, W. & Du, H. A state-of-the-art review on magnetorheological elastomer devices. *Smart Materials and Structures* **23**, 123001 (2014).

[84] Raj, K., Moskowitz, B. & Casciari, R. Advances in ferrofluid technology. *Journal of Magnetism and Magnetic Materials* **149**, 174–180 (1995).

[85] Ubaidillah, Sutrisno, J., Purwanto, A. & Mazlan, S. A. Recent progress on magnetorheological solids: Materials, fabrication, testing, and applications. *Advanced Engineering Materials* **17**, 563–597 (2015).

[86] Zhou, G. Y. Shear properties of a magnetorheological elastomer. *Smart Materials and Structures* **12**, 139–146 (2003).

[87] Garcia-Gonzalez, D., Moreno, M. A., Valencia, L., Arias, A. & Velasco, D. Influence of elastomeric matrix and particle volume fraction on the mechanical response of magneto-active polymers. *Composites Part B: Engineering* **215**, 108796 (2021).

[88] Khanouki, M. A., Sedaghati, R. & Hemmatian, M. Experimental characterization and microscale modeling of isotropic and anisotropic magnetorheological elastomers. *Composites Part B: Engineering* **176**, 107311 (2019).

[89] Liu, M., Zhang, M., Zhang, J., Qiao, Y. & Zhai, P. Experimental investigation on the effect of graphene oxide additive on the steady-state and dynamic shear properties of pdms-based magnetorheological elastomer. *Polymers* **13**, 1777 (2021).

[90] Huang, X., Mohla, A., Hong, W., Bastawros, A. F. & Feng, X.-Q. Magnetorheological brush – a soft structure with highly tuneable stiffness. *Soft Matter* **10**, 1537 (2014).

[91] Poojary, U. R., Hegde, S. & Gangadharan, K. V. Experimental investigation on the effect of carbon nanotube additive on the field-induced viscoelastic properties of magnetorheological elastomer. *Journal of Materials Science* **53**, 4229–4241 (2018).

[92] Fang, F. F., Choi, H. J. & Seo, Y. Sequential coating of magnetic carbonyliron particles with polystyrene and multiwalled carbon nanotubes and its effect on their magnetorheology. *ACS Applied Materials & Interfaces* **2**, 54–60 (2010).

[93] Jiang, W. Q., jing Yao, J., long Gong, X. & Chen, L. Enhancement in magnetorheological effect of magnetorheological elastomers by surface modification of iron particles. *Chinese Journal of Chemical Physics* **21**, 87–92 (2008).

[94] Lokander, M., Reitberger, T. & Stenberg, B. Oxidation of natural rubber-based magnetorheological elastomers. *Polymer Degradation and Stability* **86**, 467–471 (2004).

[95] Saxena, P., Pelteret, J. P. & Steinmann, P. Modelling of iron-filled magneto-active polymers with a dispersed chain-like microstructure. *European Journal of Mechanics - A/Solids* **50**, 132–151 (2015).

[96] Swaroop, K., Aruna, M., Kumar, H. & Rahman, M. Investigation of steady state rheological properties and sedimentation of coated and pure carbonyl iron particles based magnetorheological fluids. *Materials Today: Proceedings* (2020).

[97] Khanafer, K., Duprey, A., Schlicht, M. & Berguer, R. Effects of strain rate, mixing ratio, and stress–strain definition on the mechanical behavior of the polydimethylsiloxane (pdms) material as related to its biological applications. *Biomedical Microdevices* **11**, 503–508 (2009).

[98] Wang, Z., Volinsky, A. A. & Gallant, N. D. Crosslinking effect on polydimethylsiloxane elastic modulus measured by custom-built compression instrument. *Journal of Applied Polymer Science* **131**, n/a–n/a (2014).

[99] Wang, Y. *et al.* Effects of rubber/magnetic particle interactions on the performance of magnetorheological elastomers. *Polymer Testing* **25**, 262–267 (2006).

[100] Rudykh, S. & Bertoldi, K. Stability of anisotropic magnetorheological elastomers in finite deformations: A micromechanical approach. *Journal of the Mechanics and Physics of Solids* **61**, 949–967 (2013).

[101] Agirre-Olabide, I. & Elejabarrieta, M. A new magneto-dynamic compression technique for magnetorheological elastomers at high frequencies. *Polymer Testing* **66**, 114–121 (2018).

[102] Bastola, A., Hoang, V. & Li, L. A novel hybrid magnetorheological elastomer developed by 3d printing. *Materials & Design* **114**, 391–397 (2017).

[103] Boczkowska, A., Awietjan, S. F., Pietrzko, S. & Kurzydłowski, K. J. Mechanical properties of magnetorheological elastomers under shear deformation. *Composites Part B: Engineering* **43**, 636–640 (2012).

[104] Khimi, S. R. & Pickering, K. Comparison of dynamic properties of magnetorheological elastomers with existing antivibration rubbers. *Composites Part B: Engineering* **83**, 175–183 (2015).

[105] Lokander, M. & Stenberg, B. Improving the magnetorheological effect in isotropic magnetorheological rubber materials. *Polymer Testing* **22**, 677–680 (2003).

[106] Sun, T. *et al.* Study on the damping properties of magnetorheological elastomers based on cis-polybutadiene rubber. *Polymer Testing* **27**, 520–526 (2008).

[107] Varga, Z., Filipcsei, G. & Zrínyi, M. Magnetic field sensitive functional elastomers with tuneable elastic modulus. *Polymer* **47**, 227–233 (2006).

[108] Borin, D., Stepanov, G. & Dohmen, E. On anisotropic mechanical properties of heterogeneous magnetic polymeric composites. *Philosophical Transactions of the Royal Society A: Mathematical, Physical and Engineering Sciences* **377**, 20180212 (2019).

[109] Burgaz, E. & Goksuzoglu, M. Effects of magnetic particles and carbon black on structure and properties of magnetorheological elastomers. *Polymer Testing* **81**, 106233 (2020).

[110] Ginder, J. M., Nichols, M. E., Elie, L. D. & Tardiff, J. L. Magnetorheological elastomers: properties and applications. vol. 3675, 131–138 (International Society for Optics and Photonics, 1999).

[111] Gong, X., Zhang, X. & Zhang, P. Fabrication and characterization of isotropic magnetorheological elastomers. *Polymer Testing* **24**, 669–676 (2005).

[112] Soto, G. *et al.* Magnetic nanocomposites based on shape memory polyurethanes. *European Polymer Journal* **109**, 8–15 (2018).

[113] Wang, X.-X. *et al.* Conductive polymer ultrafine fibers via electrospinning: Preparation, physical properties and applications. *Progress in Materials Science* **115**, 100704 (2021).

[114] Al-Dulimi, Z., Wallis, M., Tan, D. K., Maniruzzaman, M. & Nokhodchi, A. 3d printing technology as innovative solutions for biomedical applications. *Drug Discovery Today* **26**, 360–383 (2021).

[115] Yarali, E. *et al.* Magneto-/ electro-responsive polymers toward manufacturing, characterization, and biomedical/ soft robotic applications. *Applied Materials Today* **26**, 101306 (2022).

[116] MacDonald, E. & Wicker, R. Multiprocess 3d printing for increasing component functionality. *Science* **353** (2016).

[117] Dogan, E., Bhusal, A., Cecen, B. & Miri, A. K. 3d printing metamaterials towards tissue engineering. *Applied Materials Today* **20**, 100752 (2020).

[118] Mirzaali, M. J., Pahlavani, H., Yarali, E. & Zadpoor, A. A. Non-affinity in multi-material mechanical metamaterials. *Scientific Reports* **10**, 11488 (2020).

[119] Rahman, H., Yarali, E., Zolfagharian, A., Serjouei, A. & Bodaghi, M. Energy absorption and mechanical performance of functionally graded soft–hard lattice structures. *Materials* **14**, 1366 (2021).

[120] Joshi, S. *et al.* 4d printing of materials for the future: Opportunities and challenges. *Applied Materials Today* **18**, 100490 (2020).

[121] Pei, E., Loh, G. H. & Nam, S. Concepts and terminologies in 4d printing. *Applied Sciences* **10**, 4443 (2020).

[122] Xin, X., Liu, L., Liu, Y. & Leng, J. 4d printing auxetic metamaterials with tunable, programmable, and reconfigurable mechanical properties. *Advanced Functional Materials* **30**, 2004226 (2020).

[123] Bastola, A., Paudel, M. & Li, L. Development of hybrid magnetorheological elastomers by 3d printing. *Polymer* **149**, 213–228 (2018).

[124] Yuk, H. & Zhao, X. A new 3d printing strategy by harnessing deformation, instability, and fracture of viscoelastic inks. *Advanced Materials* **30**, 1704028 (2018).

[125] de Pedro, S. *et al.* Pdms-based, magnetically actuated variable optical attenuators obtained by soft lithography and inkjet printing technologies. *Sensors and Actuators A: Physical* **215**, 30–35 (2014).

[126] Fan, D., Staufer, U. & Accardo, A. Engineered 3d polymer and hydrogel microenvironments for cell culture applications. *Bioengineering* **6**, 113 (2019).

[127] Nagarajan, B., Mertiny, P. & Qureshi, A. J. Magnetically loaded polymer composites using stereolithography—material processing and characterization. *Materials Today Communications* **25**, 101520 (2020).

[128] Lantean, S. *et al.* 3d printing of magnetoresponsive polymeric materials with tunable mechanical and magnetic properties by digital light processing. *Advanced Materials Technologies* **4**, 1900505 (2019).

[129] Hupfeld, T. *et al.* 3d printing of magnetic parts by laser powder bed fusion of iron oxide nanoparticle functionalized polyamide powders. *Journal of Materials Chemistry C* **8**, 12204–12217 (2020).

[130] Yuan, S., Chua, C. K. & Zhou, K. 3d-printed mechanical metamaterials with high energy absorption. *Advanced Materials Technologies* **4**, 1800419 (2019).

[131] Garzon-Hernandez, S., Garcia-Gonzalez, D., Jérusalem, A. & Arias, A. Design of fdm 3d printed polymers: An experimental-modelling methodology for the prediction of mechanical properties. *Materials & Design* **188**, 108414 (2020).

[132] Abramchuk, S. S., Grishin, D. A., Kramarenko, E. Y., Stepanov, G. V. & Khokhlov, A. R. Effect of a homogeneous magnetic field on the mechanical behavior of soft magnetic elastomers under compression. *Polymer Science Series A* **48**, 138–145 (2006).

[133] Li, Y., Li, J., Tian, T. & Li, W. A highly adjustable magnetorheological elastomer base isolator for applications of real-time adaptive control. *Smart Materials and Structures* **22**, 095020 (2013).

[134] Alkhalaf, A., Hooshiar, A. & Dargahi, J. Composite magnetorheological elastomers for tactile displays: Enhanced mr-effect through bi-layer composition. *Composites Part B: Engineering* **190**, 107888 (2020).

[135] Zhao, C., Gong, X., Wang, S., Jiang, W. & Xuan, S. Shear stiffening gels for intelligent anti-impact applications. *Cell Reports Physical Science* **1**, 100266 (2020).

[136] Gorman, D., Murphy, N., Ekins, R. & Jerrams, S. The evaluation and implementation of magnetic fields for large strain uniaxial and biaxial cyclic testing of magnetorheological elastomers. *Polymer Testing* **51**, 74–81 (2016).

[137] Gorman, D., Murphy, N., Ekins, R. & Jerrams, S. The evaluation of the effect of strain limits on the physical properties of magnetorheological elastomers subjected to uniaxial and biaxial cyclic testing. *International Journal of Fatigue* **103**, 1–4 (2017).

[138] Zhou, Y., Jerrams, S. & Chen, L. Multi-axial fatigue in magnetorheological elastomers using bubble inflation. *Materials & Design* **50**, 68–71 (2013).

[139] Chen, L., Gong, X. & Li, W. Effect of carbon black on the mechanical performances of magnetorheological elastomers. *Polymer Testing* **27**, 340–345 (2008).

[140] Fan, Y., Gong, X., Xuan, S., Qin, L. & Li, X. Effect of cross-link density of the matrix on the damping properties of magnetorheological elastomers. *Industrial & Engineering Chemistry Research* **52**, 771–778 (2013).

[141] Fuchs, A., Zhang, Q., Elkins, J., Gordaninejad, F. & Evrensel, C. Development and characterization of magnetorheological elastomers. *Journal of Applied Polymer Science* **105**, 2497–2508 (2007).

[142] Fuchs, A., Sutrisno, J., Gordaninejad, F., Caglar, M. B. & Yanming, L. Surface polymerization of iron particles for magnetorheological elastomers. *Journal of Applied Polymer Science* **117**, 934–942 (2010).

[143] Psarra, E., Bodelot, L. & Danas, K. Wrinkling to crinkling transitions and curvature localization in a magnetoelastic film bonded to a non-magnetic substrate. *Journal of the Mechanics and Physics of Solids* **133**, 103734 (2019).

[144] Yan, D., Pezzulla, M., Cruveiller, L., Abbasi, A. & Reis, P. M. Magneto-active elastic shells with tunable buckling strength. *Nature Communications* **12**, 2831 (2021).

[145] Laeuger, J., Wollny, K., Stettin, H. & Huck, S. A new device for the full rheological characterization of magneto-rheological fluids. 370–376 (World Scientific, 2005).

[146] Kankanala, S. & Triantafyllidis, N. On finitely strained magnetorheological elastomers. *Journal of the Mechanics and Physics of Solids* **52**, 2869–2908 (2004).

[147] Bustamante, R., Dorfmann, A. & Ogden, R. Universal relations in isotropic nonlinear magnetoelasticity. *The Quarterly Journal of Mechanics and Applied Mathematics* **59**, 435–450 (2006).

[148] Vu, D. & Steinmann, P. Material and spatial motion problems in nonlinear electro- and magneto-elastostatics. *Mathematics and Mechanics of Solids* **15**, 239–257 (2010).

[149] Pao, Y.-H. Electromagnetic forces in deformable continua. *Mechanics Today* 209–305 (1978).

[150] Eringen, A. C. & Maugin, G. A. *Electrodynamics of Continua I* (Springer New York, 1990).

[151] Maugin, G. A. G. A. *Continuum mechanics of electromagnetic solids* (1988).

[152] Brigadnov, I. & Dorfmann, A. Mathematical modeling of magneto-sensitive elastomers. *International Journal of Solids and Structures* **40**, 4659–4674 (2003).

[153] Bustamante, R. Transversely isotropic nonlinear magneto-active elastomers. *Acta Mechanica* **210**, 183–214 (2010).

[154] Bustamante, R., Dorfmann, A. & Ogden, R. On variational formulations in nonlinear magnetoelastostatics. *Mathematics and Mechanics of Solids* **13**, 725–745 (2008).

[155] Shariff, M., Hossain, M., Bustamante, R. & Merodio, J. Modelling the residually stressed magneto-electrically coupled soft elastic materials. *International Journal of Non-Linear Mechanics* **137**, 103802 (2021).

[156] Dorfmann, A. & Ogden, R. Nonlinear magnetoelastic deformations of elastomers. *Acta Mechanica* **167**, 13–28 (2004).

[157] Haldar, K., Kiefer, B. & Menzel, A. Finite element simulation of rate-dependent magneto-active polymer response. *Smart Materials and Structures* **25**, 104003 (2016).

[158] Haldar, K. Constitutive modeling of magneto-viscoelastic polymers, demagnetization correction, and field-induced poynting effect. *International Journal of Engineering Science* **165**, 103488 (2021).

[159] Saxena, P., Hossain, M. & Steinmann, P. A theory of finite deformation magneto-viscoelasticity. *International Journal of Solids and Structures* **50**, 3886–3897 (2013).

[160] Saxena, P., Hossain, M. & Steinmann, P. Nonlinear magneto-viscoelasticity of transversally

isotropic magneto-active polymers. *Proceedings. Mathematical, Physical, and Engineering Sciences / The Royal Society* **470** (2014).

[161] Ethiraj, G. & Miehe, C. Multiplicative magneto-elasticity of magnetosensitive polymers incorporating micromechanically-based network kernels. *International Journal of Engineering Science* **102**, 93–119 (2016).

[162] Garcia-Gonzalez, D. & Hossain, M. Microstructural modelling of hard-magnetic soft materials: Dipole–dipole interactions versus zeeman effect. *Extreme Mechanics Letters* **48**, 101382 (2021).

[163] Liu, Y., Chen, S., Tan, X. & Cao, C. A finite element framework for magneto-actuated large deformation and instability of slender magneto-active elastomers. *International Journal of Applied Mechanics* **12**, 2050013 (2020).

[164] Mukherjee, D., Rambausek, M. & Danas, K. An explicit dissipative model for isotropic hard magnetorheological elastomers. *Journal of the Mechanics and Physics of Solids* **151**, 104361 (2021).

[165] Mukherjee, D. & Danas, K. A unified dual modeling framework for soft and hard magnetorheological elastomers. *International Journal of Solids and Structures* 111513 (2022).

[166] Rambausek, M., Mukherjee, D. & Danas, K. A computational framework for magnetically hard and soft viscoelastic magnetorheological elastomers. *Computer Methods in Applied Mechanics and Engineering* **391**, 114500 (2022).

[167] Ivaneyko, D., Toshchevikov, V. P., Saphiannikova, M. & Heinrich, G. Magneto-sensitive elastomers in a homogeneous magnetic field: A regular rectangular lattice model. *Macromolecular Theory and Simulations* **20**, 411–424 (2011).

[168] Ivaneyko, D., Toshchevikov, V., Saphiannikova, M. & Heinrich, G. Effects of particle distribution on mechanical properties of magneto-sensitive elastomers in a homogeneous magnetic field (2012).

[169] Ivaneyko, D., Toshchevikov, V., Saphiannikova, M. & Heinrich, G. Mechanical properties of magneto-sensitive elastomers: unification of the continuum-mechanics and microscopic theoretical approaches. *Soft Matter* **10**, 2213–2225 (2013).

[170] Garcia-Gonzalez, D. & Hossain, M. A microstructural-based approach to model magneto-viscoelastic materials at finite strains. *International Journal of Solids and Structures* **208-209**, 119–132 (2021).

[171] Javili, A., Chatzigeorgiou, G. & Steinmann, P. Computational homogenization in magneto-mechanics. *International Journal of Solids and Structures* **50**, 4197–4216 (2013).

[172] Castañeda, P. P. & Galipeau, E. Homogenization-based constitutive models for magnetorheological elastomers at finite strain. *Journal of the Mechanics and Physics of Solids* **59**, 194–215 (2011).

[173] Miehe, C., Vallicotti, D. & Teichtmeister, S. Homogenization and multiscale stability analysis in finite magneto-electro-elasticity. application to soft matter ee, me and mee composites. *Computer Methods in Applied Mechanics and Engineering* **300**, 294–346 (2016).

[174] Zabihyan, R., Mergheim, J., Javili, A. & Steinmann, P. Aspects of computational homogenization in magneto-mechanics: Boundary conditions, rve size and microstructure composition. *International Journal of Solids and Structures* **130-131**, 105–121 (2018).

[175] Danas, K. Effective response of classical, auxetic and chiral magnetoelastic materials by use

of a new variational principle. *Journal of the Mechanics and Physics of Solids* **105**, 25–53 (2017).

[176] Zabihyan, R., Mergheim, J., Pelteret, J., Brands, B. & Steinmann, P. Fe2 simulations of magnetorheological elastomers: influence of microscopic boundary conditions, microstructures and free space on the macroscopic responses of mres. *International Journal of Solids and Structures* **193-194**, 338–356 (2020).

[177] Lefèvre, V., Danas, K. & Lopez-Pamies, O. Two families of explicit models constructed from a homogenization solution for the magnetoelastic response of mres containing iron and ferrofluid particles. *International Journal of Non-Linear Mechanics* **119**, 103362 (2020).

[178] Spieler, C., Kästner, M., Goldmann, J., Brummund, J. & Ulbricht, V. Xfem modeling and homogenization of magnetoactive composites. *Acta Mechanica* **224**, 2453–2469 (2013).

[179] Galipeau, E., Rudykh, S., deBotton, G. & Castañeda, P. P. Magnetoactive elastomers with periodic and random microstructures. *International Journal of Solids and Structures* **51**, 3012–3024 (2014).

[180] Keip, M.-A. & Rambausek, M. A multiscale approach to the computational characterization of magnetorheological elastomers. *International Journal for Numerical Methods in Engineering* **107**, 338–360 (2016).

[181] Kalina, K. A., Metsch, P. & Kästner, M. Microscale modeling and simulation of magnetorheological elastomers at finite strains: A study on the influence of mechanical preloads. *International Journal of Solids and Structures* **102-103**, 286–296 (2016).

[182] Keip, M.-A. & Sridhar, A. A variationally consistent phase-field approach for micro-magnetic domain evolution at finite deformations. *Journal of the Mechanics and Physics of Solids* **125**, 805–824 (2019).

[183] Kalina, K. A., Metsch, P., Brummund, J. & Kästner, M. A macroscopic model for magnetorheological elastomers based on microscopic simulations. *International Journal of Solids and Structures* **193-194**, 200–212 (2020).

[184] Mukherjee, D., Bodelot, L. & Danas, K. Microstructurally-guided explicit continuum models for isotropic magnetorheological elastomers with iron particles. *International Journal of Non-Linear Mechanics* **120**, 103380 (2020).

[185] Leonard, M., Wang, N., Lopez-Pamies, O. & Nakamura, T. The nonlinear elastic response of filled elastomers: Experiments vs. theory for the basic case of particulate fillers of micrometer size. *Journal of the Mechanics and Physics of Solids* **135**, 103781 (2020).

[186] Bleiler, C., Castañeda, P. P. & Röhrle, O. Tangent second-order homogenisation estimates for incompressible hyperelastic composites with fibrous microstructures and anisotropic phases. *Journal of the Mechanics and Physics of Solids* **147**, 104251 (2021).

[187] Metsch, P. *et al.* Magneto-mechanical coupling in magneto-active elastomers. *Materials* **14**, 434 (2021).

[188] Ortigosa, R., Martínez-Frutos, J., Mora-Corral, C., Pedregal, P. & Periago, F. Optimal control and design of magnetic field-responsive smart polymer composites. *Applied Mathematical Modelling* **103**, 141–161 (2022).

[189] Mehnert, M., Hossain, M. & Steinmann, P. Towards a thermo-magneto-mechanical coupling framework for magneto-rheological elastomers. *International Journal of Solids and Structures* **128**, 117–132 (2017).

[190] Gebhart, P. & Wallmersperger, T. A constitutive macroscale model for compressible magneto-active polymers based on computational homogenization data: Part i — magnetic linear regime. *International Journal of Solids and Structures* **236-237**, 111294 (2022).

[191] Arora, A., Kumar, A. & Steinmann, P. A computational approach to obtain nonlinearly elastic constitutive relations of special cosserat rods. *Computer Methods in Applied Mechanics and Engineering* **350**, 295–314 (2019).

[192] Herrnböck, L., Kumar, A. & Steinmann, P. Geometrically exact elastoplastic rods: determination of yield surface in terms of stress resultants. *Computational Mechanics* **67**, 723–742 (2021).

[193] Sano, T. G., Pezzulla, M. & Reis, P. M. A kirchhoff-like theory for hard magnetic rods under geometrically nonlinear deformation in three dimensions. *Journal of the Mechanics and Physics of Solids* **160**, 104739 (2022).

[194] Goshkoderia, A. & Rudykh, S. Stability of magnetoactive composites with periodic microstructures undergoing finite strains in the presence of a magnetic field. *Composites Part B: Engineering* **128**, 19–29 (2017).

[195] Chen, D. *et al.* Instability-induced patterns and their post-buckling development in soft particulate composites. *Mechanics of Materials* **175**, 104482 (2022).

[196] Polukhov, E., Pytel, L. & Keip, M.-A. Swelling-induced pattern transformations of periodic hydrogels – from the wrinkling of internal surfaces to the buckling of thin films. *arXiv* (2022).

[197] Keip, M.-A. & Rambausek, M. Computational and analytical investigations of shape effects in the experimental characterization of magnetorheological elastomers. *International Journal of Solids and Structures* **121**, 1–20 (2017).

[198] Zhao, R., Kim, Y., Chester, S. A., Sharma, P. & Zhao, X. Mechanics of hard-magnetic soft materials. *Journal of the Mechanics and Physics of Solids* **124**, 244–263 (2019).

[199] Garcia-Gonzalez, D. Magneto-visco-hyperelasticity for hard-magnetic soft materials: theory and numerical applications. *Smart Materials and Structures* **28**, 085020 (2019).

[200] Coleman, B. D. & Gurtin, M. E. Thermodynamics with internal state variables. *The Journal of Chemical Physics* **47**, 597–613 (1967).

[201] Arruda, E. M. & Boyce, M. C. A three-dimensional constitutive model for the large stretch behavior of rubber elastic materials. *Journal of the Mechanics and Physics of Solids* **41**, 389–412 (1993).

[202] Kuhn, W. & Grün, F. Beziehungen zwischen elastischen konstanten und dehnungsdoppelbrechung hochelastischer stoffe. *Kolloid-Zeitschrift* **101**, 248–271 (1942).

[203] Wang, M. C. & Guth, E. Statistical theory of networks of non-gaussian flexible chains. *The Journal of Chemical Physics* **20**, 1144–1157 (1952).

[204] Flory, P. J. & Rehner, J. Statistical theory of chain configuration and physical properties of high polymers. *Annals of the New York Academy of Sciences* **44**, 419–429 (1943).

[205] Treloar, L. R. G. *The statistical length of long-chain molecules*, vol. 42 (The Royal Society of Chemistry, 1946).

[206] Treloar, L. R. G. *The Physics of Rubber Elasticity* (Oxford University Press, USA, 1975).

[207] Garcia-Gonzalez, D., Garzon-Hernandez, S., Rusinek, A., Bernier, R. & Arias, A. Low temperature mechanical behaviour of pvdf: cryogenic pre-treatment, quasi-static, cyclic and dynamic experimental testing and modelling. *Mechanics of Materials* **147**, 103436 (2020).

[208] Treloar, L. R. G. The photoelastic properties of short-chain molecular networks. *Transactions of the Faraday Society* **50**, 881 (1954).

[209] Jolly, M. R., Carlson, J. D. & Muñoz, B. C. A model of the behaviour of magnetorheological materials. *Smart Materials and Structures* **5**, 607–614 (1996).

[210] Jiles, D. *Introduction to Magnetism and Magnetic Materials* (CRC Press, 2015).

[211] Bay, F., Labbe, V., Favennec, Y. & Chenot, J. L. A numerical model for induction heating processes coupling electromagnetism and thermomechanics. *International Journal for Numerical Methods in Engineering* **58**, 839–867 (2003).

[212] Díez, A. G., Tubio, C. R., Etxebarria, J. G. & Lanceros-Mendez, S. Magnetorheological elastomer-based materials and devices: State of the art and future perspectives. *Advanced Engineering Materials* **23**, 2100240 (2021).

[213] Koivikko, A., Drotlef, D.-M., Sitti, M. & Sariola, V. Magnetically switchable soft suction grippers. *Extreme Mechanics Letters* **44**, 101263 (2021).

[214] Zhang, J. *et al.* Voxelated three-dimensional miniature magnetic soft machines via multimaterial heterogeneous assembly. *Science Robotics* **6** (2021).

[215] Bastola, A. K. & Li, L. A new type of vibration isolator based on magnetorheological elastomer. *Materials & Design* **157**, 431–436 (2018).

[216] Bastola, A. K., Li, L. & Paudel, M. A hybrid magnetorheological elastomer developed by encapsulation of magnetorheological fluid. *Journal of Materials Science* **53**, 7004–7016 (2018).

[217] Soroor, A. O., Asgari, M. & Haddadpour, H. Effect of axially graded constraining layer on the free vibration properties of three layered sandwich beams with magnetorheological fluid core. *Composite Structures* **255**, 112899 (2021).

[218] Sun, S. *et al.* Development of magnetorheological elastomers–based tuned mass damper for building protection from seismic events. *Journal of Intelligent Material Systems and Structures* **29**, 1777–1789 (2018).

[219] Zhu, M. *et al.* Design and co-optimization of a laminated isolation bearing based on magnetorheological elastomer. *Mechanical Systems and Signal Processing* **159**, 107843 (2021).

[220] Li, H. *et al.* Vibration and damping study of multifunctional grille composite sandwich plates with an imas design approach. *Composites Part B: Engineering* **223**, 109078 (2021).

[221] Khayam, S. U., Usman, M., Umer, M. A. & Rafique, A. Development and characterization of a novel hybrid magnetorheological elastomer incorporating micro and nano size iron fillers. *Materials & Design* **192**, 108748 (2020).

[222] Yan, B. *et al.* A bistable vibration isolator with nonlinear electromagnetic shunt damping. *Mechanical Systems and Signal Processing* **136**, 106504 (2020).

[223] de Souza Eloy, F. *et al.* A numerical-experimental dynamic analysis of composite sandwich beam with magnetorheological elastomer honeycomb core. *Composite Structures* **209**, 242–257 (2019).

[224] Selvaraj, R. & Ramamoorthy, M. Dynamic analysis of laminated composite sandwich beam containing carbon nanotubes reinforced magnetorheological elastomer. *Journal of Sandwich Structures & Materials* **23**, 1784–1807 (2021).

[225] Diguet, G., Sebald, G., Nakano, M., Lallart, M. & Cavaillé, J.-Y. Optimization of magnetorheological elastomers for energy harvesting applications. *Smart Materials and Structures* **29**, 075017 (2020).

[226] Mofidian, S. M. & Bardaweel, H. A dual-purpose vibration isolator energy harvester: Experiment and model. *Mechanical Systems and Signal Processing* **118**, 360–376 (2019).

[227] Hu, G., Yi, F., Liu, H. & Zeng, L. Performance analysis of a novel magnetorheological damper with displacement self-sensing and energy harvesting capability. *Journal of Vibration Engineering & Technologies* **9**, 85–103 (2021).

[228] Hu, T., Xuan, S., Ding, L. & Gong, X. Stretchable and magneto-sensitive strain sensor based on silver nanowire-polyurethane sponge enhanced magnetorheological elastomer. *Materials & Design* **156**, 528–537 (2018).

[229] Malikan, M., Uglov, N. S. & Eremeyev, V. A. On instabilities and post-buckling of piezomagnetic and flexomagnetic nanostructures. *International Journal of Engineering Science* **157**, 103395 (2020).

[230] Bica, I. Influence of the transverse magnetic field intensity upon the electric resistance of the magnetorheological elastomer containing graphite microparticles. *Materials Letters* **63**, 2230–2232 (2009).

[231] Behrooz, M. & Gordaninejad, F. Three-dimensional study of a one-way, flexible magnetorheological elastomer-based micro fluid transport system. *Smart Materials and Structures* **25**, 095012 (2016).

[232] Amiri, A. & Talebitooti, R. Vibration and stability analysis of fluid-conveying sandwich micro-pipe with magnetorheological elastomer core, considering modified couple stress theory and geometrical nonlinearity. *The European Physical Journal Plus* **136**, 1109 (2021).

[233] Wu, C., Zhang, Q., Fan, X., Song, Y. & Zheng, Q. Smart magnetorheological elastomer peristaltic pump. *Journal of Intelligent Material Systems and Structures* **30**, 1084–1093 (2019).

[234] Bastola, A. K. & Hossain, M. The shape – morphing performance of magnetoactive soft materials. *Materials & Design* **211**, 110172 (2021).

[235] Vural, M. *et al.* Programmable molecular composites of tandem proteins with graphene oxide for efficient bimorph actuators. *Carbon* **118**, 404–412 (2017).

[236] Li, M., Pal, A., Aghakhani, A., Pena-Francesch, A. & Sitti, M. Soft actuators for real-world applications. *Nature Reviews Materials* **7**, 235–249 (2022).

[237] Moucka, R., Sedlacik, M. & Cvek, M. Dielectric properties of magnetorheological elastomers with different microstructure. *Applied Physics Letters* **112**, 122901 (2018).

[238] Fuhrer, R., Schumacher, C. M., Zeltner, M. & Stark, W. J. Soft iron/silicon composite tubes for magnetic peristaltic pumping: Frequency-dependent pressure and volume flow. *Advanced Functional Materials* **23**, 3845–3849 (2013).

[239] Chai, J. *et al.* Facile synthesis of highly conductive mos ¡sub¿2¡/sub¿ /graphene nanohybrids with hetero-structures as excellent microwave absorbers. *RSC Advances* **8**, 36616–36624 (2018).

[240] Hogan, K. J. & Mikos, A. G. Biodegradable thermoresponsive polymers: Applications in drug delivery and tissue engineering. *Polymer* **211**, 123063 (2020).

[241] Reis, P. M., Jiménez, F. L. & Marthelot, J. Transforming architectures inspired by origami. *Proceedings of the National Academy of Sciences* **112**, 12234–12235 (2015).

[242] Garcia-Gonzalez, D., Ter-Yesayants, T., Moreno-Mateos, M. A. & Lopez-Donaire, M. L.

Hard-magnetic phenomena enable autonomous self-healing elastomers. *Composites Part B: Engineering* **248**, 110357 (2023).

[243] Diller, E. & Sitti, M. Three-dimensional programmable assembly by untethered magnetic robotic micro-grippers. *Advanced Functional Materials* **24**, 4397–4404 (2014).

[244] Alfadhel, A. & Kosel, J. Magnetic nanocomposite cilia tactile sensor. *Advanced Materials* **27**, 7888–7892 (2015).

[245] Ge, J. *et al.* A bimodal soft electronic skin for tactile and touchless interaction in real time. *Nature Communications* **10**, 4405 (2019).

[246] Wang, T., Ren, Z., Hu, W., Li, M. & Sitti, M. Effect of body stiffness distribution on larval fish–like efficient undulatory swimming. *Science Advances* **7** (2021).

[247] Lee, K. Y. *et al.* An autonomously swimming biohybrid fish designed with human cardiac biophysics. *Science* **375**, 639–647 (2022).

[248] Tang, J., Yin, Q., Qiao, Y. & Wang, T. Shape morphing of hydrogels in alternating magnetic field. *ACS Applied Materials & Interfaces* **11**, 21194–21200 (2019).

[249] Zhang, Y. *et al.* 4d printing of magnetoactive soft materials for on-demand magnetic actuation transformation. *ACS Applied Materials & Interfaces* **13**, 4174–4184 (2021).

[250] Zhu, P. *et al.* 4d printing of complex structures with a fast response time to magnetic stimulus. *ACS Applied Materials & Interfaces* **10**, 36435–36442 (2018).

[251] Alapan, Y., Karacakol, A. C., Guzelhan, S. N., Isik, I. & Sitti, M. Reprogrammable shape morphing of magnetic soft machines. *Science Advances* **6** (2020).

[252] Satarkar, N. S. & Hilt, J. Z. Magnetic hydrogel nanocomposites for remote controlled pulsatile drug release. *Journal of Controlled Release* **130**, 246–251 (2008).

[253] Campbell, S., Maitland, D. & Hoare, T. Enhanced pulsatile drug release from injectable magnetic hydrogels with embedded thermosensitive microgels. *ACS Macro Letters* **4**, 312–316 (2015).

[254] Hu, S.-H., Liu, T.-Y., *, Liu, D.-M. & Chen*, S.-Y. Controlled pulsatile drug release from a ferrogel by a high-frequency magnetic field (2007).

[255] Qin, J. *et al.* Injectable superparamagnetic ferrogels for controlled release of hydrophobic drugs. *Advanced Materials* **21**, 1354–1357 (2009).

[256] Hu, X. *et al.* Magnetic field-driven drug release from modified iron oxide-integrated polysaccharide hydrogel. *International Journal of Biological Macromolecules* **108**, 558–567 (2018).

[257] Soares, P. I., Romão, J., Matos, R., Silva, J. C. & Borges, J. P. Design and engineering of magneto-responsive devices for cancer theranostics: Nano to macro perspective. *Progress in Materials Science* **116**, 100742 (2021).

[258] Hajba, L. & Guttman, A. The use of magnetic nanoparticles in cancer theranostics: Toward handheld diagnostic devices. *Biotechnology Advances* **34**, 354–361 (2016).

[259] Pankhurst, Q. A., Connolly, J., Jones, S. K. & Dobson, J. Applications of magnetic nanoparticles in biomedicine. *Journal of Physics D: Applied Physics* **36**, R167–R181 (2003).

[260] Pankhurst, Q. A., Thanh, N. T. K., Jones, S. K. & Dobson, J. Progress in applications of magnetic nanoparticles in biomedicine. *Journal of Physics D: Applied Physics* **42**, 224001 (2009).

[261] Freeman, M. W., Arrott, A. & Watson, J. H. L. Magnetism in medicine. *Journal of Applied Physics* **31**, S404–S405 (1960).

[262] Bouklas, N., Landis, C. M. & Huang, R. A nonlinear, transient finite element method for coupled solvent diffusion and large deformation of hydrogels. *Journal of the Mechanics and Physics of Solids* **79**, 21–43 (2015).

[263] Jing, L., Liang, X., Li, X., Yang, Y. & Dai, Z. Covalent attachment of mn-porphyrin onto doxorubicin-loaded poly(lactic acid) nanoparticles for potential magnetic resonance imaging and ph-sensitive drug delivery. *Acta Biomaterialia* **9**, 9434–9441 (2013).

[264] Dadfar, S. M. *et al.* Iron oxide nanoparticles: Diagnostic, therapeutic and theranostic applications. *Advanced Drug Delivery Reviews* **138**, 302–325 (2019).

[265] Sakuma, H. Coronary ct versus mr angiography: The role of mr angiography. *Radiology* **258**, 340–349 (2011).

[266] Wei, Y. *et al.* Biocompatible low-retention superparamagnetic iron oxide nanoclusters as contrast agents for magnetic resonance imaging of liver tumor. *Journal of Biomedical Nanotechnology* **11**, 854–864 (2015).

[267] Guo, Y. *et al.* Biocompatibility and magnetic resonance imaging characteristics of carbon nanotube yarn neural electrodes in a rat model. *BioMedical Engineering OnLine* **14**, 118 (2015).

[268] Fernandes, M. G., da Silva, L. P. & Marques, A. P. Skin mechanobiology and biomechanics: From homeostasis to wound healing. *Advances in Biomechanics and Tissue Regeneration* 343–360 (2019).

[269] Santos, L. J., Reis, R. L. & Gomes, M. E. Harnessing magnetic-mechano actuation in regenerative medicine and tissue engineering. *Trends in Biotechnology* **33**, 471–479 (2015).

[270] Kowalczewski, C. J. & Saul, J. M. Biomaterials for the delivery of growth factors and other therapeutic agents in tissue engineering approaches to bone regeneration. *Frontiers in Pharmacology* **9**, 513 (2018).

[271] Rouwkema, J., Rivron, N. C. & van Blitterswijk, C. A. Vascularization in tissue engineering. *Trends in biotechnology* **26**, 434–41 (2008).

[272] Filippi, M. *et al.* Magnetic nanocomposite hydrogels and static magnetic field stimulate the osteoblastic and vasculogenic profile of adipose-derived cells. *Biomaterials* **223**, 119468 (2019).

[273] Omidinia-Anarkoli, A. *et al.* An injectable hybrid hydrogel with oriented short fibers induces unidirectional growth of functional nerve cells. *Small* **13**, 1702207 (2017).

[274] Namdari, M. & Eatemadi, A. Cardioprotective effects of curcumin-loaded magnetic hydrogel nanocomposite (nanocurcumin) against doxorubicin-induced cardiac toxicity in rat cardiomyocyte cell lines. *Artificial Cells, Nanomedicine, and Biotechnology* **45**, 731–739 (2017).

[275] Huang, J. *et al.* Magnetic enhancement of chondrogenic differentiation of mesenchymal stem cells. *ACS Biomaterials Science & Engineering* **5**, 2200–2207 (2019).

[276] Yang, W. *et al.* Functionalization of novel theranostic hydrogels with kartogenin-grafted uspio nanoparticles to enhance cartilage regeneration. *ACS Applied Materials & Interfaces* **11**, 34744–34754 (2019).

[277] Akther, F., Yakob, S. B., Nguyen, N.-T. & Ta, H. T. Surface modification techniques for endothelial cell seeding in pdms microfluidic devices. *Biosensors* **10** (2020).

[278] Chuah, Y. J. *et al.* Simple surface engineering of polydimethylsiloxane with polydopamine

for stabilized mesenchymal stem cell adhesion and multipotency. *Scientific reports* **5**, 18162 (2015).

[279] Souza, A., Ribeiro, J. & Araújo, F. Study of pdms characterization and its applications in biomedicine: A review. *Journal of Mechanical Engineering and Biomechanics* **4**, 1–9 (2019).

[280] Sreekantan, S., Hassan, M., Murthe, S. S. & Seeni, A. Biocompatibility and cytotoxicity study of polydimethylsiloxane (pdms) and palm oil fuel ash (pofa) sustainable super-hydrophobic coating for biomedical applications. *Polymers* **12**, 3034 (2020).

[281] Mayer, M. *et al.* Ultra-soft pdms-based magnetoactive elastomers as dynamic cell culture substrata. *PLoS ONE* **8**, e76196 (2013).

[282] Corbin, E. A. *et al.* Tunable and reversible substrate stiffness reveals a dynamic mechanosensitivity of cardiomyocytes. *ACS Applied Materials & Interfaces* **11**, 20603–20614 (2019).

[283] Uslu, F. E. *et al.* Engineered extracellular matrices with integrated wireless microactuators to study mechanobiology. *Advanced Materials* **33**, 2102641 (2021).

[284] Garcia-Gonzalez, D. & Muñoz-Barrutia, A. Computational insights into the influence of substrate stiffness on collective cell migration. *Extreme Mechanics Letters* **40**, 100928 (2020).

[285] Brask, J. B., Singla-Buxarrais, G., Uroz, M., Vincent, R. & Trepat, X. Compressed sensing traction force microscopy. *Acta Biomaterialia* **26**, 286–294 (2015).

[286] Lua, A. M. R., Hopf, R. & Mazza, E. Factors influencing the mechanical properties of soft elastomer substrates for traction force microscopy. *Mechanics of Soft Materials* **2**, 6 (2020).

[287] Lokander, M. & Stenberg, B. Performance of isotropic magnetorheological rubber materials. *Polymer Testing* **22**, 245–251 (2003).

[288] Meyvis, T. K. *et al.* A comparison between the use of dynamic mechanical analysis and oscillatory shear rheometry for the characterisation of hydrogels. *International Journal of Pharmaceutics* **244**, 163–168 (2002).

[289] Siviour, C. R. & Walley, S. M. Inertial and frictional effects in dynamic compression testing (2018).

[290] Erenchun, A., Blanco, B., Gil-Negrete, N., Wang, B. & Kari, L. Effect of lubrication on the mechanical behavior of magnetorheological elastomers in compression mode. *Polymer Testing* **111**, 107617 (2022).

[291] Lucarini, S., Moreno-Mateos, M. A., Danas, K. & Garcia-Gonzalez, D. Insights into the viscohyperelastic response of soft magnetorheological elastomers: Competition of macrostructural versus microstructural players. *International Journal of Solids and Structures* **256**, 111981 (2022).

[292] Walter, B. L., Pelteret, J.-P., Kaschta, J., Schubert, D. W. & Steinmann, P. On the wall slip phenomenon of elastomers in oscillatory shear measurements using parallel-plate rotational rheometry: I. detecting wall slip. *Polymer Testing* **61**, 430–440 (2017).

[293] Walter, B. L., Pelteret, J.-P., Kaschta, J., Schubert, D. W. & Steinmann, P. Preparation of magnetorheological elastomers and their slip-free characterization by means of parallel-plate rotational rheometry. *Smart Materials and Structures* **26**, 085004 (2017).

[294] Liao, G., Gong, X., Xuan, S., Guo, C. & Zong, L. Magnetic-field-induced normal force of magnetorheological elastomer under compression status. *Industrial & Engineering Chemistry Research* **51**, 3322–3328 (2012).

[295] Bustamante, R., Shariff, M. & Hossain, M. Mathematical formulations for elastic magneto-electrically coupled soft materials at finite strains: Time-independent processes. *International Journal of Engineering Science* **159**, 103429 (2021).

[296] Cantera, M. A., Behrooz, M., Gibson, R. F. & Gordaninejad, F. Modeling of magneto-mechanical response of magnetorheological elastomers (mre) and mre-based systems: a review. *Smart Materials and Structures* **26**, 023001 (2017).

[297] Gao, W. & Wang, X. Experimental and theoretical investigations on magnetoelastic shear behavior of isotropic mr elastomers under gradient magnetic fields. *Journal of Magnetism and Magnetic Materials* **483**, 196–204 (2019).

[298] Qiao, Y., Zhang, J., Zhang, M., Liu, L. & Zhai, P. A magnetic field- and frequency-dependent dynamic shear modulus model for isotropic silicone rubber-based magnetorheological elastomers. *Composites Science and Technology* **204**, 108637 (2021).

[299] Borin, D., Stepanov, G. & Dohmen, E. Hybrid magnetoactive elastomer with a soft matrix and mixed powder. *Archive of Applied Mechanics* **89**, 105–117 (2019).

[300] Gaunt, P. Magnetic viscosity and thermal activation energy. *Journal of Applied Physics* **59**, 4129–4132 (1986).

[301] Kreissl, P., Holm, C. & Weeber, R. Frequency-dependent magnetic susceptibility of magnetic nanoparticles in a polymer solution: a simulation study. *Soft Matter* **17**, 174–183 (2021).

[302] Lyberatos, A. Magnetic viscosity and the field rate dependence of the magnetization. *Journal of Magnetism and Magnetic Materials* **202**, 239–250 (1999).

[303] Wohlfarth, E. P. The coefficient of magnetic viscosity. *Journal of Physics F: Metal Physics* **14**, L155–L159 (1984).

[304] Chantrell, R. W., Lyberatos, A. & Wohlfarth, E. P. The coefficient of magnetic viscosity. ii. the time dependence of the magnetisation of interacting fine-particle magnetic materials. *Journal of Physics F: Metal Physics* **16**, L145–L150 (1986).

[305] Vaganov, M., Borin, D., Odenbach, S. & Raikher, Y. Training effect in magnetoactive elastomers due to undermagnetization of magnetically hard filler. *Physica B: Condensed Matter* **578**, 411866 (2020).

[306] Stepanov, G., Borin, D., Bakhtiiarov, A. & Storozhenko, P. Negative coercivity of magnetic elastomers filled with magnetically hard particles. *Journal of Magnetism and Magnetic Materials* **498**, 166125 (2020).

[307] Borin, D., Odenbach, S. & Stepanov, G. Stress induced by the striction of hybrid magnetoactive elastic composites. *Journal of Magnetism and Magnetic Materials* **470**, 85–88 (2019).

[308] Stepanov, G. V., Kramarenko, E. Y. & Semerenko, D. A. Magnetodeformational effect of the magnetoactive elastomer and its possible applications. *Journal of Physics: Conference Series* **412**, 012031 (2013).

[309] Yan, D., Abbasi, A. & Reis, P. M. A comprehensive framework for hard-magnetic beams: Reduced-order theory, 3d simulations, and experiments. *International Journal of Solids and Structures* **257**, 111319 (2022).

[310] Stepanov, G., Borin, D. & Storozhenko, P. Rotation of magnetic particles inside the polymer matrix of magnetoactive elastomers with a hard magnetic filler. *Journal of Magnetism and Magnetic Materials* **431**, 138–140 (2017).

[311] Linke, J., Borin, D. Y. & Odenbach, S. First-order reversal curve analysis of magnetoactive elastomers. *RSC Advances* **6**, 100407–100416 (2016).

[312] Vaganov, M., Borin, D., Odenbach, S. & Raikher, Y. Effect of local elasticity of the matrix on magnetization loops of hybrid magnetic elastomers. *Journal of Magnetism and Magnetic Materials* **459**, 92–97 (2018).

[313] Kumar, A., Bourdin, B., Francfort, G. A. & Lopez-Pamies, O. Revisiting nucleation in the phase-field approach to brittle fracture. *Journal of the Mechanics and Physics of Solids* **142**, 104027 (2020).

[314] Ambrosio, L. & Tortorelli, V. On the approximation of free discontinuity problems. *Bollettino della Unione Matematica Italiana* **6**, 105–123. (1992).

[315] Ambati, M., Gerasimov, T. & Lorenzis, L. D. Phase-field modeling of ductile fracture. *Computational Mechanics* **55**, 1017–1040 (2015).

[316] Gerasimov, T. & Lorenzis, L. D. A line search assisted monolithic approach for phase-field computing of brittle fracture. *Computer Methods in Applied Mechanics and Engineering* **312**, 276–303 (2016).

[317] Kumar, A., Francfort, G. A. & Lopez-Pamies, O. Fracture and healing of elastomers: A phase-transition theory and numerical implementation. *Journal of the Mechanics and Physics of Solids* **112**, 523–551 (2018).

[318] Alessi, R., Vidoli, S. & Lorenzis, L. D. A phenomenological approach to fatigue with a variational phase-field model: The one-dimensional case. *Engineering Fracture Mechanics* **190**, 53–73 (2018).

[319] Vicentini, F., Carrara, P. & Lorenzis, L. D. Phase-field modeling of brittle fracture in heterogeneous bars. *European Journal of Mechanics - A/Solids* **97**, 104826 (2023).

[320] Lo, Y.-S., Hughes, T. J. & Landis, C. M. Phase-field fracture modeling for large structures. *Journal of the Mechanics and Physics of Solids* 105118 (2022).

[321] Hirshikesh, Natarajan, S., Annabattula, R. K. & Martínez-Pañeda, E. Phase field modelling of crack propagation in functionally graded materials. *Composites Part B: Engineering* **169**, 239–248 (2019).

[322] Miehe, C., Hofacker, M. & Welschinger, F. A phase field model for rate-independent crack propagation: Robust algorithmic implementation based on operator splits. *Computer Methods in Applied Mechanics and Engineering* **199**, 2765–2778 (2010).

[323] Loew, P. J., Peters, B. & Beex, L. A. Rate-dependent phase-field damage modeling of rubber and its experimental parameter identification. *Journal of the Mechanics and Physics of Solids* **127**, 266–294 (2019).

[324] Miehe, C. & Schänzel, L.-M. Phase field modeling of fracture in rubbery polymers. part i: Finite elasticity coupled with brittle failure. *Journal of the Mechanics and Physics of Solids* **65**, 93–113 (2014).

[325] Kumar, A., Ravi-Chandar, K. & Lopez-Pamies, O. The configurational-forces view of the nucleation and propagation of fracture and healing in elastomers as a phase transition. *International Journal of Fracture* **213**, 1–16 (2018).

[326] Li, B. & Bouklas, N. A variational phase-field model for brittle fracture in polydisperse elastomer networks. *International Journal of Solids and Structures* **182-183**, 193–204 (2020).

[327] Chaudhuri, O., Cooper-White, J., Janmey, P. A., Mooney, D. J. & Shenoy, V. B. Effects of extracellular matrix viscoelasticity on cellular behaviour. *Nature* **584**, 535–546 (2020).

[328] Tamayo-Elizalde, M., Chen, H., Malboubi, M., Ye, H. & Jerusalem, A. Action potential alterations induced by single f11 neuronal cell loading. *Progress in Biophysics and Molecular Biology* (2021).

[329] Grolman, J. M., Weinand, P. & Mooney, D. J. Extracellular matrix plasticity as a driver of cell spreading. *Proceedings of the National Academy of Sciences* **117**, 25999–26007 (2020).

[330] Mascharak, S. *et al.* Preventing engrailed-1 activation in fibroblasts yields wound regeneration without scarring. *Science* **372** (2021).

[331] Alert, R. & Trepat, X. Physical models of collective cell migration. *Annual Review of Condensed Matter Physics* **11**, 77–101 (2020).

[332] Wisniewski, E. O. *et al.* Dorsoventral polarity directs cell responses to migration track geometries. *Science Advances* **6** (2020).

[333] Bianchi, F. *et al.* Engineering a uniaxial substrate-stretching device for simultaneous electrophysiological measurements and imaging of strained peripheral neurons. *Medical Engineering & Physics* **67**, 1–10 (2019).

[334] Hu, J. *et al.* High stretchability, strength, and toughness of living cells enabled by hyperelastic vimentin intermediate filaments. *Proceedings of the National Academy of Sciences* **116**, 17175–17180 (2019).

[335] Chen, L., Yan, C. & Zheng, Z. Functional polymer surfaces for controlling cell behaviors. *Materials Today* **21**, 38–59 (2018).

[336] Wang, X. *et al.* Sensitive detection of cell-derived force and collagen matrix tension in microtissues undergoing large-scale densification. *Proceedings of the National Academy of Sciences* **118**, e2106061118 (2021).

[337] Walker, M., Rizzuto, P., Godin, M. & Pelling, A. E. Structural and mechanical remodeling of the cytoskeleton maintains tensional homeostasis in 3d microtissues under acute dynamic stretch. *Scientific Reports* **10**, 7696 (2020).

[338] Fang, C., Wei, X., Shao, X. & Lin, Y. Force-mediated cellular anisotropy and plasticity dictate the elongation dynamics of embryos. *Science Advances* **7** (2021).

[339] Park, D. *et al.* Extracellular matrix anisotropy is determined by tfap2c-dependent regulation of cell collisions. *Nature Materials* **19**, 227–238 (2020).

[340] Wei, F. *et al.* Stress fiber anisotropy contributes to force-mode dependent chromatin stretching and gene upregulation in living cells. *Nature Communications* **11**, 4902 (2020).

[341] Goren, S., Koren, Y., Xu, X. & Lesman, A. Elastic anisotropy governs the range of cell-induced displacements. *Biophysical Journal* **118**, 1152–1164 (2020).

[342] Tagge, C. A. *et al.* Concussion, microvascular injury, and early tauopathy in young athletes after impact head injury and an impact concussion mouse model. *Brain* **141**, 422–458 (2018).

[343] Garcia-Gonzalez, D. *et al.* Cognition based btbi mechanistic criteria; a tool for preventive and therapeutic innovations. *Scientific Reports* **8**, 10273 (2018).

[344] Pogoda, K. & Janmey, P. A. Glial tissue mechanics and mechanosensing by glial cells. *Frontiers in cellular neuroscience* **12**, 25 (2018).

[345] Gómez-González, M., Latorre, E., Arroyo, M. & Trepat, X. Measuring mechanical stress in living tissues. *Nature Reviews Physics* **2**, 300–317 (2020).

[346] Chevalier, N. *et al.* How tissue mechanical properties affect enteric neural crest cell migration. *Scientific Reports* **6**, 20927 (2016).

[347] Barriga, E. H., Franze, K., Charras, G. & Mayor, R. Tissue stiffening coordinates morphogenesis by triggering collective cell migration in vivo. *Nature* **554**, 523–527 (2018).

[348] Shellard, A. & Mayor, R. Integrating chemical and mechanical signals in neural crest cell migration. *Current Opinion in Genetics & Development* **57**, 16–24 (2019).

[349] Zheng, Y. *et al.* 4d hydrogel for dynamic cell culture with orthogonal, wavelength-dependent mechanical and biochemical cues. *Materials Horizons* **7**, 111–116 (2020).

[350] Ren, Z. *et al.* Soft-bodied adaptive multimodal locomotion strategies in fluid-filled confined spaces. *Science Advances* **7** (2021).

[351] Zhang, J., Guo, Y., Hu, W. & Sitti, M. Wirelessly actuated thermo- and magneto-responsive soft bimorph materials with programmable shape-morphing. *Advanced Materials* **33**, 2100336 (2021).

[352] Blaber, J., Adair, B. & Antoniou, A. Ncorr: Open-source 2d digital image correlation matlab software. *Experimental Mechanics* **55**, 1105–1122 (2015).

[353] Salas, E. & Bustamante, R. Numerical solution of some boundary value problems in nonlinear magneto-elasticity. *Journal of Intelligent Material Systems and Structures* **26**, 156–171 (2015).

[354] Garcia-Gonzalez, D. & Landis, C. M. Magneto-diffusion-viscohyperelasticity for magneto-active hydrogels: Rate dependences across time scales. *Journal of the Mechanics and Physics of Solids* **139**, 103934 (2020).

[355] Psarra, E., Bodelot, L. & Danas, K. Two-field surface pattern control via marginally stable magnetorheological elastomers. *Soft Matter* **13**, 6576–6584 (2017).

[356] Wu, H. *et al.* Chain formation mechanism of magnetic particles in magnetorheological elastomers during pre-structure. *Journal of Magnetism and Magnetic Materials* **527**, 167693 (2021).

[357] Knutsen, A. K. *et al.* In vivo estimates of axonal stretch and 3d brain deformation during mild head impact. *Brain Multiphysics* **1**, 100015 (2020).

[358] Sunyer, R. *et al.* Collective cell durotaxis emerges from long-range intercellular force transmission. *Science* **353**, 1157–1161 (2016).

[359] Valero, C., Javierre, E., García-Aznar, J., Gómez-Benito, M. & Menzel, A. Modeling of anisotropic wound healing. *Journal of the Mechanics and Physics of Solids* **79**, 80–91 (2015).

[360] Chen, K. *et al.* Role of boundary conditions in determining cell alignment in response to stretch. *Proceedings of the National Academy of Sciences* **115**, 986–991 (2018).

[361] Atcha, H. *et al.* Mechanically activated ion channel piezo1 modulates macrophage polarization and stiffness sensing. *Nature Communications* **12**, 3256 (2021).

[362] Dai, J., Wang, Y., Gong, J. & Yao, Y. Biointerface anisotropy modulates migration of breast cancer cell. *Colloids and Surfaces B: Biointerfaces* **190**, 110973 (2020).

[363] Wu, P.-H. *et al.* Single-cell morphology encodes metastatic potential. *Science Advances* **6** (2020).

[364] Moreno-Mateos, M. A. *et al.* Magneto-mechanical system to reproduce and quantify complex strain patterns in biological materials. *Applied Materials Today* **27**, 101437 (2022).

[365] Liu, X. *et al.* Magnetic living hydrogels for intestinal localization, retention, and diagnosis. *Advanced Functional Materials* 2010918 (2021).

[366] Theocharidis, G. *et al.* A strain-programmed patch for the healing of diabetic wounds. *Nature Biomedical Engineering* 1–16 (2022).

[367] Gao, Y. *et al.* Hydrogel–mesh composite for wound closure. *Proceedings of the National Academy of Sciences* **118** (2021).

[368] Wang, C. *et al.* Bioadhesive ultrasound for long-term continuous imaging of diverse organs. *Science* **377**, 517–523 (2022).

[369] Ma, Z. *et al.* Controlled tough bioadhesion mediated by ultrasound. *Science* **377**, 751–755 (2022).

[370] Zhao, X. Designing toughness and strength for soft materials. *Proceedings of the National Academy of Sciences* **114**, 8138–8140 (2017).

[371] Sanoja, G. E. *et al.* Why is mechanical fatigue different from toughness in elastomers? the role of damage by polymer chain scission. *Science Advances* **7** (2021).

[372] Lin, S., Londono, C. D., Zheng, D. & Zhao, X. An extreme toughening mechanism for soft materials. *Soft Matter* **18**, 5742–5749 (2022).

[373] Lee, S. & Pharr, M. Sideways and stable crack propagation in a silicone elastomer. *Proceedings of the National Academy of Sciences* **116**, 9251–9256 (2019).

[374] Li, C., Yang, H., Suo, Z. & Tang, J. Fatigue-resistant elastomers. *Journal of the Mechanics and Physics of Solids* **134**, 103751 (2020).

[375] Creton, C. & Ciccotti, M. Fracture and adhesion of soft materials: a review. *Reports on Progress in Physics* **79**, 046601 (2016).

[376] Akono, A.-T., Reis, P. M. & Ulm, F.-J. Scratching as a fracture process: From butter to steel. *Physical Review Letters* **106**, 204302 (2011).

[377] Swamynathan, S., Jobst, S., Kienle, D. & Keip, M.-A. Phase-field modeling of fracture in strain-hardening elastomers: Variational formulation, multiaxial experiments and validation. *Engineering Fracture Mechanics* **265**, 108303 (2022).

[378] Miehe, C., Welschinger, F. & Hofacker, M. Thermodynamically consistent phase-field models of fracture: Variational principles and multi-field fe implementations. *International Journal for Numerical Methods in Engineering* **83**, 1273–1311 (2010).

[379] Yu, Y., Landis, C. M. & Huang, R. Poroelastic effects on steady state crack growth in polymer gels under plane stress. *Mechanics of Materials* **143**, 103320 (2020).

[380] Ahmad, D., Patra, K. & Hossain, M. Experimental study and phenomenological modelling of flaw sensitivity of two polymers used as dielectric elastomers. *Continuum Mechanics and Thermodynamics* **32**, 489–500 (2020).

[381] Zhou, Y. *et al.* Flaw-sensitivity of a tough hydrogel under monotonic and cyclic loads. *Journal of the Mechanics and Physics of Solids* **153**, 104483 (2021).

[382] Chen, C., Wang, Z. & Suo, Z. Flaw sensitivity of highly stretchable materials. *Extreme Mechanics Letters* **10**, 50–57 (2017).

[383] Begley, M. R., Creton, C. & McMeeking, R. M. The elastostatic plane strain mode i crack tip stress and displacement fields in a generalized linear neo-hookean elastomer. *Journal of the Mechanics and Physics of Solids* **84**, 21–38 (2015).

[384] Long, R. & Hui, C.-Y. Crack tip fields in soft elastic solids subjected to large quasi-static deformation — a review. *Extreme Mechanics Letters* **4**, 131–155 (2015).

[385] Tan, Y., He, Y. & Li, X. Phase field fracture modeling of transversely isotropic piezoelectric material with anisotropic fracture toughness. *International Journal of Solids and Structures* **248**, 111615 (2022).

[386] Sridhar, A. & Keip, M.-A. A phase-field model for anisotropic brittle fracturing of piezoelectric ceramics. *International Journal of Fracture* **220**, 221–242 (2019).

[387] Long, R., Hui, C.-Y., Gong, J. P. & Bouchbinder, E. The fracture of highly deformable soft materials: A tale of two length scales. *Annual Review of Condensed Matter Physics* **12**, 71–94 (2021).

[388] Stephenson, R. A. The equilibrium field near the tip of a crack for finite plane strain of incompressible elastic materials. *Journal of Elasticity* **12**, 65–99 (1982).

[389] Logg, A., Mardal, K.-A. & Wells, G. (eds.) *Automated Solution of Differential Equations by the Finite Element Method*, vol. 84 (Springer Berlin Heidelberg, 2012).

[390] Rambausek, M. & Schöberl, J. Curing spurious magneto-mechanical coupling in soft non-magnetic materials. *arXiv* (2022).

[391] Pelteret, J.-P., Davydov, D., McBride, A., Vu, D. K. & Steinmann, P. Computational electro-elasticity and magneto-elasticity for quasi-incompressible media immersed in free space. *International Journal for Numerical Methods in Engineering* **108**, 1307–1342 (2016).

[392] Loew, P. J., Peters, B. & Beex, L. A. Fatigue phase-field damage modeling of rubber using viscous dissipation: Crack nucleation and propagation. *Mechanics of Materials* **142**, 103282 (2020).

[393] Zheng, D., Lin, S., Ni, J. & Zhao, X. Fracture and fatigue of entangled and unentangled polymer networks. *Extreme Mechanics Letters* **51**, 101608 (2022).

[394] Kumar, A. & Lopez-Pamies, O. The phase-field approach to self-healable fracture of elastomers: A model accounting for fracture nucleation at large, with application to a class of conspicuous experiments. *Theoretical and Applied Fracture Mechanics* **107**, 102550 (2020).

[395] Carrara, P., Ortiz, M. & Lorenzis, L. D. Data-driven rate-dependent fracture mechanics. *Journal of the Mechanics and Physics of Solids* **155**, 104559 (2021).

[396] Sánchez, P. A., Stolbov, O. V., Kantorovich, S. S. & Raikher, Y. L. Modeling the magnetostriction effect in elastomers with magnetically soft and hard particles. *Soft Matter* **15**, 7145–7158 (2019).

[397] Becker, T. I., Stolbov, O. V., Borin, D. Y., Zimmermann, K. & Raikher, Y. L. Basic magnetic properties of magnetoactive elastomers of mixed content. *Smart Materials and Structures* **29**, 075034 (2020).

[398] Bayaniahangar, R., Ahangar, S. B., Zhang, Z., Lee, B. P. & Pearce, J. M. 3-d printed soft magnetic helical coil actuators of iron oxide embedded polydimethylsiloxane. *Sensors and Actuators B: Chemical* **326**, 128781 (2021).

[399] Ceylan, H. *et al.* 3d-printed biodegradable microswimmer for theranostic cargo delivery and release. *ACS Nano* **13**, 3353–3362 (2019).

[400] Huang, H.-W., Sakar, M. S., Petruska, A. J., Pané, S. & Nelson, B. J. Soft micromachines with programmable motility and morphology. *Nature Communications* **7**, 12263 (2016).

[401] Schmidt, J., Marques, M. R. G., Botti, S. & Marques, M. A. L. Recent advances and applications of machine learning in solid-state materials science. *npj Computational Materials* **5**, 83 (2019).

[402] Kumar, S., Tan, S., Zheng, L. & Kochmann, D. M. Inverse-designed spinodoid metamaterials. *npj Computational Materials* **6**, 73 (2020).

[403] Liang, Q. *et al.* Benchmarking the performance of bayesian optimization across multiple experimental materials science domains. *npj Computational Materials* **7**, 188 (2021).

[404] Nguyen, L. T. K., Rambausek, M. & Keip, M.-A. Variational framework for distance-minimizing method in data-driven computational mechanics. *Computer Methods in Applied Mechanics and Engineering* **365**, 112898 (2020).